MECÁNICA DE MATERIALES V

EXPERIMENTACIÓN MODELADO NUMÉRICO Y TEÓRICO

MEMORIAS SMEC 2018

Jairo F. Useche, Ph.D

ISBN: 978-958-8862-50-7

Universidad Tecnológica de Bolívar
CARTAGENA DE INDIAS

MECÁNICA DE MATERIALES V

EXPERIMENTACIÓN
MODELADO NUMÉRICO Y TEÓRICO

Institución editora

Facultad de Ingeniería - Universidad Tecnológica de Bolívar

ISBN: 978-958-8862-50-7 (digital)

Contacto:

Prof. Jairo F. Useche, Ph.D

Director de Investigaciones, Emprendimiento e Innovación

Universidad Tecnológica de Bolívar

Parque Industrial Vélez – Pombo, km.1

Tel/fax: +575 6535200 ext 331

smec@utb.edu.co

August 29, 2018

MECÁNICA DE MATERIALES V

EXPERIMENTACIÓN
MODELADO NUMÉRICO Y TEÓRICO

MECÁNICA DE MATERIALES V

EXPERIMENTACIÓN
MODELADO NUMÉRICO Y TEÓRICO

Conference Program

OPENFOAM 3D Modeling of Melt Spinning Process in Non-Planar Geometry

A. Maroni[1], M. Pagnola[2,a], J. Moya[1], M. Malmoria[2]

[a]mpagnola@fi.uba.ar
[1]Grupo Interdisciplinario en Materiales, INTECIN UBA-CONICET, IESIING
Universidad Católica de Salta
Argentina
[2]University of Buenos Aires,
National Council of Scientific and Technical Research,
Institute of Technology and Engineering Sciences 'Hilario Fernández Long' (INTECIN),
Buenos Aires, Argentina

Abstract

Melt spinning is an industrial process used for the production of metallic glasses. It is a rapid solidification process whereby a liquid metal is ejected at high pressure and temperature via a nozzle onto a rotating copper wheel by solidifying in the form of a thin ribbon. In this work, we perform a 3D simulation model to reproduce the melt spinning process to get amorphous magnetic material, starting from an alloy with chemical composition $Fe_{75}Si_{10}B_{15}$(% at.). A ***CFD*** model in the OpenFoam® open source code is proposed and applied, which is based on the Finite Volume Method (***FVM***) and Volume of Fluid Method (***VOF***). The entire process without solidification is analyzed simply as a preliminary study of the ejection conditions during the melt, in order to avoid posterior turbulence in the film that would cause irregularities in subsequent stages of solidification. This preliminary analysis aims to study the generation of a regular film of molten material on a rotating cylindrical geometry. In the ***FVM*** method the coupled incompressible laminar momentum and continuity equations are solved at each time step on every mesh cell, while in the ***VOF*** scheme the fluid properties are weighed average of those of air and molten metal. The complete geometry is discretized in a block-structured mesh of pure hexahedra. The profile and dimensions of the resulting meniscus and ribbon during the transient are in good agreement with our previous numerical results.

Key Words: Melt Spinning, Solidification, Magnetic Materials, OpenFOAM®, CFD, Volume of Fluid, Numerical Methods for Multiphase Flow

1 Introduction

Metallic alloys and materials of amorphous and nanocrystalline structure have found widespread applications in industry and science. Therefore, the study and further improvement of industrial processes involved in their manufacturing is an active area of engineering research and development, attracting interest and effort from many scientific disciplines [1]. One of the most popular and promising of those production methods, the Chill Block Melt Spinning (CBMS), consists basically in an ultra-fast, almost instantaneous, solidification of molten material induced upon contact with a rotating cold surface. This way, very thin ribbons of relatively continuous width and thickness can be easily produced of desired lengths, possessing uniform material structure ranging from amorphous to nanocrystalline, depending on some variables process such as chemical composition of the alloy, velocities, temperatures, pressures of the process, etc. In the literature [2],

[3], [4], [5], and [6], there are some works where it is intended to model these parameters either mathematically or numerically. In this work we present our first results using the ***OpenFOAM™*** software to simulate, in ***3D***, the process prior to solidification and formation of the ribbon, taking into account pressures and velocities of the process and the viscosity of a $\boldsymbol{Fe_{75}Si_{10}B_{15}}$ alloy.

2 Outline of the CBMS Process

In spite of its apparent simplicity, CBMS involves a large number of process variables, some much harder to define and control than others, intertwined in complex chemical and mechanical interactions. Chemical variables, like alloy composition and controlled atmosphere, are usually fixed at the very beginning, whereas a small set of geometric variables, like nozzle-wheel gap and wheel width, are standardized according to the use of the ribbon as a final product.

3 Governing Equations and Numerical Method

The incompressible, viscous, time-dependent Navier-Stokes and continuity equations govern the mechanics of the fluid flow in a simple, connected domain Ω:

$$\begin{aligned} \partial_t \mathbf{u} + \mathbf{u} \cdot \nabla \mathbf{u} &= -\nabla p + \nu \nabla^2 \mathbf{u}, \qquad && x \in \Omega, \\ \nabla \cdot \mathbf{u} &= 0, && x \in \Omega. \end{aligned}$$

Let us first partition our fluid flow domain into non-overlapping polyhedral control volume cells, so that, by integrating the first of equations (1) over cell k, and applying the divergence theorem, we arrive at:

$$\mathbf{V}_k \frac{\partial u_i}{\partial t} + \oint_k u_i \mathbf{u} \cdot d\mathbf{A} = \oint_k \nu \overrightarrow{\nabla u_i} \cdot d\mathbf{A} - \oint_k p \hat{\boldsymbol{\imath}}_i \cdot d\mathbf{A},$$

where V_k is the volume of cell k, $\widehat{\imath}_i$ is the i-the orthonormal unit vector in the spatial basis, and the surface integrations are performed over the entire control volume boundary. Carrying out low order surface integrations, we obtain a discrete set of algebraic equations for each cell k:

$$\mathbf{V}_k \frac{\partial u_i}{\partial t} = \sum_{\text{Faces of } k} \left\{ \nu \sum \frac{\partial u_i}{\partial x_j} A_j - p A_i - u_i \sum u_j A_j \right\}_{\text{face}},$$

in which face pressure and velocity, as used in left-hand-side calculations, are taken as the face averages. Simultaneously, pressure must be calculated by solving the Poisson equation that results from the system of equations (1):

[Warning: Image ignored]

Where $\mathrm{L} = \nabla \mathrm{u}$ is the velocity gradient tensor. Methods to solve equations (3) and (4) include SIMPLE, SIMPLER, SIMPLEC, PISO, etc. Briefly speaking, the **VOF** method solves the above system of equations for a fluid whose physical properties are weighted averages of those of the two fluids present in a cell. The weight used, denoted γ, is such that, in any cell, the actual mass density is

$$\rho = \gamma \rho_{fluid1} + (1 - \gamma)\, \rho_{fluid2},$$

so that γ can also be called void fraction of fluid 1. A scalar transport equation is used to model the void fraction. Also, an extra term is added to ∇p to account for the surface tension force at the free surfaces, which is the interface between both fluids.

4 Domain Geometry and Grid Generation

The entire simulation domain, consisting of crucible, nozzle, and the atmospheric body around the gap, between nozzle and wheel, is 3D-modelled with dimensions as shown in ***Figure 1.***

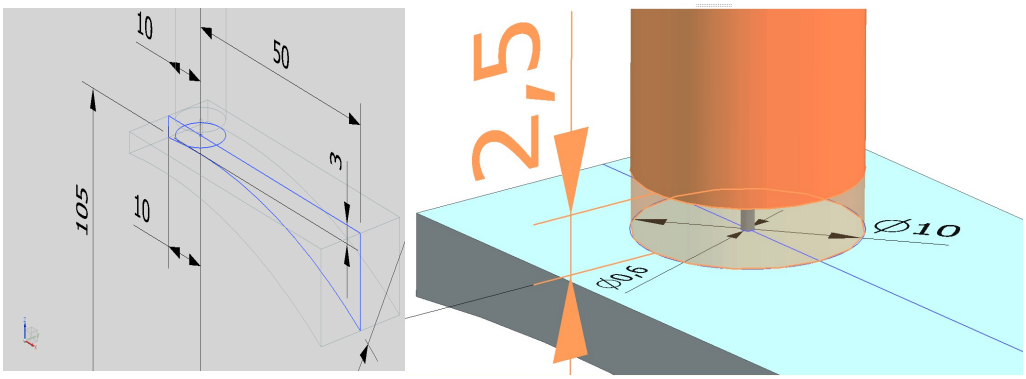

Figure 1. Dimensions of the atmospheric sub-domain extrusion (left) and of the gap and crucible (right).

A spatial discretization is carried out by dividing the domain into simply connected structured blocks, as shown in ***Figure2.a.*** Boundary layer clustering is applied on the wheel wall as well as along the ribbon and puddle, as depicted in ***Figure 2.b***, in which only the nozzle mesh is shown, along with the grid in the nozzle and around the puddle.

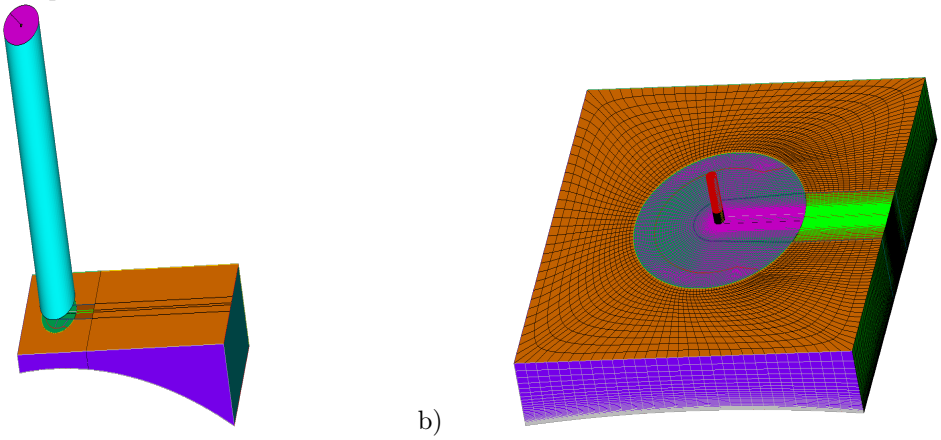

a) b)

Figure 2. a) Block partitioning for discretization. b) Detail of meshing in area around the gap and nozzle.

The total number of resulting finite volume cells was 556k Hexas, mostly clustered in the gap area shown in ***Figure 2.b.***

5 Fluid Properties and Flow Parameters

Phase 1 is set as air at 20 ℃, with $\rho = 1.225 kg/m^3$ and $\mu = 1.7894 \bullet 10^{-5} Ns/m^2$, whereas phase 2 is a molten $Fe_{75}Si_{10}B_{15}$ alloy with $\rho = 7400 kg/m^3$ and $\mu = 5.51 \bullet 10^{-2} Ns/m^2$. The surface tension force has been modeled using the "Continuum Surface Stress" scheme, with $\sigma = 0.367 N/m$. The working atmospheric pressure is 1 atm and the wheel tangential velocity is 40 m/s. The molten alloy flow rate at the nozzle was regulated partly by setting a crucible metal load height of almost 50 mm, and fine-tuned with a flow rate at the crucible top face.

6 Main Results

Time integration was performed with a first order implicit Euler scheme which allowed for greater ***CFL*** flexibility than the explicit method. Therefore, a fixed time step was used that was small enough to have the molten material cross the gap in at least 10 time steps. As expected, the molten metal forms a poodle on hitting the cold copper wheel, as shown in ***Figure 3***, then winds down into a ribbon, which, after a few centimeters, settles at a uniform width of $1.12 \bullet 10^{-3} m$ and a thickness of $37.05 \bullet 10^{-6} m$, as depicted in ***Figure 4.a*** and ***4.b.*** Boundary layer contours were also added in ***Figures 3.a*** and ***4.b***. These values are in close agreement with *Pagnola et al.*[7]

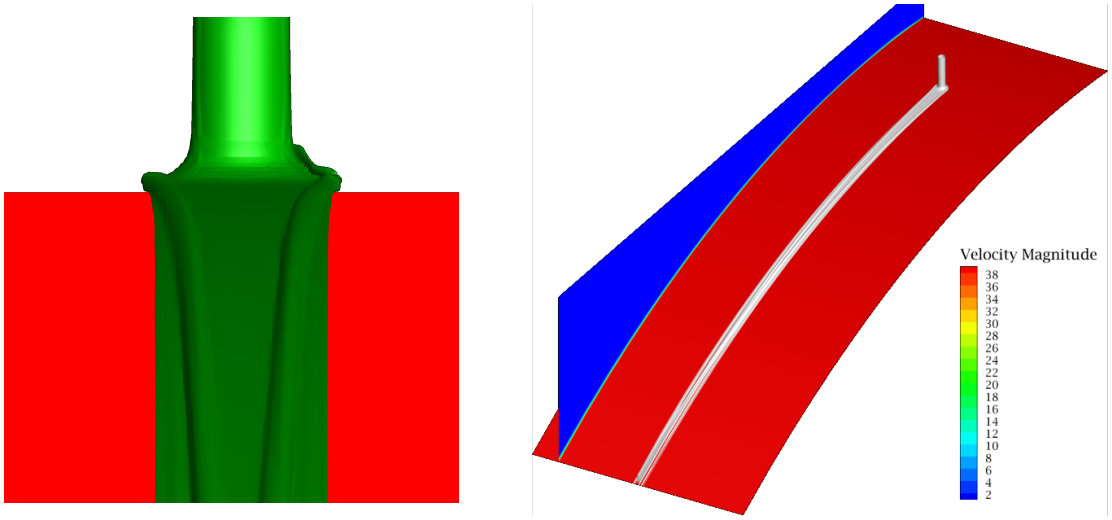

Figure 3. Ribbon at last time step, a) isometric view, b) and front view.

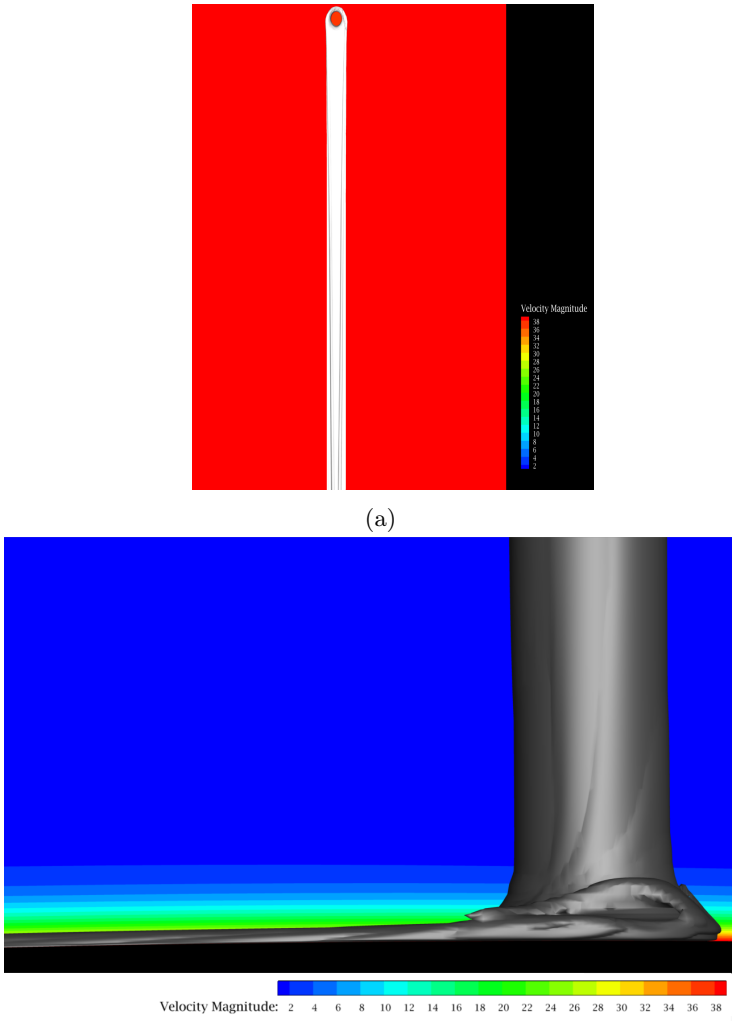

(a)

(b)

Figure 4. Ribbon at last time step, a) upper view, and b) side view.

7 Conclusions

Full ***3D CFD*** simulations of ***CBMS*** casting process have been performed in ***OpenFOAM™*** which continue our previous work [8], and, whereas based on the same model equations and displaying very good agreement with their results, add the obvious advantages of producing fully ***3D*** meniscus along with ribbon texture and features not seen in their work. This encourages us to continue our work by incorporating extra multi-physics modeling, i.e., heat transfer and solidification in future researches that complete the progress made [7,8].

References

[1] V.P. Sharma, U. Sharma, M. Chattopadhyay, V.N. Shukla, Advance Applications of Nanomaterials: A Review, Materials Today: Proceedings, Elsevier, Volume 5, Issue 2, Part 1, 2018, Pages 6376-6380.doi: doi.org/10.1016/j.matpr.2017.12.248.

[2] H.H. Liebermann, The dependence of the Geometry of glassy alloy ribbons on the chill block melt-spinning process parameters, Mater. Sci. Eng. 43 (1980) 203–210. doi:10.1016/0025-5416(80)90103-2.

[3] Y.K. Li, Y. Yang, Y.M. Song, F.R. Zhang, Numerical Simulation of Flow and Heat Transfer for Cooling Roller in Amorphous Spinning Process, Adv. Mater. Res. 1142 (2017) 276–281. doi:10.4028/www.scientific.net/AMR.1142.276.

[4] G.-X. Wang, E.F. Matthys, Modelling of rapid solidification by melt spinning: effect of heat transfer in the cooling substrate, Mater. Sci. Eng. A. 136 (1991) 85–97. doi:10.1016/0921-5093(91)90444-R.

[5] V.I. Tkatch, S.N. Denisenko, B.I. Selyakov, Computer simulation of Fe80B20 alloy solidification in the melt spinning process, Acta Metall. Mater. 43 (1995) 2485–2491. doi:10.1016/0956-7151(94)00413-7.

[6] V.I. Tkatch, A.I. Limanovskii, S.N. Denisenko, S.G. Rassolov, The effect of the melt-spinning processing parameters on the rate of cooling, Mater. Sci. Eng. A. 323 (2002) 91–96. doi:10.1016/S0921-5093(01)01346-6.

[7] M.R. Pagnola, M. Barone, M. Malmoria, H. Sirkin, Influence of z /w relation in Chill Block Melt Spinning (CBMS) process and analysis of thickness in ribbons, Multidiscip. Model. Mater. Struct. 11 (2015) 23–31. doi:10.1108/MMMS-02-2014-0008.

[8] M. Pagnola, M. Malmoria, M. Barone, Biot number behaviour in the Chill Block Melt Spinning (CBMS) process, Appl. Therm. Eng. 103 (2016) 807–811. doi:10.1016/j.applthermaleng.2016.04.077.

An Iso-Geometric Boundary Element Method Formulation for the Study Of Galvanic Corrosion in Spatial Thin-Walled Structures

H. De Avila[1], J. Useche[2]

[1]hdeavila1992@gmail.com
Departamento de Ingeniería Mecáánica,
Universidad Tecnológica de Bolívar, Cartagena, Colombia

[2]juseche@utb.edu.co
Departamento de Ingeniería Mecáánica,
Universidad Tecnológica de Bolívar, Cartagena, Colombia

Abstract

A formulation of the isogeometric boundary elements method is presented. The method is applied in calculation of potential distribution and electric flow density between two submerged metals within an electrolyte with variable height. The boundary is generated from 5 B-spline curves and the meshing is done with the knot refinement technique. Singular integrals are calculated using the subdivision of elements and rigid body technique. Finally, the results obtained are compared with the analytical equations.

Key Words: Isogeometric, Boundary element, Electrolyte

1 Introduction

Corrosion can be defined as the conversion of a metal alloy to an inorganic component of low energy,such as oxides, sulphides and carbonates, accompanied by a mass transfer of this component to the surrounding medium.This conversion is activated mainly by the acids of the surrounding environment and is accelerated by heat processes (hot corrosion), tensile loads (stress corrosion cracking) and the presence of a second metallic alloy (galvanic corrosion).Many metallic structures in the industry are subjected to these conditions of activation and/or acceleration that negatively affect their mechanical integrity by weakening the walls or its Mechanics properties (strength, stiffness,.. etc.). Thin-walled structures such as steel pipes or the hull of ships are affected by these phenomena and the economic, environmental and social consequences of failures in these are serious issuses (Hansson [2011], Kermani et al. [1996]).Understanding the different corrosion activation mechanisms allows us to understand how to prevent or mitigate its effect. In the case of galvanic corrosion is key to understand how the electrical potential is distributed between the two metal alloys to apply the corrective measures in a more efficient way.

Several research works on this subject use analytical solutions of the partial differential equations that govern this phenomenon, to model the response of various thin wall structures to different Types of galvanic corrosion. However, analytical solutions are difficult to find for different geometries, so there is a strong tendency to use numerical methods. Zamani et al. [1986] discusses the efforts made in the investigation of numerical methods capable of solving the governing equation of Laplace that allows to determine the distribution of

electrical potential presented between the interaction of an anode and a cathode in a Electrolytic medium, its work concluded that the boundary element method(BEM) is the most suitable technique for corrosion calculations. This position is also defended in the works of Brebbia and Dominguez [1994], Brebbia [1980], Brebbia and Dominguez [1977], K.AmayaAmaya and Aoki [2003], S.Aoki Aoki and Kishimoto [1991] and J.X.JiaJia et al. [2004, 2007].

BEM is based on the discretization of integral boundary equation(BIE) and this method can be applied to a wide spectrum of physical problems within the field of computational modeling Bonnet [1999]. Its main advantage lies in the fact that it is only necessary to discretized (create a mesh) The contour of the problem, this allows to significantly reduce the computational cost related to this activity and to decrease time of analysis Beer et al. [2008]. However, as in the case of finite elements, it requires the process of refining mesh, to ensure the convergence of the method in a specific problem. This process requires constant communication with Computer aided drawing (CAD) software. This activity consumes a significant amount of time that does not directly contribute to the solution of the problem (but is indispensable). T.J.R. Hughes Hughes et al. [2005] proposes Isogeometric analysis (IGA) as an alternative solution. They propose to use the exact geometric information from the CAD software through the use of the base functions which are very used by the curves and NURBS surfaces (non-uniformal rotational B-spline). The use of these functions also allows to carry out remeshing processes more easily without the communication of a CAD system, since the technique of Knot-refinement can generate finer meshes from the original grid, keeping in All levels of the remeshing geometric accuracy. In this work, its proposed a formulation of isogeometric constant boundary elements to be applied to the calculation of electrochemical potential distribution presented in a galvanic cell. The document is structured in the following way. The formulation of isogeometric boundary elements is proposed(IGABEM). explanations of how to calculate the singular integrals are given and finally proposed an examples of application of the method. The results show that the developed formulation is a reliable alternative as design tool in engineering

2 Isogeometric boundary elements Formulation

In this formulation, the B-spline curves are used to interpolate the geometry, but the solution space will be interpolated with elements of constant variation, this is because it is simpler to work with the strongly singular integrals in this way, since it can be apply rigid body. The typical integral equation of boundary elements for the solution of the Laplace equation in an isotropic medium, uniform and without potential source in the domain is:

$$\epsilon(P)\phi(P) = \int_{\Gamma} \left[\phi^*(P,Q)\overline{q} - \overline{\phi}q^*(P,Q)\right] d\Gamma \tag{1}$$

$$\left.\begin{array}{ll} 1 & \text{para } P \text{ inside } \Omega \\ 0 & \text{para } P \text{ outside } \Omega \end{array}\right\} \epsilon(P)$$

where:
$\Gamma = \{\Gamma_a + \Gamma_b\}$ The full contour
$\{\overline{\phi}, \overline{q}\}$ Potential and known flow in the contour.
$\{\phi^*, q^*\}$ Fundamental solutions.
$\{P, Q\}$ Source point and field point

As the contour will be modeled as one or several B-splines, the differential $d\Gamma$ changes to:

$$d\Gamma = J_e du \tag{2}$$

where J_e is the Jacobian

$$J_e = \sqrt{\left(N'_{i,p}P_x\right)^2 + \left(N'_{i,p}P_y\right)^2} \tag{3}$$

Where $N'_{i,p}$ is the basis function derivative. This basis function are generated from an algorithm witch has tree main inputs, the node vector, which must be not negative and not decreasing $U = [u_0, u_1, u_2, .., u_{m-1}, u_m]$, the parameter u_i and the degree of the polynomial p. The i-th term of the base function is calculated as follows:

$$N_{i,0}(u) = \begin{cases} 1 & \text{si } u_i \leq u < u_{i+1} \\ 0 & \text{de lo contrario} \end{cases}$$

$$N_{i,p}(u) = \frac{u - u_i}{u_{i+p} - u_i} N_{i,p-1}(u) + \frac{u_{i+p+1} - u}{u_{i+p+1} - u_{i+1}} N_{i+1,p-1}(u) \tag{4}$$

The derivative is define as:

$$N'_{i,p} = \frac{p}{u_{i+p} - u_i} N_{i,p-1}(u) - \frac{p}{u_{i+p+1} - u_{i+1}} N_{i+1,p-1}(u) \tag{5}$$

Then to represent higher derivatives we will denote $N^k_{i,p}(u)$ as the kth derivative of $N_{i,p}(u)$:

$$N^k_{i,p} = \frac{p}{p-k} \left(\frac{u - u_i}{u_{i+p} - u_i} N^k_{i,p-1} + \frac{u_{i+p+1} - u}{u_{i+p+1} - u_{i+1}} N^k_{i+1,p-1} \right) \tag{6}$$

Finally replacing 3 and 2 in 1 is obtained:

$$\epsilon(P)\phi(P) = \int_\Gamma (u) \left[\phi^*(P,Q)\overline{q} - \overline{\phi} q^*(P,Q) \right] J_e du \tag{7}$$

In the traditional method the contour is subdivided into straight elements, in which it is known that its source points are in the center, in the case of the isogeometric formulation, one element is the interval between two nodes u_i and u_{i+1} where $u_{i+1} - u_i < 0$, is also known as knot-span, the source point is calculated by the equation 8

$$p = \frac{u_i + u_{i+1}}{2} \tag{8}$$

The solution to the integral equation, approaching Γ with M knot-span is:

$$\epsilon(P)\phi(P) + \sum_{i=1}^{M} \int_{\Gamma_u} \overline{\phi} q^*(P_j, Q) J^i_e du = \sum_{i=1}^{M} \int_{\Gamma_u} \phi^*(P_j, Q) \overline{q} J^i_e du \tag{9}$$

Where Γ_u is the integration interval $\{u_i, u_{i+1}\}$. The equation can be assembled in a linear system of equations like the following:

$$H\phi = GI \tag{10}$$

Where H and G are the influence matrices, ϕ and I are the potential and the known flow in the contour. It should be noted that the knot span can be associated with a curved section of the contour, consequently the analytical solution of the weak singularity integrals, proposed for elements of constant variation, do not apply. Therefore, for the case of these integrals, the technique of subdivision of the element is used, this technique allows dividing the element into smaller regions and solving the integrals with Quadrature of Gauss-Legendre, so that the total result, be the total of the sum of said integrals. In this work a total of six subdivisions are made in the element. On the other hand, strongly singular integrals only exist as Cauchy principal value, so they can only be solved indirectly through rigid body motion, adding the non-singular terms outside the main diagonal as shown in the equation. 11

$$H^{ii} = -\sum_{i=1}^{M} H^i \quad \text{for } i \neq j \tag{11}$$

3 Calculation of potential and current density in galvanic cell

The IGABEM formulation is used to calculate the distribution of flux and potential on the surface of an anode and a cathode, within an electrolytic medium. Here a Thin-Walled galvanic cell model, similar to that presented in Jia et al. [2004] is analyzed. The boundary condition for the galvanic couple are:

$$I(0, x_2) = I(a, x_2) = I(x_1, w) = 0 \tag{12}$$

$$\phi(x, 0) + R_p I(x, 0) = \phi_a H(x - c) \tag{13}$$

Where H is the Heaviside step function and Rp is the polarization parameter and ϕ_a is the potential differential between the anode and the cathode. Since there is a non-linear relationship between the anode and the cathode, the numerical solution is obtained by implementing the iterative solution scheme reported in Aoki and Kishimoto [1991]. finally the solution obtained is compared with the analytical solution reported in Waber and Fagan [1956].

For this case, the constant $\phi_a = 1.0V$ and the polarization parameter $R_p = 1.0$ for a galvanic cell of $a = 1cm$, $c/a = 0.5$ and w/a has the values 0.5, 0.1, 0.05 and 0.005. The values of current and potential density are shown in the figure 3(a) and 3(b), while the geometric configuration and the distribution of nodes are shown in the figure 1(a) and 1(b).

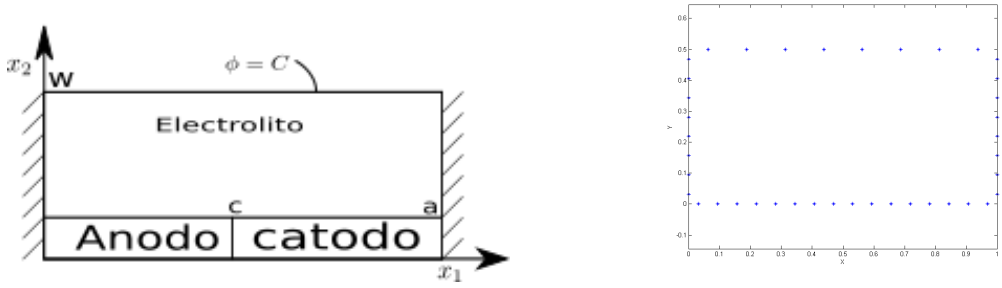

(a) (b)

Figure 1: (a) GEOMETRIC CONFIGURATION OF THE CELL; (B) IGABEM MESH FOR THE GALVANIC CELL

The contour of the cell is generated with 5 linear B-spline, with a medium conductivity equal to $1.0\Omega^{-1}cm-1$, the mesh was generate with the knot refinement technique (Piegl and Tiller [2012]) and has a size of 96 knot-span with 16 of these, evenly distributed over the cathode and the anode.

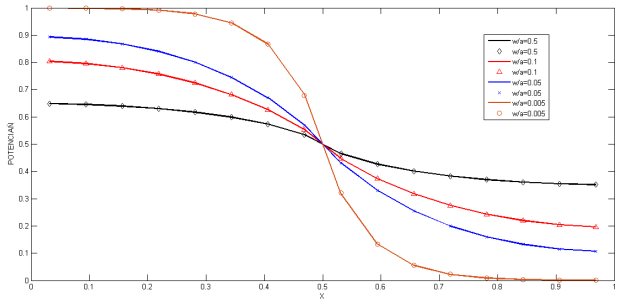

(a)

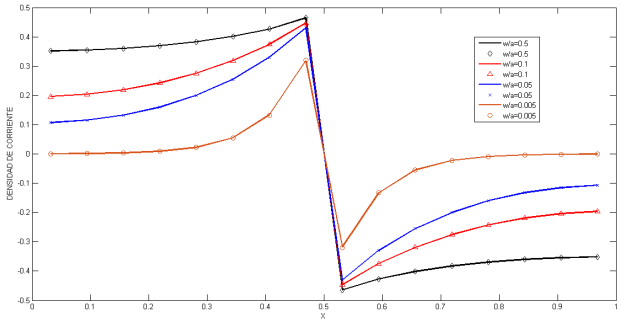

(b)

Figure 2: (a) VALUES CALCULATED OF POTENTIAL USING IGABEM VERSUS ANALYTICAL VALUES (SYMBOLS); (B) CALCULATED CURRENT DENSITY VALUES USING IGABEM VERSUS ANALYTICAL VALUES

4 Analysis and discussion of results

IGABEM method was used to perform calculation of flux and potential on thin wall galvanic cell for different electrolytes heights. The results where compared with the analytic solution, error figures show that the discrepancy between the numerical formulation and the analytic solution are below 1% for the relationship $w/a = 0.5$, $w/a = 0.1$ and $w/a = 0.05$, but when $w/a = 0.005$ the potential error increase to 30% in the left size, on the cathodic zone where the absolute value of potential tends to zero, while the flux error increase to 40% om both size, where the absolute value of flux tends to zero. It is important to note that the constant elements are uniformly distributed in the contour, while in previous studies the elements are concentrated at the intersection between the anode and the cathode. It is intended, then, to develop in future work, a knot refining technique that allows concentrating the knot-span around a specific point. On the other hand, subdividing an element into six parts to develop the integrals of weak singularity, is computationally inefficient, therefore more research should be done in this aspect.

5 Conclusions

The IGABEM method is an easy implementation method that allows calculations of potential distribution and electric current density in galvanic cells, the method is tested under different electrolyte heights maintaining the same nodal distribution for each height, it is found that the relative error increases significantly when the height of the electrolyte tends to zero, but stays below 1% for higher heights, this does not mean that

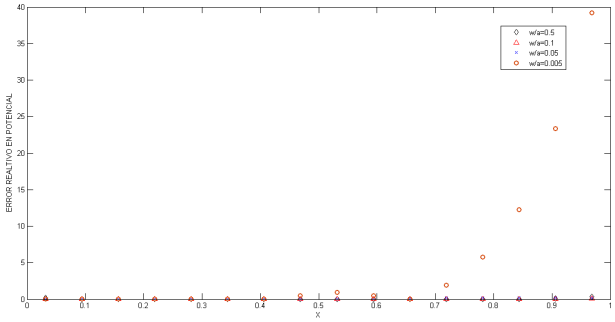

(a)

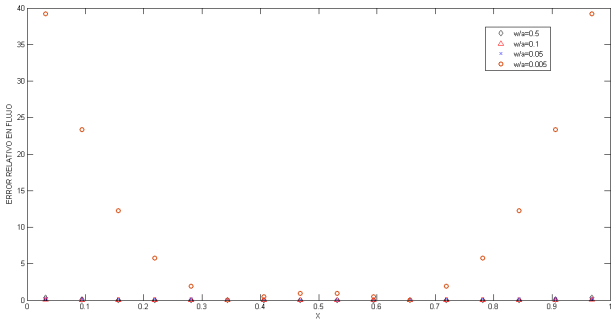

(b)

Figure 3: (a) RELATIVE ERROR BETWEEN ANALYTICAL POTENTIAL AND POTENTIAL CALCULATED WITH IGABEM; (B) RELATIVE ERROR BETWEEN ANALYTICAL FLOW AND CALCULATED FLOW WITH IGABEM

there is an error in the method, it means that the number of constant elements that model the contour must increase in the extent to which the height of the electrolyte decreases.

References

CM Hansson. The impact of corrosion on society. *Metallurgical and Materials Transactions A*, 42(10): 2952–2962, 2011.

MB Kermani, Don Harrop, et al. The impact of corrosion on oil and gas industry. *SPE Production & Facilities*, 11(03):186–190, 1996.

NG Zamani, JF Porter, and AA Mufti. A survey of computational efforts in the field of corrosion engineering. *International Journal for Numerical Methods in Engineering*, 23(7):1295–1311, 1986.

Carlos Alberto Brebbia and Jose Dominguez. *Boundary elements: an introductory course*. WIT press, 1994.

Carlos Alberto Brebbia. *The boundary element method for engineers*. Pentech press, 1980.

CA Brebbia and J Dominguez. Boundary element methods for potential problems. *Applied Mathematical Modelling*, 1(7):372–378, 1977.

K Amaya and S Aoki. Effective boundary element methods in corrosion analysis. *Engineering Analysis with Boundary Elements*, 27(5):507–519, 2003.

S Aoki and K Kishimoto. Prediction of galvanic corrosion rates by the boundary element method. *Mathematical and Computer Modelling*, 15(3-5):11–22, 1991.

JX Jia, Guangling Song, A Atrens, D St John, J Baynham, and G Chandler. Evaluation of the beasy program using linear and piecewise linear approaches for the boundary conditions. *Materials and Corrosion*, 55(11): 845–852, 2004.

Jimmy X Jia, Guangling Song, and Andrej Atrens. Experimental measurement and computer simulation of galvanic corrosion of magnesium coupled to steel. *Advanced Engineering Materials*, 9(1-2):65–74, 2007.

Marc Bonnet. Boundary integral equation methods for solids and fluids. *Meccanica*, 34(4):301–302, 1999.

Gernot Beer, Ian Smith, and Christian Duenser. *The boundary element method with programming: for engineers and scientists*. Springer Science & Business Media, 2008.

Thomas JR Hughes, John A Cottrell, and Yuri Bazilevs. Isogeometric analysis: Cad, finite elements, nurbs, exact geometry and mesh refinement. *Computer methods in applied mechanics and engineering*, 194(39-41): 4135–4195, 2005.

James T Waber and Bertha Fagan. Mathematical studies on galvanic corrosion iv. influence of electrolyte thickness on the potential and current distributions over coplanar electrodes using polarization parameters. *Journal of The Electrochemical Society*, 103(1):64–72, 1956.

Les Piegl and Wayne Tiller. *The NURBS book*. Springer Science & Business Media, 2012.

Dynamic Analysis of Elastic Membranes Coupled to Acoustic Fluids Using a Compact BEM Formulation

A. Narváez[1], J. Useche[2]

[1]anarvaez@unitecnologica.edu.co
Departamento de Ingeniería Mecánica,
Universidad Tecnológica de Bolívar, Cartagena, Colombia

[2]juseche@unitecnologica.edu.co
Departamento de Ingeniería Mecánica,
Universidad Tecnológica de Bolívar, Cartagena, Colombia

Abstract

In this paper the dynamic behavior of elastic membranes interacting with acoustic fluids is presented. For this, computational models based on a new fluid-structure interaction formulation, based on a full monolitic Boundary Element Method, is developed. Fluids are modeled using the three dimensional acoustic wave equation for ideal acoustic fluids. The dynamic response of the elastic membrane is modeled using the classical theory of linear elastic membrane based on the bi-dimensional wave equation. Boundary Element Method formulations for both fluid and membrane uses static fundamental solutions of the governing equations. In this way, existing boundary element codes can be used for the analysis of this kind of problems. Developed formulation leads to significant saving in computational time analysis of such problems. Numerical examples are presented.

Key Words: Boundary Element Method,Vibro-acoustic,Fluid structure interaction,Acoustic fluids,Elastic membranes,Dynamic analysis

1 Introduction

Nowdays fluid-structure interaction problems involving acoustic fluids and deformable structures have a wide application in acoustic ocean engineering. Whenever an elastic structure is in contact with a fluid, the structural vibrations and the acoustic pressure field in the fluid are influenced by the mutual vibro-acoustic coupling interaction. Design of vibro-acoustic control, noise isolation and sound detection problems, among others, require the study of coupled structures and sound waves [7, 15, 19]. Significant efforts are carried out in the development of acoustically invisible structures (low acoustic signature) for which the study of the behavior of acoustic fluids coupled to flexible structures is necessary.

Solution of governing equations describing fluid-structure interaction problems requires the use of computational tools. Most of these problems involves fluids contained in three-dimensional domain coupled elastic structures with cumbersome geometry. The use of discretization domain numerical methods, such as the Finite Element Method (FEM) or the Finite Difference Method (FDM), requires the use of refined three dimensional meshes, which leads a significant increase in the computational cost of the solution. To overcome this disadvantage, meshless methods such as the Boundary Element Method (BEM) are used in order to model the fluid [3, 4, 5, 6, 8, 9, 10, 11]. Although this approach allows a significant reduction in the number of degrees of freedom of the problem, still it is necessary to discretize the entirely structure due to the use of

the FEM. The main advantage of the BEM is its unique ability to provide a complete solution in terms of boundary values only, with substantial savings in modelling effort [1, 2].

Despite of study of dynamic behavior of elastic membranes interacting with acoustic fluids represent a relevant engineering problem nowdays, few BEM-BEM coupled formulations for fluid-structure interaction problems have been published [12, 13] in the last decade.

In this work, a new full BEM formulation for the dynamic analysis of acoustic fluids coupled to elastic membranes is presented. Membranes are modeled using a BEM formulation based on the linear elastic membrane theory. Acoustic fluid is modeled using a BEM formulation for the three dimensional acoustic wave equation. Fluid-structure coupling equations were established considering the continuity of the normal acceleration of the particles at fluid-structure interfaces. Domain integrals are transformed to boundary integrals using the Dual Reciprocity Boundary Element Method. The developed formulation was used to study the linear vibration response of elastic membranes coupled to acoustic fluids. Numerical exampled are presented in order to stablish the accuracy of the proposed formulation.

2 Mathematical equations

Consider a partially opened domain Ω_f partially by a flexible elastic membrane Ω_s with mass density ρ_s and thickness h (see figure 1). Cavity contains an homogeneous and isotropic acoustic fluid with mass density ρ_f. The membrane vibrations and the acoustic pressure field in the fluid are influenced by the mutual vibro-acoustic coupling interaction. In this work, the vibro-acoustic coupling interaction is modeled using an eulerian formulation where the acoustic response is described by the pressure, while the membrane response is described by the transversal displacement field.

2.1 Acoustic wave equation

The dynamic pressure of an ideal inviscid fluid under small perturbations in a spatial region Ω_f confined by the boundary surface $\Gamma_f = \Gamma_f^p \cup \Gamma_f^q$, is governed by the wave equation as shown in figure 2 [14]:

$$c_f^2 \nabla^2 p = \ddot{p} \tag{1}$$

In this equation p is the fluid pressure, $c_f^2 = \kappa/\rho_f$ stands for wave propagation velocity and κ is the bulk modulus. This equation can be modified to include the effect of presence of an acoustic source. Double dot represents a second time derivative. Indicial notation is used throughout this work. Greek indices vary from 1 to 2 and Roman indices from 1 to 3.

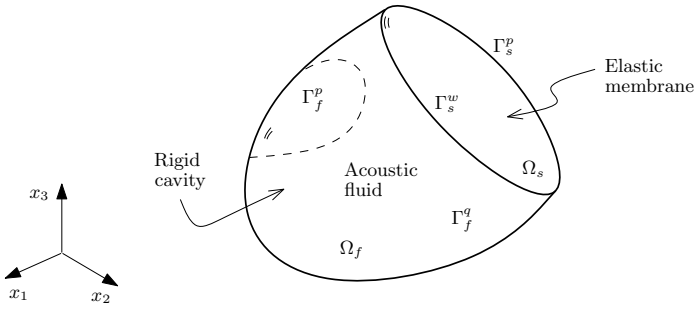

Figure 1: Fluid-structure domain

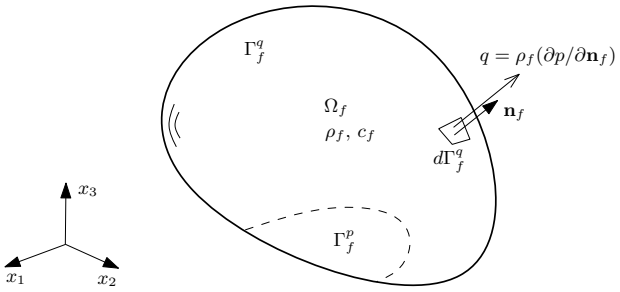

Figure 2: Acoustic domain

2.2 Dynamic equation of elastic membrane

Now consider a linear elastic membrane with thickness h ocuppying the spatial domain Ω_w confined by the boundary $\Gamma_s = \Gamma_s^w \cup \Gamma_s^f$ as presented in figure 3. An initial tension T_0 is uniformly applied to the membrane. In this work, the small deflection elastic membrane theory is considered. Thus, differential equation describing the trasversal displacement $w(\mathbf{x}, t)$ of this membrane in the time interval $[0, t^*]$ is given by:

$$T_0 \nabla^2 w + p_w = \rho_s \ddot{w} \tag{2}$$

where $p_w(\mathbf{x}, t)$ is a distributed pressure applied over the membrane.

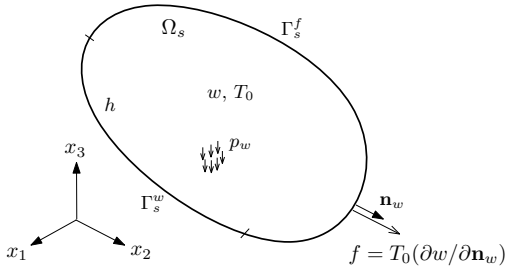

Figure 3: Membrane domain

3 Boundary element equations

3.1 Boundary element equations for acoustic wave equation

The derivation of the integral formulation for equation (1) is based on application of the Boundary Element Method to the acoustic wave equation as presented in [2]. Thus, by using the weighted residual method and making use of the Green's identity, the following equation is obtained:

$$\begin{aligned} c(\mathbf{x}')p(\mathbf{x}') + \int_{\Gamma_f} Q(\mathbf{x}', \mathbf{x}) p(\mathbf{x}) \mathrm{d}\Gamma_f = \int_{\Gamma_f} P(\mathbf{x}', \mathbf{x}) q(\mathbf{x}) \mathrm{d}\Gamma_f \\ + \frac{1}{c_f^2} \int_{\Omega_f} P(\mathbf{x}', \mathbf{X}) \ddot{p}(\mathbf{X}) \mathrm{d}\Omega_f \end{aligned} \tag{3}$$

In this equation, $\mathbf{x}'$ and $\mathbf{x}$ represent collocation and field points, respectively; $P(\mathbf{x}', \mathbf{x})$ and $Q(\mathbf{x}', \mathbf{x})$ are fundamentals solutions for pressure and gradient pressures for three dimensional acoustic problems, respectively, as presented in [2]. The value of $c(\mathbf{x}')$ is equal to $\frac{1}{2}$ when $\mathbf{x}'$ is located on a smooth boundary.

In order to threat the domain integral, the Dual Reciprocity Boundary Element Method (DRM) is used as presented in [16]. In this way, equation (3) can be re-written as:

$$c(\mathbf{x}')p(\mathbf{x}') + \int_{\Gamma_f} Q(\mathbf{x}',\mathbf{x})p(\mathbf{x})\mathrm{d}\Gamma_f = \int_{\Gamma_f} P(\mathbf{x}',\mathbf{x})q(\mathbf{x})\mathrm{d}\Gamma_f$$
$$+\frac{1}{c_f^2}\sum_{j=1}^{NDRF} \ddot{\alpha}_j(t)\left[c_i\hat{P}_{ij} + \int_{\Gamma_f} Q(\mathbf{x}',\mathbf{x})\hat{P}_j\mathrm{d}\Gamma_f - \int_{\Gamma_f} P(\mathbf{x}',\mathbf{x})\hat{Q}_j\mathrm{d}\Gamma_f\right] \tag{4}$$

In this equation, $NDRF$ represents the number of total DRM collocations points used in the fluid; $\hat{P}_j(\mathbf{x}',\mathbf{x})$ and $\hat{Q}_j(\mathbf{x}',\mathbf{x})$ are the particular solutions to equivalent homogeneous equation (1). These particular solutions were obtained considering the function $f_j(r) = 1 + r_j$ for the approximation of $\ddot{p}(t)$, as presented in [16]. Coefficients $\ddot{\alpha}_j$ are related to $\ddot{p}$ through: $\ddot{p} = F_{ij}\ddot{\alpha}_j(t)$, where F_{ij} is a matrix of coefficients, obtained by taking the value of $\ddot{p}(t)$ at different DRM points.

In order to discretize boundary surfaces of the acoustic medium, N boundary quadrilateral elements were used and $p(\mathbf{x})$ and $q(\mathbf{x})$ were assumed to be constant over each element and equal to their values at the mid-element node. Thus, the discretised form of equation (4) is given by:

$$c_i(\mathbf{x}')p(\mathbf{x}',t) + \sum_{k=1}^{N}\Big[\int_{\Gamma k} Q(\mathbf{x}',\mathbf{x})\mathrm{d}\Gamma\Big]p_k(t) - \sum_{k=1}^{N}\Big[\int_{\Gamma k} P(\mathbf{x}',\mathbf{x})\mathrm{d}\Gamma\Big]q_k(t) =$$
$$\frac{1}{c_f^2}\sum_{j=1}^{NDRF}\ddot{\alpha}_j\Big[c_i(\mathbf{x}')\hat{P}_{ij}(\mathbf{x}',\mathbf{x}) + \sum_{k=1}^{N}\int_{\Gamma k} Q(\mathbf{x}',\boldsymbol{x})\hat{P}_j(\mathbf{x}',\mathbf{x})\mathrm{d}\Gamma$$
$$-\sum_{k=1}^{N}\int_{\Gamma k} P(\mathbf{x}',\mathbf{x})\hat{Q}_j(\mathbf{x}',\mathbf{x})\mathrm{d}\Gamma\Big] \tag{5}$$

Applying this equation at each collocation point, the following system of linear equations is obtained:

$${}^f\mathbf{M}\ddot{\mathbf{p}} + {}^f\mathbf{H}\mathbf{p} = {}^f\mathbf{G}\mathbf{q} \tag{6}$$

where ${}^f\mathbf{M}$ is the fluid mass matrix, ${}^f\mathbf{H}$ and ${}^f\mathbf{G}$ are boundary element influence matrices; $\mathbf{p}$ and $\mathbf{q}$ are vectors of nodal pressures and normal derivative of pressure, respectively.

3.2 Boundary element equations for an elastic membrane

The derivation of the integral formulation for equation (2) is based on the application of the BEM to the membrane equation as presented in [2]. Thus, by using the weighted residual method, and making use of the Green's identity, the integral formulation for equation (2) is given by:

$$c(\mathbf{x}')w(\mathbf{x}',t) + \int_{\Gamma s} T(\mathbf{x}',\mathbf{x})w(\mathbf{x},t)\mathrm{d}\Gamma_s - \int_{\Gamma s} W(\mathbf{x}',\mathbf{x})f(\mathbf{x},t)\mathrm{d}\Gamma_s$$
$$= -\frac{1}{T_0}\int_{\Omega s} W(\mathbf{x}',\mathbf{x})p_w(\mathbf{x},t)\mathrm{d}\Omega_s + \frac{1}{c_w^2}\int_{\Omega s} W(\mathbf{x}',\mathbf{x})\ddot{w}(\mathbf{x},t)\mathrm{d}\Omega_s \tag{7}$$

where $\mathbf{x}$ and $\mathbf{x}'$ are field and collocation points respectively; $c_w^2 = T_0/\rho_s$; $W(\mathbf{x}',\mathbf{x})$ and $T(\mathbf{x}',\mathbf{x})$ are fundamental solutions for displacement and traction, respectively as given in [1]. $c(\mathbf{x}')$ is the jump term arising from the terms of $O(1/r)$ in the kernel $T(\mathbf{x}',\mathbf{x})$.

In this work, the DRM was used to transform domain integrals related to inertial terms into boundary integrals. In this way, this equation (7) can be re-written as [16]:

$$c_i(\mathbf{x}')w(\mathbf{x}',t) + \int_{\Gamma s} T(\mathbf{x}',\mathbf{x})w(\mathbf{x},t)\mathrm{d}\Gamma_s - \int_{\Gamma s} W(\mathbf{x}',\mathbf{x})f(\mathbf{x},t)\mathrm{d}\Gamma_s =$$

$$-\frac{1}{T_0}\sum_{j=1}^{NDRM}\alpha_j(t)\Big[c_i(\mathbf{x}')\hat{W}_j(\mathbf{x},t)+\int_{\Gamma s}T(\mathbf{x}',\mathbf{x})\hat{W}_j(\mathbf{x}',\mathbf{x})\mathrm{d}\Gamma_s - \int_{\Gamma s}W(\mathbf{x}',\mathbf{x})\hat{T}_j(\mathbf{x}',\mathbf{x})\mathrm{d}\Gamma_s\Big]$$
$$+\frac{1}{c_w^2}\sum_{j=1}^{MDRM}\ddot{\beta}_j(t)\Big[c_i(\mathbf{x}')\hat{W}_j(\mathbf{x},t)+\int_{\Gamma s}T(\mathbf{x}',\mathbf{x})\hat{W}_j(\mathbf{x}',\mathbf{x})\mathrm{d}\Gamma_s - \int_{\Gamma s}W(\mathbf{x}',\mathbf{x})\hat{T}_j(\mathbf{x}',\mathbf{x})\mathrm{d}\Gamma_s\Big] \tag{8}$$

where $NDRM$ represent the total number of DRM collocation used in the membrane; $\hat{T}_j(\mathbf{x}',\mathbf{x})$ and $\hat{W}_j(\mathbf{x}',\mathbf{x})$ are the particular solutions to equivalent homogeneous equations (2). These particular solutions were obtained considering the function $f_j(r)=1+r_j$ for the approximation of $\ddot{w}(t)$ and $p_w(t)$ terms, as presented in [16]. Coefficients α_j are related to $p_w(t)$ through: $p_w = A_{ij}\alpha_j(t)$, where A_{ij} is a matrix of coefficients, obtained by taking the value of $p(t)$ at different DRM points. Similarly, coefficients $\ddot{\beta}_j$ are related to $\ddot{w}$ through: $\ddot{w} = B_{ij}\ddot{\beta}_j(t)$, where B_{ij} is a matrix of coefficients, obtained by taking the value of $\ddot{p}(t)$ at different DRM points.

Applying this equation at each collocation point, the following system of linear equations is obtained:

$$^s\mathbf{M}\ddot{\mathbf{w}} + {}^s\mathbf{H}\mathbf{w} = {}^s\mathbf{G}\mathbf{f} - {}^s\mathbf{B}\mathbf{p}_w \tag{9}$$

Here $^s\mathbf{M}$ is the membrane mass matrix, $^s\mathbf{H}$ and $^s\mathbf{G}$ are the influence matrices, $^s\mathbf{B}$ is the influence matrix related with distributed pressure $\mathbf{p}_w$ applied over the membrane.

4 Fluid-structure coupling equations

Fluid-structure coupling equations are given by compatibility considerations about normal pressure and dynamic pressure force acting at the fluid-structure interface. Mathematically, these conditions can be written as follows [17]:

$$\mathbf{n}_f \cdot \boldsymbol{\nabla} p = \mathbf{q}_n \equiv -\rho_w \mathbf{C}_w \ddot{\mathbf{w}} \tag{10}$$

$$\mathbf{p}_w \equiv -\mathbf{C}_f \mathbf{p} \tag{11}$$

That is, pressure gradient acting on the fluid-structure interface Γ_{fs} are related to normal acceleration of the plate and the acoustic pressure is equilibrated with pressure on the membrane (see figure 4). In these equations, $\mathbf{C}_w$ and $\mathbf{C}_f$ represent connectivity matrices joining fluid and structural degree of freedom at fluid-structure interface.

By replacing equations (10) and (11) into equations (6) and (9) we obtain the coupled fluid-structure equation problem:

$$\begin{bmatrix} {}^s\mathbf{M} & \mathbf{0} \\ \mathbf{S} & {}^f\mathbf{M} \end{bmatrix}\begin{Bmatrix} \ddot{\mathbf{w}} \\ \ddot{\mathbf{p}} \end{Bmatrix} + \begin{bmatrix} {}^s\mathbf{H} & -\mathbf{A} \\ \mathbf{0} & {}^f\mathbf{H} \end{bmatrix}\begin{Bmatrix} \mathbf{w} \\ \mathbf{p} \end{Bmatrix} = \begin{bmatrix} {}^s\mathbf{G} & \mathbf{0} \\ \mathbf{0} & {}^f\mathbf{G}_{ff} \end{bmatrix}\begin{Bmatrix} \mathbf{t} \\ \mathbf{q} \end{Bmatrix} \tag{12}$$

In this equation, the off-diagonal sub-matrices $\mathbf{A} = {}^s\mathbf{B}_{fs}\mathbf{C}_f$ and $\mathbf{S} = \rho_w {}^f\mathbf{G}_{fs}\mathbf{C}_w$ are fluid-membrane coupling matrices. $^f\mathbf{G}_{fs}$ and $^f\mathbf{G}_{ff}$ are sub-matrices of $^f\mathbf{G}$ related with degrees of freedom defined on the interface Γ_{fs}. $^s\mathbf{B}_{fs}$ is a sub-matrix of $^s\mathbf{B}$ related with pressure terms defined in Ω_s.

Equations (12) can be rewritten in a general way as:

$$\mathbf{M}\ddot{\mathbf{u}} + \mathbf{H}\mathbf{u} = \mathbf{G}\mathbf{r} \tag{13}$$

where, $\ddot{\mathbf{u}} = \{\ddot{\mathbf{w}}, \ddot{\mathbf{p}}\}^T$, $\mathbf{u} = \{\mathbf{w}, \mathbf{p}\}^T$ and $\mathbf{r} = \{\mathbf{f}, \mathbf{q}\}^T$.

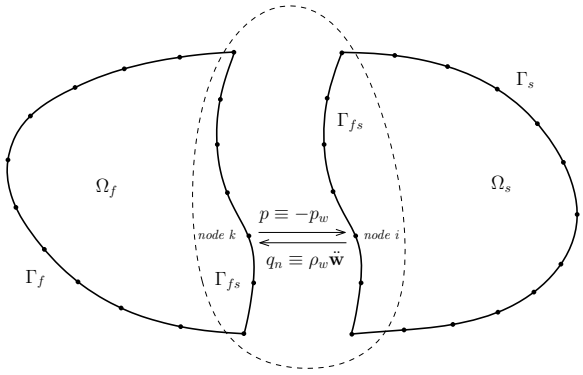

Figure 4: Fluid-structure interfase

5 Transient analysis response

The Houbolt method and the Newmark method were used in this work in order to obtain the time response for the equation (13). The Houbolt integration scheme is an explicit unconditionally stable algorithm based on backward-type finite difference formula with error of order $O(\Delta\tau^2)$. The most important aspect of this method when compared to other time integration methods based on central difference approximations or Newmark scheme is the introduction of artificial damping which truncates the influence of higher modes in the response. In this method, the acceleration is approximated as:

$$\ddot{\mathbf{u}}^{\tau+\Delta\tau} = \frac{1}{\Delta\tau^2}(2\mathbf{u}^{\tau+\Delta\tau} - 5\mathbf{u}^{\tau} + 4\mathbf{u}^{\tau-\Delta\tau} - \mathbf{u}^{\tau-2\Delta\tau}) \tag{14}$$

where $\Delta\tau$ represents the time-step. Writing equation (13) at time $\tau + \Delta\tau$:

$$\mathbf{M}\ddot{\mathbf{u}}^{\tau+\Delta\tau} + \mathbf{H}\mathbf{u}^{\tau+\Delta\tau} = \mathbf{G}\mathbf{r}^{\tau+\Delta\tau} \tag{15}$$

and substituting equation (14) into equation (15), we have:

$$(2\mathbf{M} + \Delta\tau^2\mathbf{H})\mathbf{u}^{\tau+\Delta\tau} - \frac{1}{\Delta\tau^2}\mathbf{G}\mathbf{r}^{\tau+\Delta\tau} = \mathbf{M}(5\mathbf{u}^{\tau} - 4\mathbf{u}^{\tau-\Delta\tau} - \mathbf{u}^{\tau-2\Delta\tau}) \tag{16}$$

The above equation allows calculating of the distribution of $\mathbf{u}$ at time $\tau + \Delta\tau$ by using boundary conditions at that time and information from three previous time steps. This algorithm requires a special starting procedure in which initial conditions for $\mathbf{u}$ are employed to calculate $\mathbf{u}^1$ and $\mathbf{u}^2$.

The Newmark integration method assumes a linear variation of the acceleration in each time step and is widely used for structural dynamic problems. In this method, the acceleration is approximated as:

$$\ddot{\mathbf{u}}^{\tau+\Delta\tau} = \frac{1}{\beta\Delta\tau^2}\left[\mathbf{u}^{\tau+\boldsymbol{\Delta}\tau} - \mathbf{u}^{\tau}\right] + \frac{1}{\beta\Delta\tau}\dot{u}^{\tau} - \frac{(1-2\beta)}{2\beta}\ddot{u}^{\tau} \tag{17}$$

where parameter $\beta = 1/4$ determine the stability and accuracy of the algorithm and were initially proposed by Newmark, securing the unconditional stability of the method. Substituting equation Eq. (17) into Eq. (13), we have:

$$\left(\frac{\mathbf{M}}{\beta\Delta\tau^2}+\mathbf{H}\right)\mathbf{u}^{\tau+\Delta\tau}-\mathbf{G}\mathbf{r}^{\tau+\Delta\tau}=\mathbf{M}\left[\frac{1}{\beta\Delta\tau^2}\mathbf{u}^{\tau}-\frac{1}{\beta\Delta\tau}\dot{\mathbf{u}}^{\tau}+\frac{(1-2\beta)}{2\beta}\ddot{\mathbf{u}}^{\tau}\right] \tag{18}$$

In compact way:

$$\mathbf{A}\mathbf{u}^{\tau+\Delta\tau}=\mathbf{R}^{\Delta\tau+\tau} \tag{19}$$

where:

$$\mathbf{A} = \frac{\mathbf{M}}{\beta\Delta\tau^2}+\mathbf{H}$$

$$\mathbf{R}^{\Delta\tau+\tau} = \mathbf{M}\left[\frac{1}{\beta\Delta\tau^2}\mathbf{u}^{\tau}-\frac{1}{\beta\Delta\tau}\dot{\mathbf{u}}^{\tau}+\frac{(1-2\beta)}{2\beta}\ddot{\mathbf{u}}^{\tau}\right]+\mathbf{G}\mathbf{r}^{\tau+\Delta\tau}$$

Since $\mathbf{A}$ matrix is constant Newmark method leads to the repeated solution of a system of linear algebraic equations at each time step giving the displacements at time $t+\Delta t$. Furthermore the $\mathbf{A}$ matrix is constant and thus can be factorized only once, before the actual time marching, and at each step only factorization of the right hand side and backward substitution is carried out.

6 Numerical examples

6.1 Box-shaped structure containing an acoustic fluid coupled to vertical membrane

The first example consists of a partially opened box-shaped structure with ridig walls and a flexible elastic membrane with $c_w = 0.7071$ m/s as presented in figure 5. The structure contains an acoustic fluid with mass density $\rho_f = 1.21$ kg / m^3 and a bulk's modulus $\kappa = 13.98 \times 10^4$ Pa. A distributed unit pressure load $p(t) = -1.0$ Pa is applied over the face of the structure located at $x_3 = 2$ m. Pressure gradients $q = n_i^f p_{,i}$ are considered zero at the other faces. Initial conditions for this problem are $\mathbf{u}(\mathbf{x},0) = \dot{\mathbf{u}}(\mathbf{x},0) = 0$. In order to validate BEM solution, a 3D Finite Element Method for this problem was obtained. For this, the SHYDRO®, an in-house computational code developed in MATLAB®, was used [18]. This code use transformed 8-node bricks elements with bi-linear shape functions for fluid pressure interpolation. The membrane was modeled using 4-node quadrilateral elements with bi-linear interpolation in order to approximate membrane's displacement. A monolitic fluid-structure coupled formulation based on Eqs. (11), where fluid and membrane nodes at the fluid-solid interface are coincidents, was implemented. Coupled global system of equations is solved using the Newmark time-integration method. FEM convergence analysis was developed using meshes with the dimensions presented in table 1.

BEM analysis uses 2-nodes linear constant interpolation elements for approximation of displacement and pressure gradients on the boundary of the membrane. Similarly, 4-node quadrilaterals with constant interpolation are used on the fluid boundary. Table 2 shows BEM meshes used in the analysis in order to determine the convergence of the solution.

Figure 6 shows the results obtained for displacement in the center of the membrane considering different boundary element meshes. The convergent solution is obtained using BEM 450 collocation points and 3400 elements, while the FEM solution uses a mesh with 11189 elements and 545 nodes. Furthermore, Figure 7 shows the solution for displacement in the center of the membrane considering different time steps. Analysis was performed using the method of Houbolt (HBEM) and the method of Newmark (NBEM). Convergence solution obtained by the Finite Element Method was obtained using the Method Newmark. Figure 8 presents the solution for pressure in the center of the membrane using different mesh BEM for a timestep of $\Delta t = 0.1$ s. The BEM solution converges rapidly towards the analytical solution. As noted, the FEM solution shown more marked oscillations when compared with BEM numerical solution. Finally, Figure 9 shows the convergence

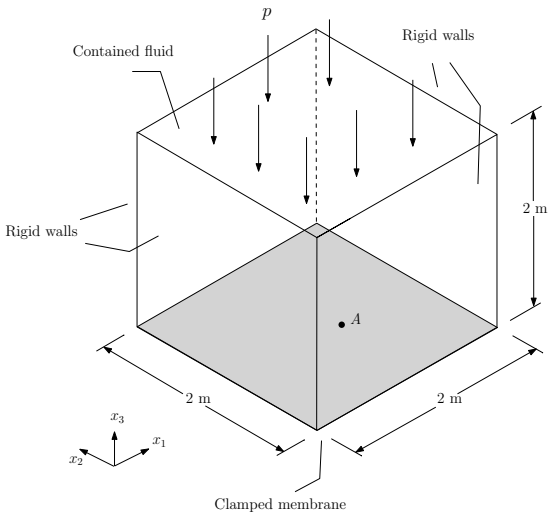

Figure 5: Box-shaped container with flexible membrane wall

Table 1: FEM Meshes for fluid and membrane

Mesh	Fluid		Membrane	
	Elements	Nodes	Elements	Nodes
FEM 6×6×6	216	343	36	49
FEM 8×8×20	1280	1701	64	81
FEM 12×12×20	2880	3549	144	169
FEM 16×16×20	5120	6069	256	289

Table 2: BEM Meshes for fluid and membrane

Mesh	Fluid		Membrane	
	Elements	Nodes	Elements	Nodes
BEM 5×5×5	125	125	20	25
BEM 7×7×7	343	125	28	49
BEM 9×9×9	729	125	36	81
BEM 11×11×11	1331	125	44	121
BEM 15×15×15	3375	125	60	225

analysis for pressure in the center of the membrane by reducing the size of the time step. High concordance with the solution is observed when using FEM method and Houbolt $\Delta t = 0.01$ s. However, both BEM and FEM solutions present high numerical oscillations in both cases.

A second case, where only the heviside pressure load was changed for an harmonic load defined as $p(t) = -P_{max} sin(\omega t)$ Pa. Here, both the frequency ω and the amplitude P_{max} was set to one. Figure 10 shows convergence of displacement in the center of the membrane for different Δt using 450 collocation points and 3400 BEM elements using the Newmark Integration Method. Additionally, the convergent solution obtained by FEM is shown in the figure. The BEM solution has a high convergence rate and a high concordance with the FEM solution. Furthermore, figure 11 shows the time response for the pressure measured at the center of the membrane for different time steps. The results show a high concordance with FEM convergent solution.

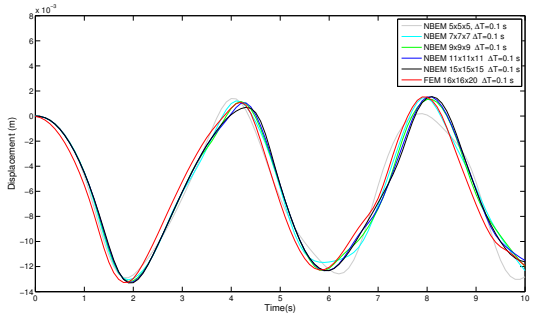

Figure 6: Displacement time history at the membrane's center (mesh convergence analysis)

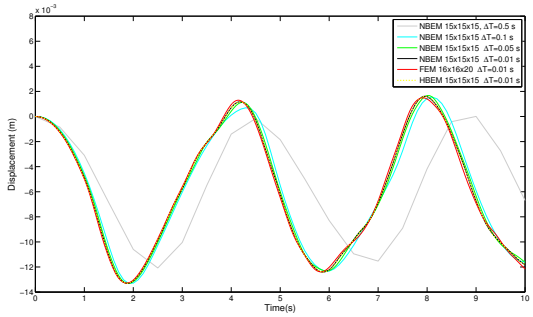

Figure 7: Displacement time history at the membrane's center ($\Delta\tau$ convergence analysis)

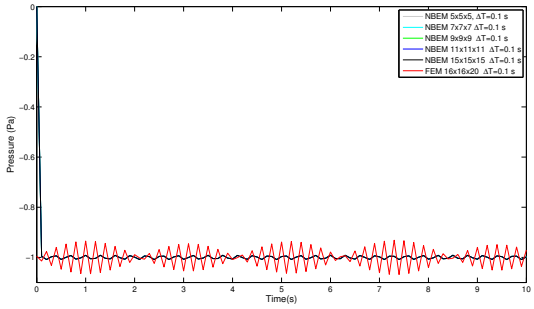

Figure 8: Pressure time history at the membrane's center (mesh convergence analysis)

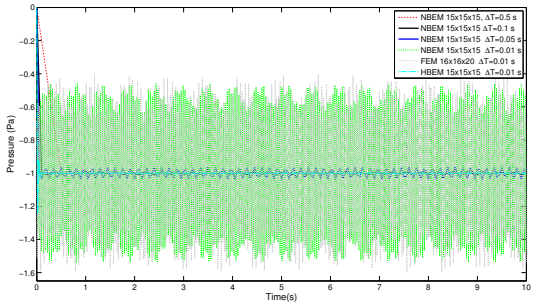

Figure 9: Pressure time history at the membrane's center ($\Delta\tau$ convergence analysis)

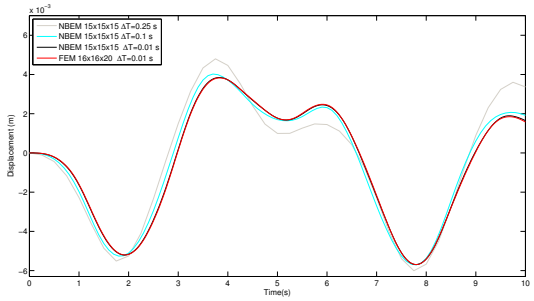

Figure 10: Displacement time history at point A(0.25,-0.25,-1) using Newmark method

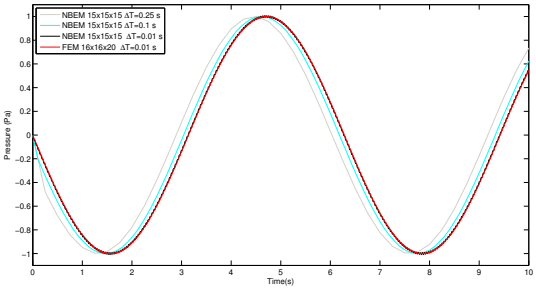

Figure 11: Pressure time history at point A(0.25,-0.25,-1) using Newmark method

6.2 Channel-shaped structure containing an acoustic fluid coupled to inclined membrane

In this example, a partially opened Channel-shaped structure with rigid walls containing an acoustic fluid coupled to a inclined flexible elastic membrane located at the right side of the channel was analyzed as shown in figure 12. The membrane wave propagation velocity, the acoustic fluid mass density and the fluid compressibility are respectively $c_w = 0.7071$ m/s, $\rho_f = 1.21$ kg / m^3 and $\kappa = 139.9 \times 10^3$ Pa. A distributed harmonic pressure load $p(t) = -sin(wt)$ Pa is applied over the membrane (see figure 10). Pressure gradients $q = n_i^f p_{,i} =$ considered zero at the rigid walls. Initial conditions for this problem are $\mathbf{u}(\mathbf{x}, 0) = \dot{\mathbf{u}}(\mathbf{x}, 0) = 0$. Figures 13 and 14 present the solution in displacement and pressure measured at the center of the membrane. A high rate of convergence was obtained using the Newmark's time integration method.

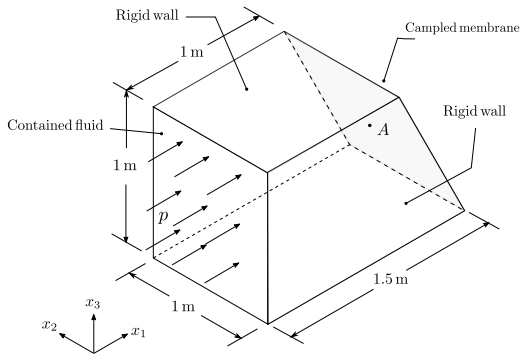

Figure 12: Box-shaped container with inclined membrane

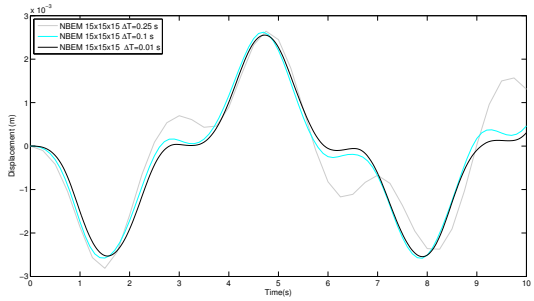

Figure 13: Displacement time history at point A(1.25,0.5,0.5) using Newmark method

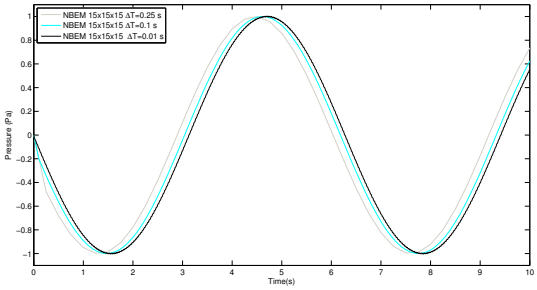

Figure 14: Pressure time history at point A(1.25,0.5,0.5) using Newmark method

7 Conclusions

In this work the dynamic behavior of stretched elastic membranes interacting with acoustic fluids was presented. For this, a new fluid-structure interaction formulation, based on a full monolitic Boundary Element Method, was developed. Boundary Element Method formulations for both fluid and membrane uses static fundamental solutions of the governing equations. Domain integrals were transformed to boundary integrals using the Dual Reciprocity Boundary Element Method. In spite of results show a good agreement with those obtained from finite element models, more research work must be done in order to improve the numerical stability and convergence characteristics of the proposed formulation.

8 Acknowledgment

The authors are grateful to the Research Office of Universidad Tecnológica of Bolívar for supporting this research work.

References

[1] L. C. Wrobel, M. H. Aliabadi, *The Boundary Element Method Volume 2: Applications in Solid and Structures*, Wiley, New York, 2002.

[2] L. C. Wrobel, *The Boundary Element Method Volume 1: Applications in Thermo-Fluids and Acoustics*, Wiley, 2002.

[3] M. R. Shekari, N.Khaji, M. T. Ahmadi, A coupled BE-FE study for evaluation of seismically isolated cylindrical liquid storage tanks considering fluid-structure interaction, *Journal of Fluids and Structures* 25(3) (2009) 567–585.

[4] V. Naumenkob, E. Strelnikovac, E. Yeselevac, Free vibrations of shells of revolution filled with a fluid, *Engineering Analysis with Boundary Elements* 34(10) (2010) 856–862.

[5] Y. Young, Fluid-structure interaction analysis of flexible composite marine propellers, *Journal of Fluids and Structures* 24 (2008) 799–818.

[6] D. Soares, Acoustic modelling by BEM-FEM coupling procedures taking into account explicit and implicit multi-domain decomposition techniques, *International Journal for Numerical Methods in Engineering* 78 (2009) 1076–1093.

[7] L. Chen, X Liang, H Yi Vibro-acoustic characteristics of cylindrical shells with complex acoustic boundary conditions, *Ocean Engineering*, 126(1) (2016) 12–21.

[8] R. Citarella, L. Federico, A. Cicatiello, Modal acoustic transfer vector approach in a fem-bem vibro-acoustic analysis, *Engineering Analysis with Boundary Elements* 31 (2007) 248–258.

[9] G. Of, O. Steinbach, Coupled fe/be formulations for the fluid-structure interaction, in: Y. Huang, R. Kornhuber, O. Widlund, J. Xu (Eds.), *Domain Decomposition Methods in Science and Engineering* XIX, volume 78 of *Lecture Notes in Computational Science and Engineering,* Springer Berlin Heidelberg, 2011, pp. 293–300.

[10] Z. He, G. Liu, Z. Zhong, G. Zhang, A. Cheng, A coupled ES-FEM/BEM method for fluid-structure interaction problems, *Engineering Analysis with Boundary Elements* 35 (2011) 140–147.

[11] S. Marburg, B. Nolte, Computational Acoustics of Noise Propagation in Fluids - Finite and Boundary Element Methods, Springer, 2010

[12] R. Burgschweiger, M. Ochmann, B. Nolte, Calculation of the acoustic target strength of elastic objects based on bem-bem coupling, *The Journal of the Acoustical Society of America* 123 (2008) 3757.

[13] D. Soares Jr, O. von Estorff, W. J. Mansur, Efficient non-linear solid-fluid interaction analysis by an iterative bem/fem coupling, *International Journal for Numerical Methods in Engineering* 64 (2005) 1416–1431.

[14] L. E. Kinsler, A. R. Freg, A. B. Coppens, J. V. Sanders, *Fundamental of acoustics*, Jhon wiley and sons Inc., 2005.

[15] T.Y. Li, G.J. Zhang, X. Zhu, L. Xiong The prediction of the elastic critical load of submerged eccentric cylindrical shell based on vibro-acoustic model, *Ocean Engineering*, 108(1) (2015) 471–479.

[16] P. Partridge, C. Brebbia, L. Wrobel, *The dual reciprocity boundary element method*, Southampton: Computational Mechanics Publications, 1992.

[17] P. Morand, R. Ohayon, *Fluid structure interaction*, John Wiley and Sons, 1995.

[18] J. Useche, VIBRAC: A finite element computational code for fluid-structure interaction analysis, *Mechanical Engineering Reseach Report MERR-201503-102* Universidad Tecnoloógica de Bolívar, 2015.

[19] X. Wang, W. Guo. Dynamic modeling and vibration characteristics analysis of submerged stiffened combined shells, *Ocean Engineering*, 127(15) (2016) 226–235

Finite Element Modeling of Piezoelectric Structures

D. Giraldo-Guzman[1], W. Montealegre-Rubio[2]

[1]dagiraldogu@unal.edu.co, [2]wmontealegrer@unal.edu.co
Mechanical Engineering Department,
National University of Colombia, Medellín, Colombia

Abstract

In this work, the Finite Element Method (FEM) is used to modeling piezoelectric and elastic coupled dynamic structures with three-dimensional Brick elements of 8 and 20 nodes with 4 degrees of freedom (DOF) per node; performing a static and a modal dynamic analysis. A software called FEMPS is developed in MATLAB® to implement the FEM and its results are compared with simulations performed in ANSYS® and, with theoretical and experimental data presented in the literature. The methodology of implementation allows us to analyze the influence of a number of different parameters such as element type and order, mesh convergence, numerical conditioning and solution methods.

Key Words: Finite Element Method, Piezoelectrics, Sensors, Actuators

1 Introduction

Smart materials, such as shape memory alloys, electrorheological or magnetorheological fluids, magnetostrictive materials and piezoelectric materials are the most celebrated materials used as sensors and as actuators for vibration suppression [1]. The latter class of materials is widely used as transducers in structural vibration control systems because of its fast response, flexibility to be used to both sensing and actuating and easy implementation as well as its lightweight and the possibility of being embedded in a variety of structures [2].

Such structures are distributed parameter systems having an infinite set of vibration modes, therefore it is required a distributed modeling and control [3]. However, a representation of an infinite-dimension system involves a mathematical framework that results in partial differential equations or equivalent formulations to describe the continuum. These equations are so complex that they simply can not be solved analytically or lack an exact solution [4]. In these cases, it is necessary to use numerical approximation methods such as finite differences, weighted residuals, approximation functions, or the best known in modern engineering: the Finite Element Method (FEM). This method, thanks to the advance in computer technologies, can solve problems from a mathematical model (differential equations), discretizing the domain by dividing the continuous medium into a finite number of parts or "finite elements". The individual behavior of each of these elements is analyzed and then the behavior of the original system is reconstructed [5].

This paper deals with the implementation and validation of a Finite Element Analysis (FEA) software called FEMPS which is able to simulate simple three-dimensional smart structures composed by two piezoelectric layers for a sensor and an actuator, and a layer for an elastic material. It is also covered the analysis for several variations in simulation parameters and an approach to control strategies utilizing state space representations.

2 Piezoelectric Finite Element Formulation

The coupled mechanical and electrical constitutive equations for piezoelectric structures are [6]:

$$\boldsymbol{T} = \boldsymbol{c^E S} - \boldsymbol{eE} \tag{1}$$

$$\boldsymbol{D} = \boldsymbol{\varepsilon^S E} + \boldsymbol{eS} \tag{2}$$

Where $\boldsymbol{T}$ is the mechanical stress, $\boldsymbol{c^E}$ the elastic properties at constant electric field, $\boldsymbol{S}$ the mechanical strain, $\boldsymbol{e}$ the piezoelectric properties, $\boldsymbol{E}$ the electric field, $\boldsymbol{D}$ the electric flux density, and $\boldsymbol{\varepsilon^S}$ the dielectric properties at constant strain. The equations that describe a piezoelectric dynamic system can be written in terms of the displacements and electric potentials. These two magnitudes represent the degrees of freedom of the system and are referred as the unknown of the problem [7]. The interpolated solution of these unknowns in any point of the domain depends on the shape functions $\boldsymbol{\mathcal{N}}$ and the nodal values $\{u_i\}$ or $\{\phi_i\}$, and its derivatives gives the relation for strains and electric fields:

$$\begin{aligned} \boldsymbol{S} &= [\mathcal{D}]\boldsymbol{\mathcal{N}_u}\{u_i\} = \boldsymbol{\mathcal{B}_u}\{u_i\} \\ \boldsymbol{E} &= -\nabla\boldsymbol{\mathcal{N}_\phi}\{\phi_i\} = -\boldsymbol{\mathcal{B}_\phi}\{\phi_i\} \end{aligned} \tag{3}$$

Where $\boldsymbol{\mathcal{B}_u}$ and $\boldsymbol{\mathcal{B}_\phi}$ are the mechanical and electrical gradient-displacement matrices, which refer to the derivative of the shape functions $\boldsymbol{\mathcal{N}}$ through the differential operators $[\mathcal{D}]$ and ∇. Using these equations and a modification of the variational principle, the general expression of movement in dynamic system including the piezoelectric effect is [8]:

$$\begin{bmatrix} \boldsymbol{M_{uu}} & \boldsymbol{0} \\ \boldsymbol{0} & \boldsymbol{0} \end{bmatrix} \begin{Bmatrix} \ddot{\boldsymbol{u}} \\ \ddot{\boldsymbol{\phi}} \end{Bmatrix} + \begin{bmatrix} \boldsymbol{D_{uu}} & \boldsymbol{0} \\ \boldsymbol{0} & \boldsymbol{0} \end{bmatrix} \begin{Bmatrix} \dot{\boldsymbol{u}} \\ \dot{\boldsymbol{\phi}} \end{Bmatrix} + \begin{bmatrix} \boldsymbol{K_{uu}} & \boldsymbol{K_{u\phi}} \\ \boldsymbol{K_{\phi u}} & \boldsymbol{K_{\phi\phi}} \end{bmatrix} \begin{Bmatrix} \boldsymbol{u} \\ \boldsymbol{\phi} \end{Bmatrix} = \begin{Bmatrix} \boldsymbol{f} \\ \boldsymbol{q} \end{Bmatrix} \tag{4}$$

Where $\boldsymbol{M_{uu}}$ is the mass matrix, $\boldsymbol{D_{uu}}$ the mechanical damping matrix, $\boldsymbol{K_{uu}}$ the stiffness matrix, $\boldsymbol{K_{u\phi}}$ the piezoelectric coupling matrix, $\boldsymbol{K_{\phi\phi}}$ the capacitance matrix, $\boldsymbol{f}$ and $\boldsymbol{q}$ are the mechanical and electric external forces, $\boldsymbol{u}$ and $\boldsymbol{\phi}$ are the solution vectors. The finite element formulation of these matrices is [4]:

$$\begin{aligned} \boldsymbol{M_{uu}} &= \rho \int_V \boldsymbol{\mathcal{N}_u^T \mathcal{N}_u} dV & \boldsymbol{K_{u\phi}} &= \int_V \boldsymbol{\mathcal{B}_u^T e^T \mathcal{B}_\phi} dV \\ \boldsymbol{D_{uu}} &= \alpha \boldsymbol{M_{uu}} + \beta \boldsymbol{K_{uu}} & \boldsymbol{K_{\phi\phi}} &= -\int_V \boldsymbol{\mathcal{B}_\phi^T \varepsilon \mathcal{B}_\phi} dV \\ \boldsymbol{K_{uu}} &= \int_V \boldsymbol{\mathcal{B}_u^T c^E \mathcal{B}_u} dV & \boldsymbol{K_{\phi u}} &= \boldsymbol{K_{u\phi}^T} \end{aligned} \tag{5}$$

3 FEMPS Software Implementation

The FEMPS software is composed essentially by five stages: initialization, mesh construction, matrices assembly, boundary conditions and a solver. In Figure 1 is presented in a diagram this sequential structure.

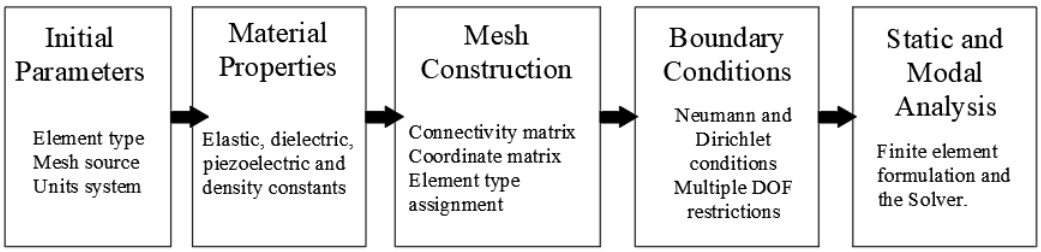

Figure 1: The simplified algorithm of FEMPS software

3.1 Piezoelectric Electrodes

A common finite element implementation problem involves a few boundary conditions that can be expressed mathematically as functions of individual DOF. These restrictions are called "*Simple DOF Restrictions*". However, some situations such as the modeling of piezoelectric electrodes require the coupling of two or more degrees of freedom. This process of coupling, known as *Restrictions of Multiple DOF*, consists in generating equations of restrictions. The most simple method to understand and implement is known as *Master-Slave Elimination*. This method consists in choosing a "Master" DOF and writing the restriction equations of the "Slaves" DOF. The solution vector $\boldsymbol{u}$ will be modified through a coupling matrix $\boldsymbol{T}$, such that:

$$\boldsymbol{u} = \boldsymbol{T}\hat{\boldsymbol{u}} \tag{6}$$

Where $\hat{\boldsymbol{u}}$ is the coupled vector solution. The finite element matrices and external forces will be:

$$\hat{\boldsymbol{M}}\ddot{\hat{\boldsymbol{u}}} + \hat{\boldsymbol{D}}\dot{\hat{\boldsymbol{u}}} + \hat{\boldsymbol{K}}\hat{\boldsymbol{u}} = \hat{\boldsymbol{f}} \tag{7}$$

Where:

$$\hat{\boldsymbol{M}} = \boldsymbol{T}^T\boldsymbol{M}\boldsymbol{T} \qquad \hat{\boldsymbol{D}} = \boldsymbol{T}^T\boldsymbol{D}\boldsymbol{T} \qquad \hat{\boldsymbol{K}} = \boldsymbol{T}^T\boldsymbol{K}\boldsymbol{T} \qquad \hat{\boldsymbol{f}} = \boldsymbol{T}^T\boldsymbol{f} \tag{8}$$

3.2 Numerical Examples

A $100 \times 5 \times 1$ mm bimorph PVDF piezoelectric beam is shown in Figure 2, which will be used for all numerical examples presented in this section. This kind of configuration consist of two identical PVDF piezoelectric patches with opposite polarities. The structure was modeled using both 8-node and 20-node elements in different mesh discretization but with the same boundary conditions and material properties. Results were compared to those obtained in ANSYS running exactly the same simulation parameters.

In Figure 2 is shown a discretization of 5 elements per piezoelectric patch, for a total of 10 elements. However, this mesh configuration was not possible to implement due to a *Shape Warning Limits* violation. To compare results, in our FEMPS program and in the ANSYS software the mesh was set for 20 elements per patch for a total of 40 elements. In Figure 3, the experimental test from [9] and [10] is compared with reported numerical examples reported from [4] and [11]. As an additional source of comparison, a theoretical result reported in [12] is presented assuming the Euler-Bernoulli beam theory and a linear variation of electric potential through the thickness of the beam.

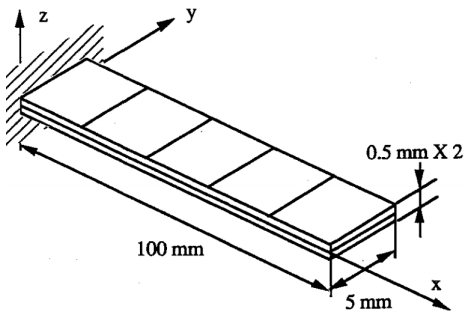

Figure 2: Piezoelectric polymeric PVDF bimorph beam. Figure taken from [11].

By analyzing Figure 3 is easy to notice similarities between experiments and numerical results. In fact, the relative error of FEMPS compared to ANSYS results are around 2% when using 20-node elements. In contrast, when using 8-node elements the relative error is about 90% as can be seen in Figure 3-a where an anomalous behavior exposes the *Shear Locking* effect on this type of finite elements. One option to face this kind of problem is using *Extra Shape Functions*. Since in this work those shape functions was not implemented, an additional curve was added in the same figure to show the results obtained in ANSYS using 8-node elements including it (green triangles in Figure 3-a).

Table 1 shows a review of relative errors for every simulation performed in this work. The error is presented as a mean of the relative errors for the Z-axis deflection with respect to its theoretical values from the Euler-Bernoulli beam theory.

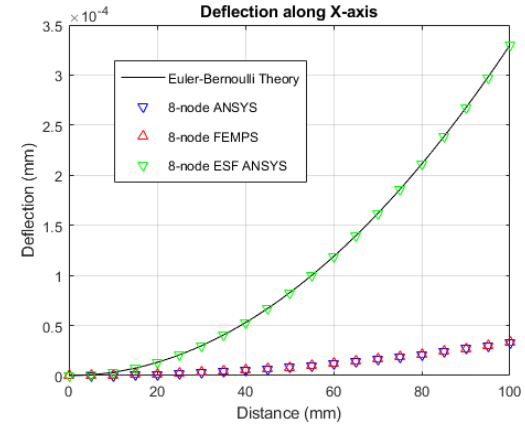

(a) Results from FEMPS with 8-node elements

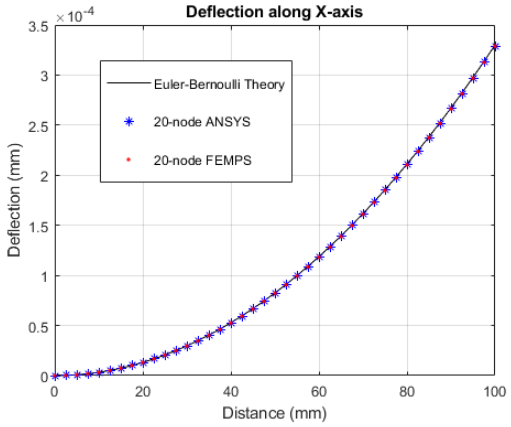

(b) Results from FEMPS with 20-node elements

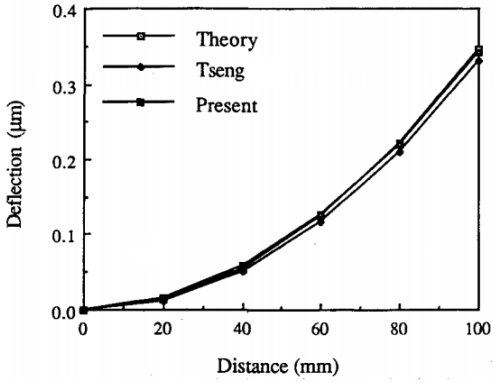

(c) Results from [11]

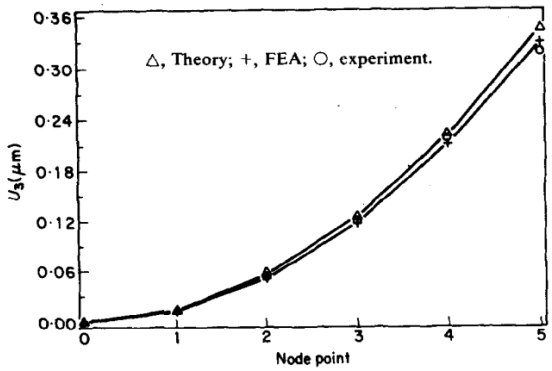

(d) Results from [9]

Figure 3: Comparison of results from different reported experiments, numerical examples and simulation obtained for the present work performed both in MATLAB and ANSYS.

Software	Element Type	# of Elements	Relative Error (%)
FEMPS	Brick 8-node	40	85.541
ANSYS	Brick 8-node	40	85.541
ANSYS	Brick 8-node with ESF	40	0.2138
FEMPS	Brick 20-node	40	1.7014
ANSYS	Brick 20-node	40	0.5124

Table 1: Relative errors respect to theory for simulations performed in FEMPS and in ANSYS.

Results presented so far evidence a correlation between ANSYS simulation results and our implemented code, which means that the stiffness matrix, the mesh, and the boundary conditions are working properly. The next section deals with the implementation of the mass matrix and a modal analysis simulation.

3.3 Modal Analysis for Piezoelectric Structures

Several vibration control strategies require a dynamic model to successfully control disturbances in the system. The general dynamic expression for movement considering a multi-physical problem with elastic and piezoelectric structures was presented in equation 4. Nevertheless, a pure eigenproblem for a modal analysis would not be affected by the presence of electrical degrees of freedom since it does not represent

a mechanical inertia in the system and could be removed. The general eigenproblem to be solve will be:

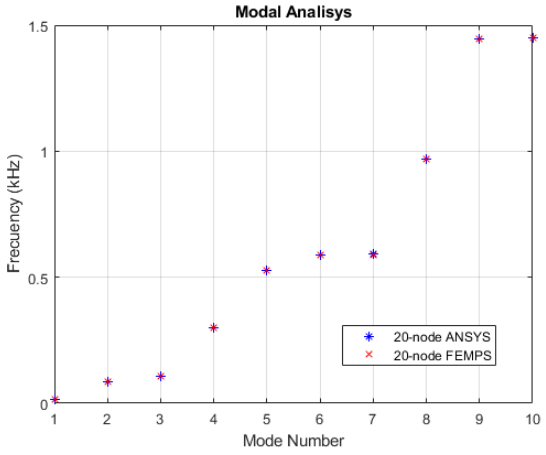

Figure 4: Comparison of results for modal analysis.

$$\boldsymbol{K_{uu}\Phi_u = M_{uu}\Phi_u\Lambda_u} \tag{9}$$

where $\boldsymbol{\Phi_u}$ is the eigenvectors matrix and $\boldsymbol{\Lambda_u}$ is the eigenvalues matrix. Figure 4 presents a modal analysis of the piezoelectric bimorph beam presented in Figure 2. It is clear the similitude between FEMPS and ANSYS results, validating the implementation of the mass matrix and the algorithm to solve a eigenproblems.

4 Conclusions

A theoretical background for the piezoelectric phenomenon was presented, followed by the formulation of finite elements in which the expression for general dynamical systems was presented including both piezoelectric and elastic matrices. Finally, a state space representation was developed to explore a vibration control approach using a modal order reduction technique.

A Finite Element Method program to simulate three-dimensional piezoelectric and elastic structures coupled in a configuration of mechanical sensors or actuators both for static and modal analysis was implemented and validated in Matlab through direct comparison amongst our code results, Ansys' simulations, theoretical results, and experimental data presented in the literature.

A setup test of a bimorph piezoelectric beam was taken as an example to perform a variety of simulations. Different implementation parameters were modified to find better results considering computing time and accuracy. In the static analysis, a comparison amongst the effects of this finite element selection was first considered to face a *shear-locking* problem besides a mesh convergence analysis. The same setup was considered to compare both eigenvalues and shape eigenvectors in the modal analysis.

References

[1] Preumont, André. Vibration control of active structures. *Dordrecht: Kluwer academic publishers*, 2011.

[2] Moheimani, SO Reza, and Andrew J. Fleming. Piezoelectric transducers for vibration control and damping. *Springer Science & Business Media*, 2006.

[3] Hwang, Woo-Seok, and Hyun C. Park. Finite element modeling of piezoelectric sensors and actuators. *AIAA journal*, **31.5**: 930-937, 1993.

[4] Vincent Piefort. Finite Element Modelling of Piezoelectric Active Structures. *Ph.D. Thesis, ULB Department of Mechanical Engineering and Robotics*, 2001.

[5] Zienkiewicz, Olek C. and Taylor, Robert L. and Zhu, J. Z. The Finite Element Method: Its Basis and Fundamentals. *Elsevier LTD, Oxford*, 2013.

[6] Meitzler, A. W. W. A. H., H. F. Tiersten, A. W. Warner, D. Berlincourt, G. A. Couqin, and F. S. Welsh III. IEEE standard on piezoelectricity. 1988.

[7] Cook, Robert D. Concepts and applications of finite element analysis. *John Wiley & Sons*, 2007.

[8] Nader, Gilder Desenvolvimento de técnicas de caracterização de transdutores piezelétricos. *Tese de Doutorado*, 2002.

[9] Tzou, H. S., and Ci-I. Tseng. Distributed vibration control and identification of coupled elastic/piezoelectric systems: finite element formulation and applications. *Mechanical Systems and Signal Processing* **5.3**: 215-231, 1991.

[10] Tzou, H. S., and R. Ye. Analysis of piezoelastic structures with laminated piezoelectric triangle shell elements. *AIAA journal* **34.1**: 110-115, 1996.

[11] Hwang, Woo-Seok, and Hyun C. Park. Finite element modeling of piezoelectric sensors and actuators. *AIAA journal* **31.5**: 930-937, 1993.

[12] Lašová, Zuzana and Zemčík, Robert Comparison of finite element models for piezoelectric materials. *Procedia Engineering* **48**: 375-380, 2012.

Creep Analysis in Asphalt Mixtures Using a Power-Modeling in Ansys

Wilson Rodrguez C.[1], Myriam Roco Pallares M.[2], Julian A. Pulecio Daz.[3]

[1]wilroca50@hotmail.com
Programa de Ingeniería Civil,
Universidad Cooperativa de Colombia, Neiva, Colombia

[2]myriam.pallares@usco.edu.co
Programa de Ingeniería Civil,
Universidad Surcolombiana, Neiva, Colombia

[3]julpul7@hotmail.com
Programa de Ingeniería Civil,
Universidad Cooperativa de Colombia, Ibagu, Colombia

Abstract

The article discusses the study of the creep phenomenon in asphalt mixtures starting with a review of the conceptual model of the material and details of the viscoelastic characterization of asphalt mixtures through the fluence test. Having clear the conceptual model, we developed the implementation and calibration of a finite element model in the finite elements program ANSYS. For the calibration a strategy adapted by the authors was developed using a few convenient steps. This strategy allows the balance of the error-model for data obtained from the laboratory Creep test, this is achieved through an optimization scheme that looks for the parameters of ANSYS's mathematical model that minimizes the overall difference between the deformations in laboratory measurements and those calculated. At the end we developed the script of the power model in ANSYS and performed relevant analyses about simulation, and comparisons with the laboratory data and the suitability of the Ansys modeling. The power model is reasonably reproducing the creep behavior of the asphalt mixtures, however, the article also shows the distances between simulations and the current data, and how balancing these distances we can get a viable model for the practice with criterion of safety factor in deformations deferred over time.

Key Words: ANSYS, power model, creep, finite element.

1 Description of the material and experimental evidence: hot-dense asphalt mixtures

The asphalt mixture is a material with viscous and elastic characteristics simultaneously. The behavior of the asphalt concrete depends on the temperature, for example, at high temperatures it presents properties of a viscous fluid, while at low temperatures its behavior is like a solid and at an intermediate temperature it is in a condition intended for pavement, viscous fluid and elastic solid [1].

To facilitate its analysis and characterization, the asphalt mixtures can be considered as homogeneous, isotropic and linear for certain ranges of stress-deformation.

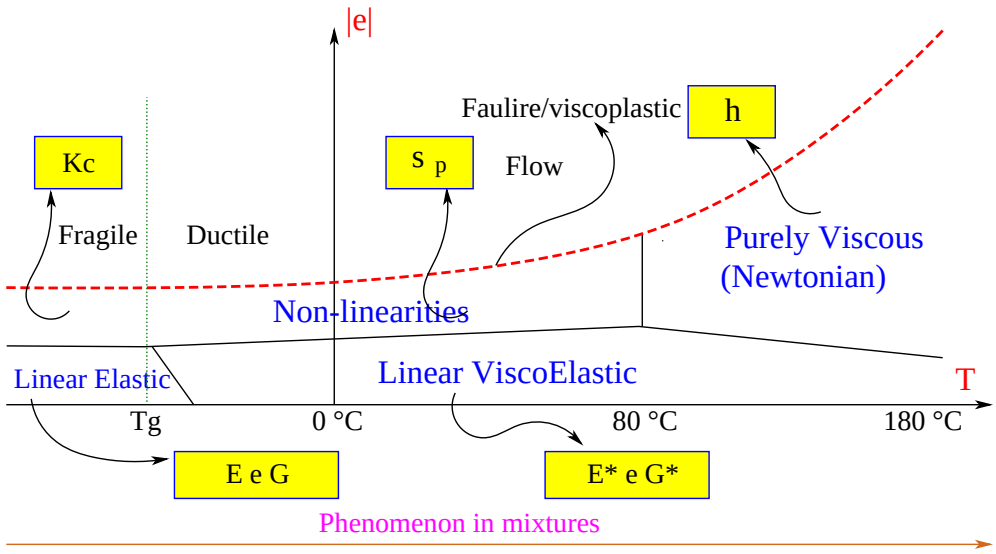

Figure 1: Typical behaviors observed on bitumens.

Figure 1 [2] shows the different ranges of behavior of an asphalt concrete, depending on the deformations and temperatures to which it is subjected. For normal thermal conditions and small deformations, the behavior of the mixture is linear viscoelastic. In these conditions it is predominantly the behavior of the binder and not the interaction between the particles of the aggregate.
In the structure of the flexible pavement, the asphalt layer is directly subjected to the action of the traffic loads and to the variation of the climatic conditions. The response of the rolling layer varies according to the applied application, causing in many cases the premature failure of the pavement. The action of traffic and the effect of temperature are the main agents that affect the behavior of the pavement.

As for the physical-mechanical characterization of asphalt mixtures there are many equipment and tests of schools highlighted, such as the French School, the American School, the English School and the Russian school. In this work we assumed the perspective of the American and English School to demonstrate mechanical characteristics related to the viscoelasticity of asphalt mixtures. In particular, the non-confined static fluency test also called static creep test is described; this assay was used for the numerical model.

The static Creep test consists of an axial load test applied for a specific time including the discharge (recovery test). This test, actually is a recovery test. On the NAT machine (Nottingham Asphalt Tester, see Figure 2) the Creep test is focuses on the following conditions:

- Applied vertical stress: 100 kPa.
- Creep Time: 3600 s
- Applied vertical stress: 100 kPa.
- Recovery time: 1800 s
- Temperature: 40 C
- Sample diameter: 100 mm
- Sample height: 65 mm
- Number of specimen in each series: 6
- Specimen preferably compacted by kneading in rotary compactor.

The data that can be obtained from the test are:

- Maximum strain ε_{max} = > Total vertical deformation at the end of loading process, at 3600 seconds.
- Permanent deformation: ε_{perm} = > remaining deformation recorded at the end of the downloading process, at 5400 seconds.
- Elastic strain: $\varepsilon_{elast} = \varepsilon_{max}$ - ε_{perm}.
- Creep rate = > The fluency velocity measured in the last 1200 seconds of loading: Vε = (ε_{3600} - ε_{2400})/1200 seconds.
- Rigidity modulus = > quotient between the applied vertical stress and the maximum deformation recorded at 3600 seconds.

Figure 2 [3]displays the dynamic machine NAT. The figure shows exactly the assembly of a sample for CREEP test. This machine has an graphical interface for the load control.

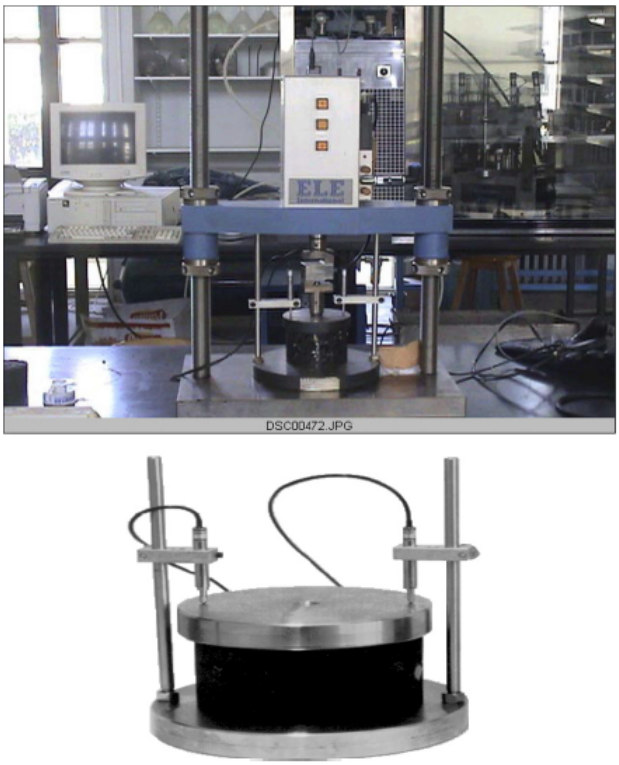

Figure 2: Mounting Test CREEP.

Figure 3 [3] shows an example of the test, however currently in the American school is done the so-called essay FLOW TIME. This test lasts only 100 second in loading process so it is a pure creep test; in this case, the test reports directly the creep function (Creep compliance).

2 Approach of the mathematical model to be used and determination of its parameters by optimization

The numerical model is made from the equation (1) which does not represent exactly the phenomenon, but it has been used in asphalt mixtures as a simplified option to model the Creep phenomenon:

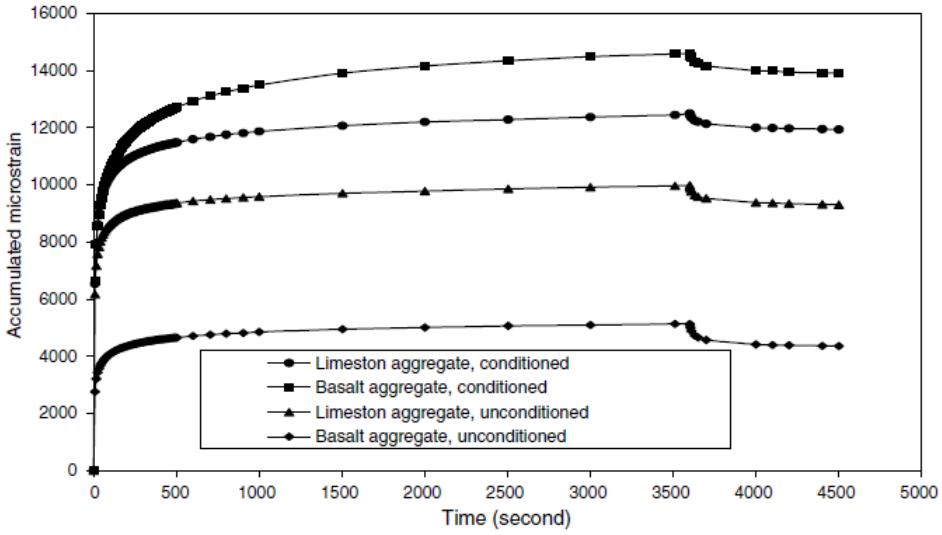

Figure 3: Results of Creep test.

$$\varepsilon_{cr} = \frac{C_1 \sigma^{C_2} t^{C_3+1} e^{\left(-\frac{C_4}{T}\right)}}{C_3 + 1} \tag{1}$$

Where
C_1,C_2,.C_3 and C_4 are coefficients of the Creep function in ANSYS.
To determine the coefficients, we developed the following procedure based on the technical review:

1. The coefficient C_4 is taken null to eliminate the influence of the temperature, since it will be despised in the analysis. Analysis will be considered whit uniform temperature, $C_4 = 0$.

2. An arbitrary value of $C_2$is taken. We assumed $C_2 = 1$, since this coefficient only is for scaling the constant $\sigma^{C}{}_{2}$.

3. The model is matched with the data at t= 1 by equalization as well:

$$f_l(1)\,\sigma = \varepsilon_{Cr}(1) = \frac{C_1 \sigma^1 1^{C_3+1}}{C_3 + 1} \tag{2}$$

   Clearing C_1, we get the last equation for calculating C_1.

$$C_1 = f_l(1) * (C_3 + 1) \tag{3}$$

4. Parameter C_3 is determined by optimization using the gradient solver tool (non-linear). The Euclidean norm of the difference between the data and the calculated model is minimized using Equation 1. Here we took C_3 as the only search variable. Using equation 3, the value of C_1 is obtained.

The figure 4 shows the optimization scheme on the Excel solver snap-in.

The following parameters are obtained:

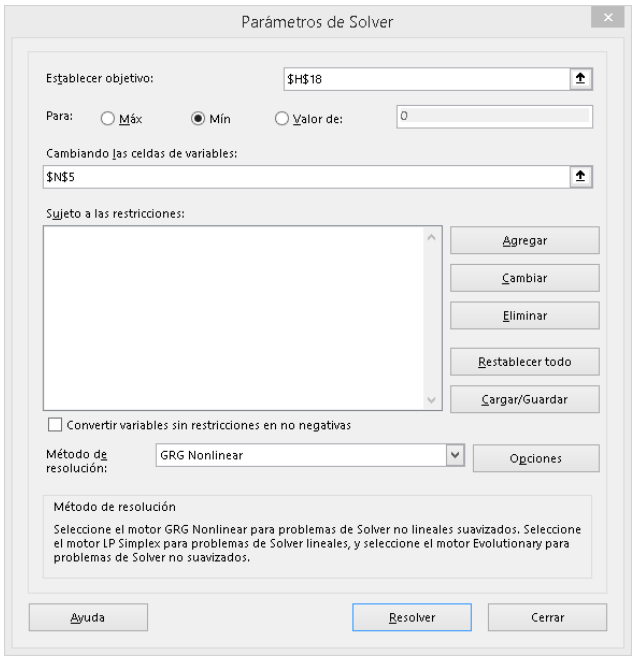

Figure 4: Optimization scheme in Solver for the calibration of a pure power model in ANSYS. Source: Authors.

c1	4.36940866806908E-06
c2	1.00000000000000E+00
c3	-8.36290420829184E-01
c4	0.00E+00

	t	ε(t) lab	σ	fl(t)	ε_{ANSYS}	ε(t)-ε_{ANSYS}	(ε(t)-ε_{ANSYS})^2
1	1	2.67E-03	100	2.669E-05	2.67E-03	0.00E+00	0.00E+00
2	3	3.86E-03	100	3.863E-05	3.19E-03	6.68E-04	4.46E-07
3	5	4.17E-03	100	4.172E-05	3.47E-03	6.98E-04	4.88E-07
4	10	4.45E-03	100	4.450E-05	3.89E-03	5.59E-04	3.13E-07
5	15	4.61E-03	100	4.612E-05	4.16E-03	4.54E-04	2.06E-07
6	20	4.73E-03	100	4.728E-05	4.36E-03	3.69E-04	1.37E-07
7	30	4.87E-03	100	4.874E-05	4.66E-03	2.16E-04	4.68E-08
8	40	4.98E-03	100	4.983E-05	4.88E-03	1.01E-04	1.01E-08
9	50	5.07E-03	100	5.068E-05	5.06E-03	4.09E-06	1.67E-11
10	60	5.13E-03	100	5.129E-05	5.22E-03	-8.83E-05	7.80E-09
11	70	5.19E-03	100	5.191E-05	5.35E-03	-1.60E-04	2.55E-08
12	80	5.24E-03	100	5.238E-05	5.47E-03	-2.31E-04	5.33E-08
13	90	5.30E-03	100	5.303E-05	5.58E-03	-2.72E-04	7.42E-08
14	100	5.34E-03	100	5.342E-05	5.67E-03	-3.30E-04	1.09E-07
						Σ	1.92E-06
						Euclidian Norm	1.38E-03

And the following table of complementary results.

Figure 5 is plotted from this data table. This figure shows low-setting, due to the simplicity of the power model and the few parameters. However, the strategy makes a balance of the model very well and the creep deformation at the final time is overrated, this is good when we calculate safety factors.

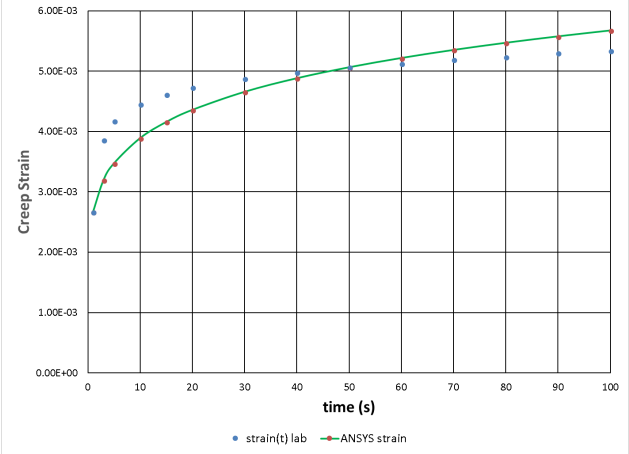

Figure 5: Calibrated curve of a pure power model for implementation in ANSYS. Source: Authors.

3 Ansys Creep model - function of pure power

The model consists of the simulation of the compression axisymmetric condition shown in Figure 6. The geometry is made using standard dimensions of a typical laboratory specimen. We use just one finite element 8 node-PLANE183 since its interpolation order is higher. The precision of the Creep model is shown later.

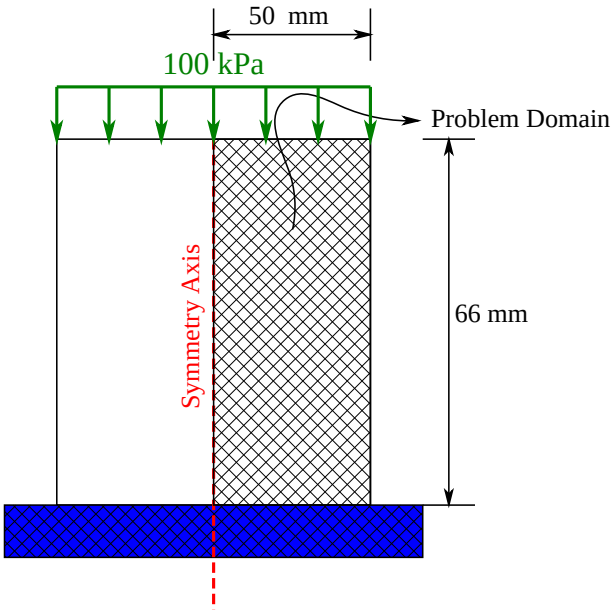

Figure 6: ANSYS creep phenomenon domain. Source: Authors.

The figure 7 shows the applied load of 100 kPa and the contour boundary conditions at the base and the symmetrical axis.

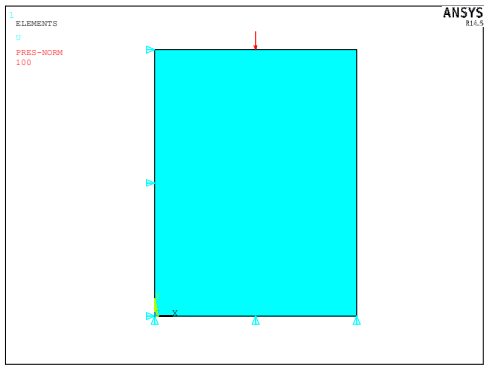

Figure 7: Contour and axial load conditions of a pure power model for Creep in ANSYS. Source: Authors.

Figure 8 shows the vertical and horizontal displacement after the load.

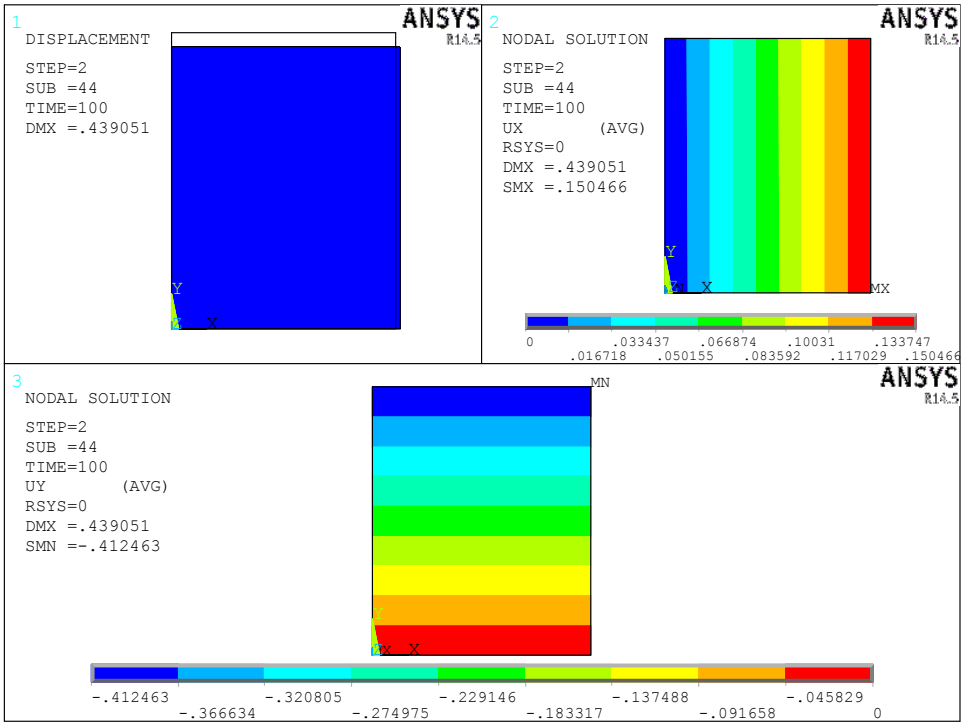

Figure 8: Deformed results, Horizontal and Vertical displacement of the sample subjected to the compression creep test. Source: Authors.

The figure 9 shows vertical creep (EPCRY) and horizontal (EPCRX).

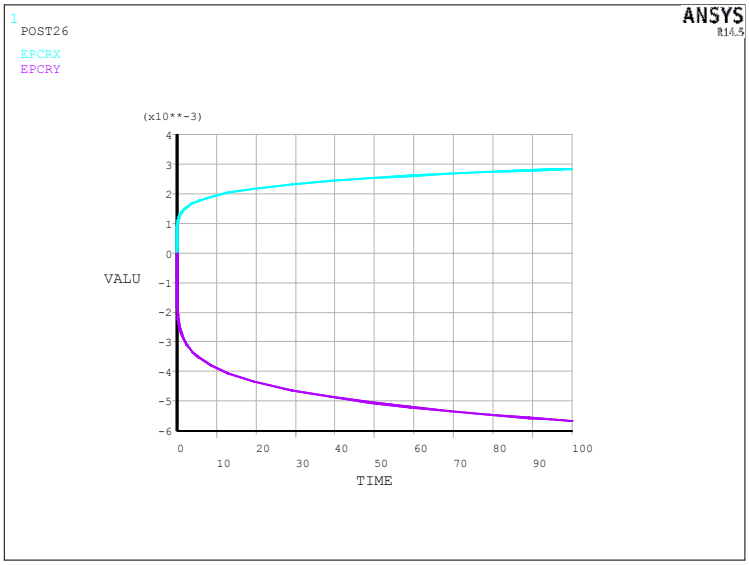

Figure 9: Deformed results, Horizontal and Vertical displacement of the sample subjected to the compression creep test. Source: Authors.

The figure 10 shows the ANSYS strain and the deformation from the initial setting of the model parameters. The parameters found are reproducing the model, but not the laboratory data as seen in Figure 2.

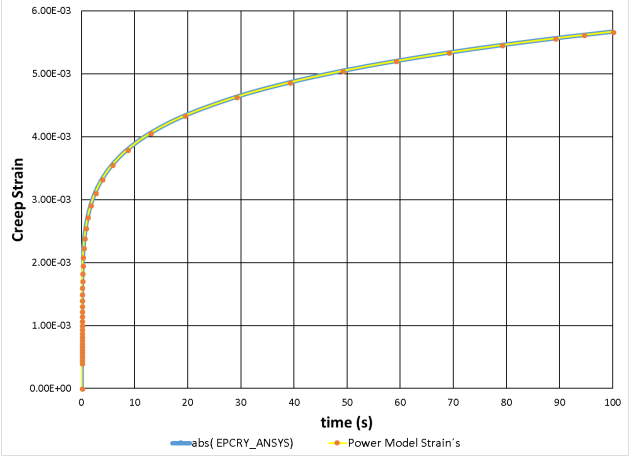

Figure 10: Deformed results, Horizontal and Vertical displacement of the sample subjected to the compression creep test. Source: Authors.

4 Conclusions

1. The experimental evidence shows as asphalt and asphalt mixtures has all the characteristics of a material viscoelastic in fluency and relaxation.

2. An approximate numerical model of fluency is made (by finite elements using ANSYS). There is only availability in ANSYS of a pure power model that is adjusted and calibrated with real data. In the literature it is a modeling alternative for the fluency in asphalt mixtures but in practice this mathematical model presents important differences with experimental data. We recommend using the generalized Kelvin formal model to obtain a better fit.

3. The pure power model implemented in ANSYS was previously calibrated in order to find the parameters using a theory of optimization and gradient algorithms nonlinear problems.

4. For proper fluency modeling in ANSYS we have to start from a small time thus the adjustment with the power model is good. This conclusion is reached after preliminary tests of the Ansys code implemented for this case.

References

[1] Asphalt Institute. The Asphalt Handbook, MS-4. Asphalt Institute, 7th Edition, 2007.

[2] Olard F., Di Benedetto H., Dony A., Vaniscote J.C. Properties of bituminous mixtures at low temperatures and relations with binder characteristics. *Materials and Structures.* **38**:121-126, 2005.

[3] Saad Abo-Qudais, Haider Al-Shweily. Effect of aggregate properties on asphalt mixtures stripping and creep behavior. *Construction and Building Materials.* **21**:1886-1898, 2007.

Micromechanical and Tensile Properties of PP-Fique Biocomposites

L.S. Correa-Martinez[1], M.F Muñoz-Velez[1], J.P. Correa-Aguirre[2], M.A. Hidalgo-Salazar[2], J.H Mina-Hernandez[1]

[1]jose.mina@correounivalle.edu.co
Grupo de Materiales Compuestos (GMC)
Universidad del Valle, Escuela de Ingeniería de Materiales,
Cali, Colombia.

[2]mahidalgo@uao.edu.co
Grupo de Investigación en Tecnología para la Manufactura (GITEM)
Universidad Autónoma de Occidente, Departamento de Energética y Mecánica,
Cali, Colombia.

Abstract

In this work biocomposites based on PP and two types of Fique Fibers (neat Fique and a modified Fique with an alkalinization treatment with NaOH) biocomposites were prepared using injection moulding. Neat PP and its biocomposites were tested following ASTM standards in order to evaluate tensile and micromechanical properties. The tensile test shows that tensile modulus and tensile strength were enhanced with the addition of 10 and 20% of neat Fique fiber. However, the addition of 20 and 30% of the modified fiber leads to a decrease in the tensile strength in comparison with PP. These results can be related with the lower interfacial shear strength of the modified Fique fibers in comparison with neat Fique.

Key Words: Biocomposites, PP, Fique, Natural fibers, Superficial modification, Interfacial shear strength

1 Introduction

In recent years research on materials has sought to expand the applications of materials reinforced with natural fibers. In the case of Polypropylene (PP), this material exhibits a wide range of physical properties including chemical resistance and an outstanding cost / performance ratio among thermoplastic polymers. On the other hand, a natural fiber as Fique provides biodegradability, low density and low resistance. These characteristics make PP-Fique biocomposites suitable materials for several applications including automotive parts. Nevertheless, PP-Fique biocomposites also have certain disadvantages caused mainly to the incompatibility between the PP and the natural fiber, due to their hydrophobic (polymer) and hydrophilic (fiber) interactions. The mixture of two different materials such as those mentioned above can lead to poorly defined morphologies with an irregular distribution of their components, for this reason, the morphological control of these mixtures is very important regarding the optimization of their mechanical and physical properties. A solution to this problem is the incorporation of coupling agents such as maleic polypropylene anhydride (MAPP). The addition of this substance could also be controlled with different treatments such as alkalization and preimpregnation. These treatments can control the morphology as well as the particle size improving the

quality of the interface between the fibers and the matrix [1]. The aim of this work was to develop PP-Fique biocomposites through injection molding and to analyze the effect of the fiber content and the alkalinization process of Fique fibers on tensile and micromechanical properties of the obtained biocomposites.

2 Materials and Methods

2.1 Materials

The PP pellets (575P), 0.95 g/m3 and a melt flow index of 10,8 g/10 min (190 °C, 2.16 kg according to ASTM D1238) were purchased from SABIC, Saudi Arabia. Fique fibers were obtained from the furcraea spp plant which belongs to the Agavaceae family. These fibers were provided by the company Empaques del Cauca of Popayán (Colombia) and were used as discontinuous reinforcement of a PP matrix. In this work, neat Fique fibers (NF) and modified Fique fibers with a surface treatment (MF) were used. The superficial modification process of the fibers was carried out by alkalinization treatment with sodium hydroxide (NaOH) at 2 %w/v following the methodology described in previous works [2]. This treatment was performed in order to remove hemicellulose, lignin and other present substances such as waxes for improve the adherence of the fibers to the matrix and decrease their hydrophilic nature. Furthermore, Fique fibers (neat and modified) were cutted with a uniform length of 3 mm and oven dried at 60 °C for 24 h before processing. This fiber length was established by preliminary tests (data not shown), which showed that greater fiber length causes difficulties in the extrusion process of the material.

2.2 Preparation of the biocomposites

Before the extrusion processing, flow measurements were made using a volumetric feeder in order to determine the process parameters which allow obtaining PP-Fique biocomposites with 10%, 20%, 30% volume of Fique. Each composition was extruded using a co-rotating twin screw extruder (Harden Industries Ltd., China) to produce PP-Fique pellets. The processing temperatures of the different zones of the extruder (from the feeding to the die zone) were set at 185, 193, 195, and 197 °C, respectively. The rotation speed of the twin-screw was 10 rpm. Once the PP-Fique pellets were obtained, they were milled and oven dried at 60 C for 24 h in order to facilitate the injection process. A microinjection machine BOY XS (BOY Machines, Inc., USA) was used to manufacture the tensile test specimens of the materials. The processing temperature was set at 180 °C. Also, an injection pressure of 68 bar for 3.8 s and a back pressure of 18 bar were used.

2.3 Tensile test

Tensile testing was performed with an INSTRON universal testing machine model 3366 according to the ASTM D 638. The tests were carried out at 23 °C, with a constant rate of 1 mm/min and injected type V samples. All the results were taken as the average value of five samples.

2.4 Interfacial shear strength (IFSS)

The interfacial shear strength (IFSS) of Polypropylene/Fique fiber system was evaluated using the single-fiber fragmentation test (SFFT), where the contribution of the alkalization treatment on the IFSS, was evaluated. During the SFFT, tensile stress are transferred to the Fique fiber, which is embebed on the Polyproylene matrix, through the interfacial region. When a gradual deformation is induced in the specimen, the ultimate tensile strength of the fiber will be exceeded in some points of fiber discontinuity, fracturing it repeatedly in short fragments, until that the fragmentation process stops; at this point, the fiber fragments length is referred to as critical length (lc) and is considered as the minimun fiber length necessary to transfer stress between matrix and fiber [3, 4]. Likewise, the critical length is a good indicator of the load transfer interfacial capacity between the components of the material. With the lc values, is possible to determinate the interfacial shear strength by the equation 1:

$$\tau = \frac{\sigma_f}{2}\frac{d}{l_c} \quad (1)$$

Where d is the fiber diameter and f is the maximum tensile strength of the fiber extrapolated to the lc fiber length. Howewer, in this work was used the equation proposed by Drzal et al. [5], who studied the statistical distribution of the fragments length and found that it fits well into a two parameters (shape and scale) Weibull distribution and modified the Kelly and Tyson equation (Equation 1) considering the Weibull parameters; the IFSS is given by Equation (2):

$$\tau = \frac{\sigma_f}{2\beta}\Gamma\Big(1-\frac{1}{\alpha}\Big) \quad (2)$$

Where f is the maximum tensile strength of the fiber extrapolated to the lc fiber length, α and β are the shape and scale parameters of the Weibull distribution of lc/d, and Γ is the gamma function. This test was performed at a strain rate of 0.5 mm/min, using a universal test machine, TINIUS OLSEN H50Ks, equipped with a 10 kN load cell. The fracture points were observed with a light source in order to determine the fragmentation saturation. Then, the specimens were observed in a high resolution optical microscope, where the fiber fragments generated during the test were measured. Considering that the IFSS depends of the maximum tensile strength of the fiber (Equation 2) measured at a test length equal to lc, was necessary to evaluate this property at different lengths, which allowed obtaining a model for predicts the tensile strength as a function of the fiber length. The tensile test of the Fique fibers was performed according to ASTM 3822 standard, using a universal test machine, TINIUS OLSEN H50Ks, equipped with pneumatic grips for fibers and a 1000 N load cell. The strain rate was of (10% of test fiber length)/min. Here 120 samples of native fiber and modified fiber, were evaluated.

2.5 Statistical analysis

Tensile properties of the materials were subjected to analysis of variance (ANOVA), and the Tukeys test was applied at the 0.05 level of significance. All statistical analyses were performed using Minitab Statistical Software Release 12 (Pennsylvania, United States).

3 Results

3.1 Interfacial shear strength (IFSS)

Figure 1 shows the average values obtained for the maximum tensile strength of the native and modified fiber as a function of the fiber length. The equations of the mathematical models that predict the maximun tensile strength were determined by the linear regression analysis of the results. The tensile strength at the critical length (lc) of the neat and modified fiber was calculated using these mathematical models. On the other hand, the figure 2 shows the Weibull distribution of lc/d for the native and modified fiber, from which the shape and scale parameters were obtained. With the maximum tensile strength and the Weibull parameters found, the IFSS was established with the equation 2. Table 1 presents the IFSS values obtained in the fiber-matrix systems. Here, a considerable decrease in the interfacial shear strength was observed in the modified fiber in comparison neat fiber.

This behavior was not expected, because it is known that the alkalization treatment promotes the fiber-matrix interfacial adhesion, by increasing the mechanical anchoring points between the fiber and the matrix [6]; it is possible to attribute the decrease in the interfacial adhesion to the incomplete fragmentation of the fiber during the test, due to increase of the rupture strain of the fiber with the alkalization treatment, which reached a value of 10.96% (determined at % in., of fiber length), approaching the Polypropylene rupture strain (13.3%).

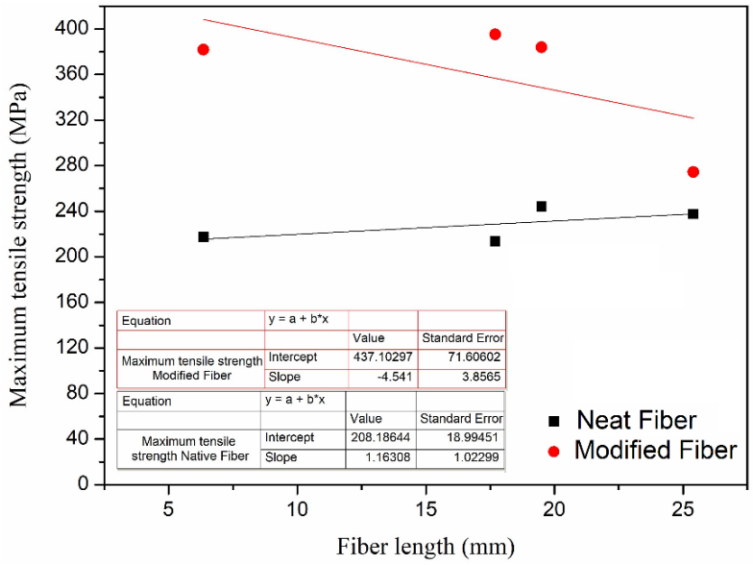

Figure 1: Maximum tensile strength of the fiber with and without surface treatment.

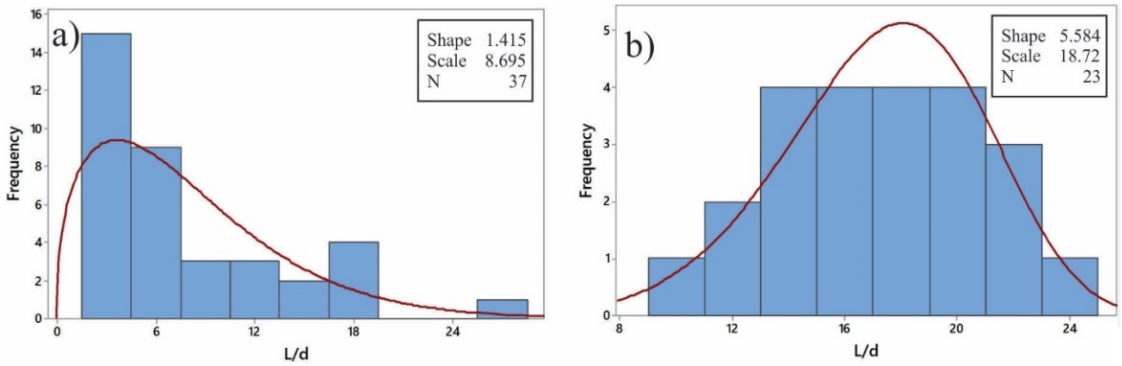

Figure 2: Length/Diameter Weibull histogram of a) Neat Fiber and b) Modified Fiber.

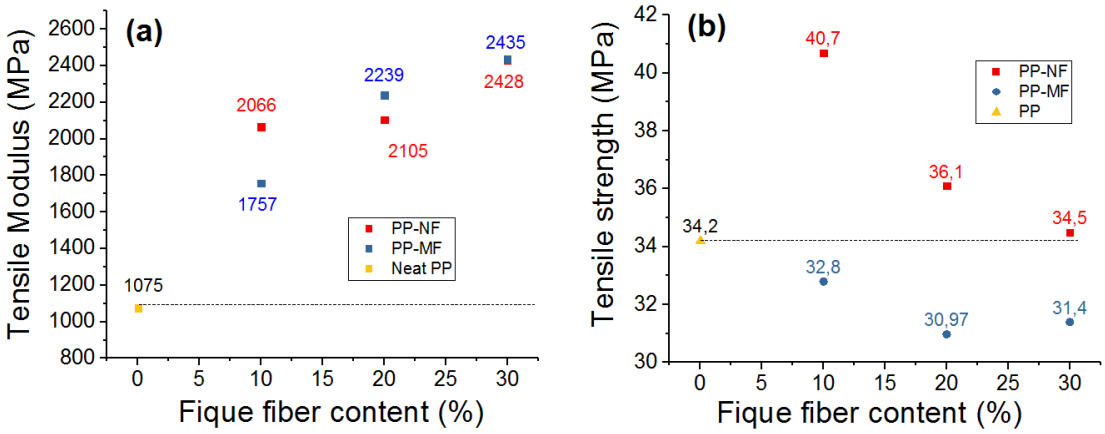

Figure 3: Maximum tensile strength of the fiber with and without surface treatment.

According to the above and taking into account the high values of standard deviation of the Weibull distribution of lc, it is possible to say that the fragmentation did not reach saturation in the modified fiber-matrix system, because with a high strain in the system, the matrix will deform plastically and the energy provided to the system, during the test, will dissipate in the deformation of the matrix, causing that the interfacial stress transfer are inefficient, and avoiding that the mechanisms of fiber fracture occur. This means that the single-fiber fragmentation test (SFFT) is not adequate to measure the fiber-matrix interfacial quality of the PP-Fique system. The SFFT has been used successfully in systems with significant differences in the rupture strain between the fiber and the matrix (e.g. the carbon fiber-epoxy resin systems, where the matrix can achieve approximately 6 times the rupture strain of carbon fiber) [3]. According to the mentioned, in systems with similar rupture strain between the fiber and matrix, it is advisable to use methods such as pull-out or micro-droplet.

Table 1: Parameters and Interfacial shear strength (IFSS) of the PP-Fique systems.

Parameter	**Neat Fique**	**Modified Fique**
Diameter (mm)	0.273	0.228
Lc - Weibull average (mm)	2.160 ± 1.54	3.944 ± 0.81
Shape Weibull parameter (α)	1.415	5.584
Scale Weibull parameter (β)	8.695	18.720
Maximum tensile strength at Lc (MPa)	210.699	419.195
Interfacial shear strength (MPa)	37.124	12.781

3.2 Tensile properties

Results of mechanical properties (Figure 3) showed that Fique addition promoted a reinforcement effect given by a significant increase in the tensile modulus (between 63% for PP-MF10 and 127% for PP-MF30), in comparison with neat PP. Concerning tensile strength (TS), the addition of 10 and 20% of neat Fique produces an increase of 20 and 6% respectively as compared with PP. It is also observed that TS values of PP and the biocomposite with a proportion of 30% of neat Fique were not significantly different ($p \geq 0.05$). These results can be related to the reinforcement effect of Fique fibers in the PP matrix and. On the other hand, TS was not influenced significantly ($p \geq 0.05$) by the incorporation of 10% of modified Fique. However, the addition of 20 and 30% of the modified fiber leads to a decrease in the TS (9 and 8%) respectively when compared with neat PP. These results can be related with the low adhesion of the system (section 3.1).

4 Conclusions

We have prepared PP-Fique biocomposites by extrusion and injection molding of PP and two types of Fique Fibers (neat Fique and a modified Fique with an alkalinization treatment with NaOH). The tensile test shows that tensile modulus and tensile strength were enhanced with the addition of 10 and 20% of neat Fique fiber. However, the addition of 20 and 30% of the modified fiber leads to a decrease in the tensile strength in comparison with PP. These results can be related with the lower Interfacial shear strength of the modified Fique Fibers in comparison with neat Fique.

5 Acknowledgement

We acknowledge to the Universidad Autónoma de Occidente, Cali-Colombia, for the technical and financial support. Universidad del Valle, Cali-Colombia, for the micromechanical analysis and Empaques del Cauca of Popayán (Colombia) for providing the Fique fibers.

References

[1] Valadez A., Herrera P.J. Mechanical properties of continuous natural fibre- reinforced polymer composites. *Composites: Part A.* **35**:339-345, 2008.

[2] Hidalgo-Salazar M.A., Mina-Hernandez J.H. Fique fiber an alternative for reinforced plastics. Influence of surface modification. *Biotecnologa en el Sector Agropecuario y Agroindustrial*, **12**: 60-70, 2014.

[3] Muñoz-Velez M.F., Valadez A., and P.J. Herrera P.J. Effect of fiber surface treatment on the incorporation of carbon nanotubes and on the micromechanical properties of a single-carbon fiber-epoxy matrix composite. *Express Polymer Letters.*, **11**: 704-718, 2017.

[4] Herrera P.J., Drzal L. T. Comparison of methods for the measurement of fiber matrix adhesion in composites. *Composites*, **23**: 2-27, 1992.

[5] Drzal L. T., Rich M. J., Koenig M. F., Lloyd P. F. Adhesion of graphite fibers to epoxy matrices: II. The Effect of Fiber Finish. *Express Polymer Letters.*, **11**: 704-718, 2017.

[6] Herrera P.J., Valadez A. A study of the mechanical properties of short natural-fiber reinforced composites. *Composites: Part B.*, **36**: 597-608, 2005.

Análisis de Sensibilidades Probabilísticas y de Confiabilidad Estructural en Armaduras Planas Usando Ansys

Wilson Rodríguez C.[1], Armando M. Awruch.[2], Jorge L. Palomino Tamayo.[2], Herbert Martins Gomes.[3]

[1]wilroca50@hotmail.com
Programa de Posgrado en Ingeniería Civil - PPGEC,
Universidade Federal do Rio Grande do Sul-UFRGS, Porto Alegre, Brasil

[2]amawruch@ufrgs.br; jorge.tamayo@ufrgs.br
Programa de Posgrado en Ingeniería Civil - PPGEC,
Universidade Federal do Rio Grande do Sul-UFRGS, Porto Alegre, Brasil

[3]herbert@mecanica.ufrgs.br
Programa de Posgrado en Ingeniería Mecánica - PROMEC,
Universidade Federal do Rio Grande do Sul-UFRGS, Porto Alegre, Brasil

Resumen

El presente artículo muestra la aplicación é implementación de un modelo computacional adaptado para el cálculo de confiabilidad estructural y sensibilidad probabilística en armaduras planas usando el programa de elementos finitos comercial ANSYS. Obtenido el modelo computacional mencionado se aplica al cálculo de confiabilidad de un caso de una armadura estructural con variables aleatorias definidas entre las que están las áreas de las barras, el módulo elástico del material y las cargas aplicadas, para su implementación se establece en la práctica el desarrollo de un código script en lenguaje APDL de ANSYS para la parametrización del problema. Se obtienen conclusiones importantes respecto a los resultados de confiabilidad estructural hallados con los diferentes métodos abordados (método de Montecarlo crudo – MC y método de Monte Carlo con muestreo por hipercubo latino – MCLH), los costos computacionales en tiempo CPU, el cálculo de sensibilidades probabilísticas y su importancia, y finalmente, la viabilidad del programa comercial ANSYS como alternativa para el cálculo de confiabilidad estructural y sensibilidad probabilística y como posible candidato para pruebas de validación frente a desarrollos propios por parte de investigadores del área. Cabe destacar, que se expone de manera previa un marco teórico que involucra conceptos asociados a los métodos empleados por ANSYS para el cálculo de confiabilidad estructural y para la evaluación de las sensibilidades probabilísticas que permiten establecer la jerarquía de significancia de las variables frente a la confiabilidad estructural del modelo de cercha analizado.

Palabras clave: ANSYS, Confiabilidad estructural, sensibilidad probabilística, elementos finitos.

1 Aspectos teóricos de los métodos de cálculo de confiabilidad y del cálculo de sensibilidades probabilísticas en problemas estructurales

Los análisis de confiabilidad se realizan a través de métodos más o menos sofisticados y más o menos precisos como los métodos FORM (First order reliability method), métodos de SORM (Second order reliability method), Método Monte Carlo (MC) y aproximaciones a este (Monte Carlo con Muestreo por importancia-MCI, Monte Carlo con muestreo por hipercubo latino-MCLH, entre otros), entre los más populares. Hay registros importantes de éstos en problemas estructurales y geotécnicos desde 1970, siendo autores prominentes Wu y Kraft (1970), Alonso (1976), Vanmarcke (1977); luego hay autores como Griffiths y Fenton (2008), Xue y K. Gavin (2007), Ching et al. (2009), Zhang et al. (2011a,b), el-Reedy (2013), Phoon y Ching (2015), Rubinstein y Kroese (2017), Melchers y Beck (2018).

Los análisis probabilísticos requieren análisis deterministas previos que evalúan una función de estado límite en el cálculo que determina la falla o no falla de la estructura analizada (elementos finitos, soluciones analíticas explícitas, entre otros), de esta manera se determina lo que se conoce como índice de confiabilidad β. A continuación, se explica de manera breve los fundamentos de los métodos explorados en el programa de elementos finitos ANSYS y conceptos para el cálculo de sensibilidades probabilísticas en problemas de confiabilidad.

1.1 Método de simulación de Monte Carlo en el cálculo de probabilidad de falla (MC)

El método de Monte Carlo (MC) es un método de cálculo de probabilidad basado en el principio de simulaciones aleatorias, apareció en el año 1949, con la publicación .el método Monte Carlo"de los autores matemáticos John von Neumann y Stanislaw Ulam. Este método proporciona facilidad para la implementación computacional en serie y paralela, buena precisión, verificación de errores estadísticos y no exige mayores conocimientos matemáticos.

A medida que los problemas se vuelven complejos, la simulación aparece como una buena opción para estimar la confiabilidad. Si se considera un sistema o una estructura cuyo comportamiento está definido por un conjunto de variables aleatorias $\mathbf{U} = \{U_1, U_2, \ldots, U_n\}$, la función de estado límite (F.E.L) g($\mathbf{U}$) que define las regiones de falla y seguridad y la función de densidad de probabilidad conjunta de las variables aleatorias $f_U(\mathbf{U}) = f_U(U_1, U_2, \ldots, U_n)$. En el caso donde la función $g(\mathbf{U}) > 0$, esto indica que U pertenece a la región o dominio seguro (DS), por lo contrario se establece la región o dominio de falla (DF) y si g($\mathbf{U}$) = 0 el estado es de falla inminente, como se puede ver en la figura 1. En general, la probabilidad de falla (P_f) de una estructura o sistema puede ser calculada como:

$$P_f = \int_{g(\mathbf{U})<0} f_{\mathbf{U}}(\mathbf{U})\, dU = \int_{Df} f_{\mathbf{U}}(\mathbf{U})\, dU \tag{1}$$

Se puede establecer una función indicadora I tal que $I[g(\mathbf{U})] = 1$ para g($\mathbf{U}$) ¡0 (Dominio de falla - D_f) y I[g ($\mathbf{U}$)] = 0 para g ($\mathbf{U}$)¿0 (Dominio de seguridad - D_s). Entonces la probabilidad de falla se puede estimar como el valor esperado de la función del indicador; Esto es:

$$P_f = \int_{Df} f_U(\mathbf{U}) dU = \int_D I[g(\mathbf{U})] f_U(\mathbf{U}) dU = E[I[g(\mathbf{U})]] \tag{2}$$

La función indicadora identifica el dominio de integración. La función g($\mathbf{U}$) es una función de desempeño en el análisis de confiabilidad, por lo que la integración proporciona la probabilidad de falla, P_f. Se observa que la integración se realiza en todos los dominios donde se definen las variables básicas (dominio $D = D_s + D_f$). Cuando esta integración es evaluada teóricamente por el método MC para infinitos puntos, P_f puede calcularse de la siguiente manera:

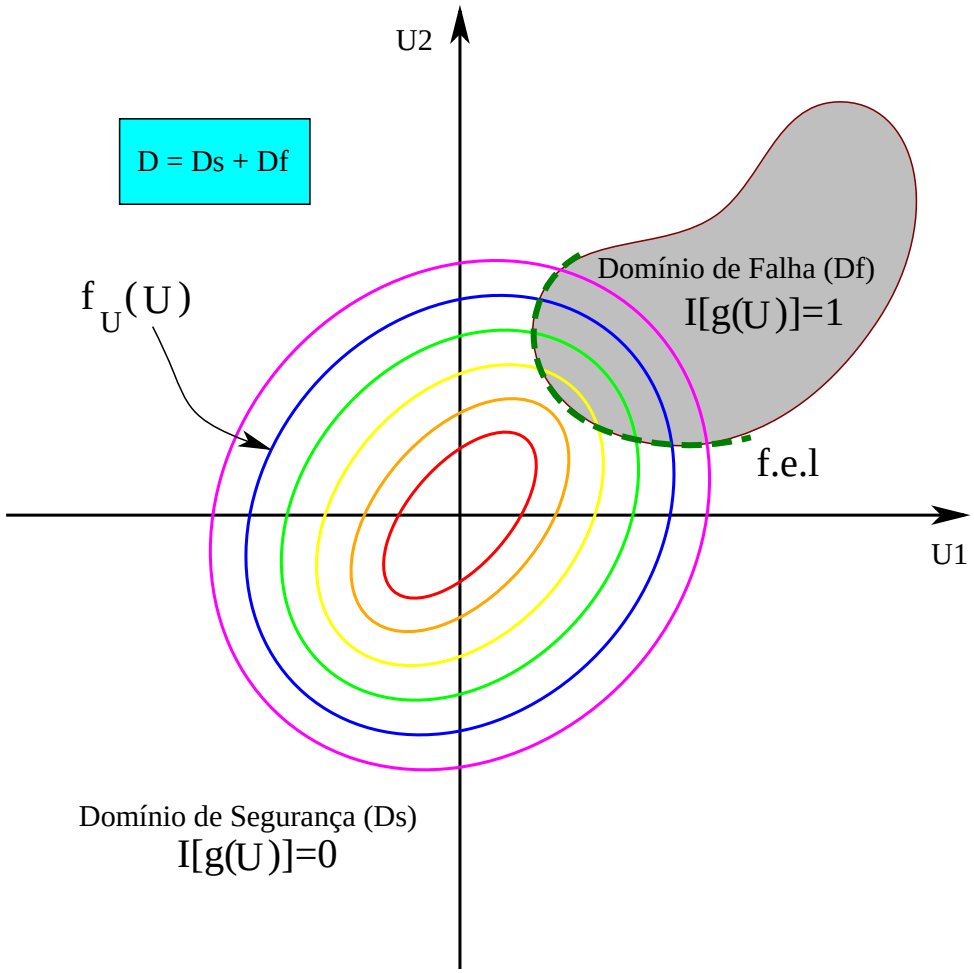

Figura 1: Descripción de los elementos básicos para el cálculo de probabilidad de falla por el método de Monte Carlo. Fuente: Autores.

$$P_f = EI\left[g\left(\mathbf{U}\right)\right] = \mu_I = \lim_{N\to\infty} \frac{1}{N}\sum_{i=1}^{N} I\left[g\left(\mathbf{U_i}\right)\right] \tag{3}$$

Donde N es el número de simulaciones. En la práctica solo es posible calcular un estimador de P_f (se usa la notación, $\hat{P}_f$ para ese estimador) por el método MC, así:

$$\hat{P}_f = \frac{1}{N}\sum_{i=1}^{N} I[g(\mathbf{U}_i)] \tag{4}$$

Puede demostrase que el coeficiente de variación CV aplicado a $\hat{P}_f$ puede calcularse como:

$$CV_{\hat{P}_f} = \frac{\sigma_{\hat{P}_f}}{\mu_{\hat{P}_f}} = \frac{\sqrt{\frac{P_f - P_f^2}{N}}}{P_f} = \sqrt{\frac{1-P_f}{NP_f}} \tag{5}$$

Si quisiéramos que $\hat{P}_f \rightarrow P_f$ entonces debemos disminuir el coeficiente de variación $CV_{\hat{P}_f}$ para que tengamos confianza en el valor de $\hat{P}_f$. En la practica se puede estimar un valor de simulaciones N pertinente para alcanzar un posible valor objetivo de $CV_{\hat{P}_f}$ que puede tomar valores razonables como 0.02 (2 % de error).

1.2 Método de simulación de Monte Carlo con muestreo por hipercubo latino (MCLH)

Dentro de las técnicas de reducción de varianza (técnicas empleadas como estrategia en la reducción del número de simulaciones necesarias para alcanzar niveles aceptables de error) , el método de hipercubo Latino (Latin Hypercube - LH) es uno de los más simples. Este método fue propuesto por McKay (1979) y ampliado en 1980 por Iman y otros.

En este método, el muestreo se realiza de manera uniforme en un hipercubo cuyo centro es el punto de proyecto, punto de diseño o punto más probable de falla (MPP- Most Probable Point) (Figura 2); en general, sólo tiene que tomarse un hipercubo p centrado en **U***. Los lados del hipercubo son paralelos a los ejes de referencia. La función de densidad uniforme en el hipercubo es $f_W(\mathbf{U}) = 1/V(p)$, donde V(p) es el volumen del hipercubo. La probabilidad de falla se escribe como:

$$\hat{P}_f = \int_{V(p)} I[g(\mathbf{U})] \frac{f_U(\mathbf{U})}{f_w(\mathbf{U})} f_w(\mathbf{U}) dvol = \int_{V(p)} I[g(\mathbf{U})] \frac{f_U(\mathbf{U})}{V(p)} V(p) dvol \tag{6}$$

La estimación de esta integral se da por la expectativa matemática de la variable $I[g(\mathbf{U})] f_U(\mathbf{U}) V(p)$ para un vector aleatorio $\mathbf{U}$ distribuido uniformemente en V(p):

$$\hat{P}_f = \frac{V(p)}{N} \sum_{i=1}^{N} I\left[g\left(\mathbf{U}_i\right)\right] f_U(\mathbf{U}_i) \tag{7}$$

Donde N es el número total de simulaciones realizadas. En la literatura el método de hipercubo latino se considera ineficiente para el cálculo de probabilidades pequeñas.

Para el cálculo del coeficiente de variación del estimador de probabilidad de falla, para n repeticiones con subintervalos de m muestras ($N = n * m$), se usa:

$$CV_{\hat{P}_f} = \sqrt{\frac{1 - P_f}{nmP_f}} \tag{8}$$

La técnica de hipercubo Latino (LH) es una forma más avanzada y eficiente para el muestreo en los métodos de simulación de Monte Carlo. La única diferencia entre la técnica LH y la técnica de muestreo directo de Monte Carlo es que la LH tiene un muestreo con "memoria", lo que significa que evita muestras repetidas que han sido evaluadas antes (Evita agrupar muestras). También obliga a las colas de una distribución a participar en el proceso de muestreo. En general, la técnica de muestreo hipercubo Latino requiere un 20 % a 40 % menos de ciclos de simulación que la técnica de simulación directa de Monte Carlo para proporcionar los mismos resultados con la misma precisión. Sin embargo, este número depende en gran parte del problema estudiado.

1.3 Calculo de sensibilidades probabilísticas mediante coeficientes de correlación de orden de Spearman

El coeficiente de correlación de orden de Spearman se usa como herramienta de cálculo de sensibilidades probabilísticas, dado que establece el nivel de significancia de una variable aleatoria con respecto a la función de estado limite en estudio. La expresión para el cálculo es:

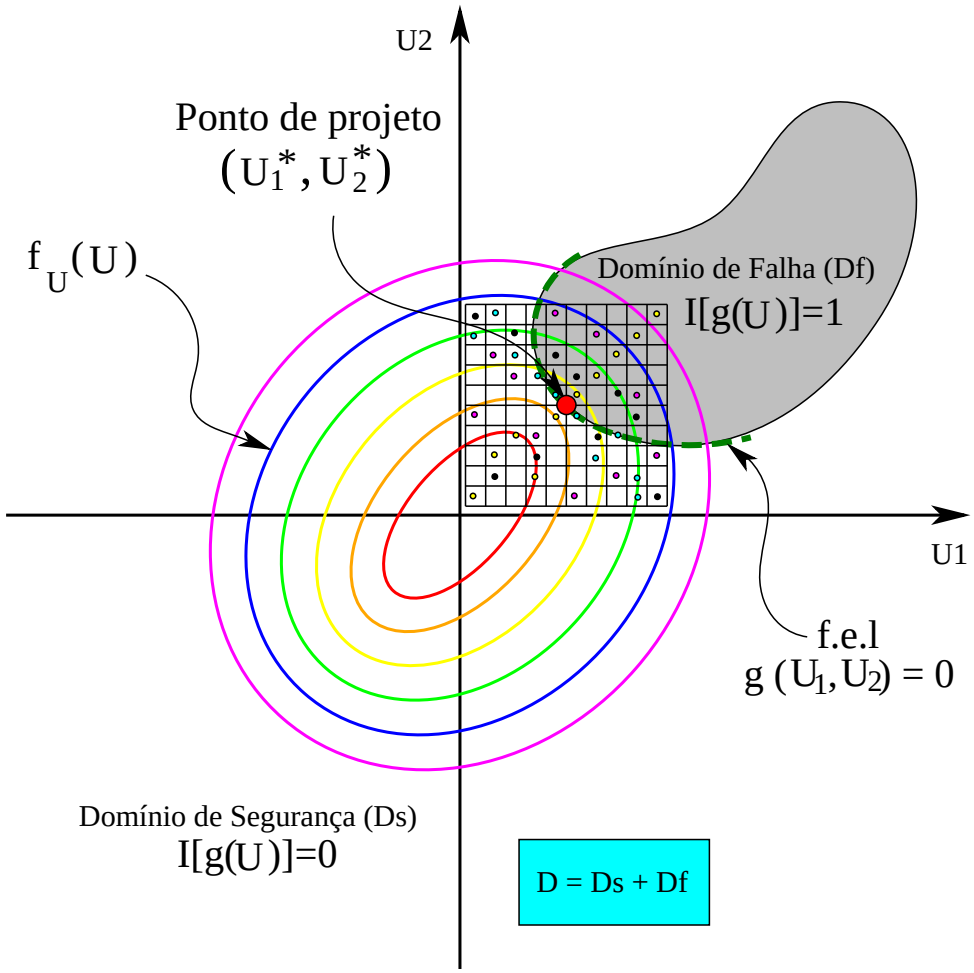

Figura 2: Descripción de los elementos básicos para el cálculo de la probabilidad de falla por el método Monte Carlo con muestreo por hipercubo Latino. Fuente: Autores.

$$r_s = \frac{\sum_i^n (R_i - \overline{R})(S_i - \overline{S})}{\sqrt{\sum_i^n (R_i - \overline{R})^2}\sqrt{\sum_i^n (S_i - \overline{S})^2}} \tag{9}$$

Donde:

R_i rango de X_i dentro del conjunto de observaciones $[X_1 X_2 \ldots X_n]^T$
S_i rango de Y_i dentro del conjunto de observaciones $[Y_1 Y_2 \ldots Y_n]^T$
$\overline{R}$,$\overline{S}$ rangos promedio de R_i y S_i respectivamente.

Establecer la sensibilidad probabilística de las variables aleatorias de un problema o diseño permite definir criterios para invertir y ahorrar dinero en las variables adecuadas que intervienen en la confiabilidad de una estructura, de esta manera se debe invertir dinero y esfuerzo en las variables más significativas para afectar positivamente la confiabilidad de manera efectiva y ahorrar dinero en variables poco significativas donde pueden realizarse recortes sin afectar significativamente la confiabilidad de una estructura, por supuesto siempre que sea humanamente posible intervenir la variable aleatoria presente en el problema.

La diferencia entre las sensibilidades probabilísticas y las deterministas es que las probabilísticas consiguen medir las posibles interrelaciones presentes entre todas las variables aleatorias, mientras que las sensibilidades deterministas aíslan cada variable de las posibles relaciones con las demás.

2 Problema De Confiabilidad En Una Cercha Plana

El problema abordado procede de Haldar-Mahadevan (2000). La figura 3 muestra la configuración geométrica, restricciones y cargas.

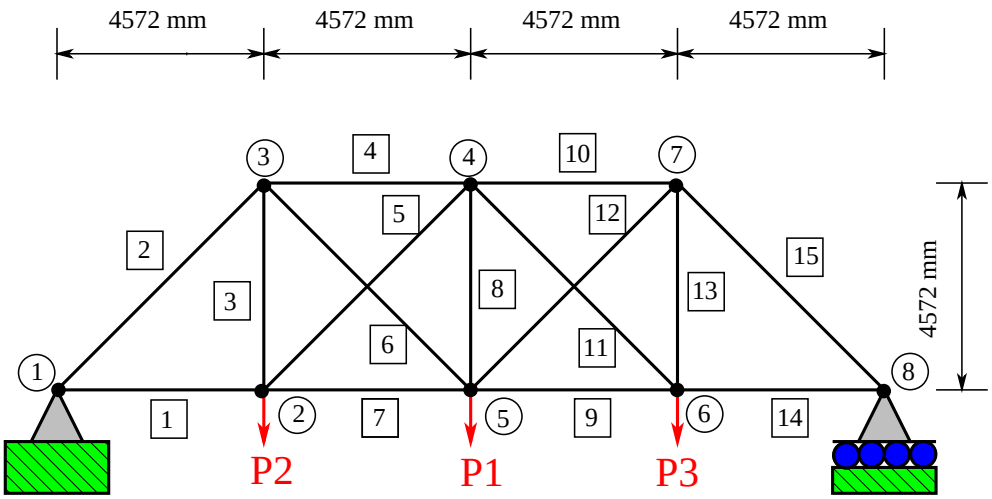

Figura 3: Cercha plana: geometría, restricciones y cargas. Fuente: Autores.

Las variables aleatorias del problema se encuentran resumidas en la tabla 1. Para el análisis se plantea una ecuación de estado limite por servicialidad, tomando como deflexión máxima en el punto medio de la armadura (nodo 5) el valor de 76.2 mm.

$$G\left(\mathbf{x},\mathbf{u},\mathbf{s}\right) = 1{,}0 - \frac{\delta}{\delta_{lim}} \tag{10}$$

Donde $\mathbf{x}$ denota el conjunto de variables aleatorias pertenecientes a la estructura (cargas, propiedades de material y geometría estructural dependiendo del caso), el vector u representa el conjunto de desplazamientos implicados en la función de estado límite G, y el vector s denota el conjunto de efectos de carga o variables secundarias del problema involucrados en la función de estado limite G (tensiones, fuerzas internas, entre otras), δ es la deflexión de control calculada y δ_{lim} es la deflexión límite establecida por el analista. Para el caso particular G es función de $\mathbf{x}$ y $\mathbf{u}$ por tratarse de una función de estado límite por desempeño en servicialidad.

El límite de deflexión de 76.2 mm escogido para el problema es igual 1/240 de la luz de la cercha, calculada como:

$$\delta_{lim} = \frac{4 * 4572}{240} = 76{,}2\ mm \tag{11}$$

Cuadro 1: Tabla de variables aleatorias y sus parámetros estadísticos característicos.

Variable	Unidad	Media	CV	Distribución
E	Mpa	199948.04	.06	Lognormal
$A_1, A_2, A_3, A_{13}, A_{14}, A_{15}$	mm^2	1032	0.05	Lognormal
$A_4, A_5, A_6, A_7, A_8, A_9, A_{10}, A_{11}, A_{12}$	mm^2	645	0.05	Lognormal
P_1	N	266890	0.10	Lognormal
P_2, P_3	N	88960	0.10	Lognormal

3 Modelo de Confiabilidad y de Sensibilidades Probabilisticas de Cercha Estructural Implementado En Ansys

3.1 Calculo de confiabilidad estructural de cercha plana en Ansys

Para este modelo se usa un tipo de análisis presente en el programa de elementos finitos comercial ANSYS, este se llama sistema de diseño probabilístico (Probabilistic Design System – PDS); a través de él es posible usar métodos de análisis de confiabilidad implementados al interior como el método de Montecarlo (MC) y el Método Montecarlo con muestreo por hipercubo Latino (MCLH). En la figura 4 se muestra un esquema resumido del funcionamiento de ANSYS para el análisis probabilístico de problemas de ingeniería usando el módulo PDS.

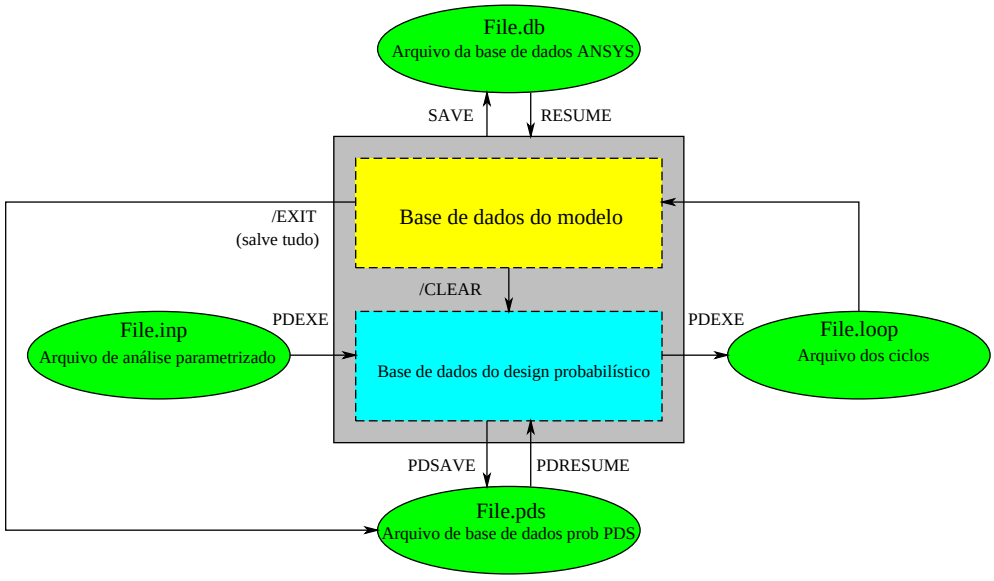

Figura 4: Flujo para la solución del problema de confiabilidad en ANSYS. Fuente: adaptación de los autores de manuales ANSYS APDL.

En la figura 4 se muestra la interacción de dos bases de datos fundamentales, una es la base de datos del modelo MEF o el analítico si este es programado por el usuario usando el lenguaje paramétrico propio de ANSYS (APDL – ANSYS Parametric Design language), y la base de datos de análisis probabilístico propiamente. Dado que las variables aleatorias no toman valor único, estas son parametrizadas y modificadas para ser enviadas al núcleo de análisis en cada simulación y así obtener los valores necesarios para la evaluación de la función de estado limite especificada para cada problema concreto. En la práctica este tipo de análisis avanzado se logra por escritura de un script que consta de dos partes; la primera es un macro que escribe el archivo de análisis donde se colocan todos los comandos necesarios para especificar el modelo MEF o

modelo de análisis analítico del usuario (en principio esta parte del archivo inicia con la definición de variable parametrizadas, el bloque de preproceso, solución y posproceso) y en seguida viene la parte del análisis probabilístico (donde se especifican las variables aleatorias, sus distribuciones y parámetros estadísticos); si las variables son correlacionadas es posible especificar el valor de correlación entre las variables, también se especifica el método probabilístico a usar (MC o MCLH) y sus valores característicos; finalmente se proporcionan comandos para el lanzamiento del módulo de cálculo probabilístico y comandos de posproceso de texto, gráficos y reportes.

La figura 5 muestra la malla de elementos finitos (LINK1, elemento de dos nodos con capacidad para carga uniaxial), numeración de nodos, numeración de elementos y condiciones de carga y apoyo.

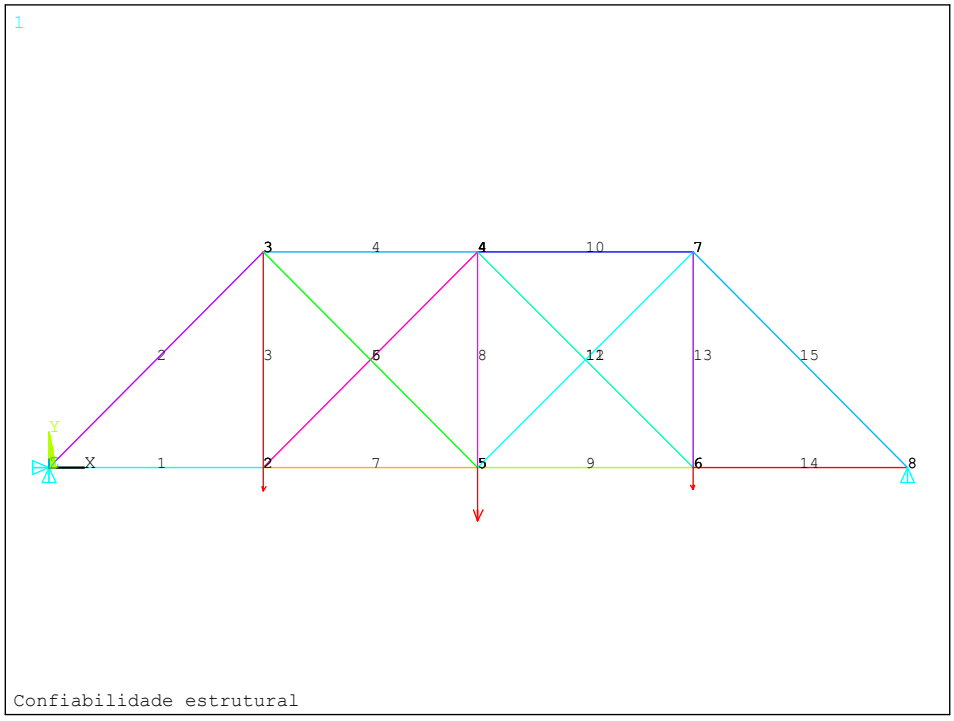

Figura 5: Malla de elementos finitos, numeración, condiciones de apoyo y de carga del problema abordado. Fuente: Autores.

En los modelos implementados se obtienen los resultados reportados en la tabla 2 para el caso de estudio, llamando la atención que se usa para ello el método de Montecarlo (MC), y el método Montecarlo con muestreo de hipercubo latino (MCLH).

Cuadro 2: Tabla de resultados de confiabilidad obtenidos y su tiempo computacional asociado para la solución hallada usando el módulo PSD de ANSYS.

Método	P_f	β	$CV_{P_f}(\%)$	**Tiempo CPU(min)**
MC (200000 sim)	0.725026E-02	2.445	2.617	440.500
MCLH (Paso 1000) (sim 10000)	0.707250E-02	2.454	—	21.416
MCLH (Paso 10000) (sim 100000)	0.746822E-02	2.434	—	299.317

Se puede apreciar que los tiempos de ANSYS en general son importantes para un tamaño relativamente

pequeño de modelo de elementos finitos, aun cuando estos resultados se obtienen usando memoria compartida en 4 núcleos físicos de la Workstation empleada para correr los análisis; esto se debe a que ANSYS es un programa general, que en algunos aspectos no puede ser adaptado para omitir algunos pasos innecesarios para la solución del problema como el cálculo de fuerzas internas en los elementos para este caso. De acuerdo con esto y para este modelo de confiabilidad pequeño puede resultar más competitivo soluciones simples y adaptadas al problema.

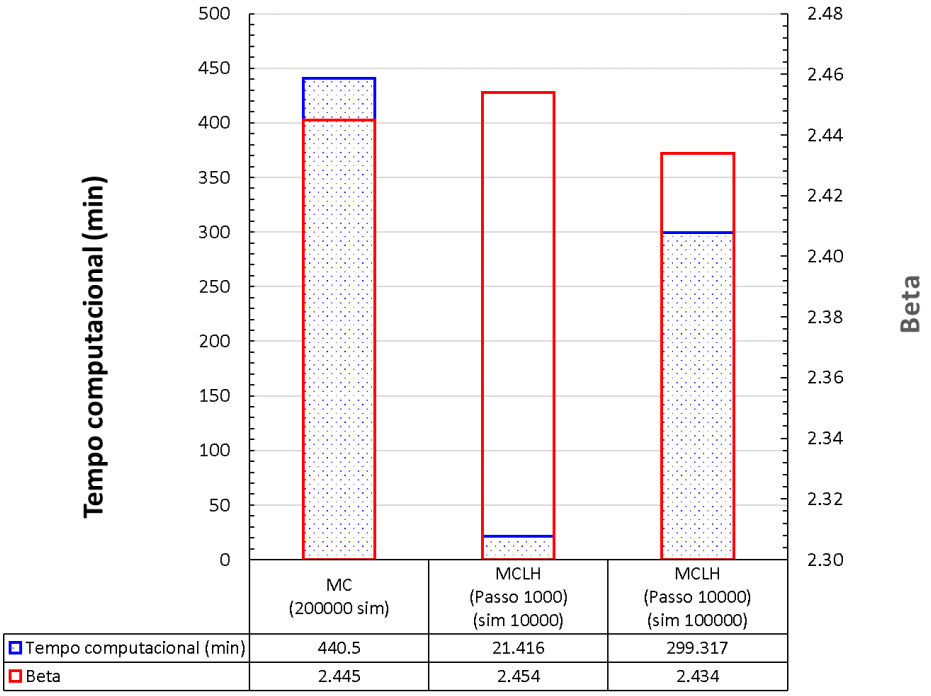

Figura 6: Resultados de índice de confiabilidad y tiempo computacional obtenidos para el problema de confiabilidad en cercha plana. Fuente: Autores.

Puede observarse en la figura 6 similitud en los resultados encontrados entre el método MC y su aproximación MCLH, de tal manera que se vislumbra que el método MCLH puede ser conveniente en términos de tiempo computacional para obtener una buena aproximación del índice de confiabilidad.

3.2 Cálculo de sensibilidades probabilísticas en modelo estructural de cercha plana en Ansys

Para el cálculo de sensibilidades probabilísticas se emplea la expresión mostrada en la ecuación 9 y esta se aplica por pares entre las variables aleatorias de entrada y las de salida, junto con la función de estado limite g(U), de amplio interés para el análisis de confiabilidad, dado que determina la falla o no falla de un modelo. Por otra parte, para la presentación de las sensibilidades, el PDS primero agrupa las variables de entrada aleatorias en dos grupos: aquellos que tienen una influencia significativa en un parámetro de salida aleatorio particular y aquellos que son bastante insignificantes, basándose en una prueba de significancia estadística. Esto prueba la hipótesis de que la sensibilidad de una variable de entrada aleatoria particular es idéntica a cero y, a continuación, calcula la probabilidad de que esta hipótesis sea cierta. Si la probabilidad excede un cierto nivel de significancia (determinando que la hipótesis es probable que sea verdadera), entonces la sensibilidad de esa variable de entrada aleatoria es insignificante. El PDS trazará sólo las sensibilidades de las variables de entrada aleatorias que se encuentran significativas. Sin embargo, las sensibilidades insignificantes

son reportadas en la gráfica de salida. También se puede revisar las probabilidades de significancia utilizadas por la prueba de hipótesis para decidir a qué grupo pertenecía una variable de entrada aleatoria particular.

El PDS permite visualizar sensibilidades ya sea como un gráfico de barras, un gráfico circular, o ambos. Las sensibilidades se clasifican para que la variable de entrada aleatoria que tiene la mayor sensibilidad aparezca primero.

En un gráfico de barras la variable de entrada aleatoria más importante (con la sensibilidad más alta) aparece en la posición más a la izquierda y las otras siguen a la derecha en el orden de su importancia. Un gráfico de barras describe las sensibilidades de una manera absoluta (tomando en cuenta los signos); una sensibilidad positiva indica que el aumento del valor de la variable de entrada aleatoria aumenta el valor del parámetro de salida aleatorio para el que se trazan las sensibilidades. Asimismo, una sensibilidad negativa indica que el aumento del valor de la variable de entrada aleatoria reduce el valor de parámetro de salida aleatorio. En un gráfico circular, las sensibilidades son relativas entre sí.

En un gráfico circular la variable de entrada aleatoria más importante (con la sensibilidad más alta) aparece primero después de la posición de las 12 en punto del reloj, y las otras siguen en dirección horaria en el orden de su importancia. La figura 7 muestra en gráficos de barras y circular los cálculos de sensibilidad probabilística obtenidos entre las variables aleatorias y la función de estado limite reportada en el grafico como el parámetro de salida GG.

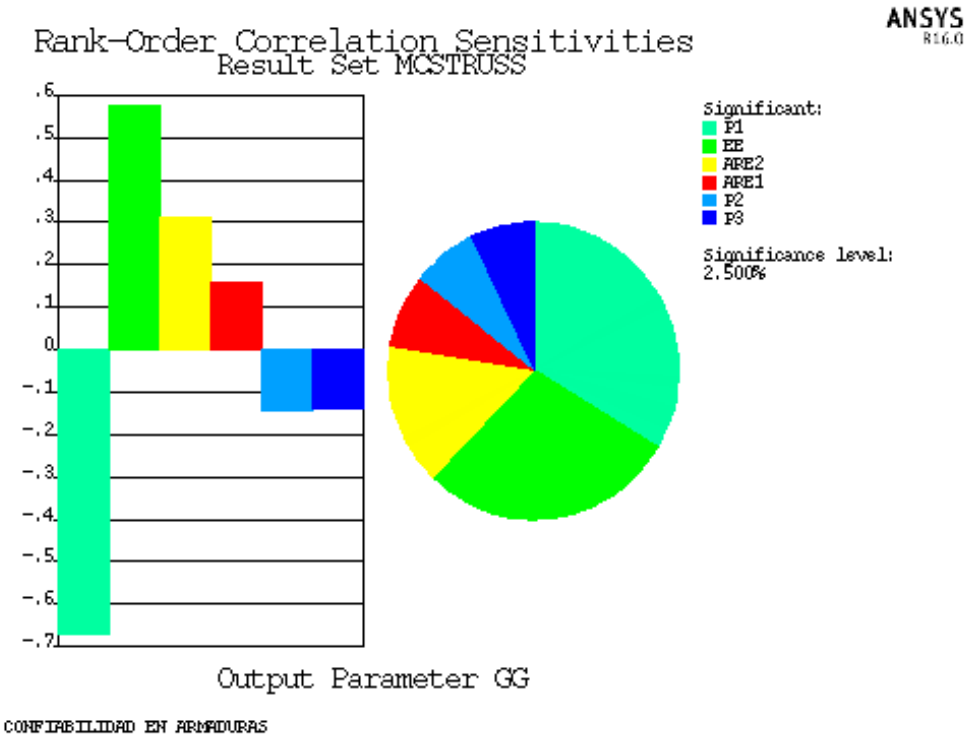

Figura 7: Gráfico de barras y circular de sensibilidad entre las variables de entrada y la función de estado límite GG (análisis de 200000 simulaciones por método MC). Fuente: Autores.

La Figura 7 muestra como la carga P_1 es la variable más significativa por estar directamente aplicada en el nodo 5 donde se verifica la función de estado limite a través de la deflexión, también puede verse como queda caracterizada la simetría de cargas P_2 y P_3 y como estas son menos importantes por estar lejanas al punto de verificación de estado limite, cumpliendo el principio teórico de actuación de las cargas por aferencia. Respecto al módulo elástico y las áreas de las barras, se nota la mayor incidencia relativa del material respecto a la dimensión del área de las barras para el control de deflexiones, con lo que en la practica una buena manera

de impactar la servicialidad es usando mejores materiales quizás de manera localizada y después intervenir las áreas de las barras, esto respetando criterios constructivos que permitan aplicar de manera racional las intervenciones, para determinada configuración de carga muy particular para el caso.

4 Conclusiones

1. Los resultados obtenidos en el método de Monte Carlo con muestreo por hipercubo latino muestran a este método como una alternativa relativamente rápida para el cálculo de confiabilidad respecto al método de Monte Carlo crudo.

2. La escalabilidad del caso mostro que, por ser el modelo de elementos finitos pequeño, este solamente requiere 4 núcleos para el cálculo paralelizado de los análisis de elementos finitos, quedando ociosos 8 núcleos disponibles en la Workstation usada.

3. Los resultados obtenidos en los cálculos de sensibilidades probabilísticas son muy importantes para la generación de conocimiento experto, respecto a criterios de diseño conceptual basados en confiabilidad. Es así como la jerarquización de las variables permite establecer un plan de inversiones y ahorros racional, esto con el fin de impactar positivamente la confiabilidad estructural de un proyecto.

4. El caso estudiado muestra que el programa comercial ANSYS es una alternativa para el análisis de confiabilidad estructural viable para la comparación con desarrollos nuevos implementados en proyectos y tesis de investigación en la academia.

5 Agradecimientos

Se agradece el apoyo de la UFGRS y el CNPQ por el financiamiento doctoral, adicionalmente se extiende este reconocimiento a los profesores que contribuyeron a este trabajo de investigación.

Referencias

[1] ALONSO, E. Risk analysis of slopes and its application to slopes in Canadian sensitive clays. *Géotechnique*, **v. 26**, p. 453-472, 1976.

[2] ANSYS, *Inc. Theory Reference (Version 16.0)*, 2016.

[3] CHING, J.; PHOON, K.; Efficient Evaluation of Reliability for Slopes with Circular Slip Surfaces Using Importance Sampling. *Journal of Geotechnical and Geoenvironmental Engineering*, **135(6):** 768-777, 2009.

[4] EL-REEDY M.A.; Reinforced concrete structural reliability. *CRC Press*, 2013, 369p.

[5] FENTON G. A., GRIFFITHS, D. V.; Risk Assessment in Geotechnical Engineering. 1 ed., *John Wiley & Sons Inc*, 2008, 463p.

[6] IMAN, R. L.; W. J. CONOVER.; Small Sample Sensitivity Analysis Techniques for Computer Models, with an Application to Risk Assessment. *Communications in Statistics: Part A- Theory and Methods*, **v. A9, n. 17**, p. 1749-1842. 1980.

[7] HALDAR, A.; MAHADEVAN, S.; Reliability assessment using stochastic finite element analysis. *John Wiley and Sons*, 2000, 328p.

[8] MCKAY, M.D.; BECKMAN, R.J.; CONOVER, W.J.; A Comparison of Three Methods for Selecting Values of Input Variables in the Analysis of Output from a Computer Code. *Technometrics*, **v. 21, n. 2**, p. 239-245, 1979.

[9] MELCHERS, R.E., BECK, A. T.; Structural reliability analysis and prediction.3rd Ed, *John Wiley and Sons*,2018, 514p.

[10] PHOON, K.K.; CHING, J.; Risk and Reliability in Geotechnical Engineering. *CRC Press*, 2015, 624p.

[11] RUBINSTEIN, R.Y.; KROESE, D. P.; Simulation and the Monte Carlo Method. 3rd Ed, *John Wiley and Sons*, 2017, 624p.

[12] VANMARCKE, E.H.; Reliability of earth slopes. *J. Geotech. Eng, ASCE*, **v. 103, n. 11**, p. 1247–1265, 1977.

[13] WU, T. H.; KRAFT L. M.; Safety analysis of slope. *J. of soil mechanics and foundations division(ASCE)*, **v. 96, n. SM2**, p. 609-630, 1970.

[14] XUE, J. F.; GAVIN, K.; Simultaneous determination of critical slip surface and reliability index for slopes. *Journal of Geotechnical and Geoenvironmental Engineering*, **n.133**, p. 878-886, 2007.

[15] ZHANG, J.; ZHANG L.M.; TANG W.H.; New methods for system reliability analysis of soil slopes. *Canadian Geotechnical Journal*, **n. 48**, p. 1138-1148, 2011a.

[16] ZHANG, J.; ZHANG, L. M.; TANG, W. H.; Reliability-Based Optimization of Geotechnical Systems. *Journal of Geotechnical and Geoenvironmental Engineeringe*, **v. 137**, p. 1211-1221, 2011b.

Experimental Evaluation of Stress Separation Techniques

J. G. Díaz R.[1]

[1]jorgeguillermo12@ustabuca.edu.co
Facultad de Ingeniería Mecatrónica,
Universidad Santo Tomás, Carrera 18# 9-27, Bucaramanga. Colombia

Abstract

The article deals with stress separation using different experimental techniques and their comparison. For the same sample coupon (SAE keyhole), measurements of fringe order, temperature or displacement were made using photoelasticity, TSA (thermoelastic Stress Analysis) or DIC (Digital Image Correlation) respectively. The results are compared to FEM simulations (Finite Element Method) using the Kt (stress concentration factor) as reference parameter. The results show consensus in measurements and calibration.

Key Words: stress separation, DIC, TSA, photoelasticity

1 INTRODUCTION

The problem of dealing with geometric discontinuities dates back to German engineer Ernst Gustav Kirsch in 1898 when he proposed a stress solution for an infinite plate with a circular hole. In 1913, British engineer Charles Inglis widened the solution to elliptical holes showing that stress will grow as the ellipse flattens. It was not until 1930 that Scottish physicist David Brewster described photoelasticity, laying the grounds for optical field measurements as opposed as widely used point measurements, such as strain gages or the newer Fiber Bragg Grating sensors (FBGS) [13]. However, such optical methods do not provide with independent measurements. Stresses show biaxial components that photoelascity gives as one value that has to be separated, so useful information can be extracted and properly analyzed. Another problem is the error when measuring close to edges. Readings can be difficult to interpret because the inherent error associated with lower correlation coefficients.

To evaluate a technique to separate stress an experiment was performed with a known analytical solution. The same test coupon was tested at elastic loads and measurements taken with photoelasticity, and an Infrared Camera (IR). To validate calibration of experimental measures, a Finite Element Analysis (FEM) was performed and results from a third experimental measure, Digital Image Correlation (DIC) was taken. The paper shows a comparison of several experimental techniques and the combination of some of them to estimate the stress intensity factor in a keyhole sample.

2 BACKGROUND

This section describes briefly the techniques used, and some schemes used to perform stress separation.

2.1 TSA

When a body is subjected to a tensile stress, its temperature is slightly reduced. Conversely, when subjected to a compressive stress a slight temperature increase is produced. When the body is subjected to cyclic loading, one can measure the small change in surface temperature (Δ T), which is in the order of ^{o}K$*$ 1e^{-3}. This change is proportional to the first stress invariant ($\Delta\ \sigma\ _1 + \Delta\ \sigma\ _2$) [1], [2] in the samples surface, as shown in Eq. (1).

$$\Delta \mathrm{T} = \frac{-\alpha_T \mathrm{T_o}}{\rho \mathrm{c}_p} \left(\Delta\sigma_1 + \Delta\sigma_2\right) \tag{1}$$

where $\alpha\ _{\mathrm{T}}$ is the linear thermal expansion coefficient, T_0 is a reference temperature, ρ is density and $\mathrm{c_p}$ is the specific heat under constant pressure. For an isotropic material subjected to plane stress, Eq. (1) can be simplified to Eq. (2).

$$S = K_m \left(\Delta\sigma_1 + \Delta\sigma_2\right) \tag{2}$$

where S is the reading from a thermal camera and Km a thermoelastic coefficient that can be either extracted from literature, calibrated in an experiment [3] or taken from a known samples region that has a known stress, i.e. remote applied stress . Because TSA gives the sum of first stress invariant, post-processing needs to be done to separate stresses.

2.2 Photoelasticity

The difference of principal stresses produced in a birefringent body by an acting load as a function of fringe number (N) is given by Eq. (3).

$$\sigma_1 - \sigma_2 = \frac{N}{t} f_\sigma \tag{3}$$

where t is the specimen thickness and f_σ the birefringent materials constant [4]. Therefore, by observing the fringe order, one can establish the difference between principal stresses.

2.3 DIC

DIC started in 1982 at the University of South Carolina [5]. Later in 1983 [6] a paper described a method to estimate deformation from a photographed deformed sample and another one [7] described how to compute rigid body displacements. Nowdays, it is the leading technique in experimental mechanics.

DIC is an optical technique that uses one (2D) or two or more (3D) cameras separated by a known distance to account for rigid body, rotation and perpendicular displacement. It takes advantage of the light intensity change in sequential photographs taken on a sample before and after deformation [8]. Photographs are digitalized as maps of bits *f(x,y)* making it possible to compare grey intensity before and after deformation to obtain displacement fields by using the minimization of a bits-correlation criteria [9] (Zero-Normalized cross-correlation), as shown in Eq. (4)

$$C = \frac{\sum_{x=-M}^{M}\sum_{x=-M}^{M}\left[f(x,y) - f\right] * \left[g(x',y') - g_m\right]}{\sqrt{\sum_{x=-M}^{M}\sum_{x=-M}^{M}\left\{\left[f(x,y) - f_m\right]^2\right\}} * \sqrt{\sum_{x=-M}^{M}\sum_{x=-M}^{M}\left\{\left[g(x',y') - g_m\right]^2\right\}}} \tag{4}$$

where f(x, y) and g(x, y) represent the grey levels of reference before and after deformation; and(x, y) and (x, y) are the coordinates of a point in the subset before and after deformation; *fm* and *gm* are the mean intensity values of reference and target subsets. The coordinate (x, y), after deformation, is related to the coordinate (x, y), before deformation, with the following relations as depicted in Figure 1 and can be calculated with Eq. (5).

$$\begin{aligned} x &= x + u + \frac{\partial u}{\partial x}\Delta x + \frac{\partial u}{\partial y}\Delta y \\ y &= y + \mathrm{v} + \frac{\partial \mathrm{v}}{\partial x}\Delta x + \frac{\partial \mathrm{v}}{\partial y}\Delta y \end{aligned} \tag{5}$$

DIC provides independent values of displacement u, v and w in directions X, Y and Z, so there is no need for post processing to use data (as opposed to photoelasticity). It is a non-contact optical technique. The technique can be used to measure small or large samples, static or dynamics events, and rigid or soft materials. The speckles can be added by ink spray, can be etched, or stamped.

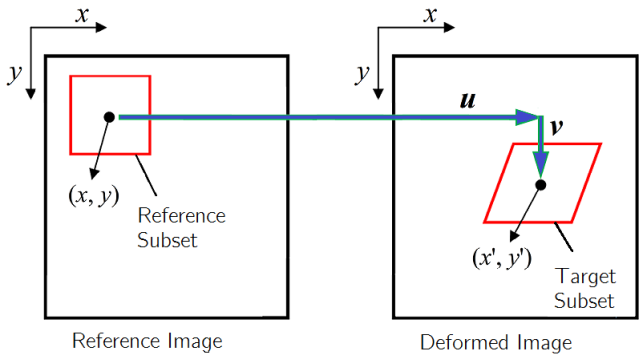

Figure 1: Image before and after deformation (adapted from [8])

Once displacements are established, using a correlation criteria such the one shown in Eq. (4), strains (ε) can be calculated using theory of elasticity Lagrangian relations as presented in Eq. (6).

$$\varepsilon_{xx} = \frac{\partial u}{\partial x}\varepsilon_{yy} = \frac{\partial \mathrm{v}}{\partial y}\gamma_{xy} = \frac{\partial u}{\partial y} + \frac{\partial \mathrm{v}}{\partial x} \tag{6}$$

By using elastic relations, stresses are calculated with Eq 7.

$$\sigma_{xx} = E(\varepsilon_{xx} - \nu\varepsilon_{yy}); \sigma_{yy} = E(\varepsilon_{yy} - \nu\varepsilon_{xx}); \sigma_{xy} = \frac{E}{1+\nu}\varepsilon_{xy}; \sigma_1 = E(\varepsilon_1 - \nu\varepsilon_2); \sigma_2 = E(\varepsilon_2 - \nu\varepsilon_1); \tag{7}$$

where E is elastic modulus and ν is poissons modulus. Extensive details about DIC can be found at [10] with commercial implementation from several is available vendors as well as open source versions accessible from Matlab central.

2.4 Stress Separation

As shown in Eq (2) and Eq (3) TSA and photoelasticity, respectively, do not provide with independent readings of stress. In 2003, Sakagami et. al. [11] proposed a hybrid method that combined TSA and photoelasticity. The sum of the first stress invariant is constant as it is the difference of principal stresses; when putting them together, they form a 2x2 linear system as shown in Eq. (8).

$$\begin{aligned} \Delta\sigma_1 + \Delta\sigma_2 &= C_{TSA}; TSA \\ \sigma_1 - \sigma_2 &= C_{Photoel}; Photoelasticity \end{aligned} \tag{8}$$

In 1996, Dulieu [12] summarized three methods to calibrate TSA readings, as follows:

- Calibration against a measured stress (directly from the experiment). If orthogonally placed SG are used, they can be used to transform first stress invariant into Eq (9).

$$\sigma_1 + \sigma_2 = \sigma_x + \sigma_y = \frac{E}{1-\nu}(\varepsilon_x + \varepsilon_y) \tag{9}$$

then substituting Eq. (2) into Eq. (9), it will return the calibration constant as Eq. (10).

$$K_m = \frac{E}{1-\nu}\frac{(\varepsilon_x + \varepsilon_y)}{S} \tag{10}$$

Although a second experiment is needed to use Eq. (9), it does not interfere with TSA readings as a SG can be allocated in the dark area of the specimen. However, care needs to be exerted as the SG equipment cannot shield or reflect heat to the IR camera.

- Calibration against a calculated stress. An area of the specimen or a different one of same material, with a known analytic solution can used to calculate a known stress for the experiment.

It has to be noted here that by performing curve fitting to an appropriate Airys stress function, one would not need a second measurement. That would be treated in an upcoming work.

3 MATERIALS AND METHODS

A SAE "keyhole" specimen made out of polycarbonate (E=2,6 GPa & ν =0,37) , with dimensions (in mm) shown in Figure 2, was subjected to tensile loading. In order to have the sample free of residual stress caused by the machining process, before the experiment it was properly stress relived in an oven.

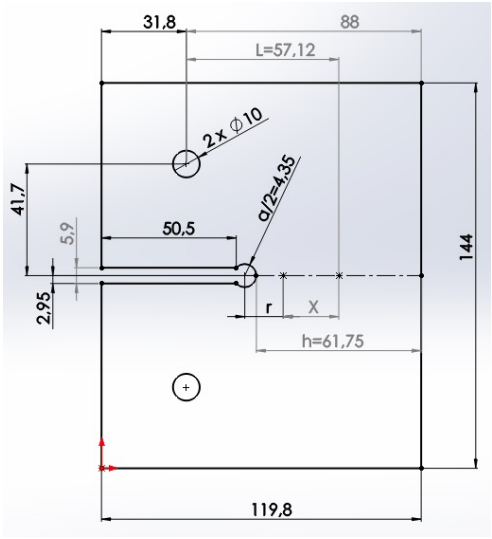

Figure 2: Test coupon dimensions

For DIC measurements, the coupon was primed with white paint and sprayed painted with black ink to achieve the needed random speckles. Two, 5-MP CCD cameras (Point Grey GRAS-50S5M) equipped with 35-mm lenses, cameras were used to capture images and VIC Snap was used for image acquisition, whereas 3D-VIC (both from Correlated Solutions, Columbia NC) was used to process images. For TSA experiments, a FLIR A655sc Infrared camera was used. Deltha Therm (Madison, WI) software was used to calibrate and acquire thermograms. For phoelasticity, a Vishay (Raleigh, NC) transmission polariscope with quarter-wave-filters was used. The material fringe value 7 mm/MPa. At last, FEM simulations were carried using SolidWorks simulation 2013 (Concord, MA).

Samples were subjected tensile loads and readings were taken with the afore mentioned techniques. The idea was to obtain two sets of experimental measures (TSA and photoelasticity in this case to form the linear system described by Eq. (8) at each measured point), DIC, and one numerical result (Finite Element Analysis).

For DIC readings, the sample coupon was subjected to tensile forces 52, 105, 160, 221, 270 and 307N successively. The 3D-VIC software delivered values for $_{xx}$, $_{yy}$, $_{xy}$, $_{1}$ and $_{2}$. For TSA, the sample was subjected to alternating loads in the range of 460N. Calibration was done by making $\Delta\ \sigma\ _2 = 0$ in a previous test of a rectangular bar of the same material subjected to simple tension, leaving K_m readily available to calculate from Eq (6). The FLIR IR camera provided S as 640x483 matrix. To extract the K_m constant several average values were taken looking for the lowest standard deviation. At last, for photoelasticity the sample was subjected to forces of 62, 102, 150, 204, and 252N. Photographs were taken to visually extract fringe numbers.

4 RESULTS

In order to find the Kt, the highest S value near the keyhole was looked for, as seen in Figure 3. Once it was found, the data on the horizontal line towards the sample side was processed using Eq. (6) with previously found Km constant. To find the distance along the pixels points, a scale factor was made using a known dimension for the coupon.

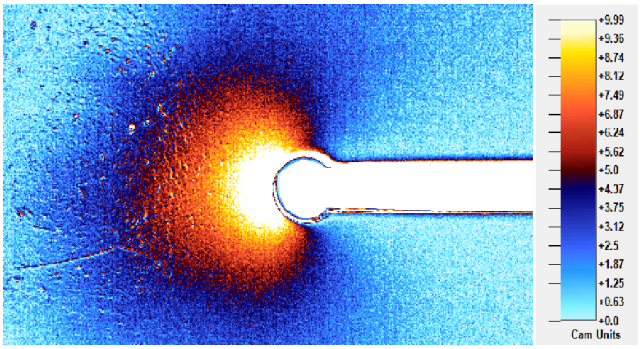

Figure 3: IR camera reading for the loading sample

To verify TSA calculations, a FEM simulation was run using E=2,4 GPa, ν =0,37 and tetragonal elements. However, when comparing stress values obtained from different loads, it is recommended to normalize them by dividing the stress over the applied load.

FEM and TSA results are shown in Figure 4 (where the horizontal axis is the distance from the edge and the vertical in normalized stress in MPa/N and one can see an agreement between experimental and numerical results. Hence, the calibration method was validated.

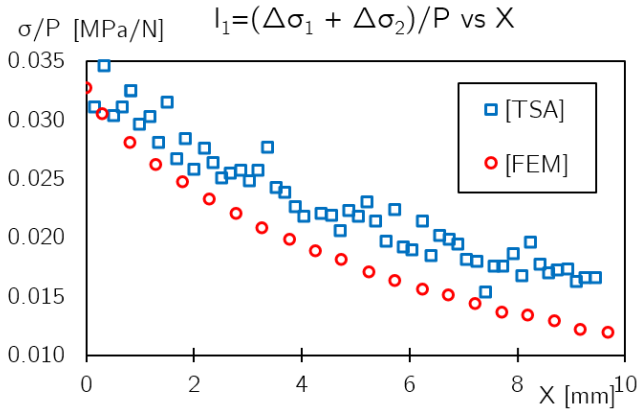

Figure 4: Normalized first stress invariant along sample horizontal axis by FEM

The separation method was tested with FEM results (for 150N & 410N not shown here for space limitations), and it worked for stress values from same load at the same point, at or away from the border.

For photoelasticity, there was a problem at the edge due to residual stresses induced while machining the sample. In Figure 5, one can see the blurry fringes as one moves closer to the bore, whereas the red numbers show fringe order.

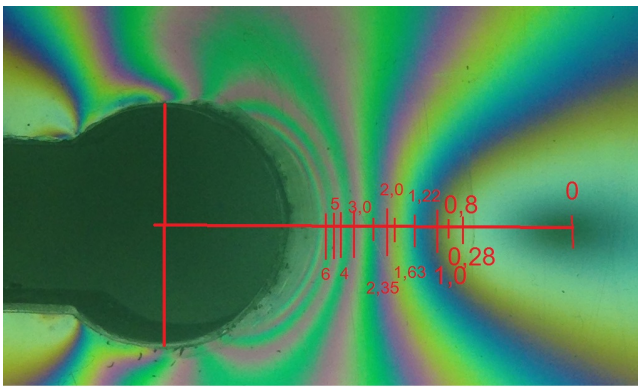

Figure 5: Fringe bands at 252N

Results from solving Eq. (8) with Photoleasticity and TSA normalized data are presented in Figure 6 which shows Kt versus r/a (distance from the center of the bore over the radius). An order two polynomial interpolation was performed giving the relationship shown in Eq. (11) and plotted in Fig

$$K_t = -1,4901\left(\frac{r}{a}\right)^2 + 3,4922\left(\frac{r}{a}\right) + 1 \tag{11}$$

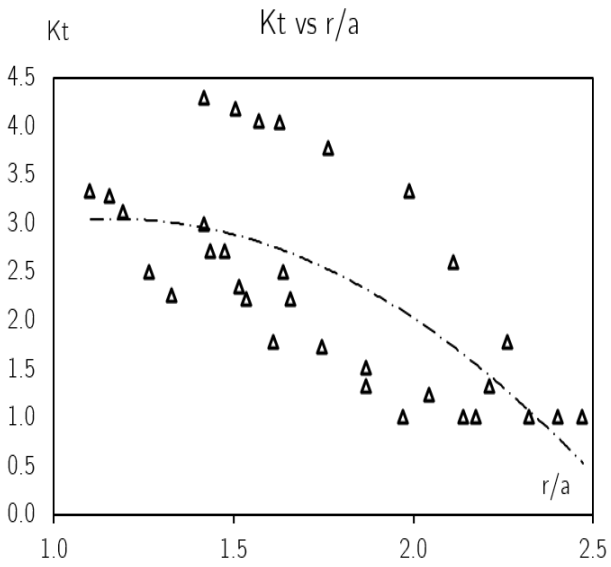

Figure 6: Kt vs r/a from photoleasticity data

For a value of (r/a) = 1 (hole border) Kt value is 3.02, which is very close to Kirsch solution.

DIC is able to provide with separated measures of vertical and horizontal displacements by using Eq (8). In case there is a second camera, perpendicular-to-focal-plane displacements are available. The white dotted line in Figure 7 shows parallel-to-load strain (ε_{yy}) field as measured by DIC, and the white dotted line represent the points where the data was extracted from to compare with TSA and photoelasticity readings.

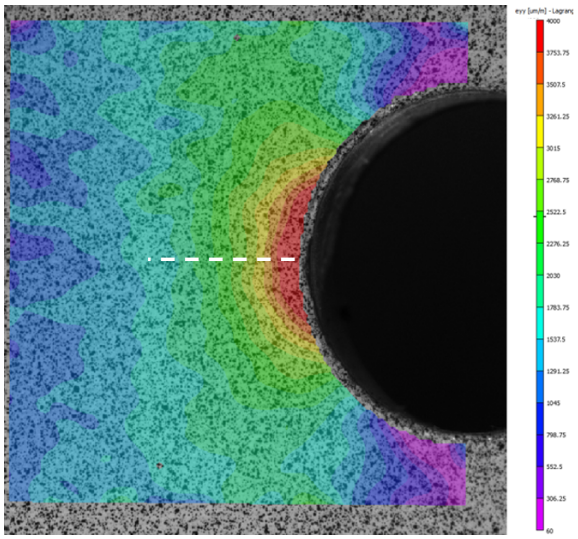

Figure 7: DIC vertical strain (ε_{yy}) field

Eq (12) shows the analytic solution for normal stresses at the edge.

$$\sigma_y = \frac{P}{ht} + \frac{12(PL_f)^{h}/_{2}}{h^3 t} \tag{12}$$

where h and t are the length and thickness of the plate, and L_f eccentricity from the load application point to the neutral plane of the plate. Hence, the stress concentrator value can be calculated by Eq. (13).

$$K_t = \frac{\sigma_{yDIC}}{\sigma_{Teor}} \tag{13}$$

Table 1 shows the Kt calculated with Eq. (13) for different actuating loads.

Table 1: Stress concentration factor (Kt) obtained with DIC data

σ y DIC (MPa)	0,89	1,78	2,67	3,55	4,45	5,33
Kt :	2,94	2,83	2,88	2,94	2,88	2,94

which gives an average Kt of 2.91, very close to Kirsch analytical solution.

Figure 8 shows a comparison between normalized stresses: TSA & photoelasticity obtained through matrix Eq (8), DIC, and FEM results along the axis. It can be seen an agreement between TSA & photoelasticty with FEM for normal and perpendicular stresses. However, for DIC normal stress (S1 DIC) the tendency agrees with other methods, but values are a little lower than their counterpart.

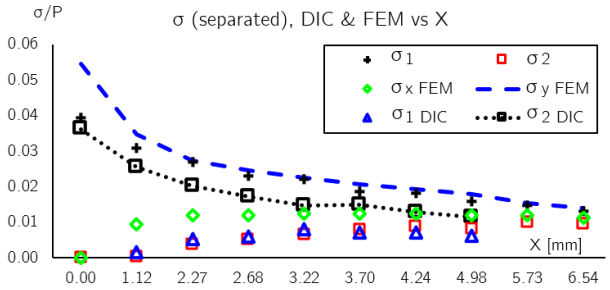

Figure 8: Normalized separated stresses obtained with TSA & photoelasticity, DIC and FEM Stress vs distance from the border

5 CONCLUSION

The evaluated stress separation technique was successful telling apart experimental stresses from TSA and photoleasticity. Results from such separation were compared with DIC and FEA. The three calculated stress values lead to a very close stress value of concentration factor.

Although the equipment used in 1996 [12] was slightly different to what it is used today, a direct calibration from experiment properties, as shown in Eq. (2) can be done. This one seems to be the most complicated method and prone to error due to uncertainties in knowledge of material properties. A much simpler approach was taken here by comparing IR camera readings with a known stress-state.

It was observed that the values of σ_{xx} and σ_2 as well as σ_{yy} and σ_1 are almost identical in DIC, which is expected for a uniaxial loading case. The difference may be due to lack of alignment between samples holes and loading device axis. Additionally, DIC appeared to provide slightly lower values than other techniques. This could be due to the correlation parameters used to run the correlation (subset, step, and Lagrangian filter) which can smooth data for large setting values. Optimal combination of parameters, along with average speckle size, is an ongoing topic of research as suggested in literature.

The method to extrapolate the stress concentration factor seems valid as seen in Figure 6 and Figure 8. Depending on the technique used, there is an inherent measuring error at the edge that prevents one to calculate stresses at that such borders. By measuring the appropriate variables and calculating stresses along a horizontal line, one can extrapolate the actual value of Kt.

References

[1] L. Marsavina and R. A. Tomlinson, "A Review of using Thermoelasticity for Structural Integrity Assessment," *Frat. ed Integrit Strutt.*, vol. 27, pp. 1320, 2014.

[2] R. A. Tomlinson and A. Patterson, "Mixed Mode Cracks From Thermoelastic Data," *Fatigue Fract. Eng. Mater. Struct.*, vol. 20, no. 2, pp. 217226, 1997.

[3] J. M. Dulieu-Smith, "Alternative calibration techniques for quantitative thermoelastic stress analysis," *Strain*, vol. 31, no. 1, pp. 916, 1995.

[4] J. L. Freire and A. Voloshin, "PHOTOELASTICITY," in *Encyclopedia of Life Support Systems (EOLSS)*, 1st ed., Oxford ,UK: UNESCO, 2009.

[5] W. H. Peters and W. F. Ranson, "Digital Imaging Techniques In Experimental Stress Analysis," *Opt. Eng.*, vol. 21, no. 3, 1982.

[6] M. A. Sutton, W. J. Wolters, W. H. Peters, W. F. Ranson, and S. R. McNeill, "Determination of Displacements using an Improved Digital Correlation Method," *Image Vis. Comput.*, vol. 1, no. 3, 1983.

[7] W. H. Peters, F. Ranson, W, M. A. Sutton, T. C. Chu, and J. J. Anderson, "Application Of Digital Correlation Methods To Rigid Body Mechanics," *Opt. Eng.*, vol. 22, no. 6, 1983.

[8] G. L. Gonzles, J. G. Daz, J. A. O. Gonzlez, J. T. P. Castro, and J. L. de F. Freire, "Determining SIF using DIC considering Crack closure and blunting," in *Experimental and Applied Mechanics. Vol 4.*, 2016, pp. 2536.

[9] R. Zhang and L. He, "Measurement of mixed-mode stress intensity factors using digital image correlation method," *Opt. Lasers Eng.*, vol. 50, no. 7, pp. 10011007, 2012.

[10] M. A. Sutton, J. J. Orteu, and H. Schreier, *Image Correlation for Shape, Motion and Deformation Measurements: Basic Concepts, Theory and Applications*. Boston: Springer, 2009.

[11] T. Sakagami, S. Kubo, Y. Fujinami, and Y. Kojima, "Experimental Stress Separation Technique Using Thermoelasticity and Photoelasticity and Its Application to Fracture Mechanics," *JSME Int. J. Ser. A*, vol. 47, no. 3, pp. 298304, 2004.

[12] J. M. Dulieu-Smith, "Alternative calibration techniques for quantitative thermoelastic stress analysis," *Strain*, vol. 31, no. 1, pp. 916, 1995.

[13] C.A. Triana-Infante, M. Varn-Durn, D. Pastor-Abelln, " *Validacin de sensores basados en redes de difraccin de bragg (fbgs) para deformacin y temperatura"* Iteckne, Vol. 11, nm. 2 pp. 172 - 182 (2014) doi: 10.15332/iteckne.v11i2.730

Mechanical Characterisation of Polycarbonate for Helicopter Windshields

S. A. Ritt[1,a], M. Vinot[a]

[1]stefan-andreas.ritt@dlr.de
[a]Institute for Structures and Design,
German Aerospace Center DLR, Germany

23.07.2018

Abstract

Transparent thermoplastics like polycarbonate are widely used as windshields for its optical properties and for their higher specific mechanical properties compared to glass. Under use in airframe front windshields, plastics transparencies can be exposed to impact scenarios such as bird-strikes. The resulting load can lead to a complex loading of the material dominated by tension and bending.
In order to generate input for realistic simulation results, experiments have been performed to characterise the materials under these loading modes at coupon level in the elastic and plastic domain. On the simulation side, numerical models comprising a discretisation with elements applying Reissner's plate bending theory have been used in the explicit finite-element method within the LS-DYNA framework with latest solver version R10.1.
Experiments were performed at different strain-rates ranging from quasi-static to approx. 75 1/s. The numerical modelling has been done with thin and thick shell elements. The thin shell element approach used the Reissner-Mindlin kinematic assumption in fully-integrated shells. Additionally, some thick shell formulations with various approaches were applied. To cover the strain-rate sensitive behaviour, a material model based on the Johnson-Cook theory was applied. The influence of the modelling was investigated and compared to the experimental characterisation.

Key Words: Damage mechanics, impact, bird-strike, windshields, glazing, transparencies, material modelling, explicit Finite Element Method, Reissner plates

1 Introduction

The present work is motivated by the numerical simulation and experimental investigation of bird-strike events on helicopter windshields. Bird-strike is a common event for helicopters as all operations are performed at low altitude. In this way, it needs to be taken into account for design and certification of larger vehicles, particularly for passenger transport. The reference here shall be the certification specifications for large rotorcraft, CS-29, from the European Aviation Safety Agency (EASA) [1].
When impacted by a soft body like a bird, a windshield material is loaded in a complex mode. However, the main loading modes of the windshield shall be defined and according to these loading modes the material shall be characterised.
Tests have shown that a bird-strike leads particularly to an indentation in areas with a higher impact angle (Figure 1). A larger indentation finally leads to a membrane loading. As typical transparent materials are weaker than the frames they are attached to, the material is bended around these support structures. Additionally, the material is loaded at different rates dependent upon time and location while a windshield is set out to a temperature range in operation too.

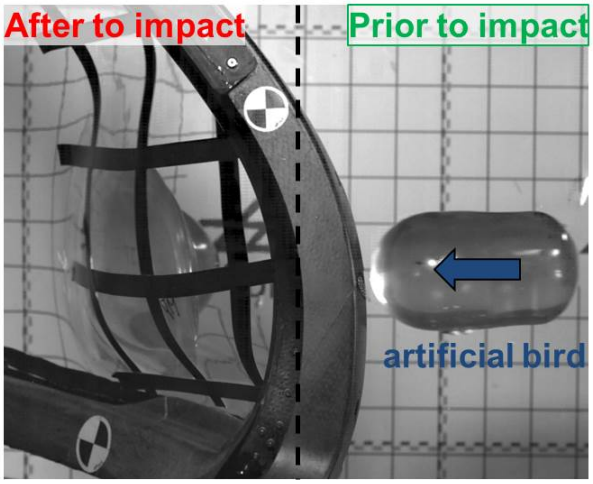

Figure 1: Deformation of windshield under bird-strike

Earlier works have touched the characterisation at coupon level in tension at different temperatures and bending. A three-point fixture was used in which the pressure fin acts precisely at the point of highest bending moment and adds through-thickness shear load. Furthermore, a rigid fin with a small radius can indent into the weaker substrate. Additionally in this work [2], hard body impact tests were used at this level for characterisation but finally bird-strike simulation was intended.
Polycarbonate is one of the superior windshield materials due to its high failure elongation [3]. In this source, the material was characterised with a brittle behaviour and was described by linear elastic fracture mechanics. Temperature and strain-rate dependencies were scaled using the Eyring formulas. However, in the numerical simulation a widely used elastic-plastic approach was used in conjunction with a generalised incremental stress-state dependent damage model (GISSMO). A tension and puncture testing is described.
A characterisation of polycarbonate over a wide strain-rate range and a determination of tension and compression behaviour can be found in [4]. Here, Split-Hopkinson tension bar (SHTB) testing has beeen applied with machined round specimens up to a strain-rate of 5000 $1/s$.
A comprehensive study of quasi-static tension tests with servo-hydraulic machines and compression test by a Split Hopkinson Pressure Bar (SPPB), both with elevated temperatures, was conducted by [5]. Tests at low strain-rates of 0.005 and 0.4 $1/s$ as well as at very high strain-rates between 1750 and 15000 $1/s$ were used to determine the parameters for the phenomenological Johnson-Cook strength model and the Zerilli-Armstrong polymer strength model with machined round specimen.
Another work [6] is showing the strain-rate and temperature dependencies under compression and impact tests at very low strain-rates. It used a multiscale approach for bridging mechanisms from the molecular scale to the continuum scale.
For the presented work it was chosen to characterise and simulate the material with planar specimens with respect to the two loading modes tension and bending. With these plain samples, the material can be cutted with the same parameters as for the future application. The specimen thickness was chosen in the same order of magnitude as in the windshield. The quasi-static tests could be performed in a temperature range relevant for the application.

2 Applied numerical model

In order to cover strain-rate and temperature dependency and make use of a larger set of characterisation test data, the tabulated Johnson-Cook (JC) [7] material model was used. This is a material model in the explicit Finite Element Analysis (FEA) code LS-DYNA which is used for the bird-strike analysis. The elastic-viscoplastic material model ∗MAT224 uses the JC approach in a phenomenological way with the option to

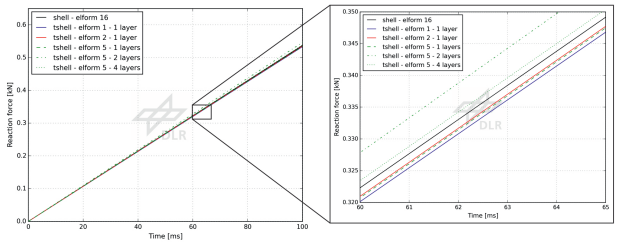

Figure 2: Force-displacement curve of a linear elastic material under bending load for various element formulation and discretisation in thickness

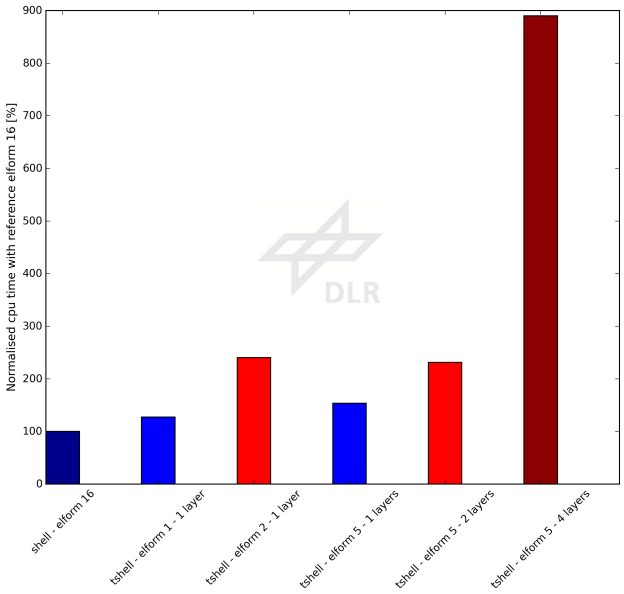

Figure 3: Comparison of the computing time depending on the element formulation and discretisation in thickness

define strain-rate and temperature dependent stress-strain curves. The plastic failure strain can be defined as a function of triaxiality, Lode parameter, strain-rate, temperature as well as element size [8]. This approachs avoids to determine the JC parameters as given in [5], e. g. which needs more appropriate and comprehensive testing.

To estimate the computing time of different numerical approaches, fully-integrated thin shell elements with element formulation (called elform in LS-DYNA) 16 and thick shell element formulations 1, 2, 3 and 5 have been compared at the example of a bending specimen. In this case, for simplification the specimen was modelled with a purely elastic material model. Additionally, different discretisation in the thickness has been investigated for the thick shell model. In all cases, an element length of 5 mm and 5 integration points per element has been chosen, the bending specimen being meshed with 400 elements in total (800 and 1600 for the models with 2 elements and 4 elements in thickness respectively).

Increasing the discretisation in thickness has a slight influence on the stiffness of the specimen, although a convergence is reached at more than 4 elements in thickness. Except for the elform 3 for thick shell elements, with which the simulation aborted at an early stage, other formulations give a similar specimen behaviour (Figure 2). However, simulating the specimen with thick shell elements results in an increase of the computing time by 20 % to 150 % depending on the elform (Figure 3). Simulating the specimen with 4 elements in the thickness leads to a severe increase in the computing time with an increase of 800 % compared to the thin shell elements.

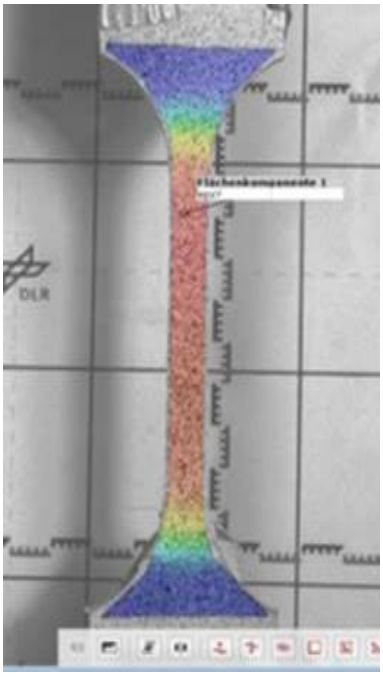

Figure 4: Tension specimen in the parallel shaped area with optical strain measurement

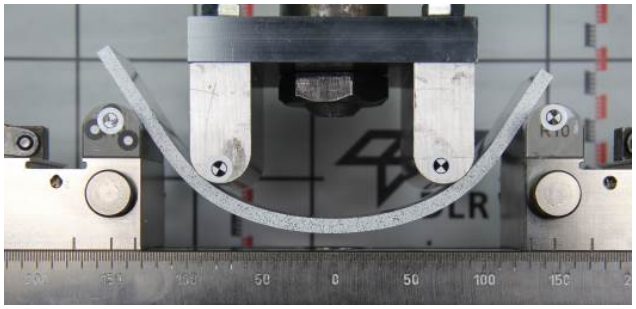

Figure 5: Four-point bending specimen with speckle pattern for optical strain measurement

3 Characterisation tests at coupon level

The characterisation of the material behaviour at a coupon level, i. e. pure material specimens, was performed with tension tests as well as four-point bending tests at various strain-rates and temperatures. As described below, the specimen were manufactured from the same plate with the same thickness. The cutting process and edge quality was the same as in future larger specimens up to full-scale. Hence, the sensitivities in material behaviour by the edges should be the same.

The tension tests were performed in an electro-mechanical (for low strain-rates) and a servo-hydraulic (for elevated strain-rates) testing system using a shouldered specimen according to SEP-1230 (Figure 4), originally developed for high-rate testing of sheet metals [9]. The specimen's characteristic dimension is 25x10x5 mm^3 (LxWxT) in the parallel shaped area.

The applied strain-rates varied from 0.005 $1/s$ for quasi-static to 75 $1/s$ for the elevated rate.

The four-point bending (4PB) tests were conducted in an electro-mechanical testing system with slight deviations from the standard ASTM-D6272 [10]. The difference to the standard concerned the larger specimen size of 200x50x5 mm^3 (LxWxT). The selected support-to-fin-distance ratio was 2.

The outer fibre strain-rate under bending was not directly verified. However, the quasi-static boundary conditions from the standard were considered with 8 mm/min crosshead velocity.
Both testing used planar digital image correlation (DIC) or optical strain measurement to analyse surface strains as visible in Figure 4. The virtual extensometers in the DIC used for strain determation were in the scale of classical strain gauges.

4 Numerical and experimental results

The tested PC material shows as expected a typical strain-rate and temperature dependency. An augmentation of yield strength is obeserved with increasing strain-rate and with decreasing temperature (Table 1). In experiment, local strains higher than 40 % have been reached without specimen failure. Using experimental values as basis for the simulation, a good correlation was achieved between the numerical prognosis and the experiment. For the tension load case this can be retrieved in Figure 6 where a range of strain-rates and temperatures has been plotted. The specimen true stress has been normalised here with the experimental and numerical yield strength at low strain-rate and temperature of 20 °C respectively.

Table 1: Experimentally measured yield strength values for input in the material card

strain rate [1/s]	**temperature [°C]**	**yield strength [GPa]**
0.1	-20.0	0.082
0.1	0.0	0.075
0.1	20.0	0.069
1.0	20.0	0.075
75	20.0	0.082

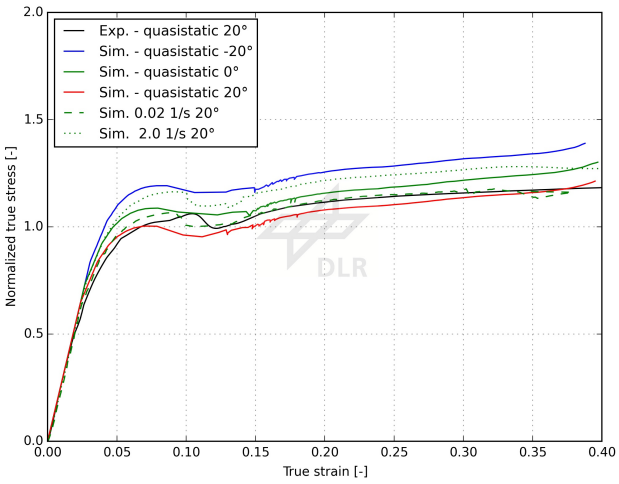

Figure 6: Strain-rate and temperature dependent behaviour of the tension specimen in experiment and in simulation

The bending specimen was subsequently simulated using the same material card without any further calibration. Figure 7 shows the good agreement which was obtained between the simulation and the experiment. Both the specimen stiffness and its strength were captured in the simulation. After a fin displacement of about 25 mm, the specimen is sliding between the lower fins and the force decreases. As shown in precedent investigation of the element formulation, no large discrepancy was to be detected between the simulation with thin shell elements and with thick shell elements.

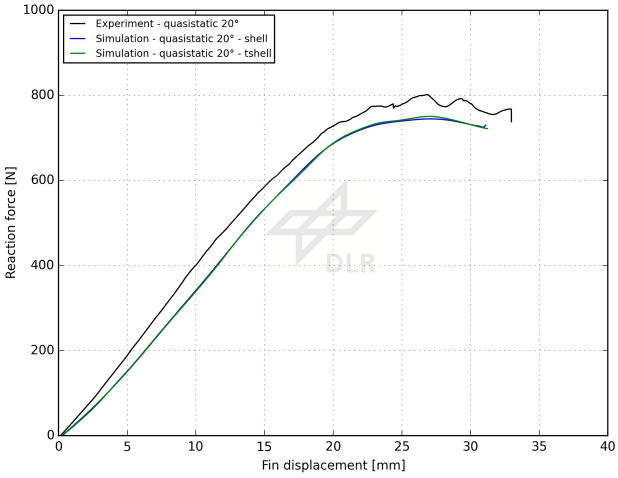

Figure 7: Behaviour of the bending specimen under quasi-static loading in experiment and in simulation

5 Conclusions

The explicit Finite Element Method using a strain-rate and temperature dependent material law was applied to model the elastic and viscoplastic behaviour of windshields under bird-strike impact. The windshields are made of polycarbonate which is an amorphous transparent thermoplastics.
The Johnson-Cook material law was used in a tabulated way with characterisation data which have had origin in coupon tests of two different loading modes. The fully integrated Reissner-Mindlin shells can model the behaviour in the given loadings as well as in larger scale applications. Extended element kinematics with thick shells have been analysed for its applicability. A solid approach has not been followed due to the high computational costs when applying to larger structures.
Next steps in the validation of the modelling comprise the mesh size regularisation which is implemented in the applied material model in LS-DYNA but could yet not be verified at structure scale. Further investigation will concern the investigation of the stress localisation and cracking process at specimen and structure scale.

6 Acknowledgement

The authors are grateful to the colleagues T. Behling, A. Kleinert, L. Schlacke and D. Schüler for their experimental contributions to this publication. The funding by EC's CleanSky programme as well as the institutional funding by the DLR aeronautic research programme for supporting this research work is acknowledged.

References

[1] European Aviation Safety Agency. Certification Specifications for Large Rotorcraft - CS-29, 11 2016.

[2] J. Markmiller and U. Burger. Impact behaviour of monolithic and multi-layered polymer windshields for light helicopters. In *Proceedings of AHS 69th Annual Forum*. American Helicopter Society, 2013.

[3] Z. Lu, M. Seifert, and C.-H. Tho. Bird impact simulation of polycarbonate windshield subject to brittle failures. In *Proceedings of AHS 71th International Annual Forum*. American Helicopter Society, 2015.

[4] S. S. Sarva and M. C. Boyce. Mechanics of polycarbonate during high-rate tension. *Journal of Mechanics of and Materials and Structures*, 2(10), 2007.

[5] A. Dwivedi, J. Bradley, and D. Casem. Mechanical response of polycarbonate with strength model fits. techreport ARL-TR-5899, Army Research Laboratory, 2 2012.

[6] J. L. Bouvard, C. Bouvard, B. Denton, M. A. Tschopp, and M. F. Horstemeyer. Simulation of impact tests on polycarbonate at different strain rates and temperatures. In *Conference Proceedings of the Society for Experimental Mechanics Series*, pages 145–147. Center for Advance Vehicular Systems, 2010.

[7] G. R. Johnson and W. H. Cook. A constitutive model and data for metals subjected to large strains, high straln rates and high temperatures. In *7th International Symposium on Ballistics*. American Defense Preparedness Association, 1983.

[8] T. Vasko. A user guide for ∗MAT_TABULATED_JOHNSON-COOK in LS-DYNA. techreport, Central Connecticut State University, 2017.

[9] SEP-1230. The determination of the mechanical properties of sheet metai at high strain rates in high-speed tensile tests. Steel Test Specification, 2007.

[10] ASTM-D6272. Test method for flexural properties of unreinforced and reinforced plastics and electrical insulating materials by four-point bending. Standard Test Method, 2010.

Comparison of Solutions for a Triangular Cantilever Beam

J. G. Díaz R.[1],A. J. Rodríguez T.[2]

[1]jorgeguillermo12@ustabuca.edu.co
Facultad de Ingeniería Mecatrónica,
Universidad Santo Tomás, Carrera 18# 9-27, Bucaramanga. Colombia

[2]andres.rodriguez04@ustabuca.edu.co
Facultad de Ingeniería Mecatrónica,
Universidad Santo Tomás, Carrera 18# 9-27, Bucaramanga. Colombia

Abstract

An analytical solution using an Airy stress function is proposed to obtain the stress field in a cantilever rectangular cross-section and triangular beam subjected to a constant load. Results are compared with the classical beam theory and a FEM simulation obtaining visible differences with the Euler-Bernoulli solution and virtual no difference with the numerical simulation. The stress function can be used to map stress, strain and or displacement fields for a beam with different dimensions or loads.

Key Words: Elasticity, stress field, FEM, Cantilever beam

1 INTRODUCTION

Triangular beams are used as machine elements, shelves supports, bridges or for less classical applications such as patented nonlinear springs [1] or patented precision load cells [2]. In a related work, Kluger et. al. [3] used energy methods to estimate deformation claiming they detect 1% of change in force over five orders of force magnitude. However, no information about the stresses is given. In order to have a load cell, one has to verify the linearity of the stress range response.

Due to the inclination angle a solar panel needs to have to guarantee an optimum position with respect to incoming solar energy [11], a triangular beam is studied here as as one possible solution. Therefore, for a cantilever beam with triangular shape and rectangular cross sectional area under an uniform load w(x), as depicted in Figure 1, it is needed to find the stress field distribution. For that reason, an Airy stress function is proposed to describe the stress field. The proposed solution is compared to the classical Euler-Bernoulli solution and to a FEM simulation to observe where the differences may lay.

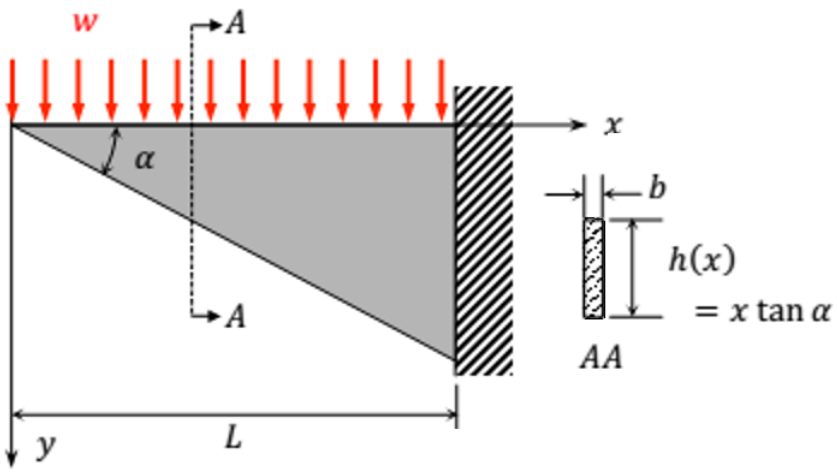

Figure 1: . Cantilever beam

Then, boundary conditions for that problem are:

$$\begin{aligned} u_{(x,0)} &= 0 \\ v_{(x,0)} &= 0 \\ \sigma_{xy(x,0)} &= 0 \\ \sigma_{xy(x,x\tan\alpha)} &= 0 \end{aligned} \tag{1}$$

where u is the displacement field in the x direction according to Figure 1 with coordinate system at the beam's upper right corner, v is the displacement field in the y direction, and σ is the stress field.

2 PROPOSED SOLUTION

If an exact solution is needed, the Euler- Bernoulli beam model cannot be used as it neglects transversal deformation. Therefore, a solution using an Airy stress function, ϕ (w, b, α , x, y), is proposed.

2.1 Elasticity conditions

However, in order to be a stress function, it has to meet conditions [4] as follows. The function has to be 2D and scalar, as shown in Eq. (2).

$$\varphi_{(x,y)} not \varphi_{(x,y,z)} \tag{2}$$

The four-gradient for the proposed function has to be equal to zero, as shown in Eq. (3).

$$\nabla^4 \varphi_{(x,y)} = 0 \tag{3}$$

Stresses are computed from the relations shown in Eq. (4).

$$\begin{aligned} \frac{\partial^2 \varphi}{\partial y^2} &= \sigma_{xx} \\ \frac{\partial^2 \varphi}{\partial x^2} &= \sigma_{yy} \\ -\frac{\partial^2 \varphi}{\partial y \partial x} &= \sigma_{xy} = \sigma_{yx} \end{aligned} \tag{4}$$

Additionally, if out-of-plane stress component needs to be computed, it can be worked out from the relations shown in Eq. (5) for plane stress and plain strain respectively.

$$\begin{aligned}\sigma_{zz} &= 0; for plane stress \\ \sigma_{zz} &= \nu(\sigma_{xx} + \sigma_{yy}); for plane strain \\ \sigma_{xz} &= \sigma_{yz} = 0\end{aligned} \tag{5}$$

Finally, should the displacement fields $u_{(x,\ y)}$ and $v_{(x,\ y)}$ are required, they may be computed by integrating the strains from out of the relations shown in Eq. (6).

$$\begin{aligned}\varepsilon_{xx} &= \frac{\partial u}{\partial x} \\ \varepsilon_{yy} &= \frac{\partial \mathrm{v}}{\partial y} \\ \gamma_{xy} &= \frac{\partial u}{\partial y} + \frac{\partial \mathrm{v}}{\partial x}\end{aligned} \tag{6}$$

2.2 Euler-Bernoulli solution

On the other hand, the Euler Bernoulli solution also known as the elastic solution for a beam is shown in Eq. (7).

$$\frac{d^2 y_{(x)}}{dx^2} = \frac{M_{(x)}}{EI_{(x)}} \tag{7}$$

Eq. (7)

where $M_{(x)}$ is the bending moment distribution and $I_{(x)}$, the second moment of area, is calculated as bx $^3/12$ tanα. As one can see, $I_{(x)}$ changes along the distance. Hence, it cannot be taken out of when integrating y(x). The axial stress in the axial direction is obtained with σ_{xx}=My/I, whereas the shear stress is calculated with σ_{xy}=VQ/Ib, where Q is the first area moment, V the shear force, and b the beam's thickness.

2.3 Proposed solution

An Airy stress's function is proposed as shown in Eq. (8) following recommendations from Gurtin [5].

$$\varphi_{(x,y)} = \frac{w}{2b\cot\alpha(1-\alpha\cot\alpha)}\left[\tan\alpha - x^2 + xy + (x^2+y^2)(\alpha - tg^{-1}\frac{y}{x})\right] \tag{8}$$

The governing equations test proof for the proposed solution in Eq. (8) is shown in Eq. (9), where the fourth partial derivative respect to x minus the fourth partial derivative respect to y is zero.

$$\frac{\partial^4\varphi}{\partial x^4} = -\frac{\partial^4\varphi}{\partial y^4} = \frac{w\cot\alpha}{2b(1-\alpha\cot\alpha)}\left[\frac{16xy^3}{(x^2+y^2)^2}\right] \tag{9}$$

The stresses, then, are found using Eq. (4) producing the relations shown in Eq. (10)

$$\begin{aligned}\frac{\partial^2\varphi}{\partial y^2} = \sigma_{xx} &= \frac{w\cot\alpha}{b(1-\alpha\cot\alpha)}\left[-\tan^{-1}\left(\frac{y}{x}\right) + \alpha - \frac{xy}{x^2+y^2}\right] \\ \frac{\partial^2\varphi}{\partial x^2} = \sigma_{yy} &= \frac{w\cot\alpha}{b(1-\alpha\cot\alpha)}\left[-\tan^{-1}\left(\frac{y}{x}\right) + \alpha + \frac{xy}{x^2+y^2}\right] \\ \frac{\partial^2\varphi}{\partial x\partial x} = \sigma_{xy} &= \frac{-w\cot\alpha}{b(1-\alpha\cot\alpha)}\left[\frac{y^2}{x^2+y^2}\right]\end{aligned} \tag{10}$$

3 RESULTS

First, there are presented the results for the Euler-Bernoulli solution. Then, the solution using the Airy's stress function are shown to be compared with a numerical solution via the Finite Element Method.

The plots of shear force (V) and bending moment (M) are obtained integrating Eq. (7) using V(L)= 0 and M(L)=0 as boundary conditions. They were solved for unit case thickness and they are presented in Figure (2a) and Figure (2b), respectively, for the case when w=1N/m, L=1m.

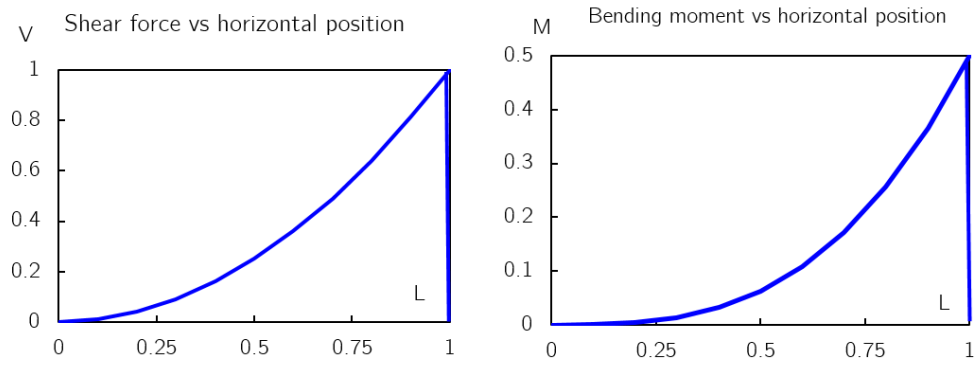

Figure 2: a) shear force, b) bending moment for the cantilever beam

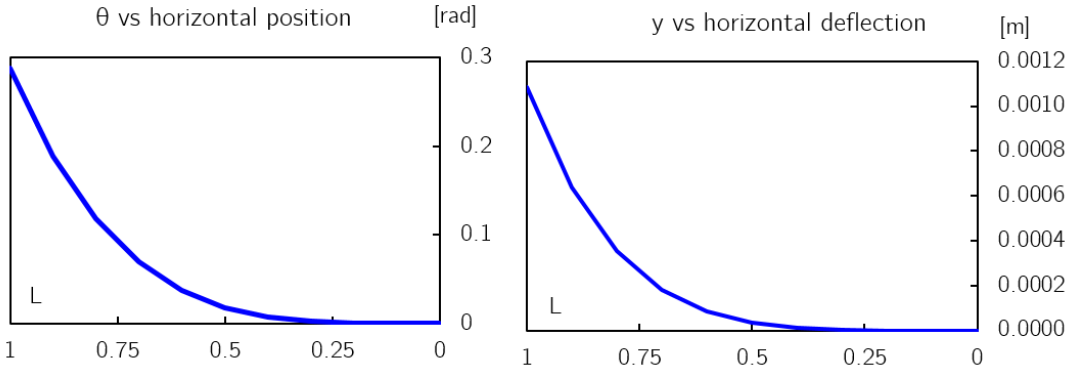

Figure 3: a) angle, b) vertical deflection for the cantilever beam

The plots of angle(θ) and vertical deflection (y) are obtained integrating Eq. (7) using θ (0)= 0 and y(0)=0 as boundary conditions. They were solved for unit case and they are presented in Figure (3a) and Figure (3b), respectively, for the case when w=1N/m, L=1m.

The Euler-Bernoulli axial stress (σ_{xx}) is proportional to the bending moment presented in Figure (2b), whereas the perpendicular Euler-Bernoulli stress (σ_{yy}) is zero.

In Figure 4 is shown the stress distribution for L/2 according to a) the proposed Airy stress function, Eq. (8), and the Euler-Bernoulli solution, Eq. (7). It can be seen that σ_{xx} is similar in the two solutions for x=L/2. For σ_{xy}, there is a more visible difference, and although they both show maximum negative values, the variation through the beam's height presents an opposite curvature. Finally, σ_{yy} is simply not considered in the Euler-Bernoulli solution, so it cannot be compared.

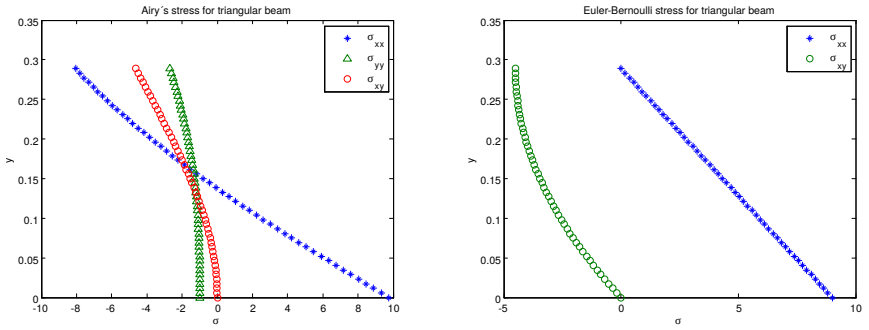

Figure 4: Stress distribution for L/2 according to: a) Airy stress function, b) Euler-Bernoulli

A FEM simulation was run in ANSYS [6] to check the accuracy of the Airy stress function. Figure 5 shows the axial, perpendicular and shear stresses obtained with this method. When comparing to the results of Figure 4 a) one can see the there is no virtual difference. The Von Misses stress field, obtained via FEM, is presented in Figure 6. As expected, the maximum normal stress is present at the origin where the beam is supported and it varies gradually until fading all the way to the beam's tip. Finally, it has be noted that an experimental measure using an analytical technique, such as the Digital Image Correlation (DIC), is on the way to assess the validity of both, numerical and stress function solutions. Data fitting to the analytical solution will be performed. The advantage of a technique [7], such as the DIC, is that it maps the whole displacement field as opposed to point measurements such as strain gages. Moreover, DIC gives the displacement fields already separated, as shown in [8], as opposed to results from classical techniques such as photoelasticity or with the new Thermo Elastic Stress Analysis (TSA). An experimental modal analysis, as described in [9] or [10], versus deformation could also be checked in the near future.

4 CONCLUSION

A stress function was proposed and the governing equations test proof showed it was valid. Strains and stresses were obtained using theory of elasticity relations and they were compared to the classical Euler-Bernoulli solution and FEM simulation. There are expected differences between the stress function and the classical theory. When comparing the proposed solution to numerical results, the differences were minimal confirming the validity of the function.

Although FEM solutions are the preferred method for solving problems that are complicated for classical mechanics of materials theory, a numerical simulation is limited to a particular situation, besides software being costly in time consuming. Furthermore, in the case of fitting experimentally measured data to verify the beam's functioning linear range, one needs an analytical solution.

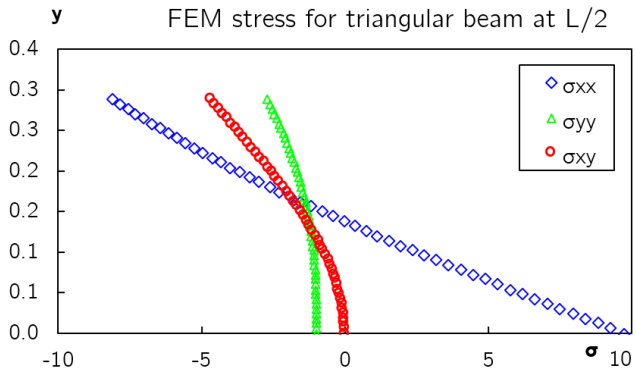

Figure 5: Stress distribution for L/2 obtained via FEM simulation

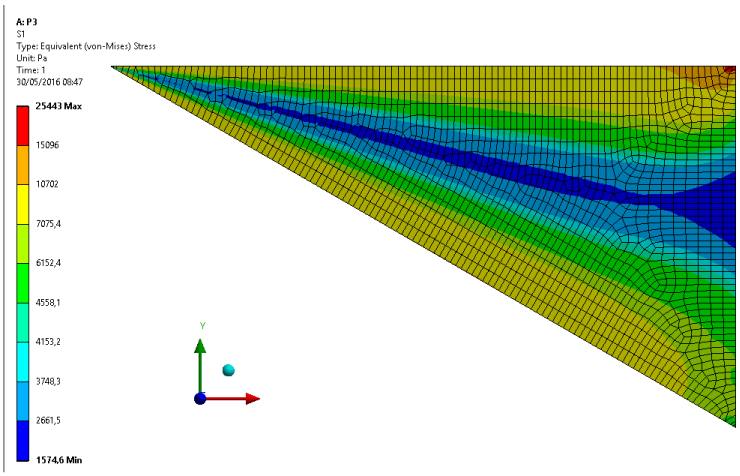

Figure 6: Von Misses stress field obtained via FEM simulation

REFERENCES

1. Kluger M, Slocum A (2014) Beam-based nonlinear spring. US9382960B2

2. Harley J, Matta F, Hoen S (2003) Compact pointing device. US7429976B2

3. Kluger M, Slocum A, Themistoklis S (2017) Ring-Based Stiffening Flexure Applied as a Load Cell With High Resolution and Large Force Range. J Mech Des. doi: 10.1115/1.4037243

4. Timoshenko S, Godier N (1970) Theory of Elasticity, 3rd ed. McGraw Hill, NY

5. Gurtin M (1972) The Linear Theory of Elasticity, 2nd ed. Springer

6. ANSYS (2014) ANSYS, Documentation Help.

7. Sutton MA, Orteu JJ, Schreier H (2009) Image Correlation for Shape, Motion and Deformation Measurements: Basic Concepts, Theory and Applications. doi: 10.1007/978-0-387-78747-3

8. Daz JG, Gonzles GL, Gonzlez JAO, Freire JL de F. (2017) Analysis of Mixed-Mode Stress Intensity Factors using Digital Image Correlation Displacement Fields. 24th COBEM. doi: 10.26678/ABCM.COBEM2017.COB17-0684

9. Gil P., Suarez L., Global loss factor in steel structures with viscoelastic dampers through state equations. ITECKNE Vol. 13 No 2. (2010) doi: 10.15332/iteckne.v7i1.346

10. Camacho J., Guzmn-Lpez R., Gmez S., Flrez M., Estimacin numrica y experimental de parmetros modales en estructuras tipo placa. MECNICA DE MATERIALES IV. SMEC 2016. Cali

11. Diaz J. G, Rodriguez, A. J., Diaz L. M., Parra A. F., Ramirez L. Estudio Tcnico-Econmico para determinar la viabilidad del uso de Energa Solar en la USTA Bucaramanga. ANDESCON 2018. Cali

Assessment of Energy Absorption in Styrene Acrylonitrile Foams at Different Strain Rates

D. Gutiérrez[1], J. Casas[2]

[1]da.gutierrezs@uniandes.edu.co
Departamento de Ingeniería Mecánica,
Universidad de los Andes, Bogotá, Colombia

[2]jcasas@uniandes.edu.co
Departamento de Ingeniería Mecánica,
Universidad de los Andes, Bogotá, Colombia

Abstract

In the present article, the dependence of the behavior of Styrene Acrylonitrile foams SAN A600, SAN A800 and SAN A1200 on the variation of the strain rate is tested using three different nominal densities (116.5, 150 y 210 kg/m^3) as a parameter of study. Quasi-static and dynamic compression tests were carried out reaching strain rates of 10^{-3} to $10^2 s^{-1}$. Furthermore,three-dimensional visual information recording techniques are implemented to perform the microstructural characterization of the materials.

Key Words: Energy absorption, Strain rates, plastic collapse, densification, computed tomography,cell morphology.

1 Introduction

With the pass of time and the constant interest of the manhood to enter into new engineering applications, it has become necessary to seek and implement materials that present high performance and effectively meet the new objectives, under this reason has presented the development of new materials with structures similar to those found in the natural environment (cork,balsa,coral,trabecular bone,etc.), as is the case of polymeric foams. Given the cellular form of these new materials, a wide field of research has been deployed due to the mechanical properties they present.

Porous materials such as polymer foams are increasingly implemented in applications such as marine, aerospace, aircraft and construction due to their unique characteristics, such as low weight, impact absorption, thermal and acoustic insulation[1].The macroscopic behavior of the foams is given as a function of the base material of the cell walls and their microstructure[3]. The foam's microstructure can vary greatly depending on the base material implemented and the method of processing, with the consequence of changing cell morphology, which is why different investigations have been developed in order to characterize the cellular structure of this type of materials[4, 5, 6, 7].

On the other hand, due to the viscoelastic nature of the solid polymer, the foams exhibit a behavior dependent on the deformation rates, analogously the energy absorption capacity is dependent too. It can be found in the literature that the capacity of energy absorption has a greater notoriety at high rates of deformation being more pronounced in high density foams[8, 9].

The objective of the present investigation is to be able to carry out a conjecture about the dependence of the behavior of the rigid polymer foam at different strain rates using three acrylonitrile styrene foams of

different densities, in addition, to determine the change in the cell morphology given the nominal density of the material and the impact on its mechanical behavior under compression load.

2 Material and methods

2.1 Material

In this study three different foams were obtained from the company GURIT®, corresponding to the nomenclature SAN A600, SAN A800 and SAN A1200 with nominal densities of 116.5, 150 and 210 kg/m^3. This type of foam is denominated as CORECELL^{TM}A and used in marine sandwich structures, developed as a solution of the inadequate PVC core technology implemented in this type of applications. Mechanical properties of these foams are provided by the manufacturer [10] and listed in Table 1.

Table 1: Properties of Styrene-Acrylonitrile foam

Property	**Unit**	**SAN A600**	**SAN A800**	**SAN A1200**
Compressive strength	Mpa	1.52	2.36	4.23
Compressive modulus	Mpa	91	141	251
Tensile strength	Mpa	2.01	2.60	3.67
Tensile modulus	Mpa	117	166	265
Shear strength	Mpa	1.48	1.95	2.82
Shear modulus	Mpa	43	60	93

2.2 Micro-structural images

The visualization and taking images belonging to the micro-structure of the foams was performed through the stereoscope OLYMPUS SZX9 under resolutions of 30X, 75X and 120X. With the purpose of a better understanding and visualization of the micro-structure of the foam along the cross sectional a computed tomography scan was implemented obtaining 256 images of size 256x256 pixels and resolution of 55 μm per pixel. In the other hand, the failure mode under dynamic load was recorded using a high speed camera OLYMPUS i-speed LT to 5000 frames per second.

2.3 Quasi-static compression testing

Quasi-static compression tests were carried out using an Instron 3367 under the normative ASTM D1621-94. The specimen dimensions are 59.51x59.41x30 mm, maintaining the original thickness of the panel. A number of 5 repetitions under same experimental conditions were developed to the different strain ratios established: 1.39^{-3}, 2.77^{-2}, 5.56^{-2} and $1.11^{-1}s^{-1}$ at the growth direction. Additionally, compression test in the x and y direction were developed.

2.4 Dynamic compression testing

A specimen of dimension 30x30x30 mm is proved through a drop weight test machine. The hammer of the DWT with 13.6 kg is positioned a height of 680 mm. The speed reached of the hammer is 3.67 m/s at the moment of contact with the specimen giving a strain ratio of $122.3s^{-1}$.

3 Results

3.1 Foam microstructure

The microstructure of the foams was captured through micrographs with the goal to identify the variation of cell topology as a function of the nominal density. First of all, in Fig.1 it can be seen that the size of the cells decreases with the rise of the nominal density having as a consequence the augmentation of the material localized in the cells edges. In the other hand, it can be stated that the geometry of the cell observed is equal for each foam and this statement could relate to the use of same base materials creating a similar tension surface during the nucleation process. Based in the literature[11], cell geometry and its contour it is proposed the tetrakaidecahedron cell as the general geometry of the cells in the foams.

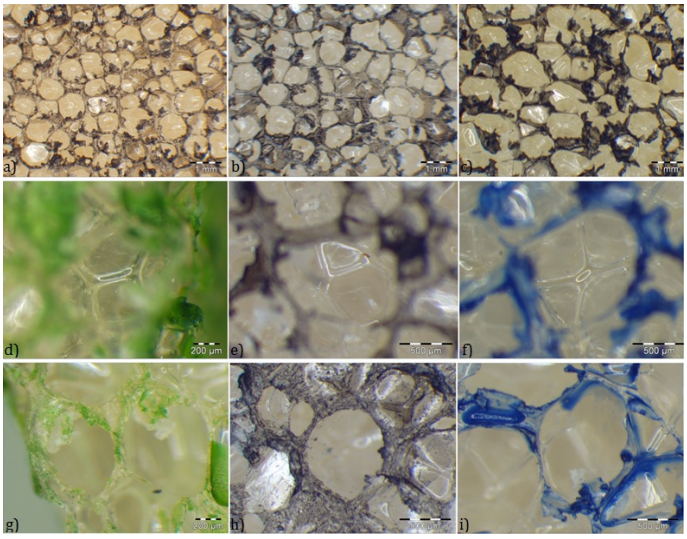

Figure 1: Micrographs of foams SAN A1200(a,d,g), SAN A800(b,e,h) and SAN A600(c,f,i) with resolution of 30x and 120x

With the purpose of ratifying the aforementioned, a measurement of the average diameter and cell wall thickness was carried out of the three foams (Fig 2). On top of that, through the software ImageJ and the CT images it was found the shape of the cell presents an elongation in the z axis (rise direction) making the tetrakaidecahedron cell orthrotopic.

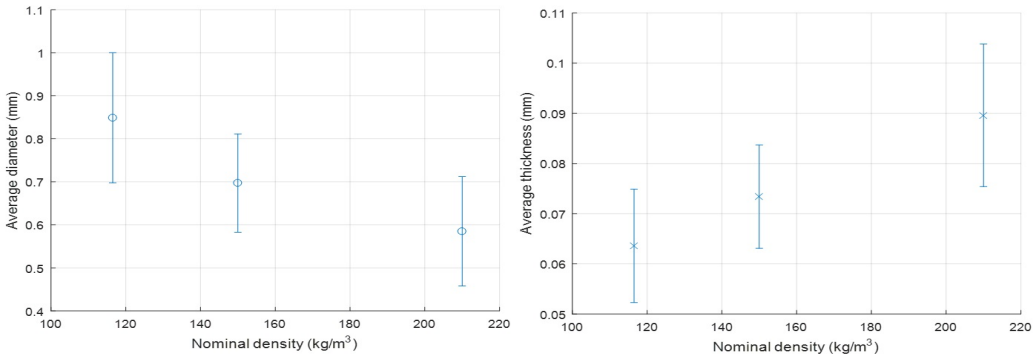

Figure 2: Micrographs of foams SAN A1200(a,d,g), SAN A800(b,e,h) and SAN A600(c,f,i) with resolution of 30x and 120x

3.2 Compressive response

The microstructural complexity usually has as a consequence the behavior shift in the different axes generating an orthotropic or anisotropic behavior in the macro scale. As has been said before, the cell shape characterized presents an elongation in the rise direction axe, which could be associated to the orthotropical behavior of the foam (Fig. 3). This type of behavior was observed in the three different foams, corroborating the idea of the same cell geometry in the materials. However, the material try to be isotropic due to the Elastic modulus presents similar slopes in each axis, at the same time can be seen a typical elasto-plastic foam behavior.

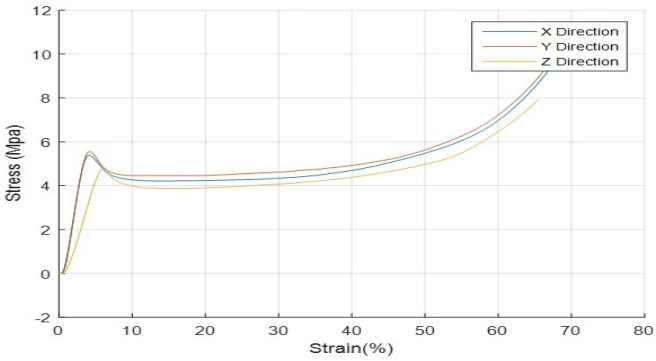

Figure 3: Quasi-static compression test for the main axes in foam SAN A1200

The results obtained in the quasi-static test were as expected (Fig. 4-a), where three principal regions can be identified. The first region is dominated by the elastic response of the foam wherein occurs the flexion of the cell wall. As the load increases the cell walls begin to collapse by buckling. It can also be mentioned the stress remains almost constant generating large deformations in the cell structure. Finally, after the complete collapse the opposite cell walls begin to come in contact with each other causing an abruptly increase of the stress.

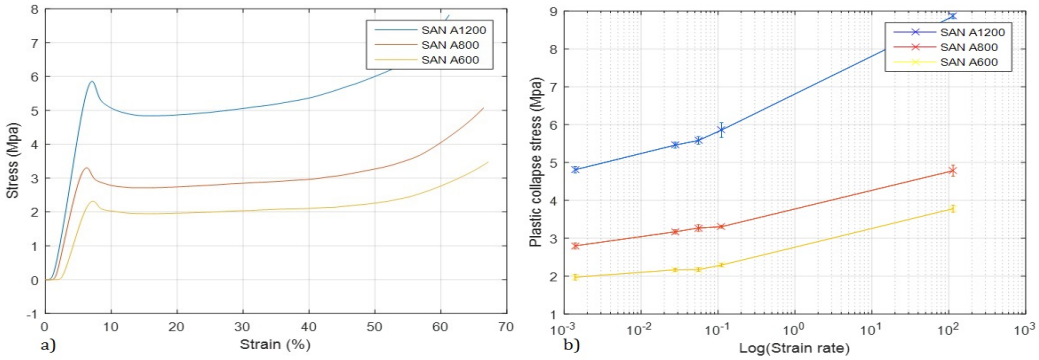

Figure 4: a)Compression test of SAN FOAM A1200,A800 and A600 at $1.11^{-1}s^{-1}$ strain ratio b) Plastic collapse stress at different strain rates

In base with the graphs shown (Fig.4-b) it is appreciated the improvement of the foam energy absorption as a function of the nominal density at a same strain rate. This improvement could be related to the amount of the material localized into the edges of the cell walls which making it difficult the buckling and stretch of the cell face. Although the foams presents the same base materials the variation of the slope at different strain ratios change without a notorious tendency.

4 Conclusions

The cellular shape perceived in the SAN A600, SAN A800 and SAN A1200 foams is the same, being related to the tetradecahedron cell proposed in the literature. However, it is evident the change of the cell geometry dimensions as well as the amount of material present at its edges based on the change in nominal density. Through the taking of images by computerized tomography an elongation of the cell in the direction of growth of the foam is identified, having relation with the orthotropic behavior of the material. By means of quasi-static and dynamic tests under compression load it is possible to determine an increase in the capacity of energy absorption according to the nominal density of the material which has a relationship with the amount of material present in the edges taking into account that the failure of cell walls in the plastic region are given by buckling. Similarly, in foams of higher density there is a dependence of the mechanical behavior more pronounced depending on the deformation rate generated by the load. Finally, the failure mode of the materials is the same, manifesting a failure due to buckling and fracture of the cell walls evidenced by the detachment of material in the lower section of the specimen, generating a propagation of the failure to the upper section.

References

[1] Y. Chen, R. Das, M. Battley. Effects of cell size and cell wall thickness variations on the stiffness of closed-cell foams. *Internal Journal of Solids and Structures* **52**:150-164, 2015.

[2] B. Koohbor, A. Kidane, W. Lu. Characterizing the constitutive response and energy absorption of rigid polymeric foams subjected to intermediate-velocity impact. *Polymer testing* **54**:48-58, 2016.

[3] I. Daniel, J-M. Cho, B. Werner. Characterization and modeling of strain-rate dependent behavior of polymeric foams. *Composites: Part A* **45**:70-78, 2012.

[4] Y. Song, Z. Wang, L. Zhao, J. Luo. Dynamic crushing behavior of 3D closed-cell foams based on Voronoi random model. *Materials and Design* **31**:4281-4289, 2010.

[5] Z. Li, C. Xi, L. Jing, Z. Wang, L. Zhao. Effect of loading rate on the compressive properties of open-cell metal foams. *Materials Science and Engineering A* **592**:221-229, 2014.

[6] N. Fahlbusch, J. Grenestedt, W. Becker. Effective failure behavior of an analytical and a numerical model for closed-cell foams. *International Journal of Solids and Structures* **97-98**:417-430, 2016.

[7] J. Yuan, Y. Li. Effects of cell wall property on compressive performance on aluminum foams. *Transactions of Nonferrous Metals Society of China* **25**:1619-1625, 2015.

[8] M.C Saha, H. Mahfuz, U.K Chakravarty, M. Uddin, Md. Kabir, S. Jeelani. Effect of density, microstructure, and strain rate on compression behavior of polymeric foams. *Materials science and Engineering A*, **406**:328-336, 2005.

[9] D. Luong, D. Pinisetty, N. Gupta. Compressive properties of closed-cell polyvinyl chloride foams at low and high strain rates: Experimental investigation and critical review of state of the art. *Composites part B*, **44**: 403-416, 2013.

[10] Gurit Corecell A General Datasheet, Structural foam core

[11] L Gibson, M. Ashby. Cellular Solids. Structure and properties - Second Edition Cambridge Solid State Science Series. Page:27.

Influence of Temperature on Ductile Damage Parameters and its Effects on FEM Orthogonal Cutting Simulations

J. Osorio[1], J. Casas[2], A. Marañon[3], S. Abolghasem[4]

[1]jc.osorio10@uniandes.edu.co
[2]jcasas@uniandes.edu.co
[3]emaranon@uniandes.edu.co
Departamento de Ingeniería Mecnica,
Universidad de los Andes, Bogotá, Colombia

[4]ag.sepideh10@uniandes.edu.co
Departamento de Ingeniería Industrial,
Universidad de los Andes, Bogotá, Colombia

Abstract

Orthogonal cutting processes simulations have demonstrated to produce accurate results when plastic and failure model parameters are coupled with high strain-rates and temperature conditions. Plastic constitutive model parameters, ductile damage threshold, damage evolution and critical damage values are directly affected by thermomechanical conditions presented during cutting processes. This study presents the experimental results for damage threshold and damage evolution for various temperature conditions using a conventional quasi-static test apparatus covering strain-rate values from 0.01 s^{-1} to 27 s^{-1} on Aluminum 6060. Results show that material damage threshold decreases with temperature rise and increases with strain rate, which directly affects orthogonal cutting Finite Element (FEM) simulations force prediction. Simulations are performed using a Non - Linear continuum damage model(CDM) with temperature and strain rate dependent damage parameters. Stress, strain, strain rate and temperatures contours are presented and cutting forces are compared with experimental measurements.

Key Words: Orthogonal Cutting, Ductile Damage, Non linear Damage, cutting process, Bonora Damage Model.

1 Introduction

Theoretical modeling and simulation of machining manufacturing processes have been increasing due to the emerging necessity for controlling, predict and design machining process. Despite the progresses in understanding the mechanics of machining, predicting and process controlling, numerous researches and industrials are yet trying to understand and predict tool material interactions with the aim of optimizing metal cutting process. Various studies had been working on numerical models and FEM simulations to examine machining performance in terms of deformation, temperature, hardness, microestructure, cutting forces and tool-wear, among others [1][2]. However, FEM simulation and physics of metal cutting process involves complex interactions among various phenomena including plasticity, friction, plastic heat generation, heat flow, ductile material damage and phase changes, among others that are dealt using different disciplines such as mechanics of continuum, heat transfer, tribology, material science and mathematics. There had been significant im-

provements in our understanding of machining, however machining still poses ample challenges to researchers and its effectiveness can still be improved due to the non-accurate representation and lack of cutting forces prediction of metal cutting[1].
The interplay between large strain and large strain-rate during high rate severe plastic deformation(HRSPD) in metal cutting processes is accompanied by elevated temperatures resulting in deformed microestructure which have been found to entail enhanced physical and mechanical properties [3].These improvements have motivated the exploration of material behaviour uncertainties in HRSPD of bulk metals which involves complex interactions among thermomechanical conditions with the advantage of not changing chemical composition of the obtained chips and machined surfaces. In this context, it is vital to investigate material behavior utilizing a constitutive model and ductile damage model that depends directly on strain, strain-rate and temperature. It has been found that constitutive model and ductile damage parameters have major influence on cutting forces, strain, strain-rate and temperature rise [4] which determine the resulting microestructure characteristics. Consequently there exists a challenging trend aiming at an adequate prediction of temperature, cutting forces, stress and strain conditions, by coupling plastic behaviour with ductile damage failure which is supposed to enhance the results . The objective of this work is to establish a ductile damage model base on the continuum damage mechanics (CDM), using different experimental techniques [5] to determine temperature dependency in damage initiation and evolution and its effect on FEM cutting simulations using MSC Marc[6].Ductile damage model is derived as a function of strain and temperature ($D(\varepsilon, T)$) and simulations results are compared using no damage model, non - linear damage model and non linear temperature dependent damage model. This experimentation allows us to understand the temperature effect in damage models and the effect of non-linear damage model in FEM cutting simulations.

2 Continuum Damage Mechanics Model

Damage in metals is mainly the process of initiation and growth of micro-cracks and cavities[7]. Continuum Damage Mechanics(CDM) makes a local approach to material failure using continuum concepts and the set of constitutive equations for damaged material taking into account micromechanisms of failure[5]. Damage variable(D) is often represented using a surface of discontinuities(A_{eff}) present in material continuum and comparing it to non-damage surface(A_0) (Figure 8) which leads to the concept of effective stress [7].Thus a damage variable con be given as $D = 1 - \frac{A_{eff}}{A_0}$

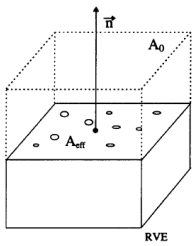

Figure 1: Damage Element showing the A_0 and A_{eff} areas [5]

If damage is assumed to be isotropic, microracks and microvoidas with an orientation distributed uniformly in all directions [5], damage will not be depending of the plane and damage can be characterized fully by D. By taking into account that $\sigma = F/A_0$ and $A_{eff} = A_0(1 - D)$, a definition of effective stress is given as [7]:

$$\bar{\sigma} = \frac{\sigma}{1 - D} \tag{1}$$

Using Equation 1 and strain equivalence, a non direct measurement based on the influence of damage on elasticity as $D = 1 - \frac{\bar{E}}{E}$.

3 Bonora Damage Model

Bonora [5] demonstrated that the plastic flow curve is a result of hardening and damage processes that are coupled in the material behaviour. To determine constitutive behaviour, Bonora [5] established the following dissipation potential [8]:

$$F_D = \left[\frac{1}{2}\left(-\frac{Y}{S_0}\right)^2 \frac{S_0}{1-D}\right] \frac{(D_{cr}-D)^{(\alpha-1)/\alpha}}{p^{(2+n)/n}} \qquad Y = \frac{1}{2E_0}\left(\frac{\sigma_{eq}}{1-D}\right)^2 R_v \tag{2}$$

Where D_{cr} is damage at failure, α is the non - linear coefficient, Y is the energy release rate, σ_{eq} is the equivalent von-Mises stress and R_v is the triaxiality function given as:

$$R_v = \frac{2}{3}(1+v) + 3(1-2v)\left(\frac{\sigma_H}{\sigma_{eq}}\right)^2 \tag{3}$$

Where v is the Poissons ratio and σ_H is the hidrostatic stress. Using the dissipation potential, energy release rate and the methodology in [5], an expression for damage and damage evolution in terms of plastic strain and damage parameters can be deduced.

$$dD = \alpha \frac{D_{cr}^{1/\alpha}}{\ln\left(\varepsilon_{cr}/\varepsilon_{th}\right)} R_v (D_{cr}-D)^{\alpha-1/\alpha} \frac{dp}{p} \tag{4}$$

Where ε_{th} is the damage threshold, ε_{cr} is strain at failure, p is the active equivalent plastic strain and p_{th} is the strain threshold taking into account triaxiality function as in [8]. α, D_{cr}, ε_{cr} and ε_{th} can be determine experimentally, however as D_{cr} varies considerable depending on the manufacturing process of the specimens and the material history, in this work, ε_{th} and α are reported.

4 Experimental Method

To determine Bonora Damage model parameters, AL 6060 was loaded until 1% of plastic deformation and then unload to measure elastic modulus degradation with plastic deformation. This procedure was repeated using different ambient temperatures (T) and different deformation velocities. Conditions are listed in Table 1 corresponding to five temperatures and 4 different strain rate values. Test where performed using a conventional quasi-static test apparatus and an Drop Weight Impact Test Machine (DWIT) with a tensile accessory. Strain was measured using an Instron strain gauge extensometer for the quasi-static tests and a laser position sensor for the DWIT tests. Results for damage evolution at different temperatures and different deformation velocities are shown in Figure 2 and Figure 3. Damage strain threshold as a function of temperature is shown in Figure 4.

Table 1: Damage Parameters for different Temperatures and Strain rates

Temperature [°C]	**Velocity**[s^{-1}]	ϵ_{th} **mm/mm**	α
23	0.03	0.042	0.66
50	0.03	0.04	0.66
100	0.03	0.038	0.66
150	0.03	0.032	0.66
200	0.03	0.030	0.66
23	4	0.048	0.48
23	15	0.051	0.43
23	27	0.0537	0.44

5 FEM Simulation

FEM simulation is performed using MSC MARC combined with Fortran Subroutiens[9] to implement non-linear damage model(UDAMAG). Simulation is carry out by cutting a rectangular block of 12x3.5 mm^2 for 20° rake angle and three different cutting velocities (126,252 and 504 mm/s) with 11° clearance angle and 0.033 mm tool edge radius. The tool is simulated as an infinite rigid material and tool - Workpiece interaction is simulated first as frictionless and then friction is added for comparison purposes. Johnson Cook material parameters are taken from [10] and critical damage with critical strain at failure are taken from [5]. Fix boundary conditions are used in the left and bottom lines of the domain. For thermal boundary conditions, ambient temperature was imposed at the bottom and left sides of the domain. The workpiece surfaces were set as a convective boundary using h values typically applied for force convection as material is rotating constantly. Material properties that are constant in the simulation are shown in Table 2.

Table 2: Material constants FEM simulation

Young Modulus	E	114	GPa
Poisson Ratio	v	0.33	-
Thermal Conductivity	λ	395	N/sK
Expansion Coefficient	γ	1.7×10^{-5}	K^{-1}
Specific Heat	C_p	3.85×10^{8}	mm^2/s^2K
Density	ρ	8.96×10^{-9}	Ns^2/mm^4

Global Remeshing penetration and element distortion energy criteria was used to generate the chip. As dynamic mesh was used, mesh sensibility was analyzed using constant number of elements in the domain and remeshing using previous number of elements. For 504 mm/s cutting speed, convergence has achieve with an element size near the tool tip of 0.011 mm. Implicit dynamic analysis is used with automatic time step cutback with convergence controls and loadcase parameters taken from [11]. Simulation is run until cutting force is stable, which for the highest speed corresponds to 3 mm.

6 Results

6.1 Damage Parameters

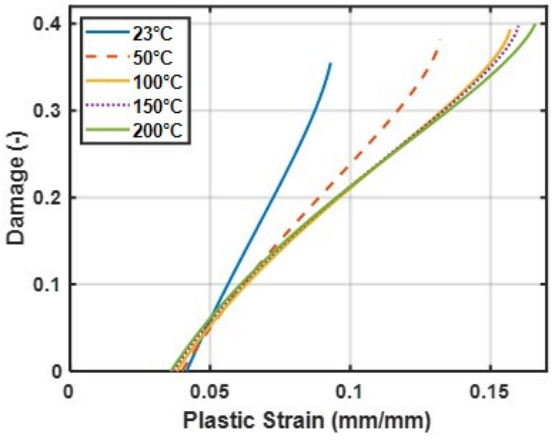

Figure 2: Damage Evolution at different Temperatures, constant strain rate.

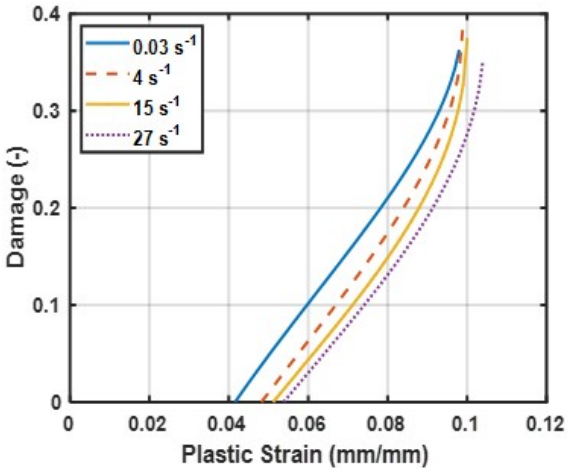

Figure 3: Damage Evolution at different Strain Rates, constant temperature.

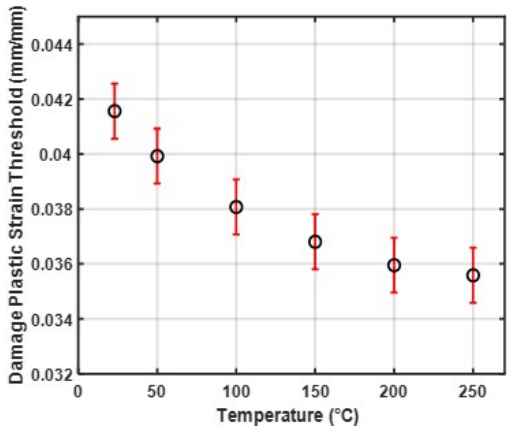

Figure 4: Damage Threshold at different Temperatures

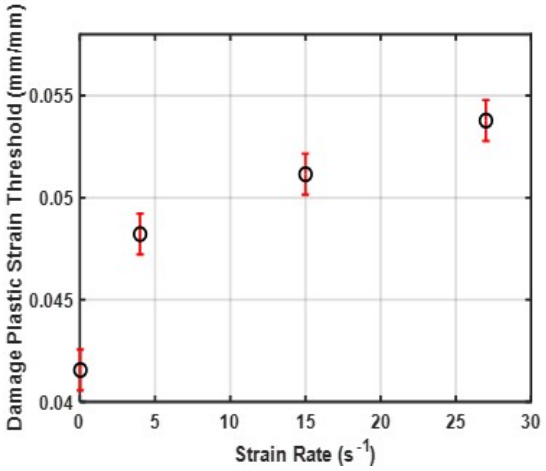

Figure 5: Damage Threshold at different Strain Rates

As temperature and strain rate start to increase, damage constant values are directly affected by them. As it can be observe in Figure 2 as temperature rises, α damage evolution exponent remain constant, strain at failure and critical damage value increases and damage threshold decreases until it reaches an stability value that can be observe in Figure 4. On the other hand, as strain rate rises, damage exponent α decreases, strain at failure increases, critical damage value remains almost constant and damage threshold rises until it reaches an stability value that can be observe in Figure 5.

6.2 FEM Simulation

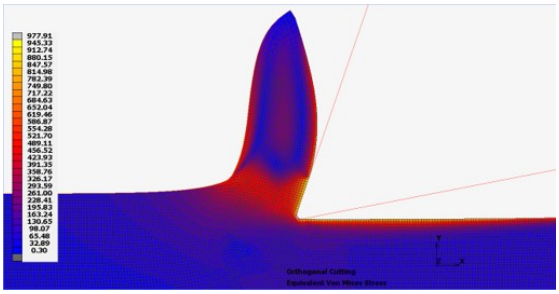

Figure 6: Stress Contours FEM Simulation with No Damage (V = 126 mm/s)

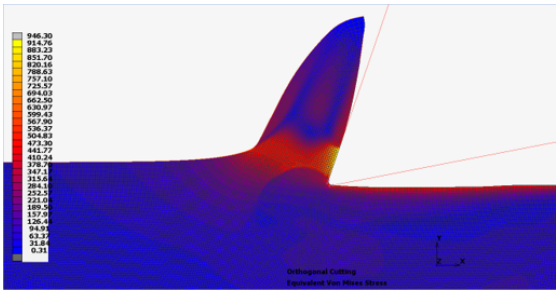

Figure 7: Stress Contours FEM Simulation with Damage(V = 126 mm/s)

With damage inclusion in the simulation, stress reduces as material softening due to damage is introduce.This comes accompanied with computational cost rise, as the software need to execute the sub-routine propose.

6.3 Cutting Forces

Cutting forces where compare using 3 times of analysis, a Non-Damage simulation, a simulation with non dependent parameters and a simulation with temperature and strain rate dependent parameters. Results show that simulated force can be accurately predicted by introducing damage models.

Figure 8: Cutting force comparison

Cutting force has predicted with 7% of error, and it had an improvement of 4 % by introducing damage dependency model parameters.

7 Conclusions

Temperature dependency of Bonora Model parameters was determine using experimental method found in [5] and [7]. Its was determine that the damage strain threshold decreases with temperature increase with a negative logarithmic tendency and was a lower limit around 0.34 mm/mm (Figure 4). On the other hand, for intermediate strain rate values it was shown that strain threshold increases with strain-rate changes, but damage evolution non - linear exponent decreases (Figure 5). Temperature and strain rate affect directly damage values as they increase total energy in the system and let dislocation move faster thrown grains and accumulate with less plastic strain. FEM simulation show that damage was a direct influence in cutting forces as it decreases its value by 15% as there is thermal and material softening involve in damage model. Stress contours present a similar behaviour but simulations with Bonora damage model show lower stress value, as shown in Figure 6 and Figure 7.

We where able to couple a continuum damage model with plastic deformation constitutive model for a orthogonal cutting FEM code in MSC Marc. Obtain results show that using an adequate damage model might improve force prediction as material softening needs to be taken into account or force would be over-predicted for the process. Temperature dependent damage model must be couple to the model, as cutting process involves temperature changes, which needs to be considered in FEM model.

8 Acknowledgement

In this study, we acknowledge the funding support from Colciencias grant code 120474557650 and the 2017 grant from Faculty of Engineering at Universidad de los Andes, Bogot, Colombia.

References

[1] L. A. Denguir, J. C. Outeiro, G. Fromentin, V. Vignal, and R. Besnard. A physical-based constitutive model for surface integrity prediction in machining of OFHC copper. *Journal of Materials Processing Technology*, 248(April):143–160, 2017.

[2] V. Madhavan and A. H. Adibi-Sedeh. Understanding of finite element analysis results under the framework of Oxley's machining model. *Machining Science and Technology*, 9(3):345–368, 2005.

[3] S. Abolghasem, S. Basu, S. Shekhar, J. Cai, and M. R. Shankar. Mapping subgrain sizes resulting from severe simple shear deformation. *Acta Materialia*, 60(1):376–386, 2012.

[4] On the selection of Johnson-Cook constitutive model parameters for Ti-6Al-4V using three types of numerical models of orthogonal cutting. 31:112–117, 2015.

[5] N Bonora. N. BONORA Industrial Engineering Department, University of Cassino, Via G. De Biasio 43, 03043 Cassino (FR), Italy. 58(1/2):11–28, 1997.

[6] User Information. Volume A : Theory and User Information. pages 82–85, 2015.

[7] Jean Lemaitre. *A course on Damage Mechanics*. Spring-Verlag, Berlin, 1992.

[8] G. H. Majzoobi, M. Kashfi, N. Bonora, G. Iannitti, A. Ruggiero, and E. Khademi. Damage characterization of aluminum 2024 thin sheet for different stress triaxialities. *Archives of Civil and Mechanical Engineering*, 18(3), 2018.

[9] MSC-Software-Corporation. Volume D: User Subroutines and Special Routines. D:338, 2016.

[10] Gordon R. Johnson and William H. Cook. A constitutive model and data for metals subjected to large strains, high strain rates and high temperatures, 1983.

[11] Olufunminiyi Abiri. Simplifications of Non-Local Damage Models. 2014.

Three-Dimensional Finite Element Analysis of the Quenching Process of Plain-Carbon Steel With Phase Transformation and Unstructured Meshes

M. J. Juha[1], J. Unfried[2], C. Dominguez[3]

[1]mario.juha@unisabana.edu.co
Programa de Ingeniería Mecánica,
Universidad de La Sabana, Chía, Colombia

[2]jimyunfried@correo.unicordoba.edu.co
Departamento de Ingeniería Mecánica,
Universidad de Cordoba, Monteria, Colombia

[3]carlos.dominguez2@unisabana.edu.co
Programa de Ingeniería Mecánica,
Universidad de La Sabana, Chía, Colombia

Abstract

Results are presented from a three dimensional finite element analysis of the quenching process of plain carbon steels to predict the generation of volume fractions of various metallurgical phases. A metallurgical model has been coupled to a thermal model that consider temperature history and latent heat generated during the phase transformation. The diffusional phase transformation for non-isothermal process was simulated using the well-known Johson Mehl Avrami Kolmogorov (JMAK) equation with the additivity rule of Scheil to account for the prediction of the incubation time for a continuous cooling curve. For handling the diffusionless transformation the Koistein and Marburguers equation was used to model the austenite martensite transformation. The effect of unstructured meshes and different time integrators on the reliability of the solution will be investigated. The use of unstructured meshes will allow the implementation of automatic meshing adaptation solutions.

Key Words: Finite element, Quenching, phase transformation, Unstructured meshes

1 Introduction

Simulation of the cooling stage in a quenching heat treatment process require the implementation of a solid phase change model. The solid phase change may be due to a diffusion process, such as the solid decomposition of austenite into ferrite, pearlite or bainte. Also the phase change may be a nondiffusive process, as for example the decomposition of austenite into martensite. This short abstract discuss the JAMK (Johnson - Mehl - Avrami - Kolmogorov) model to simulate the solid phase decomposition that is governed by a diffusion process.

2 Diffusive transformation model

According to the JAMK model, in isothermal conditions, the amount of the transformed phase, can be evaluated by

$$f_i(T) = 1.0 - \exp\left[-a(T) \cdot t(T)^{n(T)}\right] \tag{1}$$

where f_i is the volume fraction of the solid phase i, t is the time elapsed since the transformation begin, a and n are material parameters, dependent by the isothermal temperature and the forming phase. The diffusional coefficient a and the transformation expeonent n can be evaluated by the IT diagram of the considered material, taking into account the times τ_s and τ_f, needed for the conversion, in isothermal conditions, of a detectable start and finish volume fractions of the forming phase, indicated, respectively, as F_s and F_f, as follows:

$$a(T) = -\ln(F_f)\,\tau_s(T)^{-n(T)} \qquad\qquad n(T) = \frac{\ln(\ln(F_s)) - \ln(\ln(F_f))}{\ln(\tau_f(T)) - \ln(\tau_s(T))} \tag{2}$$

In the present paper F_s and F_f have been assumed, respectively, as 0.01 and 0.99. The following example clarify the use of equation (1) and equation (2).

Example

From the IT diagram of an AISI 1050 steel compute the approximated parameters a and n and plot the volume fraction for the isothermal decomposition of austenite at $T = 500\ ^\circ C$.

In figure 1 is drawn a horizontal line at $T = 500\ ^\circ C$ that intercept the two curves that defined the initial and final times of the decomposition. From the same figure is extracted the approximated times, $\tau_s = 1\ s$ and $\tau_f = 10\ s$. Replacing these values in equation (2) is obtained the following values for a and n:

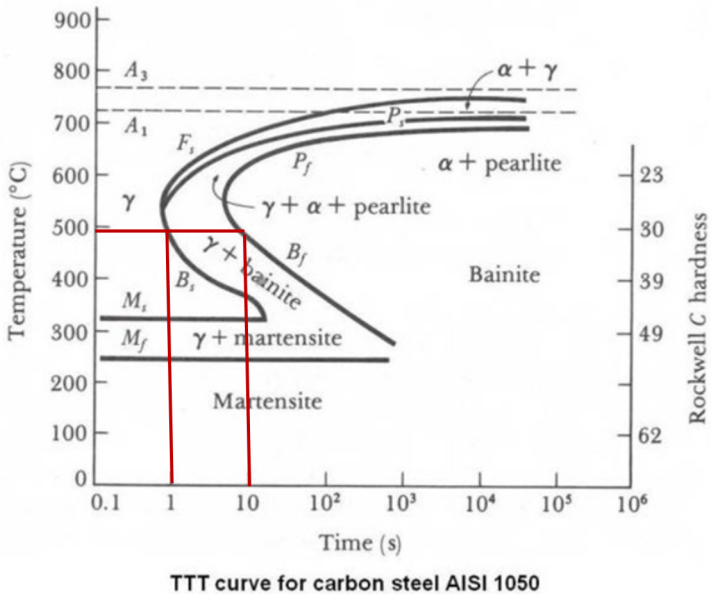

Figure 1: IT diagram for an AISI 1050 steel.

$$n(500) = \frac{\ln(\ln(0.01)) - \ln(\ln(0.99))}{\ln(10) - \ln(1)} = 2.6611 \qquad a(500) = -\ln(0.99)\,(1)^{-2.6611} = 0.0101$$

with these values now is possible to compute the volume fraction decomposition of the austenite into bainite using equation (1):

$$f_i = 1.0 - \exp\left(-0.0101 \cdot t^{2.6611}\right)$$

Figure 2 shows the volume fraction of bainite at $T = 500\ ^\circ C$ as a function of time.

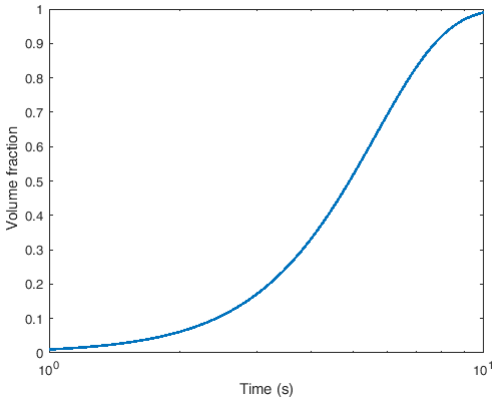

Figure 2: Volume fraction of bainite at $T = 500\ ^\circ C$.

2.1 Continuous cooling approach

A quenching process is characterized by a continuous cooling of the processing material and therefore, strictly speaking, equation (1) is not directly applicable to this case. A standard approach consist in the discretization of the cooling curve into a series of isothermal steps and for each step the corresponding volume fraction transformation is computed. To compute the cumulative volume fraction of the specific phase transformed up to the last time steps, indicated as $f_{i,j-1}$, results into a fictitious time $t_{j,\text{fict}}$, which represent the time needed, at temperature T_j to obtain the same amount of cumulative transformed phase. Therefore, the total time at step j is given by,

$$t_j = \Delta t_j + t_{j,\text{fict}} = \Delta t + \left[\frac{-\ln\left(1 - f_{i,j-1}\right)}{a\left(T_j\right)}\right]^{\frac{1}{n(T_j)}} \tag{3}$$

Total amount of the formed phase at the end of the considered time step, writes:

$$f_{i,j} = 1 - \exp\left(-a\left(T_j\right) t_j^{n(T_j)}\right) \tag{4}$$

The transformation is considered to have started when the following equation is satisfied [1, 2]:

$$\sum_{j=1}^{m} \frac{\Delta t_j}{\tau_s\left(T_j\right)} \geq 1 \tag{5}$$

where $\tau_s\left(T_j\right)$ is the time of the transformation start at the $j-$th time of the simulation. Basically, equation (5) is used to transform an isothermal diagram in a continuous cooling transformation diagram.

3 Governing heat transfer equation

Consider a three-dimensional body in heat transfer conditions. For the heat transfer analysis we assume that the material obeys Fouriers law of heat conduction [5]

$$\underline{\mathbf{q}} = -\underline{\underline{\mathbf{k}}}\,\nabla T \tag{6}$$

where, $\underline{\underline{\mathbf{k}}}$ is the conductivity matrix, ∇T is the gradient of the temperature and $\underline{\mathbf{q}}$ is the vector of heat flux conducted per unit area. In concrete, the quantities are measured respect to a Cartesian coordinate system. Considering the heat flow equilibrium in the interior of the body, we thus obtain

$$\rho C_p \frac{\partial T}{\partial t} + \operatorname{div} \underline{\mathbf{q}} = Q \tag{7}$$

where, C_p is the material specific heat capacity, ρ is density, Q is the rate of heat generated per unit volume and div is the divergence operator. On the surface of the body the following conditions must be satisfied:

$$T = T^s \qquad \text{on } S_T \tag{8}$$

$$-\underline{\mathbf{q}} \cdot \underline{\mathbf{n}} = q^s \qquad \text{on } S_q \tag{9}$$

where $\underline{\mathbf{n}}$ is the direction of the unit normal vector pointing outward to the surface, T_s is the known surface temperature on S_T and q^s is the prescribed heat flux input on the surface S_q of the body. Note that $S_T \cap S_q = 0$ and $S_T \cup S_q = S$. In the following we assume that the material parameters are temperature-dependent. Included in eq. (9) are convection boundary conditions where

$$q^s = h\left(T_e - T^s\right) \tag{10}$$

and h is the convection coefficient, which may be temperature-dependent. Here the environmental temperature T_e is known, but the surface temperature T^s is unknown. For the finite element solution of the heat transfer problem we use the weak form (or weighted residual form) of the heat flow equilibrium:

$$\int_V \theta \left(\rho C_p \frac{\partial T}{\partial t} + \operatorname{div} \underline{\mathbf{q}} - Q \right) dV = 0 \tag{11}$$

$$\int_V \theta \rho C_p \dot{T}\, dV + \int_V \nabla\theta \cdot \underline{\underline{\mathbf{k}}} \nabla T\, dV = \int_V \theta Q\, dV + \int_{S_q} \theta^s q^s\, dS \tag{12}$$

where θ is a virtual temperature that is zero where temperature boundary conditions are specified and θ^s is the same virtual temperature but at the surface of the body. Special consideration deserved Q, the rate of heat generated per unit volume. In this work, Q has the meaning of the internal heat source due to latent heat released during the solid phase transformation in the quenching of steels. This term is given by the expression:

$$Q = \sum_i^n H_i \frac{\partial f_i}{\partial t} \tag{13}$$

where H_i is the latent heat released when the phase i forms and may be temperature-dependent. Note that heat is generated at the time rate of conversion of phase i.

4 Numerical examples

4.1 Computational simulation: continuous heating of a 1080 eutectoid steel

A zero dimensional model of the heating of an AISI 1080 steel is presented in this section. We will study the transformation of perlite into fully austenite during heating. The initial temperature is 700 °C and a constant heating rate of 0.5 °C/s up to 800 °C is applied. Figure 3 show the heating curve superposed into an IT curve for carbon steel AISI 1080. The numerical computation of the austenite volume fraction transformation using the metallurgical model presented in previous section is shown in figure 4 and the result is compared with the data presented in [4]. For the numerical computations we used a time step, $\Delta t = 1\ s$.

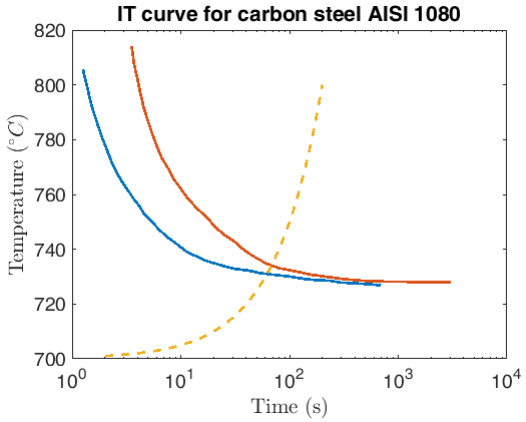

Figure 3: Isothermal transformation diagram of austenization for perlite structure of AISI 1080 steel. The solid curves represent the IT curves of Roberts and Mehl [3] and the dashed line the heating curve

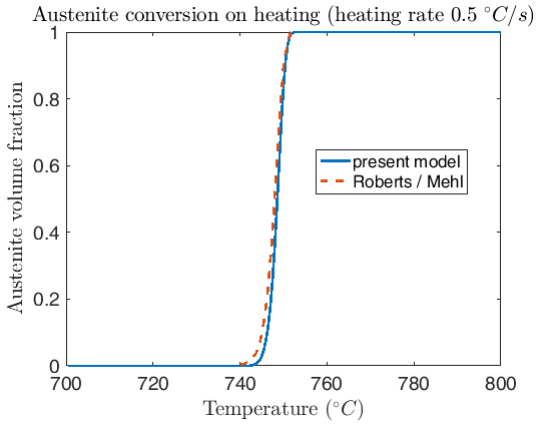

Figure 4: Austenite conversion on heating

4.2 Quenching of a 1080 steel cylinder in water

In this section we present results of phase transformation of a cylinder made of 1080 steel and quenched in water. The cylinder is infinitely long, 38-mm in diameter and was discretized using linear tetrahedral. In the simulation, the 38-mm diameter cylinder was quenched on its cylindrical surface, from an initial uniform temperature of 850 $°C$, in an agitated water bath at 850 $°C$. At the initial temperature, the microstructure was assumed 100 percent austenite. Results are presented in figure 5 to figure 8.

5 Conclusions

Linear tetrahedral finite elements were combined with the JAMK model to predict phases in a steel cylinder quenched in water. Good agreement between the numerical simulation and results in previous literature was found. Next step is to include the latent heat and mesh adaptation strategies.

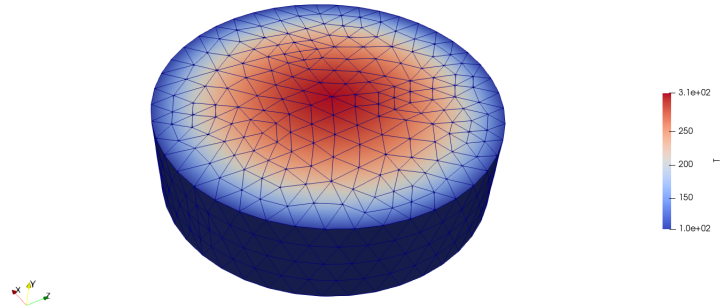

Figure 5: Temperature distribution after 60 seconds

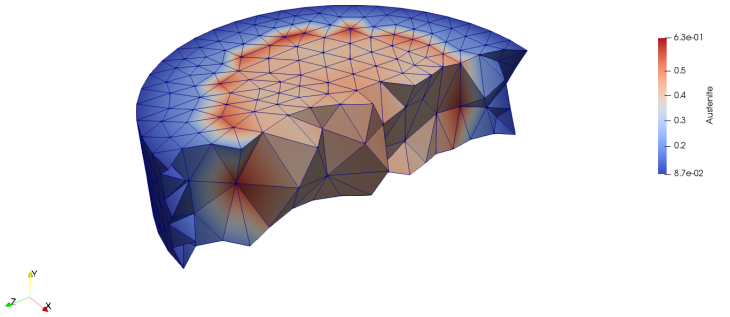

Figure 6: Austenite distribution after 60 seconds

References

[1] Carlone, P, Palazzo, G.S, Pasquino. R. Finite element analysis of the steel quenching process: Temperature field and solid-solid phase change, *Computers and Mathematics with Applications* 59 (2010) 585 - 594.

[2] Fabian, P., Mesko, J., Nikolic, R.R. Simulation of Quenching Process of Steel Creating Complex Carbides, *FME Transaction* (2017) 45, 510-516.

[3] Christian, J.W. The Theory of Transformations in Metals and Alloys, *Newnes* (2002)

[4] Tszeng, T.C., Shi, G. A global optimization technique to identify overall transformation kinetics using dilatometry data - applications to austenization of steels, *Materials Science and Engineering A* 380 (2004) 123 - 136.

[5] K.J. Bathe. Finite Element Procedures. Prentice Hall. 1996.

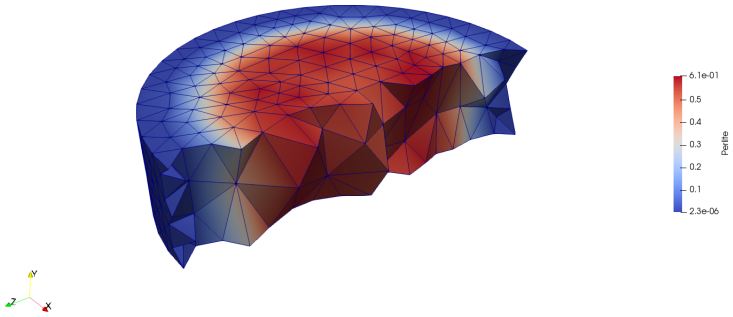

Figure 7: Perlite distribution after 60 seconds

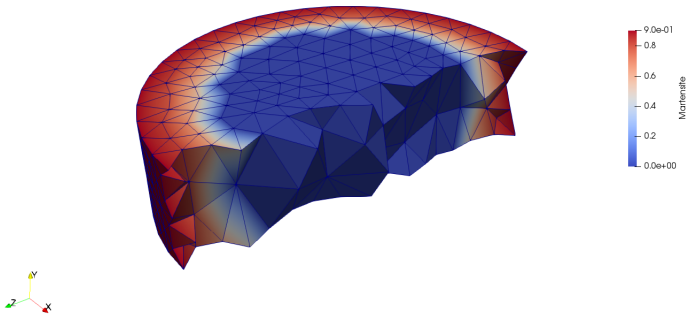

Figure 8: Martensite distribution after 60 seconds

Determination of the Concrete Elastic Modulus by Means of a Mesoscopic Approach With the Finite Elements Methods

D.L. Linero[1], M.A. Amaya[2]

[1]dllineros@unal.edu.co
Facultad de Ingeniería
Universidad Nacional de Colombia
[2]mamayaa@unal.edu.co
Facultad de Ingeniería
Universidad Nacional de Colombia

Abstract

The approach proposed in this work allows to obtain the elastic modulus of the concrete from the volumetric participation and the gradation of the aggregates and some mechanical properties of the mortar and the aggregates. This is reached by means of a mesoscopic numerical approach with the following considerations: (i) the concrete is described as a composite material formed by aggregates embedded in a mortar matrix, (ii) the placement of the aggregate within the concrete is not defined, (iii) the adherence between the aggregates and the mortar is preserved, and (iv) each aggregate is represented by a sphere, whose diameter is defined by the gradation. Likewise, this approach is divided into three steps: (i) the geometrical construction of the mortar matrix and that of the aggregate spheres with random location, (ii) the meshing process with finite elements and the definition of the boundary conditions in displacements and loads, and (iii) the solution of a linear elastic mechanical problem by means of finite elements methods. The samples set of the concrete elastic modulus is obtained by repeating the previous steps for different locations of the aggregate spheres. The elastic modulus of the concrete with aggregates from some igneous and sedimentary rocks is computed.

Key Words: Finite element methods, Meso-mechanics approach, numerical modeling of concrete, elastic modulus

1 Introduction

The concrete is composite material formed by aggregate from igneous, sedimentary or metamorphic rocks embedded in a mortar matrix. The aggregates have different sizes, are random located into the matrix and form an important part of the concrete volume.

The concrete mechanical behavior is represented by parameters as the elastic modulus, Poisson ratio, and the compressive and tensile strength. These parameters depend on the mechanical properties and the volumetric fraction of the aggregates and the mortar that conforms it.

The structural response of concrete member has been represented for different analysis scales by means of the finite elements methods and the constitutive models [30]. The macro-mechanics approaches consider a homogeneous behavior of the material, presenting low computational cost with a satisfactory accuracy. These approaches are defined by a failure criterion [7, 16, 24, 29], and a constitutive relationship [2, 9–13, 15, 17, 18, 22, 23, 25].

Other models distinguish aggregates and the mortar in the material. The micro-mechanics models define two scales of analysis: the homogenized material point and the representative volume element with aggregate particles and mortar matrix. These models have high accuracy and computational cost [5, 6, 8, 19, 21, 27, 28].

The meso-mechanics models represent the mortar and each aggregate particle in the same scale, demanding finite meshes very fine and showing a good accuracy and an acceptable computational cost [4, 14].

The proposed numerical approach in this work computes the elastic modulus of the concrete by means of a finite elements analysis, meshing the mortar and each aggregate particle as two different materials. The approach depends on the volumetric participation and the gradation of the aggregates, as well as of the elastic modulus and Poisson relation of both materials. This work is the first part of a research intending to represent the mechanics response of the concrete from the elastic behavior until the collapse.

2 Methods

The concrete is described as a composite material formed by aggregates embedded in a mortar matrix. The volumetric fraction of aggregate k_a and of mortar k_m are defined in terms of the volume of aggregate V_a, of mortar V_m and of concrete V as: $k_a = V_a/V$ and $k_m = V_m/V$.

The aggregate volume is $V_a = \sum_{i=1}^{ni} V_i$, where V_i is the volume of i-th aggregate particle and ni is the amount of aggregate particles. Moreover, the location of each aggregate particle within the concrete specimen is random.

The proposed approach considers that each aggregate particle is represented by a sphere of volume V_i, whose diameter is defined by the gradation. The latter establishes the parameters g_A, g_B, g_C and g_D as the aggregate fraction with size between $1\frac{1}{2}$" and 1", between 1" and 3/4", between 3/4" and 1/2", and between 1/2" and 3/8", respectively. On the other hand, total adherence between aggregates and mortar is considered.

The first step of this numerical approach is the geometrical construction of aggregate spheres within the concrete specimen. The location of each sphere is chosen from 1000 random positions inside the problem domain, avoiding overlaps. Likewise, the radio of the spheres is selected from 1000 random values in the range of each aggregate gradation. The volume mortar corresponds to the subtraction between the total volume and the aggregate spheres volume. Figure 1 shows four simulations of random distribution of aggregate spheres within a cylinder concrete.

In the second step, the volumes of aggregate and mortar are discretized with a mesh of linear tetrahedral elements that represent the specimen domain. Likewise, the boundary conditions of the mechanical problem are included.

The third step is the solution of the mechanical problem by means of finite elements methods, considering linear elastic behavior of both materials, infinitesimal strains and static loads. Consequently, the mechanical parameters of the simulation are the elastic modulus and Poisson ratio of the aggregate E_a, ν_a and of the mortar E_m, ν_m. The forces and displacements computed in the last step allow to obtain the concrete elastic modulus E.

These three steps are repeated for different locations and radius of aggregate spheres, preserving approximately the same aggregate volumetric fraction. The results obtained from the simulations set corresponds to a statistical sample of the concrete elastic modulus E, whose mean $\bar{E}$ and coefficient of variation cv are computed.

3 Results

The concrete elastic modulus is obtained by means of the numerical simulation of a cylinder of diameter $d = 3$" and height $h = 6$", subjected to normal pressure p as shown Figure 2(a). The aggregate has volumetric fraction $k_a = 0.20$ and gradation $g_A = 0.100$, $g_B = 0.275$, $g_C = 0.375$ and $g_D = 0.250$ [1]. The numerical approach generates approximately 75 aggregate spheres that are distributed within the concrete specimen.

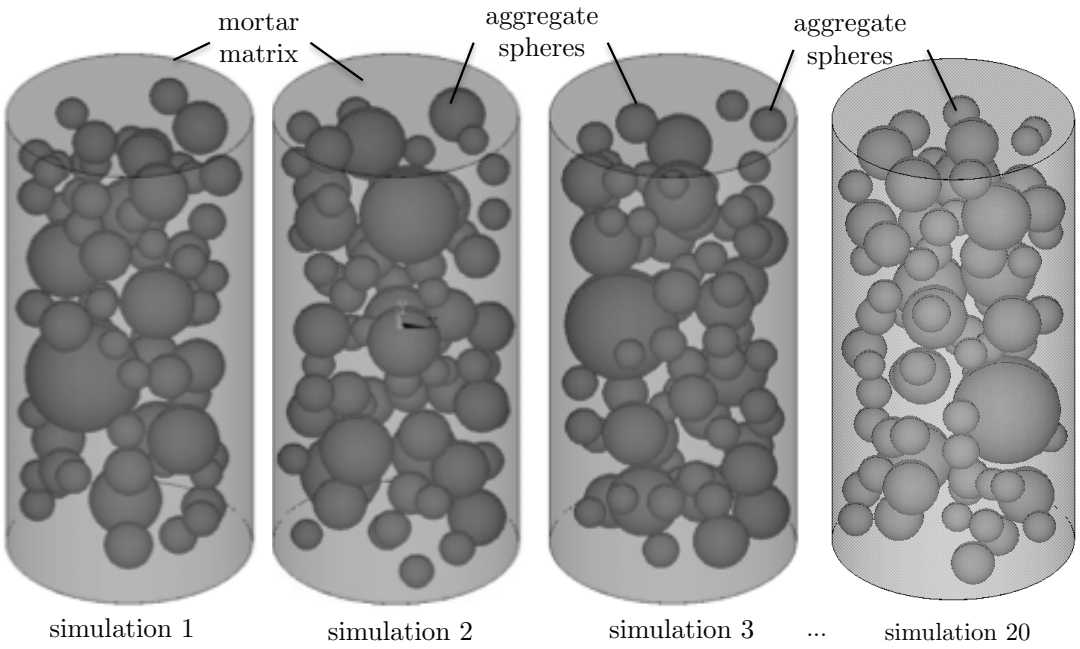

Figure 1: Four simulations of random distribution of the aggregate spheres within a concrete cylinder.

The pressure p on the upper side of the cylinder produces an elongation δ in z-direction. The macroscopic strain of the specimen is equal to $\varepsilon = \delta/h$, the macroscopic normal stress is $\sigma = p$, and the concrete elastic modulus is $E = \sigma/\varepsilon$.

For each type aggregate, 20 geometrical configurations with random aggregates distribution are calculated. From these configurations, meshes of approximately 220 000 tetrahedral finite elements are generated (Figure 2(b).

In the first set of simulations, a pressure in positive z-direction, normal to the upper side of the cylinder is applied and an aggregate elastic modulus $E_a = 70$ GPa is considered. The concrete mean elastic modulus computed of 20 simulations is $\bar{E} = 30.04$ GPa with coefficient variation $cv = 0.2\%$, as shown in Figure 2(c). This result is very similar to the elastic modulus of 30.00 GPa obtained by Caballero, Lopez and Carol [3].

The representation of aggregate and mortar with different elastic modulus and the random location of the aggregate particles, produce non–uniform normal stresses in the pressure direction σ_{zz}; although the specimen is subjected to uniform pressure. Figure 3(a) indicates the aggregate and mortar zones in a slice on xy-plane at $z = h/2$ of a concrete cylinder. The relation between the normal stress of the aggregate or the mortar σ_{zz} and the mean normal stress of the concrete $\bar{\sigma}_{zz}$ is shown in Figure 3(b). The normal stress in the aggregates is greater than in the mortar, and changes between the 0.70 and 1.21 times the mean normal stress of the concrete.

In the second simulations set, cylinder concretes subjected to pressure $-p$ with four aggregates types are represented (Figure 2(a)). The elastic modulus of the aggregates used in the simulations are the following [20, 26]. For igneous rocks as the gabbro or the diabase the elastic modulus is $E_a = 86$GPa, and for the granite is $E_a = 61$ GPa. For sedimentary rocks, the elastic modulus is $E_a = 31$ GPa in sandstones and $E_a = 28$ GPa in limestones. Poisson relation of aggregates ν_a and of mortar ν_m is considered 0.2. The mortar elastic modulus used is $E_m = 25$ GPa [3]. Figure 4(a) shows the concrete elastic modulus with aggregates from igneous rocks as gabbro, diabase and granite, and Figure 4(b) shows the concrete elastic modulus with aggregates from sedimentary rocks as sandstones and limestones. The mean elastic modulus of the concrete $\bar{E}$ computed with different aggregates as gabbro, diabase, granite, sandstone, and limestone is 31.07 GPa, 31.07 GPa, 29.33 GPa, 25.86 GPa and 25.36 GPa, respectively. The coefficient of variation cv

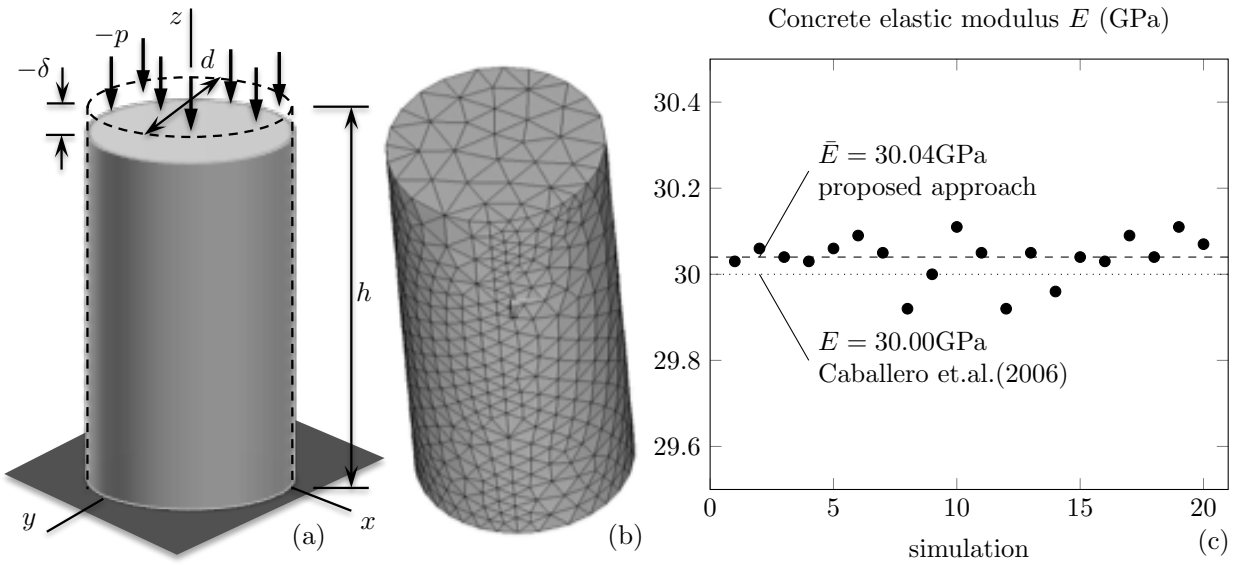

Figure 2: Concrete cylinders subjected to normal pressure: (a) sketch of the applied pressure p and the displacement δ, (b) external view of the finite element mesh of the specimen, and (c) concrete elastic modulus for aggregates with $E_a = 70$ GPa.

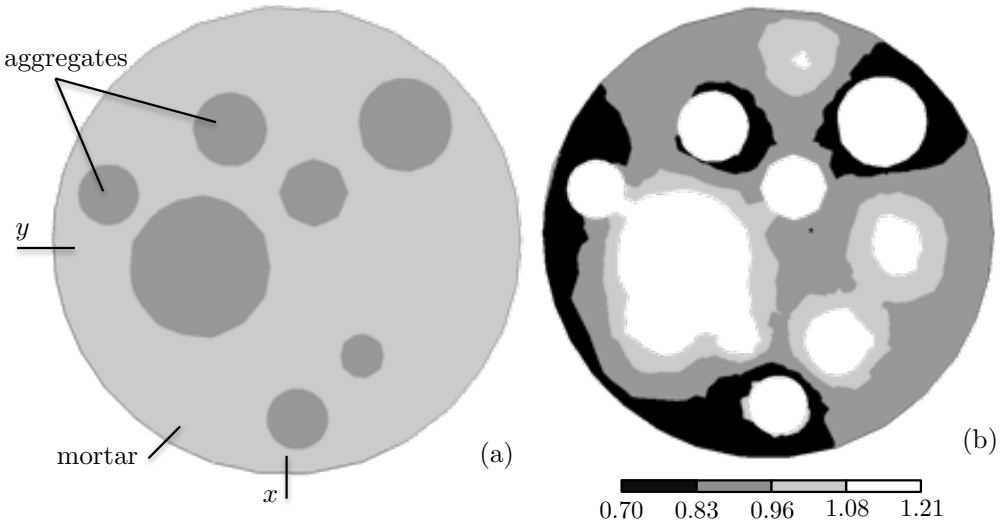

Figure 3: Slice on xy-plane at $z = h/2$ of a concrete cylinder subjected to compression: (a) location of the aggregate and mortar zones, and (b) relation $\sigma_{zz}/\bar{\sigma}_{zz}$, where σ_{zz} is the macroscopic normal stress in the pressure direction and $\bar{\sigma}_{zz}$ is the macroscopic normal stress of the concrete.

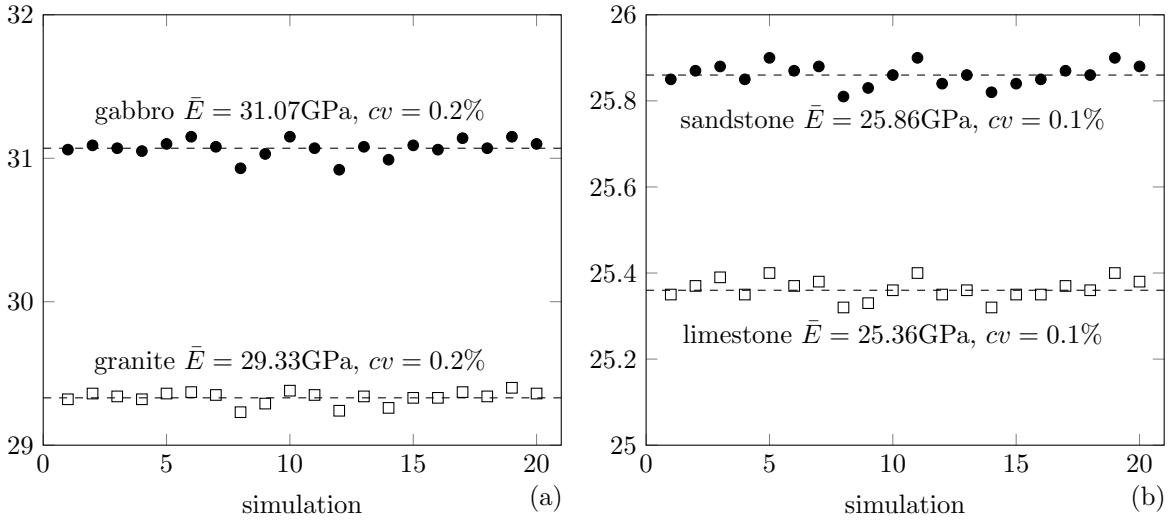

Figure 4: Concrete elastic modulus E in GPa with the 20% of aggregates from different origin: (a) aggregate from some igneous rocks as gabbro, diabase and granite, and aggregate from some sedimentary rocks as sandstones and limestones.

of each sample is less than 0.2%.

4 Conclusions

The sample of concrete elastic modulus obtained from simulations with random location of the aggregates exhibits very low dispersion and presents a reliable mean value. This result is approximately equal to the elastic modulus obtained numerically by other authors.

The elastic modulus of the concrete depends on the type and the amount of its aggregates. A concrete with 20% of volumetric fraction of gabbro or diabase presents elastic modulus 1.2 times greater than with aggregates of sandstone or limestone.

References

[1] ASTM. Standard specification for concrete aggregates astm c 33-03, 2003.

[2] O. Buyukozturk and S.S. Shareef. Constitutive modeling of concrete in finite element analysis. *Computers and Structures*, 21(3):581–610, 1985.

[3] A. Caballero, C.M. Lopez, and I. Carol. 3d meso-structural analysis of concrete specimens under uniaxial tension. *Computational Methods in Applied Mechanics and Engineering*, 195:7182–7195, 2006.

[4] I. Carol, C. M. Lpez, and O. Roa. Micromechanical analysis of quasi-brittle materials using fracture-based interface elements. *International Journal for Numerical Methods in Engineering*, 52(1-2):193–215, 2001.

[5] C. S. Chang, T. K. Wang, L. J. Sluys, and J. G. M. Van Mier. Fracture modeling using a micro structural mechanics approach - i. theory and formulation. *Engineering Fracture Mechanics*, 69(17):1941–1958, 2002.

[6] C. S. Chang, T. K. Wang, L. J. Sluys, and J. G. M. Van Mier. Fracture modeling using a microstructural mechanics approach - ii. finite element analysis. *Engineering Fracture Mechanics*, 69(17):1959–1976, 2002.

[7] A. C.T. Chen and W.F. Chen. Constitutive relations for concrete. *Journal Engineering Mechanics ASCE*, 101, 1975.

[8] V. F. P. Dutra, S. Maghous, A. C. Filho, and A. R. Pacheco. A micromechanical approach to elastic and viscoelastic properties of fiber reinforced concrete. *Cement and Concrete Research*, 40(3):460–472, 2010.

[9] P. H. Feenstra and R. De Borst. A composite plasticity model for concrete. *International Journal of Solids and Structures*, 33(5):707–730, 1996.

[10] P. Fuschi, M. Dutko, D. Peri, and D. R. J. Owen. On numerical integration of the five-parameter model for concrete. *Computers and Structures*, 53(4):825–838, 1994.

[11] K. H. Gerstle. Simple formulation of biaxial concrete behavior. *ACI Journal*, 78(1):62–68, 1981.

[12] K. H. Gerstle. Simple formulation of triaxial concrete behavior. *ACI Journal*, 78(5):382–387, 1981.

[13] P. Grassl and M. Jirsek. Damage-plastic model for concrete failure. *International Journal of Solids and Structures*, 43(22):7166–7196, 2006.

[14] P. Grassl and M. Jirsek. Meso-scale approach to modelling the fracture process zone of concrete subjected to uniaxial tension. *International Journal of Solids and Structures*, 47(7):957–968, 2010.

[15] P. Grassl, K. Lundgren, and K. Gylltoft. Concrete in compression: a plasticity theory with a novel hardening law. *International Journal of Solids and Structures*, 39(20):5205–5223, 2002.

[16] S. S. Hsieh, E. C. Ting, and W. F. Chen. A plastic-fracture model for concrete. *International Journal of Solids and Structures*, 18(3):181–197, 1982.

[17] H. D. Kang and K. J. Willam. Localization characteristics of triaxial concrete model. *Journal of Engineering Mechanics*, 125(8):941–949, 1999.

[18] J. Mazars and G. Pijaudier-Cabot. Continuum damage theory - application to concrete. *Journal Engineering Mechanics ASCE*, 115:345–365, 1989.

[19] A. R. Mohamed and W. Hansen. Micromechanical modeling of concrete response under static loading - part 1 : Model development and validation. *ACI Materials Journal*, 96(2):196–203, 1999.

[20] L. Obert and W. I. Duvall. *Rock Mechanics and the Design of structures in rock*. John Wiley and Sons, Inc., United States, 1967.

[21] J. Oliver, M. Caicedo-Silva, E. Roubin, and A. Huespe. Continuum approach to computational multi-scale modeling of propagating fracture. *Computational Methods in Applied Mechanics and Engineering*, 294:384–427, 2015.

[22] J. Oliver, M. Cervera, S. Oller, and J. Lubliner. Isotropic damage models and smeared crack analysis of concrete. In N. Bicanic et. al., editor, *SCI-C Computer Aided Analysis and Design of Concrete Structures*, pages 945–958.

[23] M. Ortiz. A constitutive theory for inelastic behaviour of concrete. *Mechanics of Materials*, 4:67–93, 1985.

[24] N.S. Ottosen. A failure criterion for concrete. *Journal Engineering Mechanics ASCE*, 103, 1977.

[25] R. Raveendra Babu, G. Benipal, and A. Singh. Constitutive modeling of concrete: An overview. *Asian Journal of Civil Engineering*, 6(4):211–246, 2005.

[26] E. Rivva. *Naturaleza y materiales del concreto*. ACI Peru, Lima (Peru), 2000.

[27] J. Sanahuja and C. Toulemonde. Numerical homogenization of concrete microstructures without explicit meshes. *Cement and Concrete Research*, 41(12):1320–1329, 2011.

[28] S. Toro, P. Snchez, J. Podesta, P. Blanco, A. Huespe, and R. Feijo. Cohesive surface model for fracture based on a two-scale formulation: computational implementation aspects. *Computational Mechanics*, 58(4):549–585, 2016.

[29] K.J. Willam and E.P. Warnke. Constitutive model for triaxial behaviour of concrete. In *Concrete structures subjected to triaxaial stresses*. International Association for Bridges and Structural Engineering, 1974.

[30] K. William. *Constitutive Models for Engineering Materials*, volume 3, pages 603–633. Academic Press, 2002.

Finite Element Analysis of the Thermo-Mechanical Behavior in Additive Manufacturing Processes by Powder Bed Fusion (PBF)

J.J. Quitero Duarte[1], J.F. Rincón Franco[1], R. Guzmán López[2]

[1]Departamento de Ingeniería Mecánica, Semillero de Ingeniería Mecánica
Universidad Pontificia Bolivariana, Bucaramanga, Colombia

[2]rolando.guzman@upb.edu.co
Departamento de Ingeniería Mecánica,Grupo GideTechMA
Universidad Pontificia Bolivariana, Bucaramanga, Colombia

Abstract

Additive manufacturing (AM) processes for the manufacture of metal parts, through the addition of multiple overlapping layers, requires the knowledge of thermal-mechanical history essential in the determination of the residual stresses and distortion of the manufactured parts. In this work, a simulation methodology is presented that allows to simulating the behavior of the process of additive manufacturing, by means of the Powder Bed Fusion (PBF) process, in order to analyze the thermal fields that part forms by spreading thin layers of powder, these analyzes are done through the commercial code ANSYS V 18.2 in conjunction with the ACT TOOL "Additive Manufacturing Process Modeling Technology v1.1" and "Command Obj to ACT v1". In the first part a review of the variables of influence in the manufacturing process and the respective methodological considerations is made, to later perform the thermo-mechanical simulation evaluating the internal stress and strain produced in a simple geometry, the results prove the main problems of the manufacturing process as the influence of the positioning angle in the final quality of vertical and horizontal areas in thin wall objects, as well as the need for support and compensation of the structure to prevent distortion dimensional .

Key Words: Additive manufacturing (AM), 3D printing, Powder Bed Fusion (PBF), Additive Manufacturing Process Modeling, Thermal-Mechanical analysis

1 Introduction

Metallic additive manufacturing processes, also known as 3D printing, refer to the construction of objects by the addition of multiple overlapping layers that make up a whole, with the particularity of not having enough waste material characteristic of subtractive processes, but that they may need a post-process [1]. But despite the design freedom of additive manufacturing, one of the main drawbacks is production defects due to thermal phenomena caused by a series of heating and cooling between layers that generate residual stresses and distortions due to temperature changes [2], which is why the development of a numerical modelling that makes it possible to better understand the nature of the additive process becomes essential, under the understanding of some physical considerations made in ANSYS and thus obtain representative solutions.

2 Powder Bed Fusion Process

2.1 Heat source

The heat supplied by the laser is commonly defined by a Gaussian distribution model of energy in motion that can be represented using the Goldak model [3], observed in figure 1, this formulation has been widely used in the simulation of welds and is defined by means of two sources in the form of an ellipsoid [4], described in the following equations:

$$\dot{Q}_{f_{x,y,z}} = \frac{6\sqrt{3} f_f \eta_{abs} P}{a_f bc\pi} e - \left(\frac{3x^2}{a_f^2} + \frac{3y^2}{b^2} + \frac{3z^2}{c^2} \right) \tag{1}$$

$$\dot{Q}_{r_{x,y,z}} = \frac{6\sqrt{3} f_r \eta_{abs} P}{a_r bc\pi} e - \left(\frac{3x^2}{a_r^2} + \frac{3y^2}{b^2} + \frac{3z^2}{c^2} \right) \tag{2}$$

Where *af* and *ar*, measured in meters, are parameters of the front and rear ellipsoids respectively, the value of b corresponds to the width of the source, c indicates the depth, P is the power of the laser and *nabs* is the absorption coefficient of the powder [5]. Additionally, the frontal fraction (*ff*) of heat is considered 0.6, the posterior fraction (*fr*) 1.4 and each flow is a function of the Cartesian coordinates in which it moves [3].

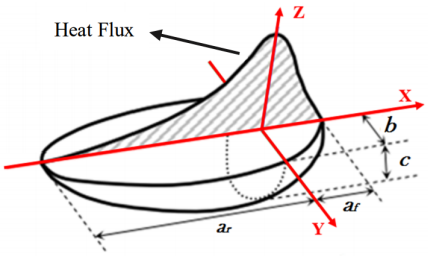

Figure 1: Double ellipsoid heat source model [3],[5].

The pattern and scanning speed of the PBF process, as well as the laser power, determine the impact of the heat source on the powder material, a good management of these variables will determine if the material is melted totally or incomplete zones remain, in addition, the time of cooling between the different layers is key to avoid the phenomenon of overheating, which could deform the layers formed.

3 Numerical Model

The numerical analyses have been made in the commercial code of ANSYS V.18.2 using the technique of inactive mesh elements, also known in ANSYS as "Birth and Death Element", which are activated as the layer is being built, whereby the mesh must have uniform dimensions throughout the object, so when activating each layer of elements they have the same height corresponding to the dust deposition of the real situation. Due to the complexity of a Multiphysics analysis, the modelling is divided into two, first, a thermal analysis that allows extracting the temperature history of each node and then these thermal loads are taken to a structural analysis for the respective calculations of elastic-plastic [6], [7].

3.1 Meshing

Due to the progressive activation of elements of each layer, the mesh is composed of equal hexahedral elements, as shown in Figure 2, the size of the elements is fundamental for the precision of the simulation because the mesh method makes a discretization of the figure, modifying the non-orthogonal borders, therefore a very large element size will generate geometric problems in the simulation. The elements of the base plate can

be larger because their temperature variation in the transient state will be considerably smaller but also hexahedral elements are chosen to facilitate computational processing.

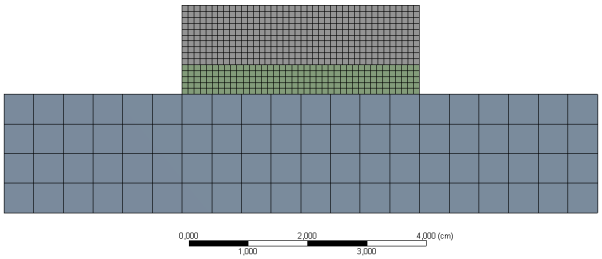

Figure 2: Hexedric mesh, 1 mm thick layer

3.2 Layer Compounds

In real machines the layer thicknesses for different materials range from 20 m to 80 m [8], it is not feasible to simulate each of the deposited layers because it would require a lot of calculation time, therefore an abstraction has been implemented in the which is considered that contiguous layers can be united in a single one, because when applying a heat source to multiple layers of such small thicknesses the nearby material melts again and consequently will have the same temperature record, this means that the thermal and mechanical loads between these will be similar.

3.3 Heat Source Input

The modeling of the heat source in additive processes can vary according to the level of abstraction desired, for this case a uniform heat input is applied in the whole of the layer, thus omitting the Gaussian definition of the heat source and its vector behavior through the scan path of the machine. Because the gradients in the XY plane are neglected, it is necessary to establish a thermal load time that compensates for the scanning time of the layer and simultaneously induces a heat flow through the piece, equivalent to that necessary to process the multiple layers in a mesh element [9].

3.4 Behaviour of the material

The charges that exist in the physical problem are thermal loads produced by cooling from the melting temperature to room temperature. The behaviour of the material is thermoplastic, which allows the obtaining of properties (eg Young's modulus (E), elastic limit (σy), ultimate strength, Poisson's coefficient, density, conductivity, etc.) as a function of the temperature from a family of experimental curves at different test conditions, these input data allow to approach the behavior generated by the micro-structural changes of the piece without having to make an explicit analysis of it, because the experimental data show some of the effects generated by the phase changes at different temperatures, such as the variation of the specific heat, in this way reliable results can be obtained. On the other hand, the effects of powder around the piece are calculated by approximating its effects to an equivalent convective cooling of the outer surface [10].

4 Results and Discussion

Figure 3 shows the two models of simple geometry that were valued. The following process parameters were used for simulation setting:

- *Material:* 316 stainless steel

- *Melting temperature:* 1250 [C]
- *Preheating temperature:* 100 [C]
- *Layer thicknes:* 0.005 [m]
- *time between layers:* 10 [s]
- *Chamber temperatures:* 80 [C]

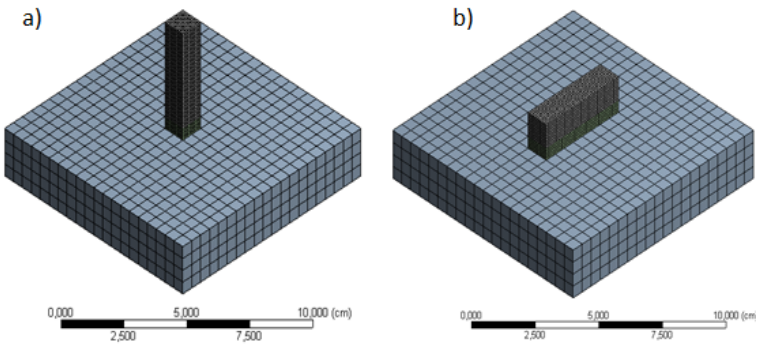

Figure 3: Models of simple geometry (a) (b).

Through the simulations performed it is possible to observe the different phenomena that occur in additive manufacturing to better understand its thermo-mechanical behavior. Figure 4 shows the global temperature history of the geometry A system (figure 3-a), in this, it is possible to visualize the different heating to which the built part is subjected. First, the layer generates a peak equivalent to the melting temperature at which the material is deposited, then a rapid cooling occurs due to the convection heat flow and then the cooling rate decreases because at this moment the heat transfer occurs mainly due to thermal conduction. It must be taken into account that in a real process the cooling and heating rates in each layer are faster due to the thinness of the layer, but the resulting gradients after a series of heating are comparable, because the thermal load is maintained enough time for the adjacent elements to heat up, additionally the piece is cooled for a time equivalent to that required by a real system to travel the entire layer and distribute again the next.

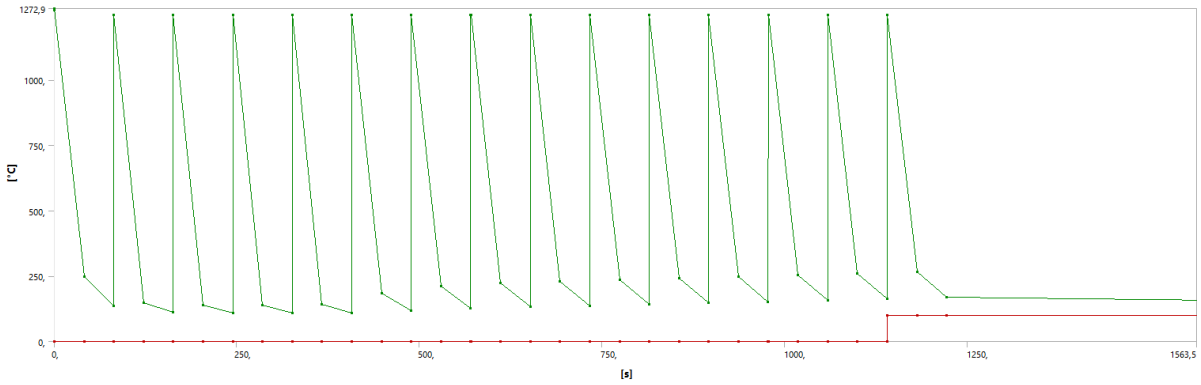

Figure 4: Global thermal history of geometry .

The evolution of the different layers over time causes the piece to accumulate more heat and increase the minimum temperature reached by the system before a new layer, which can lead to higher temperature

gradients in a stable state, thus generating higher stresses thermal and deformations. This relationship between the minimum temperature and internal stresses depends directly on the ability of the geometry to transmit heat to the environment, so in some cases, as in Figure 5-a, the exposed area of the piece allows a uniform heat flow which results in a difference of 0.28 [C] between the minimum and maximum temperature of the entire system at the end of the process, in other cases, as shown in Figure 5-b, the exposed area does not allow sufficient heat transfer to dissipate the energy entered by each layer, due to this the thermal gradient increases up to 460 [C] in stable state, with a noticeable accumulation in the upper part.

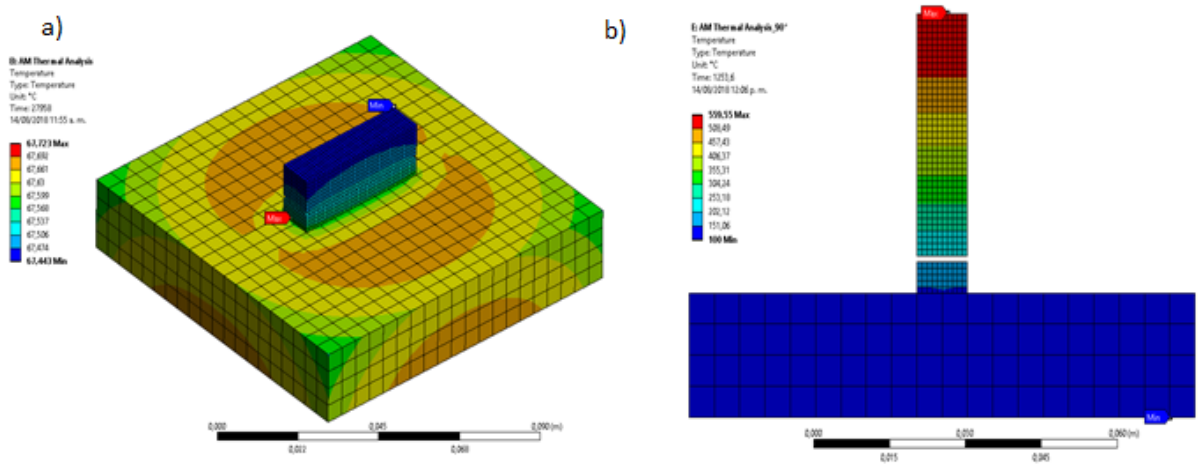

Figure 5: a) Final temperature in test tube at 0 inclination b) Final temperature in a test tube at a 90 inclination.

The temperature gradients resulting from the manufacturing process generate deformations and internal stresses, which can permanently deform the piece, as seen in Figure 6 the horizontal surfaces and vertical edges are totally distorted, especially in the geometry inclined (90 C), due to the Heat accumulation mentioned above.

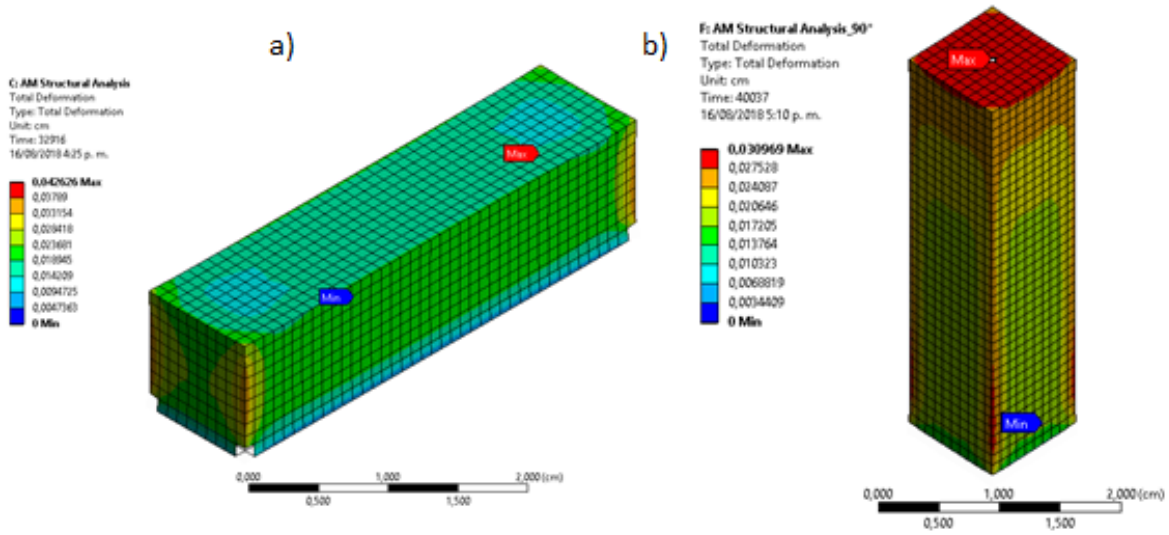

Figure 6: a) Deformation in a test tube at 0 inclination, b) Deformation in the specimen at a 90 inclination .

5 Conclusions and Future Work

The minimum temperatures of the system are directly related to the geometric shape of the piece, due to the influence of the area exposed to convection, therefore, the orientation of an object is decisive in the resulting deformations and stresses; additionally the ambient temperature and the preheating of the base can reduce the thermal gradients in the inter-layer cooling. The numerical analysis performed has the potential to give reliable results in acceptable processing times, but it is not a reliable representation of the reality that allows knowing the optimal parameters of the machine, so this type of analysis should be considered only an approximation that helps to improve deposition design and orientation parameters. To achieve realistic results it is necessary to implement an exact modeling of the micro-structure and take into account the vector behavior of the heat source.

References

[1] Gebhardt, A. Understanding Additive Manufacturing Rapid Prototyping - Rapid Tooling - Rapid Manufacturing. *Carl Hanser Verlag GmbH*, 2011.

[2] Gu, D. Meiners, W. Wissenbach, K & Poprawe, R. Laser additive manufacturing of metallic components: materials, processes and mechanisms. *Int. Mater. Rev*, **57**: 133-169, 2002.

[3] Goldak, J. Chakravarti, A & Bibby, M. New Finite Element Model for Welding Heat Sources. *Metall. Trans. B*, **15**(2): 299-305, 1984.

[4] Hwang, S. Lee, J. Kim, S & Viswanathan, K. Numerical Simulation of Welding Residual Stress Distribution on T-joint Fillet Structure. *International Journal of Ocean System Engineering*, **2**012

[5] De Moraes, D & Czekanski, A. Thermal Modelling of 304L Stainless Steel for Selective Laser Melting: Laser Power Input Evaluation. *Proceedings of ASME 2017 International Mechanical Engineering Congress and Exposition*, **2**017.

[6] Bayerlein, F. Zeller, C. Wunderer, M. Weirather, J. Schmid, M & Seidel, C. Validation of modeling Assumptions for the Build-up Simulation of Laser Beam Melting on the Basis of The Residual Stress Distribution. *ECCOMAS Congress 2016 VII European Congress on Computational Methods in Applied Sciences and Engineering*, **2**016.

[7] Seidel, C. Krol, T. Schilp, J. Zaeh, M & Groth, C. Ansaetze zur rechenzeiteffizienten Struktursimulation additiv gefertigter, filigraner Bauteile. *CADFEM GmbH (ed.): ANSYS Conference 30. CADFEM Users' Meeting. Kassel*, **2**012.

[8] EOS GmbH Electro Optical Systems EOS GmbH Electro Optical Systems *Mnchen. 2010*

[9] Branner G. Modellierung transienter Effekte in der Struktursimulation von Schichtbauverfahren. *Dissertation Technische Universitaet Muenchen*, Munich, 2010.

[10] Krol, T. Westhuser, S. Zh, M. Schilp, J & Groth, G Development of a Simulation-Based Process Chain Strategy for Different Levels of Detail for the Preprocessing Definitions. *SNE Technical Note, Symposium Simulationstechnik*, Winterthur, Switzerland, 2011.

Stress Distribution Analysis in Single Lap Joint Specimens of Composite Materials With Different Adhesive Thicknesses Under Quasi-Static and Cyclic Impact Loadings

A. Bautista[1], J.P. Casas[2], M. Silva[3], A. Porras[4]

[1]aa.bautista@uniandes.edu.co
[2]j.casas@uniandes.edu.co
[4]n-porras@uniandes.edu.co
Department of Mechanical Engineering,
Universidad de los Andes, Bogotá, Colombia

[3]maribel.silva@fac.mil.co
Researcher,
Colombian Air Force

Abstract

The Colombian aeronautical industry has stimulated research in the mechanical behavior of materials under different loading conditions aircrafts are generally exposed during its operation. The Calima T-90 is the first military aircraft built in the country, used for primary flight training of Colombian Air Force Pilots, therefore, it may be exposed to adverse operating situations such as hard landings which cause impact loads on the aircraft that might produce the impact fatigue phenomenon. The Calima T-90 structure is mainly manufactured by composites materials generating assemblies and subassemblies of different components of it. The main method of bonding these components is by using adhesive joints. Each type of adhesive bond must be studied on its own since its performance depends on the conditions of the manufacturing process and operating characteristics.

This study aims to characterize the typical adhesive joints of the aircraft under usual loads. To this purpose, the evaluation of the effect of adhesive thickness on the mechanical performance of the joint under quasi-static loading conditions and cyclic impact fatigue using single lap-joint (SLJ) specimens was performed. Additionally, an analysis of the stress distribution in SLJ specimens with different adhesive thicknesses, provide insights into the variation of the mixed mode fracture due to bending moment caused by the eccentricity of applied loading.

Key Words: Adhesive bonded Joints; Impact fatigue; Mixed mode fracture; Single lap joints, Composite materials

1 Introduction

Composite materials are widely used nowadays especially in applications related to transportation due to their exceptional specific strength and stiffness and their physical properties [1]. In the aerospace industry, over the past 30 years, the number of composite materials used in commercial aircraft structure has increased 40%. For example, Boeing 757 in the 1980s had less than 10% by weight of composite materials while Boeing 787 has 51%. Currently this usage is approaching 70 percent on the Eurofighter and other advanced aircraft,

with entire airframes and support structures being constructed of composite materials [2].
There are a wide variety of methods of joining components and parts. The adhesive bonding process let join substrates placing an adhesive between them. This method provides many advantages over conventional mechanical fasteners such as lower structural weight, reduction of stress concentrators and high performance under fatigue conditions, resulting in an increasing of the structural integrity of the system [3].
The Calima T-90 is the first military aircraft built in the country, used for primary flight training of Colombian Air Force Pilots, therefore, it may be exposed to adverse operating situations such as hard landings which cause impact loads on the aircraft that might produce the impact fatigue phenomenon. The aircraft is mainly manufactured by composites materials assembled by adhesive joints. The adhesive is composed of a mixture of epoxy resin/hardener with a filler substance called Flocked Cotton Fiber.
This paper aims to analyze the influence of adhesive bond thickness in the mechanical performance and stress distribution of single lap joint specimens (SLJ) under quasi-static and cyclic impact loading conditions using the adhesive and substrates of the Load Pads (support for fuselage and wing beams joint) of the Calima T-90 aircraft, including the mechanical characterization of tensile properties of the adhesive with different mixing ratios resin/flocked cotton fiber.

2 Materials and experimental procedure

The adherends of SLJ's specimens are made of fiber glass cloth as the dispersed phase and a epoxy laminating resin as the continuous phase or the matrix. The laminates are stacked by wet lay up procedure. The nominal thickness of the fiber reinforced polymer (FRP) is 3mm. The adhesive is composed of an epoxy resin and a filler substance called flocked cotton fiber, which increases the adhesive viscosity and enable to apply it in the surface with an specific thickness. The geometry of the SLJ's specimens is described in the ASTM D5868 standard. The specimens dimensions are 1in width, 7in length and 1in length on the overlap, moreover they are manufactured with 3 different adhesive bonded joint thicknesses: $\frac{1}{2}$ in, $\frac{1}{4}$ in and $\frac{1}{8}$ in.
Adhesive specimens geometry is based on the ASTM D638 standard, besides the specimens are manufactured with 3 different mixing ratios of resin:flocked cotton fiber: 100:16, 100:20 and 100:24. The tensile properties of the adhesive system are obtained following the procedure of the ASTM D638 standard too. The adhesive used in the SLJ's specimens is made with the mixing ratio of resin:flocked cotton fiber which exhibits the best tensile properties.

3 Stress distribution in SLJ's specimens

SLJ's specimens under tensile loading experience a bending moment due to the eccentricity of acting forces. As the line of action of the tensile loading is not parallel to the adherends plane, this line will trend to be aligned, so that it will produce a rotation of substrates. The bending moment makes the adhesive bonded joint to bear mixed mode loading (I/II) thus the bonded surface develops shear and peel stresses that are not constant in the overlap length [4].
The first elastic analysis of adhesive joints began in 1938 with the shear-lag model proposed by Volkersen [5]. In his work the effect of the adherend elongation on the shear strain in the adhesive layer described by an ordinary differential equation of second order is considered. It was assumed that the adhesive deforms only in shear but the adherends can deform in tension [6]. Volkersen gave a solution for the differential equation and showed the shear stress distribution in the overlap length which reaches a maximum value at the extremes of the bonded line. In this study the effect of peel stresses associated to mode I fracture was not considered and it does not account for the bending effect caused by the eccentric load path of SLJ's [7] .
Goland & Reissner were the first to take in consideration the effect of bending moment caused by eccentric acting forces and adherends rotation. The determination of the loads at the edges of the joints is obtained using the finite deflection theory of cylindrical bent plates. Additionally this model deals with the peel stresses developed in SLJ's [8] [9].

The adhesive shear stress distribution (τ) proposed by Goland & Reissner is given by:

$$\tau = -\frac{1}{8}\frac{\overline{P}}{c}\Big(\frac{\beta c}{t}(1+3k)\frac{cosh((\beta c/t)(x/c))}{sinh(\beta c/t)} + 3(1-k)\Big) \tag{1}$$

Where, c is half of the overlap length, $\overline{P}$ is the acting tensile load per unit width, t is the adhered thickness and k is the bending moment factor. k and β are obtained from the following equations respectively:

$$k = \frac{cosh(u_2 c)}{cosh(u_2 c) + 2\sqrt{2}sinh(u_2 c)} \qquad \beta^2 = 8\frac{G_a t}{E t_a}$$

Where, G_a is the adhesive shear modulus, E is the adherend modulus and t_a is the adhesive thickness. u_2 depends on the Poisson's ratio (ν), the adherend modulus, the adherend thickness (t) and the applied tensile load per unit width as follows:

$$u_2 = \sqrt{\frac{3(1-\nu^2)}{2}}\frac{1}{t}\sqrt{\frac{\overline{P}}{tE}} \tag{2}$$

The adhesive peel stress distribution σ is given by:

$$\sigma = \frac{\overline{P}t}{\delta c^2}(A+B) \tag{3}$$

Where A , B and Δ are respectively:

$$A = \Big(R_2\lambda^2\frac{k}{2} + \lambda k' cosh(\lambda)cos(\lambda)\Big)cosh\Big(\frac{\lambda x}{c}\Big)cos\Big(\frac{\lambda x}{c}\Big) \tag{4}$$

$$B = \Big(R_1\lambda^2\frac{k}{2} + \lambda k' sinh(\lambda)sin(\lambda)\Big)sinh\Big(\frac{\lambda x}{c}\Big)sin\Big(\frac{\lambda x}{c}\Big) \tag{5}$$

$$\Delta = \frac{1}{2}(sin(2\lambda) + sinh(2\lambda)) \tag{6}$$

Where;

$$\lambda = \gamma\frac{c}{t} \qquad \gamma^4 = 6\frac{E_a t}{E t_a}$$

$$R_1 = cosh(\lambda)sin(\lambda) + sinh(\lambda)cos(\lambda) \qquad R_2 = -cosh(\lambda)sin(\lambda) + sinh(\lambda)cos(\lambda)$$

Additionally the transverse force factor k' depends on the bending moment factor (k), adherend thickness (t), the Poisson's ratio (ν), the adherend modulus (E), half of the overlap length (c) and the applied tensile load per unit width as follows:

$$K' = \frac{kc}{t}\sqrt{3(1-\nu^2)\frac{\overline{P}}{tE}} \tag{7}$$

Ojalvo & Edinoff [10] modified Goland & Reissner model due to the latter one has an incomplete shear-strain/displacement equation for the adhesive, so they corrected the deficiency found and proposed the following elastic shear stress distribution in the overlap length of the bonded joint [11] :

$$\tau(x) = Acosh(\lambda\sqrt{2+6(1+\beta)^2}x) + B \tag{8}$$

Where the constants A and B are obtained from differentiation and integration of latter equation and be replaced into:

$$\frac{d}{dx}\tau = 2\lambda^2(1+3(1+\beta)^2 k) \tag{9}$$

$$\int \tau dx = 2 \tag{10}$$

The peel stress distribution is given by:

$$\sigma(x) = Csinh(\alpha_1 x)sin(\alpha_2 x) + Dcosh(\alpha_1 x)cos(\alpha_2 x) \tag{11}$$

C and D constants are obtained from differentiation of the previous peel stress distribution equation and substitution into:

$$\frac{d}{dx^3}\sigma - 6\beta\lambda^2\frac{d}{dx}\sigma = k\gamma\rho^2(1+\beta) \tag{12}$$

$$\frac{d}{dx^2}\sigma = k\gamma\rho^2(1+\beta) \tag{13}$$

The variables in the previous equations are:

$$\alpha_1^2 = \frac{3\beta\lambda^2+\rho}{2} \qquad \alpha_2^2 = \frac{-3\beta\lambda^2+\rho}{2} \qquad \gamma = t/2c \qquad \beta = h/t$$

$$\rho^2 = \frac{24E_a c^4}{Eht^3} \qquad \lambda^2 = \frac{G_a c^2}{Eht} \qquad k = \frac{M_0}{(N_0 t/2)(1+\beta)}$$

G_a, c , E, t are the same variables as defined previously and h is the adhesive thickness. k is the bending moment factor and M_o is the bending moment and N_0 the acting tensile force [12] .

4 Results

4.1 Bulk adhesive

The bulk adhesive was tested under quasi-static loading conditions with 3 different mixing ratios of resin : flocked cotton fiber: 100:16, 100:20 and 100:24. The mixing ratio 100:20 increases the strength by 12.8% in comparison with 100:16 and 7.7% in comparison with 100:24, nevertheless, there is no a significant influence of the flocked cotton fiber in the bulk adhesive strength as seen in figure (1). For the mixing ratio 100:20 the young modulus E of the adhesive is 4,266 MPa.

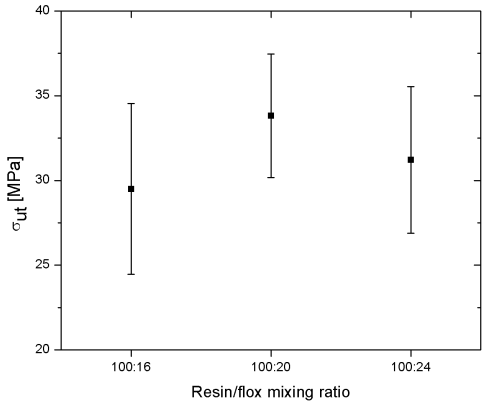

Figure 1: Adhesive tensile strength

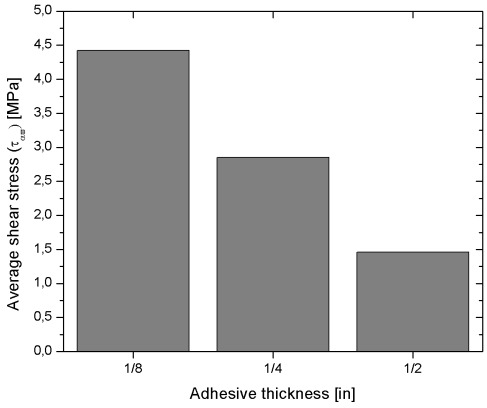

Figure 2: Average shear stress of SLJ's specimens

4.2 SLJ's specimens under quasi-static loading conditions

SLJ's specimens of $\frac{1}{2}$ in, $\frac{1}{4}$ in and $\frac{1}{8}$in were tested under quasi-static loading conditions. The average shear stress τ_{a_v} is determined from the ultimate tensile load F_{u_t} and the contact area A of the adhesive with the adherend surface: $\tau_{a_v} = F_{u_t}/A$.

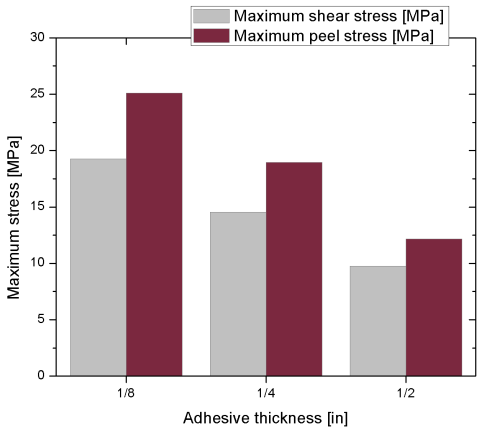

Figure 3: Maximum shear and peel stress in SLJ's specimens as a function of adhesive thickness applying Ojalvo & Edinoff model .

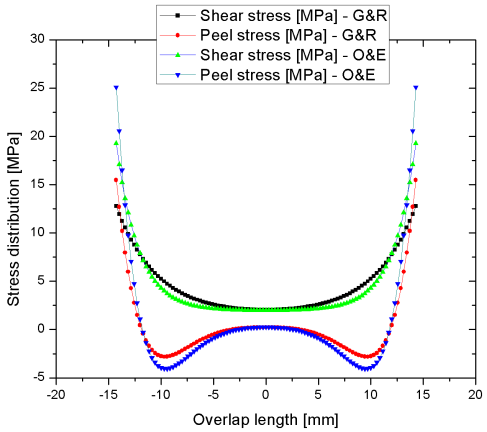

Figure 4: Peel and shear stress distribution in SLJ's specimens with adhesive thickness of $\frac{1}{8}$ in.

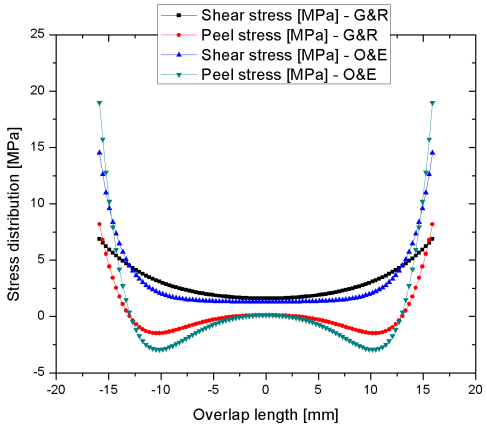

Figure 5: Peel and shear stress distribution in SLJ's specimens with adhesive thickness of $\frac{1}{4}$ in.

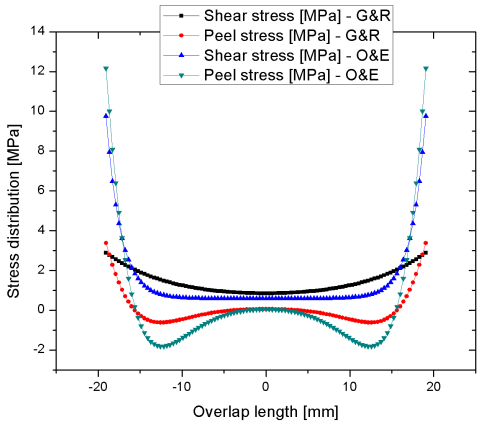

Figure 6: Peel and shear stress distribution in SLJ's specimens with adhesive thickness of $\frac{1}{2}$ in.

Comparing Ojalvo & Edinoff and Goland & Reissner models, the latter one predicts lower peel and shear stresses at both ends of the overlap as seen in figures (4),(5) and (6), besides, both models foretell accurately the average shear stress with less than 6% of error, nonetheless the average peel stress calculated by Ojalvo & Edinoff are closed to the experimental results according to [12]. In this way it is obtained the ratio of average peel to shear stress using the Ojalvo & Edinoff model. For the adhesive thicknesses of $\frac{1}{2}$ in, $\frac{1}{4}$ in and $\frac{1}{8}$ in the average of peel to shear stress ratio is respectively 0.243, 0.186 and 0.148. Then it upholds the assertion that as the adhesive thickness is increased in SLJ's specimens they bear more mode I loading. In figures (2) and (3) it can be seen that as the adhesive thickness increases the bonded joint strength reduces. Even though the bending moment is higher as the the adhesive thickness increases, the obtained peel to shear stress ratios allow to normalize the bonded joint strength letting comparing the results in the same mixed-mode conditions.

4.3 SLJ's specimens under impact fatigue

SLJ's specimens of $\frac{1}{4}$ in and $\frac{1}{8}$in were tested under low energy ($< 10J$) and speed ($< 10m/s$) cyclic impacts. Figures (7) and (8) evince a logarithmic decrease of impact energy vs cycles to failure. For SLJ's specimens with adhesive thickness of $\frac{1}{8}$in the fitting curve has a correlation coefficient of 0.95 and the diagram for specimens with adhesive thickness of $\frac{1}{4}$in has a correlation coefficient of 0.92. Cyclic impact life depends largely on the fracture mechanism of the specimens. Additionally SlJ's specimens with adhesive thickness of $\frac{1}{4}$in fail approximately with a 70% of the impact energy in the same number of cycles of SlJ's specimens with adhesive thickness of $\frac{1}{8}$in.

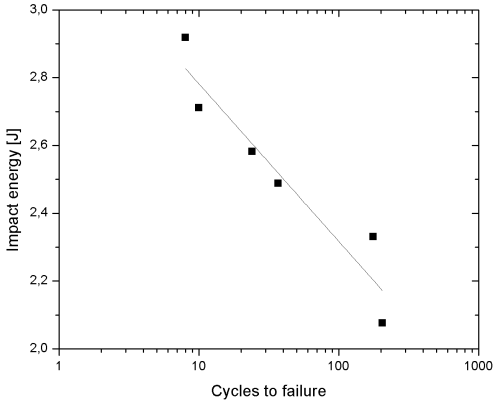

Figure 7: Impact energy vs cycle to failure diagram for SLJ's specimens with adhesive thickness of $\frac{1}{8}$ in.

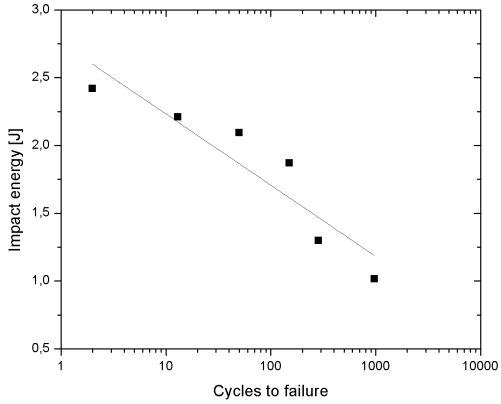

Figure 8: Impact energy vs cycle to failure diagram for SLJ's specimens with adhesive thickness of $\frac{1}{4}$ in.

5 Conclusions

Stress distribution in SLJ's specimens were predicted using Ojalvo & Edinoff and Goland & Reissner models and were compared with experimental data. The average of peel to shear stress ratio was obtained for different adhesive joint thicknesses using Ojalvo & Edinoff model which foretell more accurately peel stress distribution in the overlap length of SLJ's specimens. Additionally the effect of the adhesive joint thickness of SLJ's specimens was analyzed under quasi-static and cyclic impact loadings. Finally it was determined that the filler substance in the bulk adhesive (Flocked Cotton Fiber) does not have a significant influence in the the bulk adhesive strength under tensile acting forces.

6 Acknowledgement

Author is grateful to Escuela de Posgrados de la Fuerza Aerea Colombiana, Colciencias, Colombian Air Force and Structural Integrity Research Group from Universidad de los Andes for supporting this research work.

References

[1] F. Boussu, N. Trifigny, C. Cochrane and V. Koncar. 17 - Fibrous sensors to help the monitoring of weaving process, In Woodhead Publishing Series in Textiles. Edited by Vladan Koncar. *Woodhead Publishing, Oxford, 2016.* **P**ages 375-400, Smart Textiles and their Applications, ISBN 9780081005743.

[2] Going to extremes: Meeting the Emerging Demand for Durable Polymer Matrix Composites. (2005). 1st ed. Washington, D.C. *National Academies Press*, **p**p.9-11.

[3] Banea, M. and da Silva, L. (2009). Adhesively bonded joints in composite materials: An overview. *Proceedings of the Institution of Mechanical Engineers, Part L: Journal of Materials: Design and Applications,*, **p**p.1-18.

[4] P. Weigraeber, W. Becker, Finite Fracture Mechanics model for mixed mode fracture in adhesive joints, *International Journal of Solids and Structures*,**V**olume 50, Issues 1415, 2013, Pages 2383-2394, ISSN 0020-7683.

[5] O. Volkersen, Die Nietkraftverteilung in Zugbeanspruchten Nietverbindungen mit Konstanten Laschenquerschnitten, Luftfarhtforschung, **v**ol. 15, pp. 4147, 1938.

[6] Xiaocong He and Yuqi Wang, An Analytical Model for Predicting the Stress Distributions within Single-Lap Adhesively Bonded Beams, *Advances in Materials Science and Engineering*, **v**ol. 2014, Article ID 346379, 5 pages, 2014.

[7] Lucas F. M. Da Silva, Ricardo F. T. Lima, Rui M.S. Teixeira and A. Puga. *Closed-form solutions for adhesively bonded joints.* Universidade do Porto.

[8] Goland M, Reissner E. *J Appl Mech* **1**944; 66:A17.

[9] Ren Quispe Rodrguez, William Portilho de Paiva, Paulo Sollero, Marcelo Ricardo Bertoni Rodrigues, der Lima de Albuquerque, Failure criteria for adhesively bonded joints, *International Journal of Adhesion and Adhesives*,**V**olume 37, 2012,Pages 26-36, ISSN 0143-7496.

[10] Ojalvo IU, Eidinoff HL. Bond thickness effects upon stresses in single-lap adhesive joints. *AIAA J*, **1**978; 16:204-11.

[11] Rodríguez, René & Paiva, William & Sollero, Paulo & Albuquerque, Eder & Rodrigues, M.B.. (2010). Analytical and numerical tools for bonded joint analysis. *Mecánica Computacional*. **7**557-7569.

[12] Parente da Costa, M. (2013) *Development of a web application for the design of adhesive joints (Master Thesis)*, Universidade do Porto, Porto, Portugal.

Failure Analysis on Mixed Mode I and II Under Dynamic Impact Loads in Fiberglass/Vinyl Ester Composite.

P. Londoño[1], J. Casas[2]

[1]pa.londono10@uniandes.edu.co
Departamento de Ingeniería Mecánica,
Universidad de los Andes, Bogotá, Colombia

[2]jcasas@uniandes.edu.co
Departamento de Ingeniería Mecánica,
Universidad de los Andes, Bogotá, Colombia

13/06/2018

Abstract

In the past, several studies on composite materials and adhesive joints in mixed modes of loading under constant test speed have been made. But recently there is a need of studying low energy impacts effects on components and structures, due to the fact that these loads can cause material failure bellow critical conditions in quasi-static loads at low energy impacts in mixed mode I and II, to study the interlaminar fracture resistance of the material and compare it with the behavior under quasi-static loads obtained from previous studies. As well this study presents the effects of mode of loading in the crack grow rate. The results of the impact test were affected by the Bridging phenomenon for this reason, some data was no taking into account in the analysis.

Key Words:Composites, Delamination, Low energy impacts, Mixed-mode, Mode of loading, Failure criteria, Failure mechanisms, Fiberglass, Fracture mechanics, Toughness testing

1 Introduction

Composite materials present different failure characteristics. Damage growth and the failure mechanisms are not predictable, this happens because of the damage zone, that can include fiber rupture, fibers extraction, matrix rupture, delamination, debonding bridging phenomenon or any combination of all these mechanisms [1]. Investigations of the effects of the Bridging phenomenon have concluded that this phenomenon generates an increase in the energy release rate [2], [3] and [4]. Among the different mechanisms of failure mentioned previously, the delamination has been one of the most studied and can happen under different load modes (mode I, II y III) but is produced usually because of the combination of the mode of loading I and II [5]. The interest of knowing the effects of low speed impacts in the behavior of the composite materials have recently increased, in comparison with other load conditions. This is due to studies performed under impact fatigue, that showed a lower level of energy with the same accumulated damage in comparison with test by sinusoidal fatigue and quasi static loads [13]. And studies that have shown a relation between the interlaminar fracture energy with the test speed [7], [8], [9], [10], [11] and [12]. For a PEEK/unidirectional carbon-fiber composite the loci curves for mixed mode I and II decrease of 20 % when the test speed change from $10^{-4} m/s$ to $3 m/s$

[10]. In this investigation, the value of the strain energy release rate under low speed impacts was obtained aiming to understand the effects of the low speed impact on components and structures of composite materials to compare their behavior under quasi static loads (1 mm/min). It was tested at various mixed-mode ratios from pure mode I to pure mode II for the same composite material used in [6]. This test was registered in a high-speed camera in order to determine the crack grow rate in each mode of loading and verify the mechanisms of failure, using the techniques based on video image processing proposed in [14].

2 Mathematical model : Mixed mode loading

The mixed mode bending test (MMB) was used to measure the mixed-mode delamination toughness. According to [15] based on the beam theory analysis, the strain energy release rate equations used are:

$$\begin{aligned} G_I &= \frac{3a^2P^2}{4b^2h^3L^2E_I}(3c-L)^2 \\ G_{II} &= \frac{9a^2P^2}{16b^2h^3L^2E_{II}}(c+L)^2 \end{aligned} \tag{1}$$

Where the MMB loading P_I and P_{II} expressed in terms of the applied load P and the geometry of the superposition analysis of loading on MMB sample are:

$$\begin{aligned} P_I &= \frac{3c-L}{4L}P \\ P_{II} &= \frac{c+L}{L}P \end{aligned} \tag{2}$$

In contrast to [15], [16] and [11], in this investigation was assumed that the GFRP was an orthotropic material since the fiberglass fabrics configurations have multidirectional plies and crossply plies which generate isotropy in directions 1 and 2. For this reason the value of Young Module can be expressed as: $E \cong E_I \cong E_{II}$

Also, the corresponding equations for the mixed-mode ratio and the total mixed-mode strain energy release rate are:

$$\begin{aligned} G_I/G_{II} &= \frac{4}{3}\left[\frac{3c-L}{c+L}\right]^2 \quad for \quad c \geq L/3 \\ G &= \frac{3a^2P^2}{16b^3h^3L^2E} \end{aligned} \tag{3}$$

3 Samples preparation

For the impact test, the samples were manufactured in a fiberglass/vinyl ester resin composite. The composite has 8 plies of Mat fiber of $456g/m^2$ (M) and 2 plies of Woven Roving fiber of $800g/m^2$ (WR) with Derakane 411-350 epoxy vinyl ester resin by Ashland.The plies had the following configuration M-M-M-WR-M-M-WR-M-M-M with a nominal fiber volume fraction of 30 %, where a $12\mu m$ Mylar layer was used to induce the initial crack length (nominal length 2.5 mm) according to the ASTM D6671 standard. To ensure the accuracy of the high speed camera measurement, several factors were controlled. The samples were painted white on the side to maximize contrast. In addition, it was necessary to control the lamp to illuminate only the samples during the impact time. Thus, avoid the heating effects on the samples and the components of the impact machine. The reflections and shadows were avoided with the correct positioning of the lamp, the use of matte paint for the samples and the coating of the MMB apparatus with talcum powder. Likewise, the end of the

initial crack was marked with a point and, to measure the length of delamination and crack growth rate, every 5 mm were drawn lines along the specimen. With the purpose of compare the delamination length values obtained with the videos, it was also measured by inspection of the samples tested after impact test.

4 Impact test parameters

The samples were tested in 5 mixed-mode I/II ratios (G_I/G_{II}) and one pure mode (mode II). The mixed-mode ratios were 1/5, 3/5, 6/5, 11/5, 15/5. In the investigation was required to test the samples with enough height to propagate the crack with a single impact. For this reason, the test was developed with two different hammer weights (7.38 kg and 3.61 kg) and different initial height for each mixed-mode of loading. The impact energy value was increasing as G_I/G_{II} became smaller, meaning a range of impact speed of 0.6 m/s to 1.28 m/s, this with the purpose of avoid the dynamic effects of the MMB apparatus vibrations and ensure the propagation length of the crack to be inside the range of the ASTM D6671 standard.

5 Results and Discussion

5.1 Delamination Toughness and failure mechanisms

The delamination toughness for each mixed-mode I/II ratio values are shown in the Figure 1. It can be noted, that the critical energy release rate values in pure mode II are overestimated since the friction between the MMB apparatus and the samples is not considering in the mathematical model. With the high-speed camera was possible to establish 3 failure mechanisms. It was found matrix rupture, fiber rupture and Bridging.A link was found between the samples that presented Bridging and the values of delamination toughness. The 7 samples with this failure mechanism had values of G_I and G_{II} highest than the other samples in each loading mode, this corresponds to the conclusions presented by the studies [2], [3] and [4]. The grey dots present samples with the Bridging phenomenon. For the specimens in pure mode II, the presence of the Bridging phenomenon was not possible to identify with the video processing because the shear load does not open the crack at the moment of propagation.

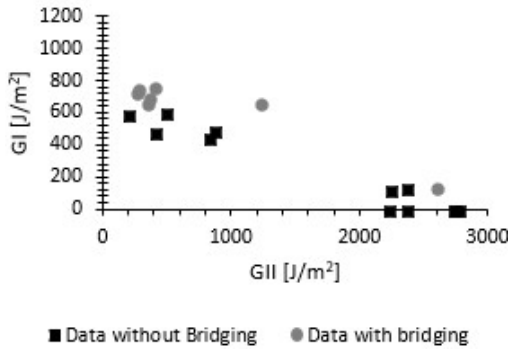

Figure 1: Influence of Bridging phenomena in the delamination toughness measurement

5.2 Power law criterion

To know if the material response to the usual failure in a composite material. The experimental data was fitted to the parameters of the "Power Law Criterion" [16].

$$\left(\frac{{G_{Ic}}^m}{G_{Ic}}\right)^{\alpha} + \left(\frac{{G_{IIc}}^m}{G_{IIc}}\right)^{\beta} = 1 \tag{4}$$

After the iterance of the parameters, the optimum values founded with $R^2 = 0.977$ were: $\alpha = 1.4$ and $\beta = 1.1$. For $G_{Ic} = 600 J/m^2$ and $G_{IIc} = 2460 J/m^2$. The results of the fit of the criterion with the data are shown in the Figure 2. Where the fit curve of Power Law criterion for quasi static loads was obtained from [6].

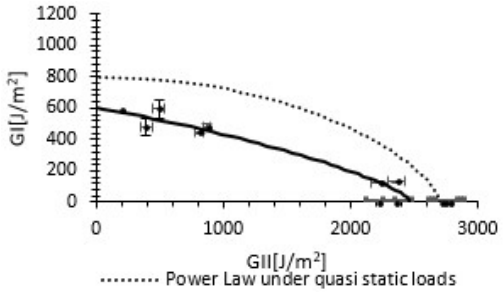

Figure 2: The parameters of the criterion under quasi-static loads were obtained from:[6]

The maximum error in the G_I values is 11% (vertical error bars), such as G_{II} (horizontal error bars). This percentage is considered low because of the many sources of error. For example, errors presented in the samples adjustment with the assembly, in the hinges alignment, in the compound lamination, in the measurement system, the effects of the friction between the sample and MMB apparatus and the MMB apparatus vibrations. In the other hand, the values of G_{Ic} and G_{IIc} decrease 25% and 8.14% respectively under dynamic loads, compared with the G_{Ic} and G_{IIc} under quasi static loads presented by [6]. Due to the fact that dynamic effects were not taken into account in this research, it is possible to affirm that the data obtained could be overestimating the real value of G_{Ic} and G_{IIc}. Therefore, it causes that the percentage of decrease compared to quasi-static loads to be even greater. Under quasi-static loads when the percentage of G_I is $< 53\%$, load mode I has a greater incidence on the material failure since the curve tends to remain horizontal [6]. While, under dynamic loads, no greater incidence of a load mode is observed, because the curve of the failure criterion tends to be linear. One of the consequences of this behavior is the small amount of data that is being evaluated, leaving aside the samples that presented Bridging.

5.3 Determination of crack growth rate

The video processing allows the calculations of the crack growth rate during the time lapse in which the hammer was in contact with the MMB apparatus. To obtain the crack growth rate values, it was measured the time that takes to the crack to grow 5 mm. This data is shown in the Figure 3 for each mode of loading. Considering that in this investigation the tests were performed without maintaining the impact energy constant for all load modes, it was found that the crack growth rate is 64 times higher on pure mode II, comparing with pure mode I. It is possible to show that when the percentage of mode II is greater, the time of initiation of the crack decreases 1.3 times comparing pure mode I with pure mode II.

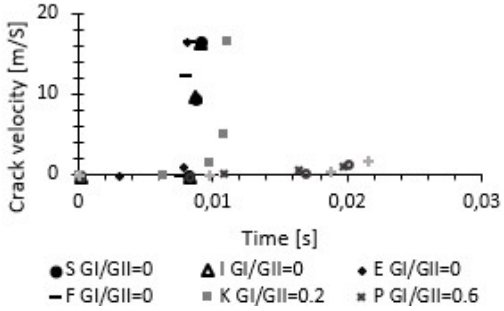

Figure 3: Crack growth rate for each load mode

6 Conclusions

Firstly, it has been shown that under dynamic impact loads the resistance to delamination of the fiberglass in mixed loading mode decreased. Same happened to the strain energy release rate on loading modes I and II, in comparison with the data obtained from [6] under quasi static loads. Secondly, the obtained data are comparable with one of the Failure Criteria to predict the delamination growth in mixed loading modes with and R^2 of 0.977. Finally, the test samples with higher G_I and G_{II} in each loading mode presented Bridging, phenomenon that cause the data dispersion. It was observed that the delamination starts early on pure loading mode II, and the starting time decreases as it approaches the loading mode I. Also, the crack growth rate is higher on a pure loading mode II and it decreases as the percentage of loading mode I rises.

References

[1] S. Mazumdar, State of the Composites Industry, *Compos. Manuf. Mag.*, p.6, 2016.

[2] A. B. De Morais, A new fibre bridging based analysis of the Double Cantilever Beam (DCB) test, *Compos. Part A Appl. Sci. Manuf.*, vol. 42, no. 10, pp. 1361-1368, 2011.

[3] L. Yao, R. Alderliesten, M. Zhao, and R. Benedictus, Bridging effect on mode i fatigue delamination behavior in composite laminates, *Compos. Part A Appl. Sci. Manuf.*, vol. 63, pp. 103 - 109, 2014.

[4] W. S. Johnson and P. D. Mangalgiri, Investigation of fiber-bridging in double cantilever specimens, *J. Compos. Technol. Res*, vol. 9, no. 1, pp. 10 - 13, 1987.

[5] R. Rikards, Interlaminar fracture behaviour of laminated composites, 2000.

[6] M. Alejandra and G. Aguilln, Delaminacin en modos combinados I/II para componentes de fibra de vidrio bajo cargas cuasi estticas: un anlisis analtico y computacional, p. 33, 2017.

[7] A. J. Smiley and R. B. Pipes, Rate Effects on Mode I Interlaminar Fracture Toughness in Composite Materials, *J. Compos. Mater.*, vol. 21, no. 7, pp. 670 - 687, Jul. 1987.

[8] P. Bguelin, M. Barbezat, and H. Kausch, Mechanical characterization of polymers and composites with a servohydraulic high-speed tensile tester, *J. Phys. III, EDP Sci.*, vol. 1, no. 3, pp. 1867 - 1880, 1991.

[9] B. R. K. Blackman et al., The failure of fibre composites and adhesively bonded fibre composites under high rates of test - Part I Mode I loading-experimental studies, *J. Mater. Sci.*, vol. 30, no. 23, pp. 5885 - 5900, 1995.

[10] B. R. K. Blackman et al., The failure of fibre composites and adhesively bonded fibre composites under high rates of test Part III Mixed-mode 1/11 and mode II Ioadings, *J. Mater. Sci.*, vol. 31, pp. 4467 - 4477, 1996.

[11] B. R. K. Blackman, A. J. Kinloch, F. S. Rodriguez-Sanchez, and W. S. Teo, The fracture behaviour of adhesively-bonded composite joints: Effects of rate of test and mode of loading, *Int. J. Solids Struct.*, vol. 49, no. 13, pp. 1434 - 1452, 2012.

[12] T. Kusaka et al., Rate Dependence Of Mode I Fracture Behaviour In Carbon-Fibre/Epoxy Composite Laminates, *Compos. Sci. Technol.*, vol. 58, 1998.

[13] V. V. S. J.P. Casas-Rodriguez, I.A. Ashcroft, Damage in adhesively bonded CFRP joints: Sinusoidal and impact-fatigue, *ELSEVIER.*, 2008.

[14] F. Lahuerta, T. Westphal, R. P. L. Nijssen, F. P. van der Meer, and L. J. Sluys, Measuring the delamination length in static and fatigue mode I tests using video image processing, *Compos. Part B Eng.*, vol. 63, pp. 1 - 7, 2014.

[15] H. J. Crews and R. J. Reeder, A Mixed-Mode Bending Apparatus For Delamination Testing, *NASA*, 1988.

[16] J. R. Reeder, A Bilinear Failure Criterion for Mixed-Mode Delamination, *Elev. Vol. Compos. Mater. Des.*, vol. 94, pp. 303 - 303 - 20, 1993.

Homogenization of Periodic Cellular Materials: An Application to Periodic Cells With Constant Density

H. Alvarez[1], H. Zambrano[2],
[1]halvarez@uninorte.edu.co
Departamento de Ingeniería Mecánica,
Universidad del Norte, Barranquilla, Colombia

[2]hzambrano@uninorte.edu.co
Departamento de Ingeniería Mecánica,
Universidad del Norte, Barranquilla, Colombia

Abstract

This work presents the homogenization procedure for periodic cellular materials for linear elastic structures under plane stress. An application example considering unit cells with a single hole with constant volume was presented. The hole geometry was generated using the genetic algorithm optimization method to fit a fourth order polynomial curve. The procedure was validated with benchmark results available in the literature for a rectangular cells with a rectangular hole. Nine different cells with constant volume were obtained and the its homogenized properties were reported to evaluate the range of mechanical properties that can be obtained using the proposed approach.

Key Words: Homogenization, cellular materials, genetic algorithm

1 Introduction

Periodic cellular materials (PCM) can be found in nature structures as bones, honeycombs, foams etc, and also can be artificially produced by different methods for several applications such as: sandwich plates cores [5] and foams for packaging materials [8, 1]. The possibility to design architected PCM, it gives us the ability to create lightweight structures [11] with outstanding tuned mechanical properties, such as materials with maximum bulk and shear modulus, negative Poisson ratio, etc.

As mentioned above cellular materials are increasingly used in many industrial applications. In order to predict the structure behaviour in macroscopic scale, it is necessary to consider a full-scale model considering the internal architecture of the cellular material. If the cellular material architecture is defined into the model geometry, then the computational cost for the model become too high. On the other hand, the cellular material architecture can be taking into account in the material constitutive model using the material properties as the homogenized values obtained from the homogenization procedure for a single unit cell. To obtain the properties of PCM it is necessary to implement some mathematical approach, in order to compute the overall material properties from a single cell, these techniques are called homogenization procedures. The problem of finding the equivalent mechanical properties for a unit cell which represents a PCM was stated by [3], this theory define the material properties in a coarse or macroscopic scale from the properties of its micro-structure or unit cell. The homogenization procedure presented by [6], considers the equations for obtaining the tensor of elastic constants by means of an asymptotic expansion, these homogenization equations are expressed as a function of the strain fields and the base material properties

using index or tensor notation, the way in which [6] state the homogenization procedure is suitable when the displacement and strain fields are computed by means of a tailored finite element code intended for this application. On the other hand [10] presents an equivalent homogenization procedure based on the element strain energy, denoting the homogenized tensor of elasticity using matrix notation, which is more readable and easy to implement, this procedure is widely used in numerical coarsening techniques in which a fine mesh with heterogeneous properties is turned into a coarse mesh with the same mechanical behaviour, this task is common in computer graphics applications. Another method to homogenize PCM was proposed by [13] who used a strain energy based method with simplified programming, to estimate the homogenized properties.

The formulations mentioned above are equivalent from the point of view of elasticity theory and mathematical homogenization, therefore the difference among these formulations only lies in its computational implementation.

2 Homogenization of periodic cellular materials

The mathematical formulations for the homogenization procedure are presented in this section.

2.1 Homogenization using index notation

Considering a representative unit cell with periodic boundary conditions, the homogenized elasticity or stiffness tensor in the domain Ω which represents the material macroscopic behavior, can be calculated as follow [7]:

$$C^H_{ijkl} = \frac{1}{|Y|}\int_\Omega C_{ijpq}\left(\bar{\varepsilon}^{kl}_{pq} - \tilde{\varepsilon}^{kl}_{pq}\right) d\Omega \tag{1}$$

Where $|Y|$ denotes the cell volume Ω. $\bar{\varepsilon}^{kl}_{pq}$ are the four three linearly independent unit strains: $\bar{\varepsilon}^{11}_{pq} = (1\ 0\ 0)^T$,$\bar{\varepsilon}^{22}_{pq} = (0\ 1\ 0)^T$ and $\bar{\varepsilon}^{12}_{pq} = (0\ 0\ 1)^T$, $\tilde{\varepsilon}^{kl}_{pq}$ is the obtained strain field for the imposed displacements in the boundary and C_{ijpq} is the stiffness for the base material.

The most intuitive way to understand the equation 1 is to re-write it in terms of element mutual energies as follow [9]:

$$C^H_{ijkl} = \frac{1}{|Y|}\int_\Omega C_{pqrs}\tilde{\varepsilon}^{ij}_{pq}\tilde{\varepsilon}^{kl}_{rs} d\Omega \tag{2}$$

2.2 Homogenization using matrix notation

Using matrix notation, the equation 2 can be written in discrete form, considering the solution obtained with the finite element method [10, 4] as:

$$\mathbb{C} = \frac{1}{Y}\sum_{i=1}^{k}\left(Y_i G_i^T : C_i : G_i\right) \tag{3}$$

Where Y_i is the volume of element i, G is the matrix of strain tensors and C is the stiffness tensor for the base material.

For each element i, the matrix G can be expanded as:

$$G_i = \begin{bmatrix} \varepsilon^{11}_{11} & \varepsilon^{22}_{11} & \varepsilon^{12}_{11} \\ \varepsilon^{11}_{22} & \varepsilon^{22}_{22} & \varepsilon^{12}_{22} \\ \varepsilon^{11}_{12} & \varepsilon^{22}_{12} & \varepsilon^{12}_{12} \end{bmatrix}_i \tag{4}$$

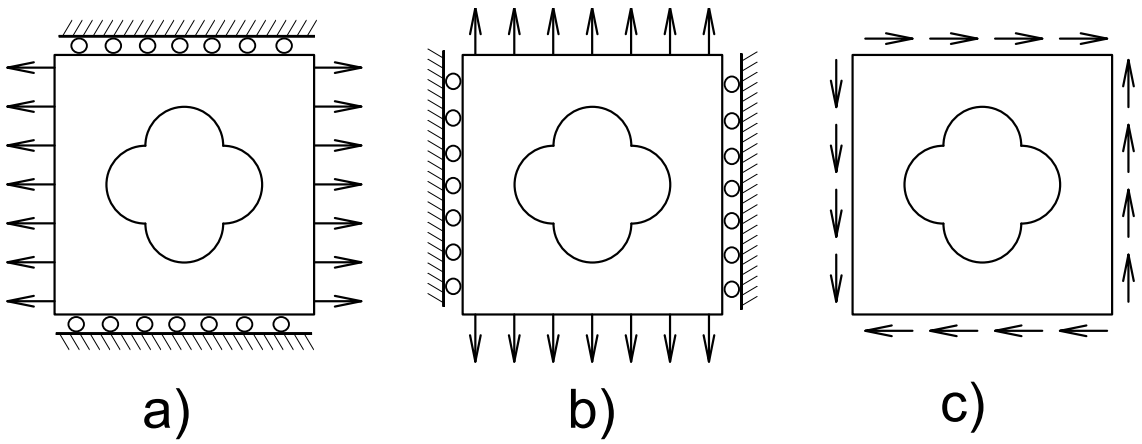

Figure 1: Load cases for the homogenization procedure for 2D problems. a) $\varepsilon^{(11)} = (1\ 0\ 0)$, b) $\varepsilon^{(22)} = (0\ 1\ 0)$, c) $\varepsilon^{(12)} = (0\ 0\ 1)$

Where the three columns of G_i are the strain tensors for the modes a, b and c shown in the figure 1 for the element i. Considering an isotropic elastic base material under plane stress condition, the tensor C can be written as:

$$C_i = \frac{E}{1-\nu^2}\begin{bmatrix} 1 & \nu & 0 \\ \nu & 1 & 0 \\ 0 & 0 & \frac{1-\nu}{2} \end{bmatrix}_i \tag{5}$$

Where E and ν are the elastic and Poisson modulus respectively.

2.3 Elastic problem solution

In order to compute the homogenized stiffness tensor described in the sub-sections above it is necessary to obtain a set of representative displacements for different load cases. These displacements are named *harmonic displacements* $\mathbf{u}_{ab}$ and are the solution of the following boundary value problem [4].

$$\begin{aligned} &\nabla \cdot \sigma(\mathbf{u}_{ab}) = 0 && \text{on } \Omega \\ &\sigma(\mathbf{u}_{ab}) \cdot \mathbf{n} = \frac{1}{2}\left(\mathbf{e}_a\mathbf{e}_b^T + \mathbf{e}_b\mathbf{e}_a^T\right) \cdot \mathbf{n} && \text{on } \partial\Omega \end{aligned} \tag{6}$$

Where $\mathbf{e}_a$ is the unit vector along the $a-th$ direction, $\frac{1}{2}\left(\mathbf{e}_a\mathbf{e}_b^T + \mathbf{e}_b\mathbf{e}_a^T\right)$ are the tractions on the boundary $\partial\Omega$, and $\mathbf{n}$ is the unit vector normal to the boundary.

The problem in equation 6 represents the plane stress formulation with periodic boundary conditions. For 2D problems there are three different harmonic displacements (cases a, b and c) as shown in figure 1.

2.4 Periodic boundary conditions

The plane stress problem described in equation 6 have to be solved using periodic boundary conditions in order to obtain the strain field $\tilde{\varepsilon}_{pq}^{ij}$. If it is considered a periodic displacement field, under a given strain, then $\bar{\varepsilon}_{pq}^{ij}$ can be computed as the sum of a macroscopic displacement field and a periodic field $\tilde{u}_p$ [9] as:

$$u_p = \bar{\varepsilon}_{pq}^{ij} y_q + \tilde{u}_p \tag{7}$$

Where y_q is the cell's length in the direction q. Considering the cell depicted in figure 2, the displacements on the opposite boundaries are defined by:

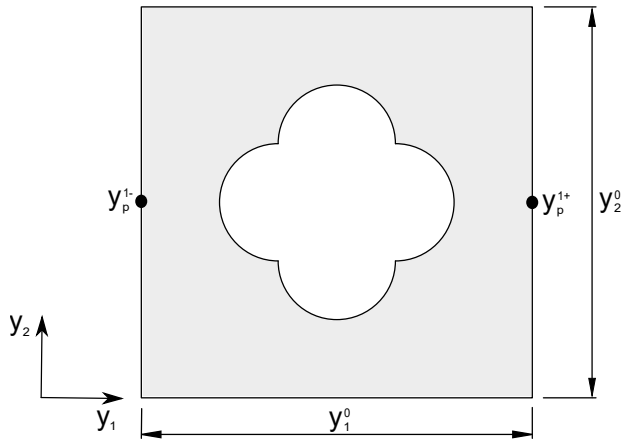

Figure 2: Periodic cell

$$\begin{aligned} u_p^{k+} &= \bar{\varepsilon}_{pq}^{ij} y_q^{k+} + \tilde{u}_p \\ u_p^{k-} &= \bar{\varepsilon}_{pq}^{ij} y_q^{k-} + \tilde{u}_p \end{aligned} \tag{8}$$

Where superscripts "$k+$" and "$k-$" define two pair of opposite parallel boundary surfaces. Eliminating $\tilde{u}_p$ from equation 8 is obtained the following periodic boundary condition:

$$u_p^{k+} - u_p^{k-} = \bar{\varepsilon}_{pq}^{ij} \Delta y_q^k \tag{9}$$

This condition relates the displacements in the cell opposite faces , in such a way that simulates an infinite mount of adjacent material surrounding the cell under consideration.

Once obtained the plane stress problem solution under periodic boundary conditions, the homogenization procedure described in the equation 3 can be easily implemented in the Python interpreter of the commercial finite element software Abaqus® as described in Appendix A

2.5 Model verification

The homogenization problem was solved into the commercial finite element software Abaqus®, the plane stress solution was obtained using 'CPS4R' quadrilateral elements, the periodic boundary conditions were applied using the command `*Equation` as defined in [12]. To satisfies the equation 9, the nodes pairing for the left/right and top/bottom boundaries was completed using a Python subroutine for the sets generation.The homogenized stiffness tensor described in equation 3 was obtained with a Python subroutine reading the strain field solution for each load case described in the figure 1 and computing it summation over the cell. The obtained results with the homogenization procedure implemented in this work was compared with a benchmark problem reported in [2]. The problem consist on a 100×100 square cell with a central rectangular hole of 40×60, the base material is characterized by $C_{1111} = C_{2222} = 30$ and $E_{1122} = E_{1212} = 10$. The comparison between the results reported by [2] and the values calculated with the equation 3, are summarized in the table1.

2.6 Application case

It is required to find a family of orthotropic materials with different mechanical properties and the same global density. In order to obtain the desired set of cellular materials, the internal hole of the cell is considered to

Table 1: Results comparison for the homogenized coefficients

	Mesh	C_{1111}	C_{1122}	C_{2222}	C_{1212}
M.Bendsøe [2]	Init	13.015	3.241	17.552	2.785
	1st Adap	12.910	3.178	17.473	2.714
	2nd Adap	12.865	3.146	17.437	2.683
	3rd Adap	12.844	3.131	17.421	2.668
Equation 3	540 Elem	13.057	2.986	17.622	2.632
	1279 Elem	13.037	3.011	17.617	2.612
	2520 Elem	13.042	3.032	17.624	2.613
	5212 Elem	13.042	3.045	17.627	2.613

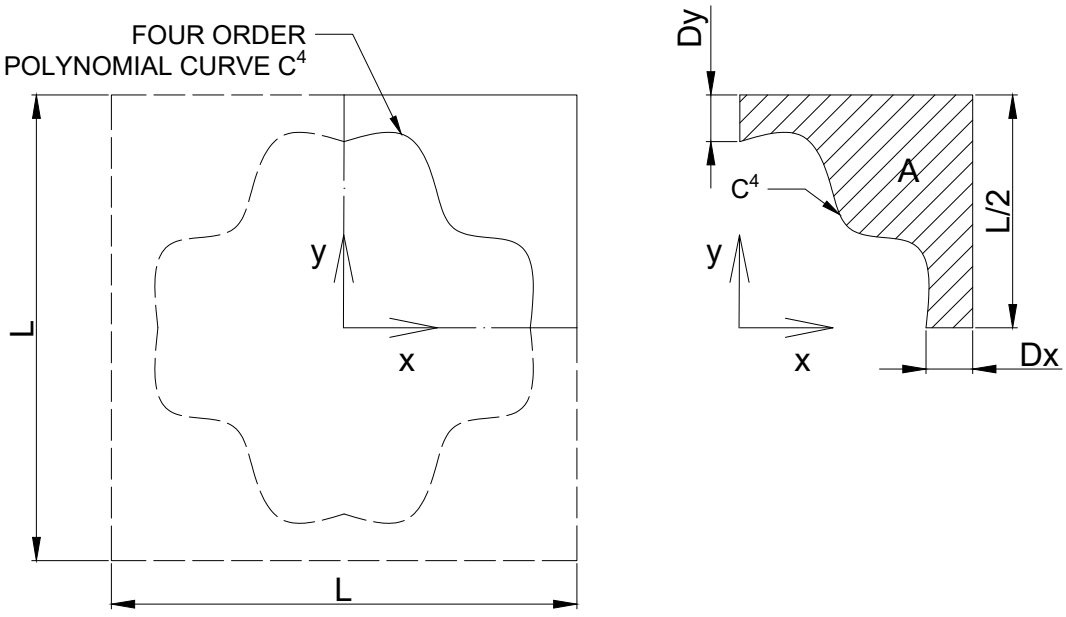

Figure 3: resulting unit cell, with a hole defined by a polynomial curve

be formed by a four order polynomial curve denoted as C^4 as shown in the figure 3. to obtain orthotropic behaviour, the cell is required to be one quarter symmetrical. The general form of a four order polynomial is given by:

$$y = ax^4 + bx^3 + cx^2 + dx + e \tag{10}$$

Where the coefficients a, b, c, d, e are the unknowns parameters such that, the area under the curve C^4 is a constant A. The area A is given by the integral:

$$\begin{aligned} A &= \int_0^{L/2-Dx} (ax^4 + bx^3 + cx^2 + dx + e)dx \\ A &= \frac{a(0.5L - Dx)^5}{5} + \frac{b(0.5L - Dx)^4}{4} + \frac{c(0.5L - Dx)^3}{3} + \\ &\quad \frac{d(0.5L - Dx)^2}{2} + e(0.5L - Dx) \end{aligned} \tag{11}$$

Considering five arbitrary points $P_1(x_1, y_1), \ldots, P_5(x_5, y_5)$ on the curve, a system of equations expressed in

matrix form can be obtained as follow:

$$\begin{bmatrix} x_1^4 & x_1^3 & x_1^2 & x_1 & 1 \\ x_2^4 & x_2^3 & x_2^2 & x_2 & 1 \\ x_3^4 & x_3^3 & x_3^2 & x_3 & 1 \\ x_4^4 & x_4^3 & x_4^2 & x_4 & 1 \\ x_5^4 & x_5^3 & x_5^2 & x_5 & 1 \end{bmatrix} \begin{Bmatrix} a \\ b \\ c \\ d \\ e \end{Bmatrix} = \begin{Bmatrix} y_1 \\ y_2 \\ y_3 \\ y_4 \\ y_5 \end{Bmatrix} \tag{12}$$

Then, the coefficients a, b, c, d, e can be obtained using a linear solver for the system of equations above. Therefore the problem consist to find a set of points $P_1(x_1, y_1), \ldots, P_5(x_5, y_5)$ such that the area under the curve is a constant A.
Considering the required area as $\tilde{A}$, the optimization problem can be stated as follow:

$$\begin{aligned} \underset{x_i, y_i}{\text{minimize}} \quad & |\tilde{A} - A(x_i, y_i)| \\ \text{subject to} \quad & 0.5L \geq x_i, y_i \geq 0 \end{aligned} \tag{13}$$

As can be observed the optimization problem above has no unique solution for the design variable $P_i(x_i, y_i)$, therefore, the set of feasible solutions represent a cellular materials family with the same global density and different mechanical properties.

2.6.1 Genetic Algorithm

In this work, is used a real-coded genetic algorithm (GA) approximation in order to find a set of solutions for the points $P_i(x_i, y_i)$ to solve the problem described in equation 13.

The initial population is represented by the points P_i^1 (The superscript of P_i represent the generation j) defined as 100 individuals generated with an uniform probability distribution $P_i^1 \sim U(0, 0.5L)$. The generation j of the population P_i^j consist of: 40 mutated individuals generated with a mutation operator as a multiplier $\gamma \sim N(1, 0.2)$ defined with a normal probability distribution with mean 1 and standard deviation 0.2, $P_{1:40}^j = \gamma P_{1:40}^1$ (The notation $1:40$ for the subindex i represent a range of 40 individuals), an offspring of 30 individuals defined with a crossover operation such that $P_{41}^j = 0.5(P_1^{j-1} + P_n^{j-1})$, $P_{42}^j = 0.5(P_2^{j-1} + P_{n-1}^{j-1}) \ldots P_m^j = 0.5(P_m^{j-1} + P_{n-m}^{j-1})$, where n is the total number of individuals in the population and m is the index for the current crossed individual, and 30 new individuals generated with an uniform probability distribution.

The fitness function implemented to evaluate how close a given solution is to the optimum solution, is considered as the magnitude $F_I = |\tilde{A} - A(x_i, y_i)|$, therefore the population P_i^j have to be sorted in ascending order of F_I to ensure that the first individuals have the best fitness value. The implemented genetic algorithm can be represented in pseudocode as follow, the comment lines are specified with the # character:

```
#cont: Counter
#NOC: Number of cell to be generated
#POP: Numbers of individuals in the population

START
Define initial population P^1_{1:100} ~ U(0, 0.5L)
cont = 0
WHILE cont < NOC
cont  = cont + 1
- compute coefficients a,b,c,d,e #for all POP
- Compute cell area A
- evaluate the fitness as F_I = |Ã - A(x_i, y_i)|
- Sort the population acccording the best fitness value
- Apply mutation operator P^j_{1:40} = γ P^1_{1:40}
- Apply crossover operator P^j_m = 0.5(P^{j-1}_m + P^{j-1}_{n-m})
```

Table 2: Computed values for the stiffness tensor for every cell

Cell	C_{1111}	C_{1122}	C_{2222}	C_{1212}	Vol
1	5.480	0.965	9.813	0.441	4999.860
2	6.310	0.658	7.055	0.245	5000.271
3	8.473	1.027	7.834	0.625	5000.091
4	5.259	0.771	8.631	0.222	4999.910
5	8.639	1.238	8.463	0.877	5000.362
6	7.145	0.974	8.106	0.767	5000.143
7	5.399	0.929	9.753	0.361	5000.073
8	8.352	1.282	8.828	0.882	5000.239
9	7.175	1.097	8.561	0.879	5000.212

```
– Complete the population with new random individuals
– Check and save the feasible solution until cont < NOC
END
FINISH
```

The iteration process is stopped when the algorithm finds a solution for the required area $\tilde{A}$ and its repeated with different start solutions in order to obtain unit cells with different shapes. Not all the obtained solutions are feasible, the unfeasible solutions are the curves which intercept itself or the cell's boundaries. The feasible solutions obtained with the proposed genetic algorithm are shown in the figure 4, and the results obtained with the homogenization code for the homogenized stiffness tensor are summarized in the table 2 for nine different unit cells. As can be observed in the table 2 each cell exhibit its own mechanical behaviour with peak values for specific components of the stiffness tensor.

3 Conclusions

The homogenization procedures for periodic cellular materials were presented and implemented, the obtained results were compared with a benchmark solution available in the literature in order to validate the code, obtaining good agreement with the reference solutions. Different cell geometries were created as a square cell with a central hole generated with a fourth order polynomial curve and genetic algorithm optimization procedure, this methodology allowed to obtain a set of cells with the same global density and different stiffness tensor. In further works this methodology can be used to implement inverse homogenization procedures in which given an stiffness tensor is obtained the cell shape with the desired properties, This can be achieved using cells with multiple holes and defining the holes with high order polynomials or spline curves.

4 Acknowledgement

Author are grateful to the Research Office of Universidad del Norte for supporting this research work on computational homogenization.

5 Appendix A (Python Code for Homogenization)

```
#Load Python libraries
#-----------
from odbAccess import *
from abaqusConstants import *
import visualization
import numpy as np
#----------------Open Odb solution files for all load cases
odb1 = openOdb('FModel1.odb') # Solution for load case a)
```

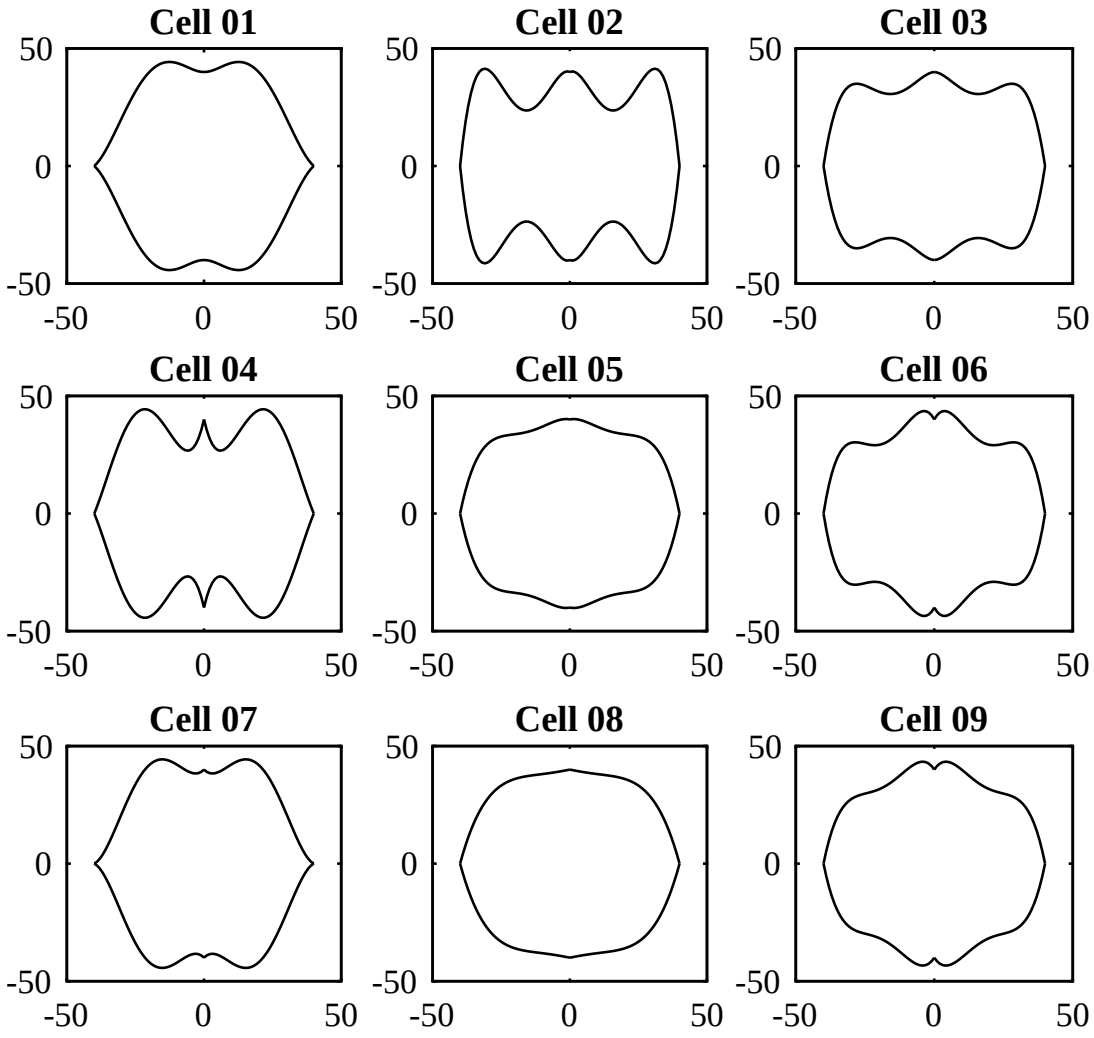

Figure 4: 100×100 unit cells with a hole of one half of total area, obtained with the GA algorithm

```
odb2 = openOdb('FModel2.odb') # Solution for load case b)
odb3 = openOdb('FModel3.odb') # Solution for load case c)
# Element volume
ELVOL = odb1.steps['Step-apply-constraint'].frames[-1].fieldOutputs['EVOL'].values
#Strain Tensor solution for all load cases
#-------------------------------------------------
E_M1 = odb1.steps['Step-apply-constraint'].frames[-1].fieldOutputs['E'].values
E_M2 = odb2.steps['Step-apply-constraint'].frames[-1].fieldOutputs['E'].values
E_M3 = odb3.steps['Step-apply-constraint'].frames[-1].fieldOutputs['E'].values
#-------------------------------------------------
CELLVOL = 100.0*100.0 #Cell Volume
NUMEL = len(E_M1)     #Number of elements
Gi = np.zeros((3,3))  #Initialize strain matrices
G = np.zeros((3,3))   #Initialize strain matrices for summation
#-------------------------------
C = np.zeros((3,3))  #Initialice Stiffness matrix
#--------Define material properties from model---------
E = 26.6667
nu = 0.333
GMOD = E/(2*(1+nu))
#--------------Stiffness matrix plane stress-----------------
C[0,0] = E/(1.-nu**2)
C[0,1] = nu*E/(1.-nu**2)
#-----------------------
C[1,0] = nu*E/(1.-nu**2)
C[1,1] = E/(1.-nu**2)
#-----------------------
C[2,2] = GMOD
#-----------------------
TVOL = 0. #Initialize volume counter
for i in xrange(0, NUMEL):
#---------------------------------
STRAIN_E11_M1 = E_M1[i].data[0]
STRAIN_E22_M1 = E_M1[i].data[1]
STRAIN_E12_M1 = E_M1[i].data[3]
# #-------------------------------
STRAIN_E11_M2 = E_M2[i].data[0]
STRAIN_E22_M2 = E_M2[i].data[1]
STRAIN_E12_M2 = E_M2[i].data[3]
# #-------------------------------
STRAIN_E11_M3 = E_M3[i].data[0]
STRAIN_E22_M3 = E_M3[i].data[1]
STRAIN_E12_M3 = E_M3[i].data[3]
#-------------------------------
Gi = np.array([[STRAIN_E11_M1, STRAIN_E11_M2, STRAIN_E11_M3],
[STRAIN_E22_M1, STRAIN_E22_M2, STRAIN_E22_M3],
[STRAIN_E12_M1, STRAIN_E12_M2, STRAIN_E12_M3]])
G = G + ELVOL[i].data*np.dot(np.dot(np.transpose(Gi),C),Gi)
#---------Total Cell Volume---
TVOL  = TVOL + ELVOL[i].data
#-----------------------
SUM_GCG = G*(1/CELLVOL)
np.savetxt('test.out',SUM_GCG, delimiter=' ') #Save homogenized stiffness tensor
```

References

[1] C. Barbier, P.M. Michaud, D. Baillis, J. Randrianalisoa, and A. Combescure. New laws for the tension/compression properties of voronoi closed-cell polymer foams in relation to their microstructure. *European Journal of Mechanics - A/Solids*, 45:110–122, 2014.

[2] Martin Philip. Bendsoe and Noboru. Kikuchi. Generating optimal topologies in structural design using a homogenization method. *Computer Methods in Applied Mechanics and Engineering*, 71(2):197–224, 1988.

[3] Alain Bensoussan, Jacques Louis Lions, and George Papanicolaou. *Introduction*, volume 5 of *Studies in Mathematics and Its Applications*. Elsevier, 1978.

[4] Schumacher. Christian, Bickel. Bernd, Rys. Jan, Marschner. Steve, Daraio. Chiara, and Gross. Markus. Microstructures to control elasticity in 3d printing. *ACM Trans. Graph.*, 34(4):1–13, 2015.

[5] Kumar P. Dharmasena, Zhenyu Xue, and John W. Hutchinson. Mechanical response of metallic honeycomb sandwich panel structures to high-intensity dynamic loading. *International Journal of Impact Engineering - INT J IMPACT ENG*, 35:1063–1074, 2008.

[6] B. Hassani and E. Hinton. A review of homogenization and topology optimization i: homogenization theory for media with periodic structure. *Computers and Structures*, 69(6):707–717, 1998.

[7] X. Huang, A. Radman, and Y.M. Xie. Topological design of microstructures of cellular materials for maximum bulk or shear modulus. *Computational Materials Science*, 50(6):1861–1870, 2011.

[8] Zhiqiang Li, Jianjun Zhang, Jianhui Fan, Zhihua Wang, and Longmao Zhao. On crushing response of the three-dimensional closed-cell foam based on voronoi model. *Mechanics of Materials*, 68:85–94, 2014.

[9] Xia. Liang and Breitkopf. Piotr. Design of materials using topology optimization and energy-based homogenization approach in matlab. *Structural and Multidisciplinary Optimization*, 52(6):1229–1241, 2015.

[10] Kharevych. Lily, Mullen. Patrick, Owhadi. Houman, and Desbrun. Mathieu. Numerical coarsening of inhomogeneous elastic materials. *ACM Trans. Graph.*, 28(3):1–8, 2009.

[11] Konstantinos Daniel Tsavdaridis, James J. Kingman, and Vassilli V. Toropov. Application of structural topology optimisation to perforated steel beams. *Computers and Structures*, 158:108–123, 2015.

[12] Weidong. Wu and Joseph. Owino. Applying periodic boundary conditions in finite element analysis. In *Simulia Community Conference*, pages 707–719, 2014.

[13] Weihong Zhang, Fengwen Wang, Gaoming Dai, and Shiping Sun. Topology optimal design of material microstructures using strain energy-based method. *Chinese Journal of Aeronautics*, 20(4):320–326, 2007.

Element Free Galerkin Like Truly Meshless Method With Cartesian Transformation Integration Method

J.A. Martinez-Trespalacios[12], E.A Arrieta-Ortiz[1]

[1]jmartinezt@utb.edu.co
Departamento de Ingeniería Mecánica,
Universidad Tecnológica de Bolívar, Cartagena, Colombia

[2]Facultad de diseño e ingeniería
Fundacíon Tecnológica de Bolívar, Cartagena, Colombia

Abstract

This work proposes the element Free Galerkin (EFG) like a really truly meshless method, thank to use at cartesian transformation method (CTM) to integration in the domain. It's techniques can be applied with irregular domains with holes, leaving aside the traditional approach integrate with background cells. In order to demonstrate the capability of EFG with CTM to solve two-dimensional static structural analysis, numerical examples are presented and results compared with traditional approach with background mesh.

Key Words: Truly meshless, Element free Galerkin method, Gauss quadrature scheme

1 Introduction

With computers development, engineering simulations have gained great importance in the day to day of the engineer. Currently, talking about simulations in engineering is not possible without mentioning the finite element method (FEM), and this thanks to its great versatility [14], ease of implementation and robustness becomes the main ally of all CAD/CAE/CAM applications of the market. However, FEM has some difficulties when trying to solve problems with large deformations, problems of fluid mechanics, problems of optimizations, among others, and this by the need to require a mesh to simulate the domain under study.

In this field, the so-called meshless methods emerge, which make it possible to eliminate the arduous task of meshing a domain, or at least pose strategies that facilitate such work, to achieve a reliable approach. As an example of these methods, it is possible to highlight the Boundary elements method (BEM) [15], the extended finite element method (X-FEM)[16], the methods based on the MLS functions [17, 18, 19], among others. Of these methods, the element Free Galerin method stands out, due to the precision of its results and because it has been tested in different scenarios, demonstrating to exceed in precision at FEM.

Currently, a new term is added in numerical simulations area, which refers to the truly meshless methods, referring to methods that do not require meshes or to achieve the approximation, nor to solve the integrals product of the development of the method . EFG in its initial approach requires some bouckgrand cells not allowing this to be a truly meshless method [8].

The present work seeks to pose the EFG like a truly meshless method, through a Cartesian integration scheme , with easy implementation and even more reliable results than those achieved with the traditional

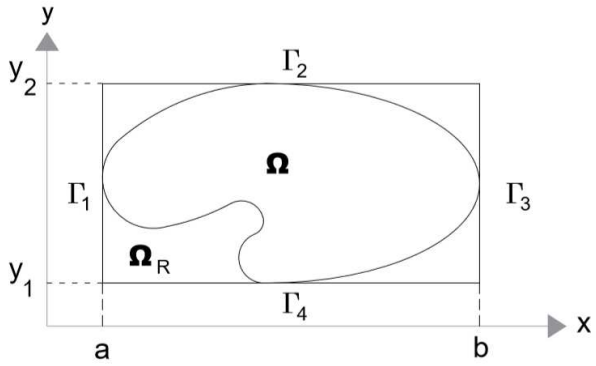

Figure 1: Auxiliary domain Ω_R and main domain of problem Ω.

approach without the need to sacrifice computing time.

2 Cartesian transformation method

To continue, the Cartesian integration method presented by A. Khosravifard and M. Rahim H in [2] will be shown. The following domain integral is to be computed.

$$I = \int_{\Omega} f(x,y)\, d\Omega \tag{1}$$

Suppose that the integral domain (Ω) is contained for a simple domain Ω_R, such as circle, triangle or rectangle, see Fig. 1. Ω_R is called auxiliar domain, and it will be necessary to define a new function in Ω_R:

$$h(x) = \begin{cases} f(x,y) & (x,y) \in \Omega \\ 0 & (x,y) \notin \Omega \end{cases} \tag{2}$$

Rewriting Eq. 25:

$$I = \int_{\Omega} f(x,y)\, d\Omega = \int_{\Omega_R} h(x,y)\, d\Omega_R \tag{3}$$

Remembering Green's theorem, which is possible to apply to convert a domain integral to a contour integral [7]. If Ω and Γ are the domain and boundary, respectively, Green's theorem can be expressed as follows:

$$I = \int_{\Omega} \frac{\partial u(x,y)}{\partial x}\, d\Omega = \int_{\Gamma} u(x,y)\, dy \tag{4}$$

if $h(x,y) = \partial u(x,y)/\partial x$, then Green's theorem can be applied as follows:

$$I = \int_{\Omega_R} h(x,y)\, d\Omega_R = \int_{\Gamma_R} \left(\int_c^x h(\xi,y)\, d\xi \right) dy \tag{5}$$

Where c is an arbitrary constant. It can be observed that the original domain integral is transformed into a double integral (A boundary integral and a 1D integral), a proper double auxiliary domain must be

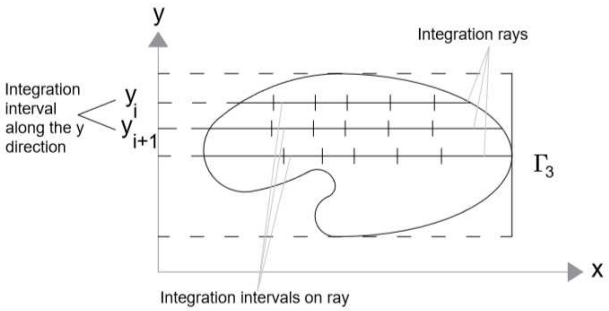

Figure 2: Integration ray and intervals.

selected. Hematiyan [2] propose to use rectangular auxiliary domain for to obtain fourth boundary portions, as follows:

$$\Gamma_1 : y = y_1, \quad \Gamma_2 : x = b, \quad \Gamma_3 : y = y_2, \quad \Gamma_4 : x = a \tag{6}$$

For the evaluation of the outer integral of Eq. 5, if the arbitrary constant c is set equal to a (See 1), the integrals on the boundaries Γ_1, Γ_2 and Γ_4 are vanishes an it need to be evaluated only on Γ_3, for more details see [2]. Therefore, the integral in Eq.5 can be rewritten in the following form:

$$I = \int_{y_1}^{y_2} \left(\int_a^b h(x, y)\, dx \right) dy \tag{7}$$

As can be seen, the domain integral in Eq. 25 has been written as two 1D integrals, the outer and inner integral of Eq. 7. To evaluated the integrals we make use of the composite Gaussian quadrature method. Considering:

$$g(y) = \int_a^b h(x, y)\, dx \tag{8}$$

Then,

$$I = \int_{y_1}^{y_2} g(y)\, dy \tag{9}$$

First is necessary to evaluated integral of Eq. 10, and for this we must divide the boundary Γ_3 into n integration intervals and m-point Gaussian quadrature method can the be applied to each individual interval, as follows:

$$I = \sum_{i=1}^{n} \sum_{j=1}^{m} J_y w_j g(y(\eta_j)) \tag{10}$$

Where, η_j and w_j are the Gaussian points and weights, respectively, for numerical integration. J_y is the Jacobian of the transformation. The line $y = y(\eta_j)$ is called the integration ray (See Fig. 2) and represents a horizontal line. To compute the value of $g(y)$ this must be calculated for each ray in each integration points along the boundary Γ_3, and each rays is divided into several integration intervals, depending of desired

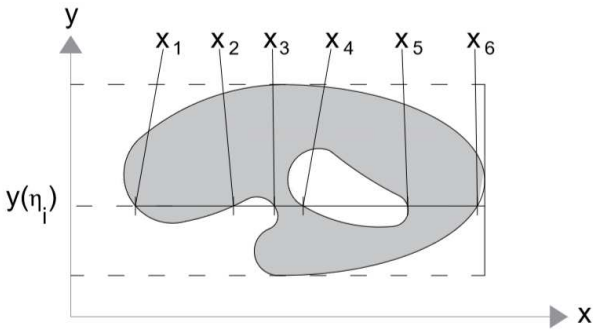

Figure 3: Interval ray into the domain.

accuracy (See Fig. 2). When ray intersected with boundary, this interval is eliminated and just interval ray into the domain will be divided. the integral in Eq. 8 can be write as follows:

$$g(y_i) = \int_{x_1}^{x_2} f(x, y_i)\, dx + \int_{x_2}^{x_3} f(x, y_i)\, dx ... \int_{x_{l-1}}^{x_l} f(x, y_i)\, dx \tag{11}$$

$$g(y_i) = \sum_{j=1}^{l} \left(\int_{x_1}^{x_{l+1}} f(x, y_i) dx \right) \tag{12}$$

Finally, solving Eq. 12 using composite Gaussian quadrature method in each interval rays of each integration interval the answer of Eq. 25 is:

$$I = \sum_{j=1}^{n_y} \left(\sum_{i=1}^{n_{xj}} J_y J_{xi} f \left(\frac{b-a}{2} x_{ji} + \frac{a+b}{2}, \frac{y_2 - y_1}{2} y_j + \frac{y_2 + y_1}{2} \right) w_i \right) w_j \tag{13}$$

Where, n_{xj} is the number of Gaussian points in the integration ray with $y = y_j$, where y_i is a y-coordinate Gaussian point in a interval between y_1 and y_2, x_{ji} is a x-coordinate Gaussian points into a interval of ray with $y = y_j$ and n_y is the total number of Gaussian points between y_1 and y_2, which is equal to the total integration rays in the domain.

3 Element-free Galerkin Method

3.1 MLS approximattion

The EFG is based in Moving last square function (MLS), it's was presented by Lancaster ans Salkauskas [1], is used to find a functoin that fits a discrete set of data. In the MLS method, it's possible to approximate a $u(x)$ function in the domain Ω using:

$$u^h(x) = \sum_{i=1}^{n} \phi_i(X) u_i \tag{14}$$

Where, u_i is the nodal parameter of the function at approximated $(u(x))$ at node i and $\phi_i(x)$ is the MLS shape function corresponding to the node i, defined by:

$$\phi_i(x) = \sum_{j=1}^{m} p_j(x)(A^{-1}(x)B(x))_{ji} = P^T(A^{-1}(x)B(x))_i \tag{15}$$

Where $P(x)^T = [p_1(x) \quad p_2(x) \quad p_3(x) \ldots p_m x)]$ is functions created from polynomial bases, defined in a node j, with m equal to the number of terms that will depend on the degree of the polynomial constructed with the pascal triangle.

$A(x)$ and $B(x)$ are expressed as follows:

$$A(x) = P^T(x)W(x - x_i)P(x) \tag{16}$$

$$B(x) = P^T(x)W(x - x_i) \tag{17}$$

where $W(x - x_i)$ is a diagonal matrix of weight functions. In this paper, we used the quadratic spline function as:

$$W(x - x_i) = \begin{cases} 1 - 6r_i^2 + 8r_i^3 - 3r_i^4 & r_i \leq 1 \\ 0 & r_i > 1 \end{cases} \tag{18}$$

Where $r = d_i/d$ with d_i distance between x and the node of support domain i and d is the dimension of the support domain.

3.2 EFG formulation

The discretized system in Eq.19 is obtained by solving a two dimensional elastostatic problem using a Galerkin weak form [8].

$$[K + K^\alpha]U = F + F^\alpha \tag{19}$$

In which

$$K_{ij} = \int_\Omega (L\Phi_i)^T D(L\Phi_j)\, d\Omega \tag{20}$$

$$K_{ij}^\alpha = \int_\Omega (L\Phi_i)^T \alpha(L\Phi_j)\, d\Omega \tag{21}$$

$$F_i = \int_{\Gamma_t} \Phi_i \bar{t}\, d\Gamma + \int_\Omega \Phi_i b\, d\Omega \tag{22}$$

$$F_i^\alpha = \int_{\Gamma_t} \Phi_i^T \alpha \bar{u}\, d\Gamma \tag{23}$$

Where $\bar{t}$, D, b and α are specified traction vector, matrix of elastic constants, body force vector, and diagonal matrix of penalty factor respectively. The matrix L is the divergece operator defined as follows:

$$L = \begin{bmatrix} \partial/\partial x & 0 \\ 0 & \partial/\partial y \\ \partial/\partial y & \partial/\partial x \end{bmatrix} \tag{24}$$

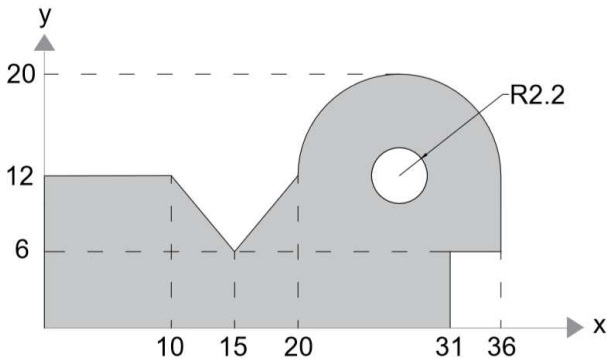

Figure 4: Integration domain, case 1.

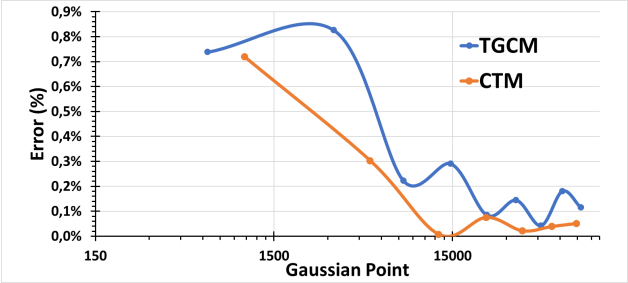

Figure 5: Comparison of CTM and GBM, case 1.

4 Numerical examples

To demonstrate the advantages of the CTM, the processing times and the convergence to the traditional approach background mesh will be compared. To simulate the conventional Gaussian quadrature method [11] with a background cell, a mesh will be created in limited by the maximum and minimum points of the domain, then the cells that are outside the domain will be deleted, The remaining cells will contain the Gaussian points and the points that are outside the domain (Because they are contained in cells that intercept the boundary) will have a zero weight ($w = 0$).

For the analysis of cases the codes have been developed in Scilab, and this was run on a system with an Intel ®Core^{TM}i7-4700MQ processor and 8.00 GB of RAM. In all cases, 8- point GAussian quadrature method is employed.

4.1 Case 1: Calculation of irregular area

In the first case, Irregular figure area will be calculated using integrals. In other words, an empty integral will be calculated throughout the domain shown in the Fig.4, this in order to demonstrate the way an area is approximated from the CTM compared to the traditional approach.

Fig.5 shows the errors reached compared to the Gaussian points used to achieve the approximation, from the graph it is possible to affirm that the traditional Gaussian quadrature approach with background mesh (TGCM) requires more integrand evaluations to achieve stability. Fig. 6 shows how for the traditional approach requires a greater computational resource (greater processing times), this due to the difficulties involved in making the mesh (Determine which cells and nodes are outside the domain).

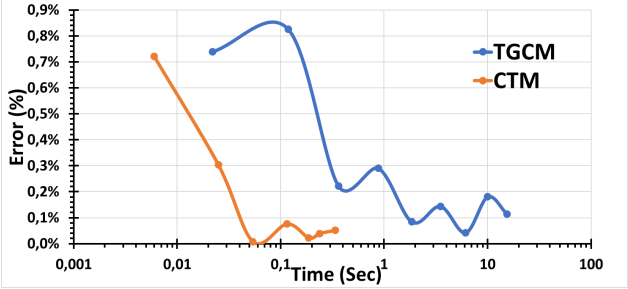

Figure 6: CPU time comparison of CTM and GBM, case 1.

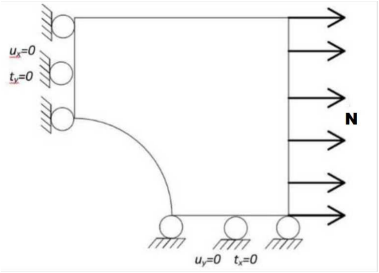

Figure 7: Plate with hole, case 2.

4.2 Case 2: Plate with hole

In this case, a plate with hole as shown in the Fig.7 will be analyzed, the mechanical properties was used are loading (integration of the distributed traction) $P = 100$ MN, Youngs modulus : $E = 211$ GPa, Poissons ratio : $\upsilon = 0.3$, its height : $D = 0.8$ m, its length : $L = 0.4$ m, its ratio $r = 0.05$ m and a unit thicknes. Eq. 25, 26 and 27 are the analytical model of the stesses presented for Timoshenko and Goodier [10] to an infinite plate with a hole in the center.

$$\sigma_x = N_x \left[1 - \vartheta \left(\frac{3cos(2\theta)}{2} + cos(4\theta) \right) + \frac{3\vartheta^2 cos(4\theta)}{2} \right] \tag{25}$$

$$\sigma_y = N_x \left[-\vartheta \left(\frac{3cos(2\theta)}{2} - cos(4\theta) \right) - \frac{3\vartheta^2 cos(4\theta)}{2} \right] \tag{26}$$

$$\tau = N_x \left[-\vartheta \left(\frac{3sin(2\theta)}{2} + sin(4\theta) \right) + \frac{3(\vartheta^2) sin(4\theta)}{2} \right] \tag{27}$$

The plate with hole was modeled with a uniform grid of 30 x 20 nodes, for the approximation functions $(p(x))$, see Eq.15 , first-order polynomial functions were used by facility [9], for the weight functions the shown in Eq. 18 was used.

The error Will be calculated using energy norm, for being the most used in elasticity [3, 4, 5]. Energy norm will be calculated as follow:

$$\epsilon_{\%} = \frac{\left(\int (\sigma_{exac} - \sigma_{efg}) D^{-1} (\sigma_{exac} - \sigma_{efg}) dA \right)^{1/2}}{\int \sigma_{exac} dA} \tag{28}$$

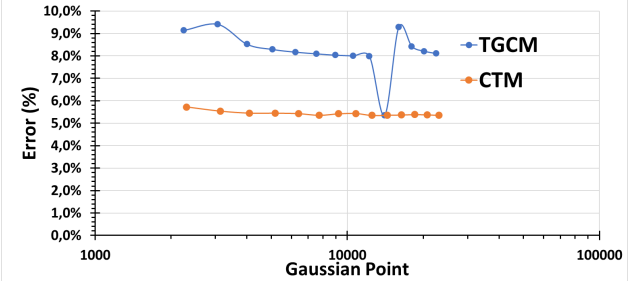

Figure 8: Error comparison of CTM and GBM, case 2.

Fig. 8 shows the errors reached by CTM and TGCM from the variation of the number of Gaussian points. Also, Fig 8 shows that EFG with CTM is stabilized at approximately 5.3 %, while EFG with TCM stabilizes at about 8.2 %, thus demonstrating that with the CTM it is possible to obtain better results.

5 Conclusions

A novel integration scheme has been presented, in which it is possible to convert a domain integral as two 1D integral, which when solved with numerical methods such as Gaussian quadrature allows to get rid of the integration mesh and use integration rays, allowing to obtain a meshfree integration method. Thanks to the CTM it is possible to convert the EFG into a truly meshless method since that does not require mesh to perform the approximation or to solve the resulting integrals. It showed the advantages in terms of implementation, processing time and precision presented by the CTM compared to the traditional approach. This is shown in the simplest possible case (calculation of irregular area) and in a specific case of the elasticity where the EFG is already used as a truly meshless method. For future work it is recommended to study other parameters of the EFG method already seen as a truly meshless method in more complex applications, and thus to generate a recipe for how it can be applied to different engineering problems.

6 Acknowledgement

Author is grateful to the Sergio Rivera and Edgardo Arrieta engineer for depositing their trust and unconditional support.

References

[1] Lancaster, Peter and Salkauskas, Kes A sSurfaces generated by moving least squares methods. *Mathematics of computation* **37**:141-158, 1981.

[2] Khosravifard, Amir and Hematiyan, Mohammad Rahim. A new method for meshless integration in 2D and 3D Galerkin meshfree methods. Engineering Analysis with Boundary Elements, **34**(1): 30-40, 2010.

[3] Luis, Jorge and Ochoa, Restrepo. Error en la solución de problemas de elasticidad con el método de los elementos finitos. Revista Universidad EAFIT, **34**(111): 107-118, 1998.

[4] Falcón, Santiago and Gavete, Luis. Condiciones de contorno esenciales en un método sin malla. Un indicador del erro Revista internacional de métodos numérico, 2001.

[5] Belytschko, Ted, Yun Yun Lu, and Lei Gu. Element-free Galerkin methods. International journal for numerical methods in engineering, **37**(2): 229-256, 1994.

[6] Mhamed, M., & Idir, B. Applying Element Free Galerkin Method on Beam and Plate. International Journal of Chemical, **10**: 627-635, 2016.

[7] Lai, W. M., Rubin, D. H., Krempl, E., & Rubin, D. Introduction to continuum mechanics. Butterworth-Heinemann.2009.

[8] Liu, Gui-Rong and Gu, Yuan-Tong. An introduction to meshfree methods and their programming.2005.John Wiley & Sons.

[9] Kiasat, A., Moradi, M., and Hashemolhosseini, H. Application of high order basis functions in solid mechanics by element free galerkin (efg) method. Computational Methods: 1453-1457, 2006. Springe.

[10] Timoshenko, S. and Goodier, J. Theory of elasticity (1970). McGrawHill New York.

[11] Bilal M. Ayyub and McCuen. Numerical Analysis for Engineers Method and Applications (2016). CRC Press Taylor & Francis Group.

[12] Chowdhury, H. A., Wittek, A., Miller, K., and Joldes, G. R. An element free galerkin method based on the modied moving least squares approximation. Journal of Scientic Computing: 1-15, 2016.

[13] Dabboura, E., Sadat, H., and Prax, C. A moving least squares meshless method for solving the generalized kuramoto-sivashinsky equation. Alexandria Engineering Journal**55**(3): 2783-2787, 2016.

[14] Rao, Singiresu S. The finite element method in engineering. Butterworth-heinemann, 2017

[15] YASUDA, Yosuke; SAKUMA, Tetsuya. Boundary Element Method. Computational Simulation in Architectural and Environmental Acoustics, Tokyo: 79-115, 2014.

[16] Dolbow, J., Zhang, Z., Spencer, B., & Jiang, W. Fracture capabilities in grizzly with the extended finite element method (x-fem) Fracture capabilities in grizzly with the extended finite element method (x-fem)2015.

[17] Shivanian, E. Meshless local PetrovGalerkin (MLPG) method for three-dimensional nonlinear wave equations via moving least squares approximation. Engineering Analysis with Boundary Elements**50**: 249-257, 2015.

[18] Taleei, A., & Dehghan, M. An efficient meshfree point collocation moving least squares method to solve the interface problems with nonhomogeneous jump conditions. Numerical Methods for Partial Differential Equations**31**(41): 1031-1053, 2015.

[19] AVESANI, Diego; DUMBSER, Michael; BELLIN, Alberto. An A new class of Moving-Least-Squares WENOSPH schemes. Journal of Computational Physics**270**(41): 278-299, 2014.

Rheological Behavior of Thermosetting Resins in Vacuum Infusion Molding Process

M. Gómez[1], M. Altamiranda[2], M. Arias[3]

[1]maryelegomez18@hotmail.com
Estudiante de Ingeniería Química,
Universidad Tecnológica de Bolívar, Cartagena, Colombia

[2]mafeanayaladeus@hotmail.com
Estudiante de Ingeniería Química,
Universidad Tecnológica de Bolívar, Cartagena, Colombia

[3]mariast@utb.edu.co
Departamento de Ingeniería Química
Universidad Tecnológica de Bolívar, Cartagena, Colombia

Abstract

The study of the rheological behavior of thermoset resins in a vacuum infusion molding process (PMIV) is necessary since the changes in the molecular structure of the resin are evident while the curing reaction occurs, which will influence positively or negatively on the properties and quality of the final product. In the first stage of this work, a bibliographic review of the rheological models that allow studying this behavior is made, finding that the empiric dual-Arrhenius model, which is appropriate when there is no way to measure the speed of the curing reaction experimentally. However, for the implementation of the model, yet experimental viscosity data measured by traditional rheometry techniques are used; what would offer an opportunity to use the simulation by Molecular Dynamics in the physical rheological characterization of the resin that allows obtaining these data and then be implemented to the model. It is expected then to find the operating conditions for the manufacture of composite materials with specific characteristics for use in the shipbuilding industry.

Key Words: Chemorheoloy, Composites, Thermosetting resins, Slip-Links Model

1 Introduction

The Vacuum Infusion Molding Process (PMIV) is an economical and widely used method for the large-scale production of fiber/polymer resin composite parts used in the civil-architectural, aerospace, automobile and shipbuilding industry [1,2,5]. The success of the PMIV depends on the low viscosity of the resin so that its rheological behavior allows the infiltration and complete humidification of the fiber [2]. Nevertheless, when processing thermosetting resins, the interdependence of factors such as viscosity, temperature-time, pressure and the ratio of thermoset resin-curing agent must be considered; since the rheological changes that occur during such processing have a great influence on the properties and quality of the final product [3,5,6]. In this work it is intended to combine the Molecular Dynamics simulation technique with the rheological model, as an alternative for the rheological characterization of the resin, and to later study the rheological behavior of the thermosetting resin-curing agent system during the isothermal curing reaction; which allows to find operating conditions and characteristics of the equipment before being implemented a real production

process, which would help reduce uncertainty, time and costs in the implementation and operation of the production process for commercial purposes.

2 Objectives

2.1 General Objective

Study the rheological behavior of the thermosetting resin-curing agent system during the Vacuum Infusion Molding Process for the manufacture of composite materials used in shipbuilding applications, using Rheological Models for isothermal curing and Simulation by Molecular Dynamics.

2.2 Specific Objectives

Review the existing literature on rheological models for the study of the behavior of the resin-curing agent system for isothermal conditions.
Evaluate the rheological characteristics of the thermosetting resin, using computational simulation for soft materials based on Molecular Dynamics.
Predict the behavior of the viscosity of the thermosetting resin-curing agent system in the isothermal curing reaction, using Rheological Models.
Obtain the operating conditions for the manufacture of composite materials thermosetting Fiber / Polymeric Matrix for shipbuilding use.

3 Literature review

The fact that the viscosity of the molten polymer is reduced during its processing is of great importance; for this reason it is necessary to express and understand the dependence relations between viscosity η and deformation velocity γ; and the way these variables are affected by temperature, structure, composition, etc. Nonetheless, the rheological behavior of thermosetting polymers is considered critical during its processing; due to it implies considering the chemical reactions that occur during the curing thereof [4]. For many years empirical, probabilistic, relationship and free volume analysis models have been proposed [2,6,7], which allow characterizing this behavior for isothermal conditions. To understand this behavior [3], proposes to discuss methods that allow to make rheological measurements on the systems of thermosetting polymers (especially resins) - curing agent, developing a procedure for the analysis of the data in terms of the molecular changes that occur during the cross-linking. Subsequently [4], uses the empirical dual-Arrhenius model that has been the most reported in the literature for isothermal conditions of curing, using computational tools, allowing greater precision in the results of the calculation of the parameters of the model. The empirical model dual-Arrhenius proposes the basic hypothesis that the viscosity of the thermosetting resin system-curing agent is equal to the sum of the physical viscosity and the chemical viscosity; the first measured by experimental techniques and the second measuring parameters by linear regression. Based on this hypothesis, [2,6,10] conclude that this model is appropriate when there is no way to measure the speed of the curing reaction experimentally, since it does not depend explicitly on the scope of the reaction; nevertheless, experimental physical viscosity data, measured in commercial rheometers, are used to implement this model. As yet there are no records of works that use simulation techniques that allow the physical rheological characterization of the resin and be coupled to this empirical model. This is why the Simulation by Molecular Dynamics is presented as an alternative for this characterization, which aims to completely model the rheological properties, using the forces involved, the change of position, speed and orientation of the polymer chain, while they are exposed to stimuli of temperature, pressure, stress, etc., [11]. The Slip-Link Model is part of the set of models used by Molecular Dynamics to explain the internal behavior of polymers. Considering that real polymers present molecular entanglements, the Slip-Links Model considers entanglement points as sliding links and chains between entanglement points as simple springs. Additionally, two chains are

connected by a slip-links, to form a pair, and thus represent an entanglement, which are formed or destroyed by the movement of the polymer chain [12,13].

4 Justification

The need to supply the demand that today's society requires for composite products leads to the gradual increase of its production, and therefore to make optimal use of raw materials, used in production processes, allowing constant progress in research, to have final products with the desired properties and quality. This work aims to predict the behavior of raw materials before and during the production process, using mathematical models and simulation techniques that allow to find operating conditions and characteristics of the equipment before being implemented a real production process, which would help to reduce uncertainty, time and costs, in the implementation and operation of the production process for commercial purposes.

5 Methodology

The methodology for this research consists of several stages according to the objectives: 1) A bibliographic review of the models that allow to predict the rheological behavior for the thermosetting resin system - curing agent for isothermal conditions during the curing reaction is made, 2) Perform Simulation by Molecular Dynamics using the OCTA software in the PASTA module, for the rheological characterization of the resin, 3) Use the viscosity data vs. the proposed temperature, obtained from the rheological characterization by Molecular Dynamics Simulation, and implement them in the dual-Arrhenius empirical model to predict the viscosity behavior of the thermosetting resin-curing agent system during the isothermal curing reaction, 4) To propose the conditions or operation window for composite materials manufacturing laminates with characteristics and properties for shipbuilding applications, using the results obtained from the prediction of the empirical dual-Arrhenius model.

6 Results

The results correspond to partial results of this research, fulfilling the first objective. It is found that the model most used in the study of the rheological behavior of the curing reaction for isothermal conditions is the empiric model dual-Arrhenius; which is appropriate when there is no way to measure the speed of the curing reaction experimentally, since it does not depend explicitly on the scope of this. It is also found that until now all the models to predict the rheological behavior in the reaction of curing use data measured experimentally by means of traditional rheometry techniques. There is then an opportunity for the use of Molecular Dynamics Simulation to perform the physical rheological characterization of the resin, obtaining data that will be implemented in the model.

7 Conclusions

The empirical rheological models, based on probability, relationship and free volume analysis, have been used for many years to predict the rheological behavior of the thermosetting resin-curing agent system during the curing reaction under isothermal conditions, but most of these require parameter data specific to the kinetics of the reaction that can only be measured experimentally. Considering that the empirical dual-Arrhenius model allows the calculation of these from the values obtained by physical rheology, it has been and is still used to predict such behavior.

8 Acknowledgement

Author are grateful to Luis Alejandro Paternina Castro for his comments on the work and Ivan E. Batista-Ochoa for the technical and administrative support.

References

[1] Halley P., Mackay M. Chemorheology of Thermosets-An Overview. *Polymer Engineering And Science.* **1**(3S):593-609, 1996.

[2] Yang J., Xiao J., Zeng J., Peng Ch., Feng X., Hou B. An Empirical Model for Resin Viscosity During Cure in Vacuum Infusion Molding Process. *Appl Compos Mater*, **19**:57358, 2012.

[3] Macosko Ch. Rheological Changes During Crosslinking. *British Polymer Journal*, **17**(2):239-245, 1985

[4] Roller M. B. Rheology of Curing Thermosets: A Review. *Polymer Engineering and Science*, **26**(6):432-440, 1986.

[5] Kenny J. M., Apicella A., Nicolais L. A Model for the Thermal and Chemorheological Behavior of Thermosets. *I: Processing of Epoxy-Based Composites. Polymer Engineering and Science*, **2** (15):973-983, 1989.

[6] Liu Z., Zeng J., Xiao J., Jiang D., Peng Ch. Rheological Behaviors and Processing Windows of Low Viscosity Epoxy Resin for VIMP. *Journal of Wuhan University of Technology-Mater*, 931-934, 2011.

[7] Bullions T. A., Mcgrath J. E., Loos A. C., Development of a Two-Stage, Dual-Arrhenius Rheology Model for a High-Performance PhenylEthynyl-Terminated Poly(Etherimide). *Polymer Engineering and Science*, **42**(1):21822192, 2002.

[8] Tungare A. V., Martin G. C., Gotro J. T. Chemorheological Characterization of Thermoset Cure. *Polymer Engineering and Science*, **28**(16):1071-1075, 1988.

[9] Hsieh T. H, Wang T. L, Ho K. S. Chemorheological Analysis of an Epoxynovolac Molding Compound. *Polymer Engineering and Science*, **40**:418-429, 2000.

[10] Kiunaa N., Lawrencea C. J., Fontanab Q. P. A Model for Resin Viscosity During Cure in the Resin Transfer Moulding Process. *Composites: Part A*, **33**:1497-1503, 2002.

[11] Haile J. M. Molecular Dynamic Simulation: Elementary Methods. Jhon Wiley & Sons Inc. New York, 1992.

[12] Doi M., Takimoto J. Molecular modeling of entanglement. The Royal Society (361):641-652, 2012.

[13] Computer Simulation of Polymeric Materials Applications of the OCTA System. Japan Chemical Innovation Institute (JCII), 2012.

Numerical Modeling of Bio-Polymer Membrane Under Axial Load Using Hyperelastic Finite Element Models

D.R. Brewer [1], J. Useche[2].

[1]davidbrewer123@gmail.com
Departamento de Ingeniería Mecánica,
Universidad Tecnológica de Bolívar, Cartagena, Colombia

[2]juseche@utb.edu.co
Departamento de Ingeniería Mecánica,
Universidad Tecnológica de Bolívar, Cartagena, Colombia

Abstract

The objective of this article is to model the behavior of biopolymer membranes subjected to uniaxial stresses using the finite element method. The bio-polymer membrane material is assumed to be homogeneous and isotropic and incompressibility of materials has been considered. The geometry of the membrane was discretized by uniting rectangular elements of the shell type. The hyperleastic models used were those of Mooney Rivlin (2 and 5 parameter) and Haines and Wilson. The constants of each model were adjusted using the finite element method. The proposed model of finite elements allowed to describe the uniaxial stress test for the experimental conditions used.

Key Words: Hyperelasticity, membrane, biopolymer, finite element analisys

1 Introduction

Large deformation of membrane structures has been the subject of extensive research in recent years due to their applicability in numerous fields, such as scientific ballooning, shock and vibration absorbers, thermal shields, and bioengineering and medical devices.[1]
A characteristic feature of polymeric and bio-polymeric membranes is their hyperelasticity, which is a beneficial attribute particularly in situations where the engineered membrane barrier can experience large deformational behaviour. The hyperelasticity and the accompanying rate-dependency of polymeric membranes is a result of plasticizers that are introduced into the material during its manufacture.[2]
The objective of the present paper is is to simulate numerically the behavior of membranes of biopolymers subjected to uniaxial tensile using the hyperelastic finite element model.

2 Hyperelastic Model

The constitutive behaviour of hyperelastic material is derived from stress energy function W, for isotropic materials (e.g., rubbers) can be represented in terms of right (or left) Cauchy - Green tensor $\mathbf{C}$ (or $\mathbf{B}$) invariants (I_1, I_2, I_3) or eigen values of deformation gradient tensor $\mathbf{F}$, called principal stretches (λ_1, λ_2, λ_3) i.e, [3]:

$$W = W(I_1, I_2, I_3) \quad or \quad W = W(\lambda_1, \lambda_2, \lambda_3)$$

where

$$I_1 = tr(\mathbf{C})$$
$$I_2 = \frac{1}{2}\left[I_1^2 - tr(\mathbf{C}^2)\right]$$
$$I_3 = det(\mathbf{C})$$

The I_1, I_2 and I_3 are three invariants of Green deformation tensor defined in terms of principal stretch ratios λ_1, λ_2 and λ_3 given by [4]:

$$I_1 = \lambda_1^2 + \lambda_2^2 + \lambda_3^2$$
$$I_2 = \lambda_1^2\lambda_2^2 + \lambda_2^2\lambda_3^2 + \lambda_3^2\lambda_1^2$$
$$I_3 = \lambda_1^2\lambda_2^2\lambda_3^2$$

Generally, hyperelastic materials are considered incompressible, i.e. $I_3 = 1$; hence only two independent strain measures namely I_1 and I_2 remain. This that W is a function of I_1 and I_2 only [5]

$$W = W(I_1 - 3, I_2 - 3)$$

2.1 Mooney- Rivlin Model

Mooney [6] proposed a phenomenological model with two parameters based on the assumption of a linear relation between the stress and strain during simple shear deformation. He considers W under the following form:

$$W = C_1(I_1 - 3) + C_2(I_2 - 3) \tag{1}$$

where C_1 y C_2 are two material parameters. This model is widely used for rubber parts in which deformation remains moderate (lower than 200%).
Rivlin [7] extended the previous model by developing W as a polynomial series of (I_1 - 3) and (I_2 - 3)

$$W = \sum_{i,j=0}^{\infty} C_{ij}(\bar{I}_1 - 3)^i(\bar{I}_2 - 3)^j$$

donde C_{ij} are material parameter and $C_{00} = 0$. This series may be truncated according of the order invariantes in:

- First Order (2 parameter):

$$W = C_{10}(\bar{I}_1 - 3) + C_{01}(\bar{I}_2 - 3)$$

- Second Order (5 parameter):

$$W = C_{10}(\bar{I}_1 - 3) + C_{01}(\bar{I}_2 - 3) + C_{11}(\bar{I}_1 - 3)(\bar{I}_2 - 3) + C_{20}(\bar{I}_1 - 3)^2 + C_{02}(\bar{I}_2 - 3)^2$$

2.2 Haines and Wilson Model

This model [8, 9] expands the energy density function W proposed by Rivlin, with six coefficients as:

$$W = C_{10}(\bar{I}_1 - 3) + C_{01}(\bar{I}_2 - 3) + C_{20}(\bar{I}_1 - 3)^2 + C_{11}(\bar{I}_1 - 3)(\bar{I}_2 - 3) + +C_{02}(\bar{I}_2 - 3)^2 + C_{30}(\bar{I}_1 - 3)^3$$

3 Methodology

3.1 Uni-axial Tensile Tests of Bio-Polymer Membrane

The biopolymer membrane is constituted by a mixture of gelatine type B 150 - 170 bloom, distilled water and glycerine. The mechanical behaviour, uni axial tensile tests are carried out according to ASTM standard method D882 (ASTM, 1992). Testing samples have dimension of 80 mm x 25 mm x 0.762 mm with con gauge length of 20 mm. The tensile tests are carried out at a speed of 250 mm/min. The averaged experimental load-displacement results are plotted in Fig.1. The bio-polymer membrane samples are pulled up to an engineering strain of 0.5.

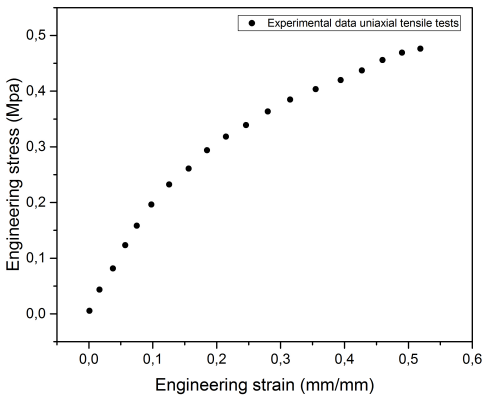

Figure 1: Uni-axial tensile testing results of the bio-polymer membrane

3.2 Numerical Simulation

Finite element model is used to obtain the constants for hyper-elastic material models. The material parameters were determined by the fitting of the strain energy function to stress-strain data using LSDYNA. The material model used was the MAT 77_H proposed in LSDYNA. This material provides a general hyperlelastic model, which expands the energy density function proposed by Rivlin (cite) for the constants:

- C_{01} y C_{10} (Mooney- Rivlin model)
- C_{01}, C_{10}, C_{11}, C_{02} and C_{20} (Mooney- Rivlin model - 5 Parameter)
- C_{01}, C_{10}, C_{11}, C_{02}, C_{20} and C_{30} (Haines and Wilson model)

The membrane was modelled by rectangular shell element, with 1000 elements and 1071 nodes, as shown in the figure 2. A fixed boundary condition was defined along the left edge ($x = 0$) of the rectangular domain, and a defined horizontal velocity of 4.167 mm/s was imposed along its right edge ($x = 20$). This velocity corresponding to implemented in the experimental uni-axial tensile testing.

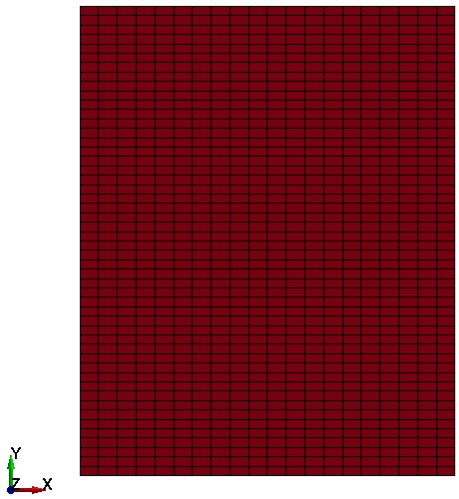

Figure 2: Finite element model

4 Results and Discusions

Figure 1 shows the adjustment of the models proposed with the experimental data of uniaxial tensile tests. The coeffcients of Mooney-Rivlin (2 and 5 parameter) and Haines and Wilson model as calculeted by finite element analysis in LSDYNA, are given in Tables 1-3.

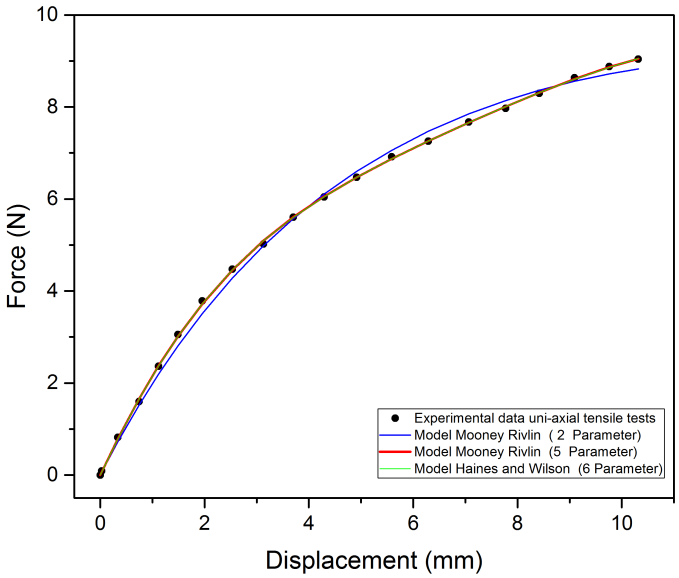

Figure 3: Fitting data experimental uniaxial tensile tests to Model Mooney Rivlin

.

Table 1: Coefficients of Mooney Rivlin model (2 parameter)

C_{10}	C_{01}	R^2
-0.1254	0.5151	0.997899622

Table 2: Coefficients of Mooney Rivlin material model (5 parameter)

C_{10}	C_{01}	C_{11}	C_{20}	C_{02}	R^2
-0.09890	0.5258	5.926	-2.040	-4.366	0.999872107

Table 3: Coefficients of Heines and Wilson Model

C_{10}	C_{01}	C_{11}	C_{20}	C_{02}	C_{30}	R^2
0.02942	0.3935	14.02	-5.577	-9.153	0.1743	0.999874216

The finite element model for the uniaxial tensile tests of is shown in Fig. 4.

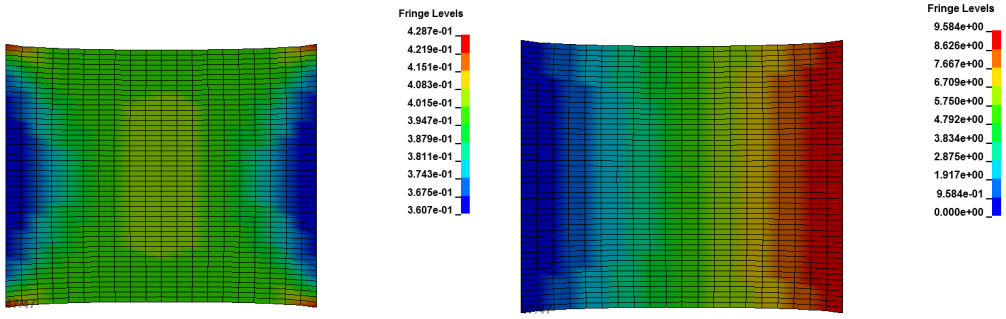

(a) Von Misses Stress (b) Displacement

Figure 4: FE Simulation using Mooney Rivilin model of 5 parameter

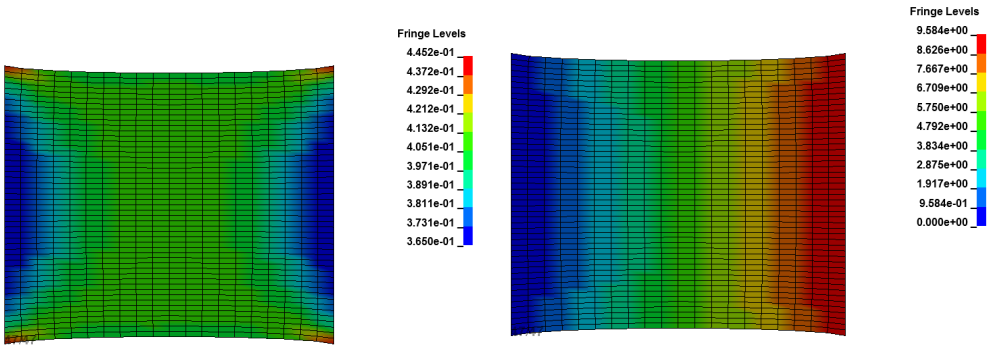

(a) Von Misses Stress (b) Displacement

Figure 5: FE Simulation using Mooney Rivilin model of 5 parameter

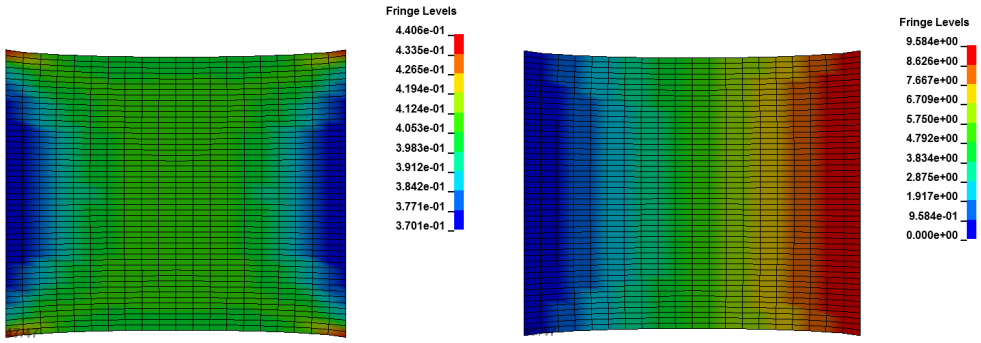

(a) Von Misses Stress (b) Displacement

Figure 6: FE Simulation using Haines and Wilson Model

It is observed from the results of the numerical simulation, that for each hyperelastic model proposed in this study, the finite elements model allows to describe the uniaxial tension test to the experimental conditions.

5 Conclusions

In this work the model of Mooney Rivlin of two and five parameters, and Haines and Wilson model were presented to describe the behavior of the biopolymer membrane. The proposed finite element model allows to simulate adequately the uniaxial experimental stress test, so comparing simulation results with experimental data, it is shown that the model hyperelastic of Mooney Rivlin can properly characterize the mechanical behaviour of the material.

6 Acknowledgement

Author are grateful to the Research Office of Technological Universidad Tecnologica de Bolivar for supporting this research work.

References

[1] Sang Jianbing, Li Xiang, Xing Sufang, and Wang Wenjia, Mechanical Property Analysis of Circular Polymer Membrane under Uniform Pressure. *International Journal of Polymer Science.* vol. 2017, Article ID 4183686, 9 pages, 2017.

[2] Selvadurai, APS and Yu, Q. Mechanics of polymeric membranes subjected to chemical exposure. *International Journal of Non-Linear Mechanics.* **43**:264-276, 2008.

[3] Khajehsaeid, Hesam and Arghavani, Jamal and Naghdabadi, Reza. A hyperelastic constitutive model for rubber-like materials. *European Journal of Mechanics - A/Solids.* **38**: 144-151, 2013

[4] Dolwichai P, Limtragool J, Inban S and Piyasin S. In: *Hyperelastic Material Models for Finite Element Analysis with Commercial Rubber, Technology and Innovation for Sustainable Development Conference (TISD2006).* Khon Kaen, Thailand. Khon Kaen: Khon Kaen University, 2006.

[5] Gent AN. Engineering with rubber: how to design rubber components. *2nd ed. Munich: Hanser Gardener Publication*, 2000.

[6] M. Mooney, A theory of large elastic deformation. *Journal of Applied Physics,.* **2**(9): 582-592, 1940

[7] R.S.Rivlin, Large elastic deformations of isotropic materials.I. fundamental concepts. *Philosophical Transactions of the Royal Society of London. Series A. Mathematical and Physical Sciences.* **240**(9): 459 - 490, 1948

[8] D.W. Haines and W.D. Wilson. Strain-energy density function for rubberlike materials. *Journal of the Mechanics and Physics of Solids.* **27**(4): 345 - 360, 1979

[9] James, A Gr and Green, A and Simpson, GM Strain energy functions of rubber. I. Characterization of gum vulcanizates. *Journal of Applied Polymer Science.* **19**(7): 2033- 2058, 1975

Stochastic Failure Analysis of Submerged Composite Pipes Under Vortex Induced Loads Vibration

L. Pertuz[1], J.Useche[2]

[1]lpertuz@outlook.com
Ingeniero Mecáánico,
Universidad Tecnológica de Bolívar, Cartagena, Colombia

[2]juseche@utb.edu.co
Departamento de Ingeniería Mecánica,
Universidad Tecnológica de Bolívar, Cartagena, Colombia

Abstract

Este trabajo tiene como objetivo, el estudio de una tubería fabricada con material compuesto al ser sometidas a cargas y vibraciones dinámicas producidas por vórtices generados por corrientes submarinas. A través del método de elemento de volumen representativo, elementos finitos y método estadístico de Montecarlo se analizara el comportamiento del material compuesto conociendo sus propiedades físicas (modulo de Young, coeficiente de Poison, modulo de rigidez) generadas a partir de su distribución estocástica de dichas propiedades.

Key Words: Elementos Finitos, Materiales compuestos, vibración por vórtices

1 Introducción

Los métodos numéricos y elementos finitos han generado alternativas en el estudio de los materiales compuestos, ya que estos por su complejidad geométrica y como la variabilidad en sus propiedades físicas son de difícil estudio. Uno de estos métodos es la homogenización del material a través de un elemento de volumen representativo.[8]

El método de elemento de volumen representativo (RVE) consiste en tomar del material compuesto la porción mas pequeña del material, de tal manera que este en su distribución mantenga la proporción de los materiales que lo componen, este volumen representativo contiene las propiedades físicas del material compuesto.[8]

El método Montecarlo es un método numérico que permite resolver problemas estocásticos mediante simulación. La importancia actual del método Montecarlo se basa en la existencia de problemas que tienen difícil solución por métodos exclusivamente analíticos o numéricos, pero que dependen de factores aleatorios o se pueden asociar a un modelo probabilística artificial (resolución de integrales de muchas variables, minimización de funciones, etc.). Gracias al avance en diseño de los ordenadores, cálculos Montecarlo que en otro tiempo hubieran sido inconcebibles, hoy en día se presentan como asequibles para la resolución de ciertos problemas. En estos métodos el error $1/\sqrt{N}$, donde N es el número de pruebas y, por tanto, ganar una cifra decimal en la precisión implica aumentar N en 100 veces. La base es la generación de números aleatorios de los que nos serviremos para calcular probabilidades.[1]

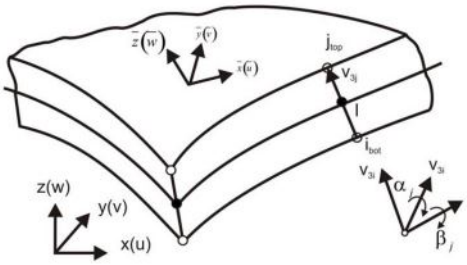

Figure 1: Coordenadas globales y locales [3]

1.1 Descripción del problema

El problema en este trabajo consiste en el estudio de un material compuesto tipo Woven el cual es sometido a cargas dinámicas producidas por vórtices, para este caso se estudiara una tubería sumergía, la cual estará sometida a corrientes submarinas, se analizaran los esfuerzos y deformaciones que ocurren sobre la tubería. Se determinara a partir de los criterios de falla de materiales compuestos, el numero de fallas presentadas durante el proceso estadístico de MonteCarlo, teniendo en cuenta las condiciones estocásticas que presenta el material compuesto, así como la ayuda de un software de dinámica de fluido computacional para simular la generación de vórtices sobre la tubería, y el uso de los elementos finitos para el análisis sobre la tubería.

2 Formulación de elementos finitos

Consideremos un elemento de cáscara. El elemento de cáscara tiene ocho nodos, para los cuales se realiza el análisis.Sean (ξ, η) las coordenadas naturales en la superficie media. Y ς es la coordenada natural a lo largo de la dirección del grosor.[3][9]

La posición de cualquier punto dentro del elemento de carcasa puede escribirse en términos de coordenadas nodales como [3]:

$$\begin{Bmatrix} X \\ Y \\ Z \end{Bmatrix} = \sum_{i=1}^{8} N_i(\xi,\eta) \; \{ \tfrac{1+\varsigma}{2} \begin{Bmatrix} X_i \\ Y_i \\ Z_i \end{Bmatrix}_{top} + \tfrac{1+\varsigma}{2} \begin{Bmatrix} X_i \\ Y_i \\ Z_i \end{Bmatrix}_{botton} \}$$

Puesto que se supone que ς es normal a la superficie media, la expresión anterior se puede reescribir en términos de un vector que conecta los puntos superior e inferior de la carcasa como [3]:

$$\begin{Bmatrix} X \\ Y \\ Z \end{Bmatrix} = \sum_{i=1}^{8} N_i(\xi,\eta) \; \{ \tfrac{1}{2} \begin{Bmatrix} X_i \\ Y_i \\ Z_i \end{Bmatrix}_{top} - \begin{Bmatrix} X_i \\ Y_i \\ Z_i \end{Bmatrix}_{botton} + \tfrac{\varsigma}{2} \begin{Bmatrix} X_i \\ Y_i \\ Z_i \end{Bmatrix}_{top} - \begin{Bmatrix} X_i \\ Y_i \\ Z_i \end{Bmatrix}_{botton} \}$$

O

$$\begin{Bmatrix} X \\ Y \\ Z \end{Bmatrix} = \sum_{i=1}^{8} N_i(\xi,\eta) \; \{ \begin{Bmatrix} X_i \\ Y_i \\ Z_i \end{Bmatrix} + \tfrac{\varsigma}{2} V_{3i} \; \}$$

La relación entre la deformación y el desplazamiento se describe por [3][9]:

$$\{\varepsilon\} = \{B\}\{d\} \tag{1}$$

La relación de deformación de tensión es dada por:

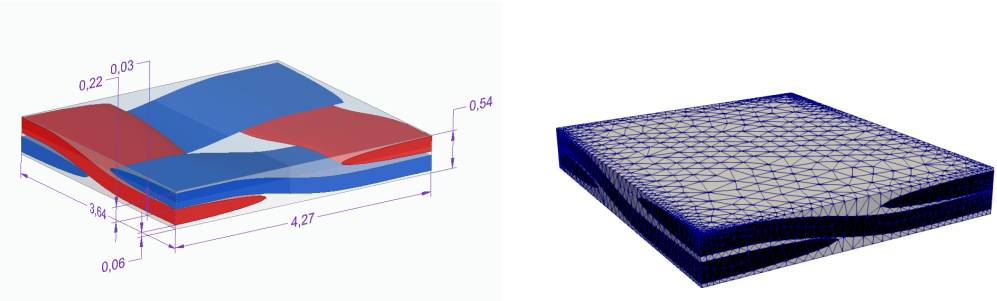

Figure 2: Modelo CAD y mallado del modelo el elemento de volumen representativo del compuesto tipo Woven

$$\{\sigma\} = \{Q\}\{\varepsilon\} \tag{2}$$

$$\begin{bmatrix}\sigma_1\\ \sigma_2\\ \sigma_4\\ \sigma_5\\ \sigma_6\end{bmatrix}^{(k)} = \begin{bmatrix}\bar{\mathrm{Q}}_{11} & \bar{\mathrm{Q}}_{12} & 0 & 0 & \bar{\mathrm{Q}}_{16}\\ \bar{\mathrm{Q}}_{12} & \bar{\mathrm{Q}}_{22} & 0 & 0 & \bar{\mathrm{Q}}_{26}\\ 0 & 0 & \bar{\mathrm{Q}}_{44} & \bar{\mathrm{Q}}_{45} & 0\\ 0 & 0 & \bar{\mathrm{Q}}_{45} & \bar{\mathrm{Q}}_{55} & 0\\ \bar{\mathrm{Q}}_{16} & \bar{\mathrm{Q}}_{26} & 0 & 0 & \bar{\mathrm{Q}}_{66}\end{bmatrix}^{(k)} \begin{bmatrix}\varepsilon_1\\ \varepsilon_2\\ \varepsilon_4\\ \varepsilon_5\\ \varepsilon_6\end{bmatrix} - \begin{bmatrix}\bar{\mathrm{e}}_{31}\\ \bar{\mathrm{e}}_{32}\\ 0\\ 0\\ \bar{\mathrm{e}}_{36}\end{bmatrix}^{(k)} \quad H\zeta \tag{3}$$

La matriz de relación de deformación de tensión está representada por:

$$\begin{bmatrix}N\\ M\end{bmatrix} = \begin{bmatrix}[A] & [B]\\ [B] & [D]\end{bmatrix}\begin{bmatrix}\varepsilon^0\\ k\end{bmatrix} - \begin{bmatrix}N\\ M\end{bmatrix}^M \tag{4}$$

Donde los coeficientes de rigidez de la lamina (A_{ij}, B_{ij}, D_{ij}) son definidas por:

$$A_{ij} = \sum_{i=1}^{N} \overline{Q}_{ij}^k(\zeta_{k+1} - \zeta_k), i, j = 1, 2, 6$$

$$B_{ij} = \frac{1}{2}\sum_{i=1}^{N} \overline{Q}_{ij}^k(\zeta_{k+1}^2 - \zeta_k^2), i, j = 1, 2, 6$$

$$D_{ij} = \frac{1}{3}\sum_{i=1}^{N} \overline{Q}_{ij}^k(\zeta_{k+1}^3 - \zeta_k^3), i, j = 1, 2, 6$$

$$A_{ij} = \sum_{i=1}^{N} \overline{Q}_{ij}^k(\zeta_{k+1} - \zeta_k), i, j = 4, 5 \tag{5}$$

El modelo de elemento representativo del material compuesto tipo Woven se realizo en un software CAD a partir de dimensiones tomadas del propio material. En la **figura 2** se muestra el modelo elaborado en el sistema CAD para el análisis por elementos finitos.

El modelo esta compuesto por elementos tetraedros, un numero aproximado de 5000 elementos, numero obtenido a partir de un análisis de convergencia. Se tomo esta forma del elemento de volumen representativo, debido a la configuración geométrica de la fibra, ya que es una fibra bidimensional simétrica, esta forma se repite a lo lago del material compuesto.

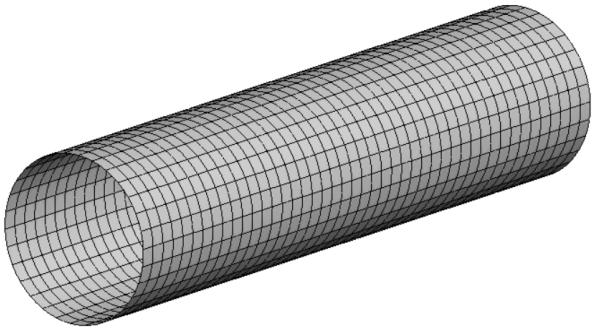

Figure 3: Modelo de la tubería de material compuesto utilizada para el análisis

2.1 Características de la tubería para análisis de elementos finitos

La tubería utilizada para este análisis consiste en una fabricada con material compuesto (Woven-Eglass/Epoxi), con diámetro externo de 0.1 m y 0.41 m de longitud, la tubería para la simulacion tendrá apoyos en el borde superior e inferior, y la superficie a lo largo de esta quedara libre de restricciones para ver el comportamiento de la presión generada por los vórtices en cada instante de tiempo.

La tubería para el analisis de elementos finitos utiliza el elemento shell, un numero de 1350 elementos y 4110 nodos.

3 Análisis Hidrodinámico

Las cargas aplicadas al modelo de la tubería, serán extraídas de una simulación por dinámica de fluido computacional, en las que en un canal se ubica un tubo, y a través de este fluye agua, la cual se generaran vórtices de Von Karman al transcurrir determinado tiempo.

Para la simulación se utilizo un software libre (OpenFoam) de dinámica de fluidos computacional, estableciendo las siguientes propiedades para la simulación:

Propiedades para simulacion en OpenFoam del fluido	
Velocidad de salida del fluido	0.0125 m/s
Velocidad de salida del fluido	zeroGradient
Presion a la entrada	zeroGradient
Presion a la salida	uniform 0
Tiempo inicial	0 seg
Tiempo final	500 seg
Delta de tiempo	0.01 seg

La malla para el modelo CFD consta de 169536 nodos y 83968 elementos hexaedros, este numero de elementos y nodos es obtenido a partir del análisis de convergencia que se le realiza a la malla del modelo, ver la **figura 5**.

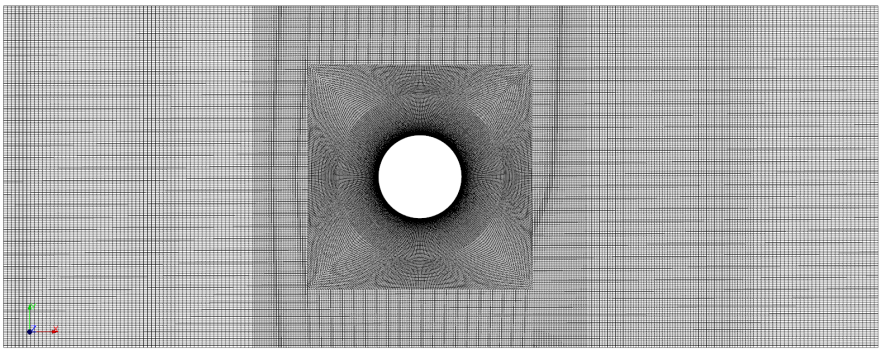

Figure 4: Malla utilizada para análisis del modelo CFD

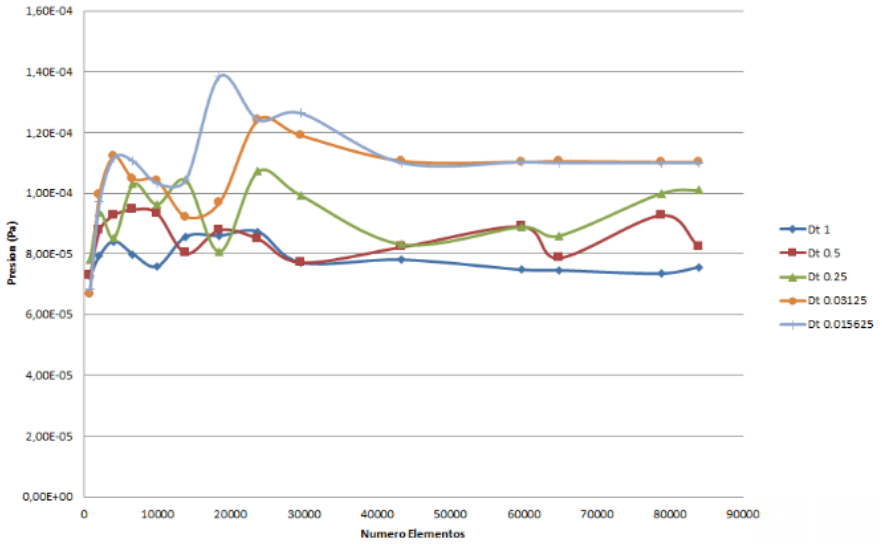

Figure 5: Analisis de convergencia para la malla utilizada en el analisis CFD

4 Resultados

4.1 Análisis de la tubería bajo criterios de falla para material compuesto

Los resultados obtenidos en la simulacion utilizando el método de MonteCarlo se registraron en los siguientes histogramas, en los cuales se utilizaron los siguientes criterios de falla para materiales compuestos:

- Máximo esfuerzo en X, Y o XY [2]:

$$\sigma_1 = F_1, \sigma_2 = F_2, \sigma_6 = F_6 \tag{6}$$

- Máxima deformación en X, Y o XY [2]:

$$\sigma_1 = F_1 + v_{12}\sigma_2, \sigma_2 = F_2 + v_{12}\frac{E2}{E1}\sigma_1, \sigma_6 = F_6 \tag{7}$$

- Marin Modificado [2]:

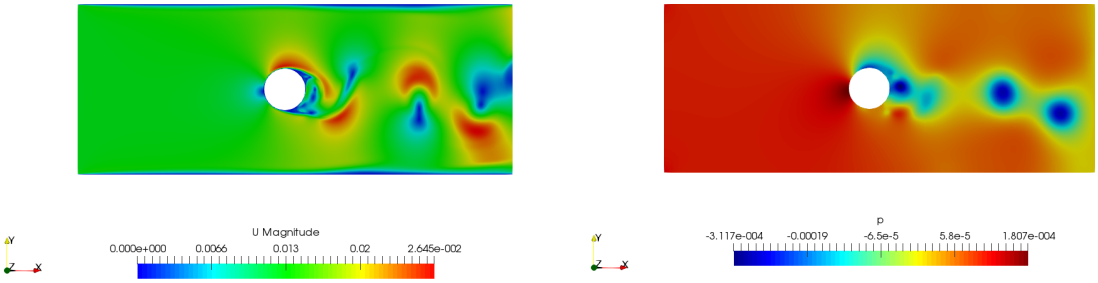

Figure 6: Modelado CFD de la presion y velocidad del fluido sobre la tubería en estudio

$$(\frac{\sigma_1^2 - K_2\sigma_1\sigma_2}{F_{1t}F_{1c}}) + (\frac{\sigma_2^2}{F_{2t}F_{2c}}) + (\frac{F_{1c} - F_{1t}}{F_{1t}F_{1c}})\sigma_1 + (\frac{F_{2c} - F_{2t}}{F_{2t}F_{2c}})\sigma_2 + (\frac{\sigma_6}{F_6})^2 = 1 \tag{8}$$

- Energía distorcional de Norris [2]:

$$(\frac{\sigma_1}{F_1})^2 - (\frac{\sigma_1\sigma_2}{F_1F_2}) + (\frac{\sigma_2}{F_2})^2 + (\frac{\sigma_6}{F_6})^2 = 1 \tag{9}$$

- Interacción de Norris [2]:

$$(\frac{\sigma_1}{F_1})^2 + (\frac{\sigma_2}{F_2})^2 + (\frac{\sigma_6}{F_6})^2 = 1 \tag{10}$$

- Tsai-Hill [2]:

$$(\frac{\sigma_1}{F_1})^2 - (\frac{\sigma_1\sigma_2}{F_1^2}) + (\frac{\sigma_2}{F_2})^2 + (\frac{\sigma_6}{F_6})^2 = 1 \tag{11}$$

Una primera parte de estos histogramas (Figura 6) hace referencia al numero de fallas en tuberías dentro de un numero de cien iteraciones, esta muestra la cantidad y el tiempo a lo largo de la simulacion de las cargas dinámicas donde se presenta la falla, los otros histogramas (Figura 7) hacen referencia a la lamina donde se presenta la falla.

5 Conclusiones

Con ayuda de los métodos numéricos, el análisis de elementos finitos y métodos estadísticos podemos realizar problemas muy complejos de ingeniería donde se puedan realizar un numero grande de pruebas a través de la computación, esto ayuda a ahorrar costos económicos y de tiempo, el numero de pruebas físicas a realizar se reduciría debido a que estas solo servirían como parámetro inicial para obtener los valores típicos, en este caso de los materiales compuestos en estudio.

Otro análisis en la elaboración de este trabajo, es la variedad de teorías que se utilizan para el análisis de materiales compuestos, vemos que la variación que se presentan en los resultados es debido a que las teorías de falla dependen del tipo de falla que se este estudiando, por lo cual no existe una teoría de falla que involucre todos los tipos de falla que se presentan en los materiales compuestos.

References

[1] Licesio J. Rodriguez - Aragon Simulacion, Método de Montecarlo. *.Área de Estadística e Investigación Operativa*, 2011.

[2] M.N. ABOUELWAFA, HASSAN EL-GAMAL, YASSER S. M. AND WAEL A. AL-TABEY A New Failure Criterion for Woven-roving GFRE Thick Tube Subjected to Combined Fatigue Bending Moments and Internal hydrostatic Pressure . **Pag**:105, 2017.

[3] J.N. Reddy Mechanics of Laminated Composite Plates and Shells: Theory and Analysis, Second Edition **Pag**:449-453, 2004.

[4] M. Schäfer, S. Turek Benchmark Computations of Laminar Flow Around a Cylinder **Pag**:3, 1996.

[5] Jasper van Dillewijn, Roselma Velasquez Diseño de tramos libres de tuberias submarinas sometidas a fuerzas hidrodinamicas *Universidad Catolica Andres Bello* , 2011.

[6] David Roylance Laminate Composite Plates *Massachusetts Institute of Technology* , 2000.

[7] Michael W. Hyer Stress Analysis of fiber-Reinforced composite materials *McGraw-Hill International Editions* , 1998.

[8] Robert M. Jones Mechanics Of Composite Materials - Second Edition *Taylor and Francis* , 1998.

[9] J. N. Reddy Theory and Analysis of Elastic Plates and Shells , 2006

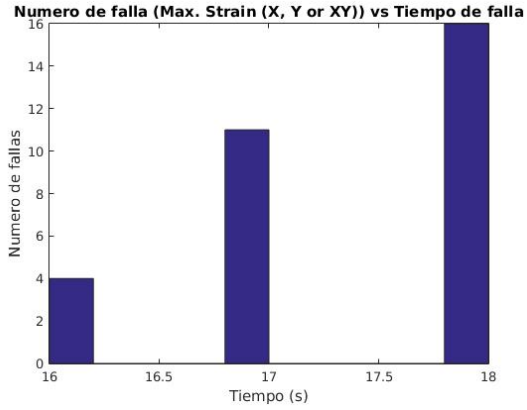

(a) Histograma bajo criterio de maxima deformacion en X, Y y XY

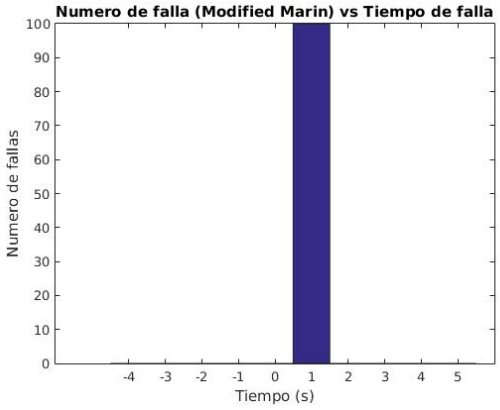

(b) Histograma bajo el criterio de Marin modificado

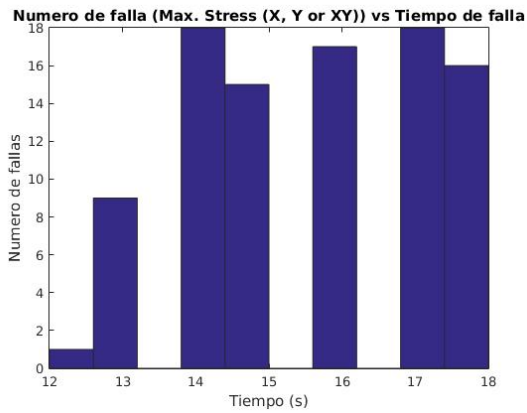

(c) Histograma bajo criterio de maximo esfuerzo en X, Y y XY

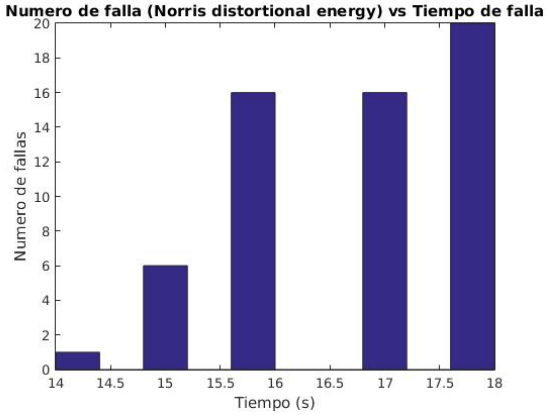

(d) Histograma bajo criterio de energia distorcional de Norris

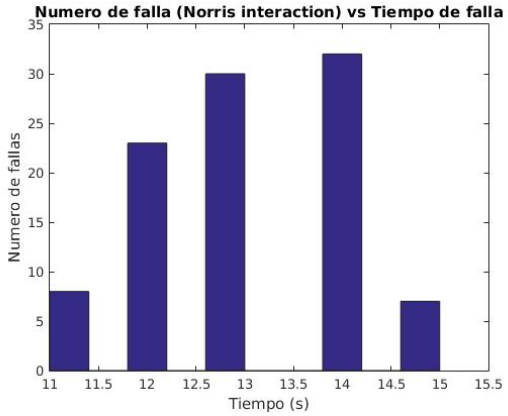

(e) Histograma bajo criterio de interaccion de Norris

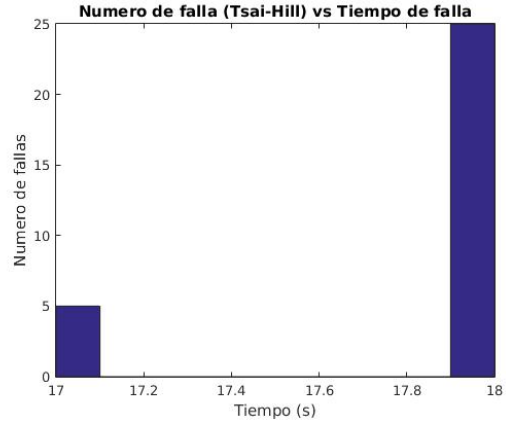

(f) Histograma bajo criterio de Tsa-Hill

Figure 7: Histogramas de numero de fallas vs tiempo (s) de falla de la tubería en la simulación de Montecarlo

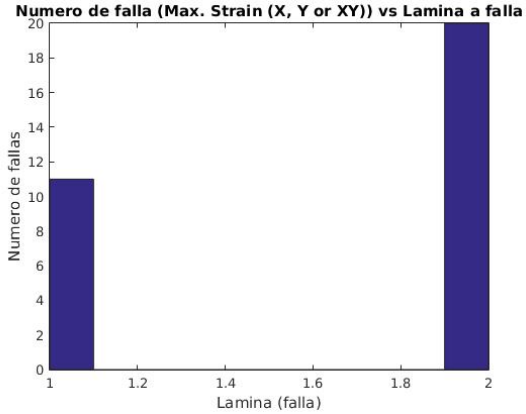

(a) Histograma bajo criterio de maxima deformacion en X, Y y XY

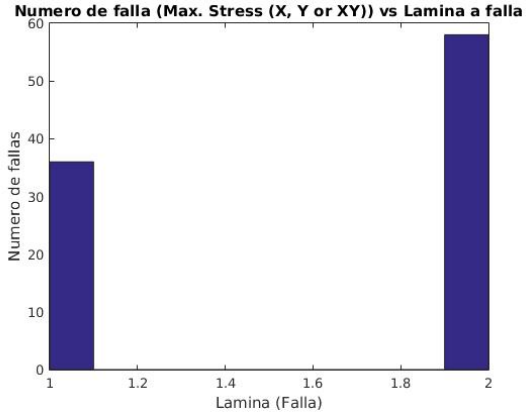

(b) Histograma bajo criterio de maximo esfuerzo en X, Y y XY

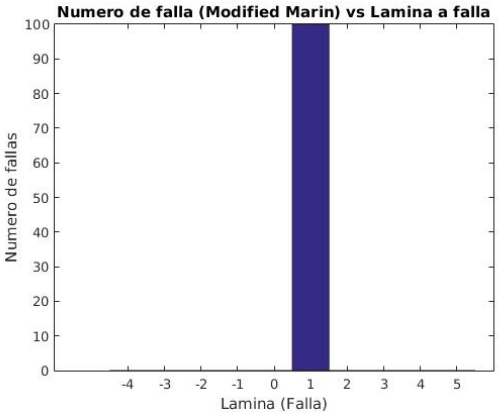

(c) Histograma bajo el criterio de Marin modificado

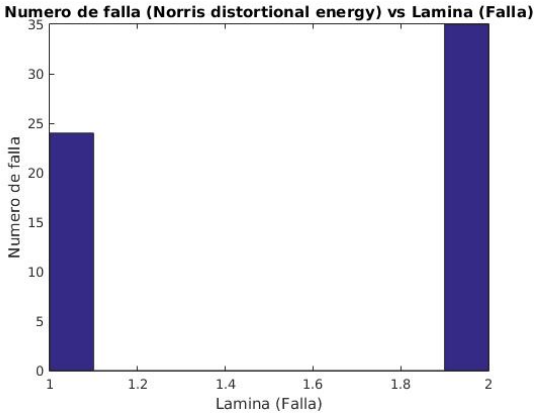

(d) Histograma bajo criterio de energia distorcional de Norris

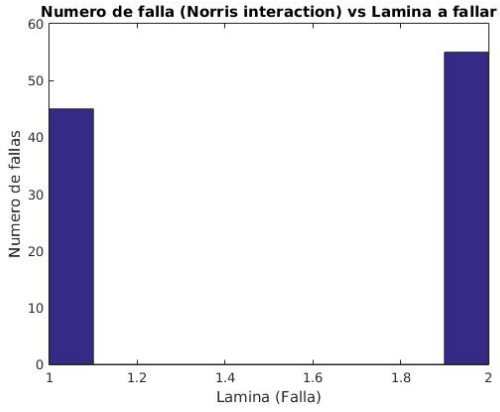

(e) Histograma bajo criterio de interaccion de Norris

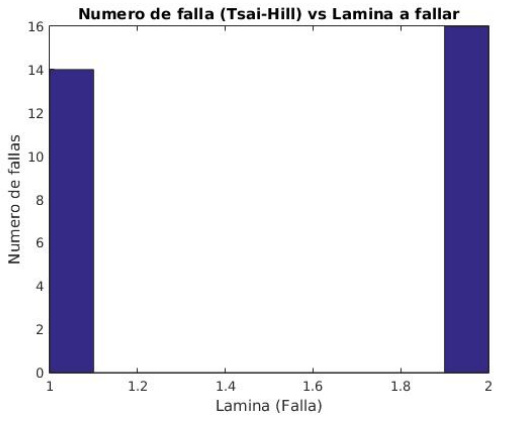

(f) Histograma bajo criterio de Tsa-Hill

Figure 8: Histogramas de numero de fallas vs lamina de falla de la tubería en la simulación de Montecarlo

Analysis of Plates Through MLPG 3D Solid Elasticity

L. Paternina[1], E. Arrieta[2], J. Useche[3]

[1]lapc1917@hotmail.com
Departamento de Ingeniería Mecánica,
Universidad Tecnológica de Bolívar, Cartagena, Colombia

[2]dirmec@utb.edu.co
Departamento de Ingeniería Mecánica,
Universidad Tecnológica de Bolívar, Cartagena, Colombia

[3]juseche@utb.edu.co
Departamento de Ingeniería Mecánica
Universidad Tecnológica de Bolívar, Cartagena, Colombia

Abstract

Recent studies in numerical methods for three-dimensional elasticity have been influenced by the presence of meshfree methods. Though some methods does not use mesh for main variable interpolation, they still need one for the integration (integration background mesh). In this work, the implementation of a truly meshless method for the description of three-dimensional elastic phenomena is carried out for estimation of the minimum size where linear elasticity can work in objects with shape similar to plates. An initial calcutation was perfomed in a cantilever beam with squared cross section and later its width was decreased. The meshless model and the results are presented.

Key Words: Three-dimensional, linear elasticity, Meshless Local Petrov Galerkin, plates

1 Introduction

Meshless methods have been considered like a recent alternative to the Finite Element Method (FEM) for the computational modelling of diverse engineering phenomena. These methods were needed when the characteristic mesh from FEM became an obstacle to the description of events like fracture, great deformations, nonlinear behavior or discontinuities in materials.

One of the proposed meshless methods that has been popular is Element-Free Galerkin, which is based on the global weak form of the partial differential equation of interest. The drawback of the method was in the presence of a integration background mesh for the solution of the weak form integrals, which make the meshing problems still present.

Similar to EFG -a pure Galerkin scheme-, MLPG (Meshless Local Petrov-Galerkin) was proposed method where the inner product of the functions is made with different basis functions. This method has been used to solve three-dimensional problems with linear materials [1, 2], with anisotropy in functionally graded materials [4], in nonlinear materials with plastic deformation [6, 7, 8] and bi-dimensionally in naval plates [9].

In this paper the Meshless Local Petrov-Galerkin Method is applied to a cantilever beam with variable width. The weakened equations for three-dimensional linear elasticity are established. The essential boundary conditions (displacements) are enforced via Lagrange Multipliers. The displacement and energy relative errors are going to be calculated through the L2 norm. The behavior of those error parameters will be evaluated

depending of the width of the beam in order to estimate the minimal size when 3D solid numerical formulation can solve 3D problems.

2 Linear elasticity equations

For a three-dimensional body, the Cauchy tensor or stress tensor is defined as:

$$[\sigma] = \begin{bmatrix} \sigma_{xx} & \sigma_{xy} & \sigma_{xz} \\ \sigma_{yx} & \sigma_{yy} & \sigma_{yz} \\ \sigma_{zx} & \sigma_{zy} & \sigma_{zz} \end{bmatrix} \tag{1}$$

In this work, repeated indices refer to normal stresses and different indices refers to shear stresses.

The strain-stress equations for isotropic bodies are given by:

$$\begin{bmatrix} \sigma_{xx} \\ \sigma_{yy} \\ \sigma_{zz} \\ \sigma_{xy} \\ \sigma_{yz} \\ \sigma_{zx} \end{bmatrix} = \frac{E}{(1+\nu)(1-2\nu)} \begin{bmatrix} 1-\nu & \nu & \nu & 0 & 0 & 0 \\ \nu & 1-\nu & \nu & 0 & 0 & 0 \\ \nu & \nu & 1-\nu & 0 & 0 & 0 \\ 0 & 0 & 0 & \frac{1-2\nu}{\nu} & 0 & 0 \\ 0 & 0 & 0 & 0 & \frac{1-2\nu}{\nu} & 0 \\ 0 & 0 & 0 & 0 & 0 & \frac{1-2\nu}{\nu} \end{bmatrix} \begin{bmatrix} \varepsilon_{xx} \\ \varepsilon_{yy} \\ \varepsilon_{zz} \\ \varepsilon_{xy} \\ \varepsilon_{yz} \\ \varepsilon_{zx} \end{bmatrix} \tag{2}$$

where, E is the Young's modulus and ν the Poisson's ratio.

The inner equilibrium equations of the solid object are given by:

$$\begin{aligned} \frac{\partial \sigma_{xx}}{\partial x} + \frac{\partial \sigma_{xy}}{\partial y} + \frac{\partial \sigma_{xz}}{\partial z} + \rho_o f_x = 0 \\ \frac{\partial \sigma_{yx}}{\partial x} + \frac{\partial \sigma_{yy}}{\partial y} + \frac{\partial \sigma_{yz}}{\partial z} + \rho_o f_y = 0 \\ \frac{\partial \sigma_{zx}}{\partial x} + \frac{\partial \sigma_{zy}}{\partial y} + \frac{\partial \sigma_{zz}}{\partial z} + \rho_o f_z = 0 \end{aligned}$$

where, ρ_o is the density of the object, f_x, f_y, and f_z are cartesian components of the body forces.

3 Meshless approximation

Due the lack of a connectivity mesh in the discretization of the geometry, the desired solution function must be obtained from a set of scattered points. Therefore, other types of interpolation or approximation functions are preferred than Lagrange polynomials. The Moving Least Squares scheme (MLS) provides continuity, good smoothness and high accuracy. The equations for the main field function are:

$$\phi(x) = \sum_{i=1}^{n} \alpha^T p(x_i) \omega(x_i) \tag{3}$$

where $\phi(x)$ is the MLS function, $p(x_i)$ is the monomial basis vector (this vector defines the order of the MLS scheme) and $\omega(x_i)$ is the weight function, which ensures the smoothness of the approximation while the local interpolation subdomain is moving through the whole geometrical domain. α is an intermediate vector that can be calculated by the matrix:

$$A = \sum_{i=1}^{n} \omega(x)(x_i) p^T(x_i) \tag{4}$$

$$A\alpha = p(x) \tag{5}$$

For the calculation of the MLS derivatives, the equations are:

$$\frac{\partial \phi}{\partial x_j} = \sum_{i=1}^{n} \frac{\partial \alpha}{\partial x_j}^T p\left(x_i\right) \omega\left(x_i\right) + \alpha^T p\left(x_i\right) \frac{\partial \omega\left(x_i\right)}{\partial x_j} \tag{6}$$

$$\frac{\partial \alpha}{\partial x_j} = A^{-1}\left(-\frac{\partial A}{\partial x_j}\alpha + \frac{\partial p}{\partial x_j}\right) \tag{7}$$

$$\frac{\partial A}{\partial x_j} = \sum_{i=1}^{n} \frac{\partial \omega\left(x_i\right)}{\partial x_j} p\left(x_i\right) p^T\left(x_i\right) \tag{8}$$

4 Meshless Local Petrov Galerkin

The Meshless Local Petrov Galerkin (MLPG) is a numerical method based in the local weak form of the partial differential equations. Its main characteristic is the use of different functions for the approximation for the trial and test functions, which in this work, are the MLS functions and its weight functions used in their conformation respectively. The equation (3) is weakened -the conversion of the strong form (derivative form) to the weak form through the Gauss Divergence Theorem- and after many algebraic procedures -introducing the meshless approximation- the integral equations can be written as:

$$\int_{\Omega_s} \left(B_\psi\right)^T D B_\phi d\Omega - \int_{\Gamma_{su}^I} V N D B_\phi d\Gamma = \int_{\Gamma_{su}^I} V \bar{t} d\Gamma + \int_{\Omega_s} V b d\Omega \tag{9}$$

where B_ψ, B_ϕ and V are matrices operators for three-dimensional problems which contains the test, trial and weight functions respectively.

$$B_\psi = \begin{bmatrix} \partial\psi/\partial x_1 & 0 & 0 \\ 0 & \partial\psi/\partial x_2 & 0 \\ 0 & 0 & \partial\psi/\partial x_3 \\ 0 & \partial\psi/\partial x_3 & \partial\psi/\partial x_2 \\ \partial\psi/\partial x_3 & 0 & \partial\psi/\partial x_1 \\ \partial\psi/\partial x_2 & \partial\psi/\partial x_1 & 0 \end{bmatrix} \quad B_\phi = \begin{bmatrix} \partial\phi/\partial x_1 & 0 & 0 \\ 0 & \partial\phi/\partial x_2 & 0 \\ 0 & 0 & \partial\phi/\partial x_3 \\ 0 & \partial\phi/\partial x_3 & \partial\phi/\partial x_2 \\ \partial\phi/\partial x_3 & 0 & \partial\phi/\partial x_1 \\ \partial\phi/\partial x_2 & \partial\phi/\partial x_1 & 0 \end{bmatrix} \quad V = \begin{bmatrix} \psi & 0 & 0 \\ 0 & \psi & 0 \\ 0 & 0 & \psi \end{bmatrix}$$

The algebraic form of the equation (9) is:

$$K_I U = f_I \tag{10}$$

where

$$K_I = \int_{\Omega_s} \left(B_\psi\right)^T D B_\phi d\Omega - \int_{\Gamma_{su}^I} V N D B_\phi d\Gamma \tag{11}$$

$$f_I = \int_{\Gamma_{su}^I} V \bar{t} d\Gamma + \int_{\Omega_s} V b d\Omega \tag{12}$$

The boundary conditions can be enforced through lagrange multipliers. The equations are written as:

$$\mathbf{G}_{IK} = -\int_{\Gamma_u} \phi_I N_K d\Gamma \tag{13}$$

$$\mathbf{q}_K = -\int_{\Gamma_u} N_K d\Gamma \tag{14}$$

When the interpolation function used for the equations (13) and (14) is the Dirac delta function, the enforcement method is known as collocation point [10] and the equations are:

$$\mathbf{G}_{IK} = -\phi_I(x_K) \tag{15}$$

$$\mathbf{q}_K = -\mathbf{u}(x_K) \tag{16}$$

After assembling the global stiffness matrix, the final linear system of equations in a matrix form is obtained:

$$\begin{bmatrix} \mathbf{K} & \mathbf{G}^T \\ \mathbf{G} & 0 \end{bmatrix} \begin{bmatrix} \mathbf{U} \\ \boldsymbol{\lambda} \end{bmatrix} = \begin{bmatrix} \mathbf{f} \\ \mathbf{q} \end{bmatrix} \tag{17}$$

5 Numerical examples

5.1 Cantilever beam with variable width

5.1.1 Numerical implementation and definition of geometry

The weight function used in this work is the quartic spline -this is not referring to geometric splines for CAD geometric tools- which is defined as:

$$w_i(\rho) = \begin{cases} 1 - 6\rho^2 + 8\rho^3 - 3\rho^4 & \text{if} \quad \rho \leq 1 \\ 0 & \text{if} \quad \rho > 1 \end{cases} \tag{18}$$

where

$$\rho = \frac{d}{R} \tag{19}$$

d is the distance between the center of the local domain and the point of interest and R is the characteristic size of the local domain -it it is a circle, R is its radius, but if it is a rectangle, R is the width or height-.

In this work, the local domains will be rectangular (in three dimensions, it is a box) so that there are three values for R: R_x, R_y and R_z. The size of the local domains can be different for the domain integration (test function) or the approximation domain (trial function). Those sizes are scaled through dimensionless factors for the two domains and a characteristic nodal spacing. Therefore:

$$r_q = \alpha_q h \quad r_s = \alpha_s h$$

where α_q and α_s are the dimensionless factor for integration and approximation domain sizes respectively.

The MLS functions will be of order 1 and 2.

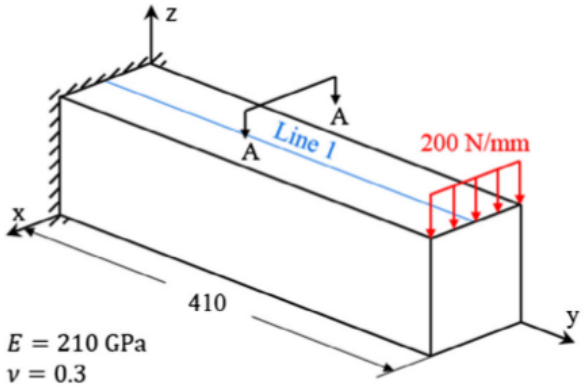

Figure 1: Cantilever beam [5]

Consider a cantilever beam, with a rectangular cross area as showed in figure 1. The length L, the width T and the H height are extended in the cartesian axis y, x and z respectively. The free extreme is subjected to the action of a parabolic traction τ. The boundary condition equations for the displacement and stresses can be obtained when the analytical equations presented in [2, 3] are evaluated in the coordinated belonging to the boundary of interest:

- Displacements ($y = 0$)

$$u(y,z) = \frac{Pz}{6EI}\left[(6L - 3y)\,y + (2+\nu)\left(z^2 - \frac{D^2}{4}\right)\right]$$

$$v(y,z) = \frac{-P}{6EI}\left[3\nu z^2\,(L-y) + (4+5\nu)\,\frac{D^2 y}{4} + (3L-y)\,y^2\right]$$

- Stresses ($y = L$)

$$\sigma_{yy} = \frac{P\,(L-x)\,y}{I}$$

$$\sigma_{xx} = 0$$

$$\sigma_{zz} = 0$$

$$\tau_{yz} = -\frac{P}{EI}\left(\frac{D^2}{4} - y^2\right)$$

For a preliminary calculation, many nodal configurations were tested. In the numerical solution, there was used a configuration of 21 x 5 x 5 nodes along the x, y and z axis. The size of the domain integration was $\alpha_q = 1.0$ and for the approximation domain $\alpha_s = 4.0$ with MLS of quadratic order. The L2 and energy error were approximately 0.0289 and 0.0679. The displacement and stress values along many lines are shown afterwards.

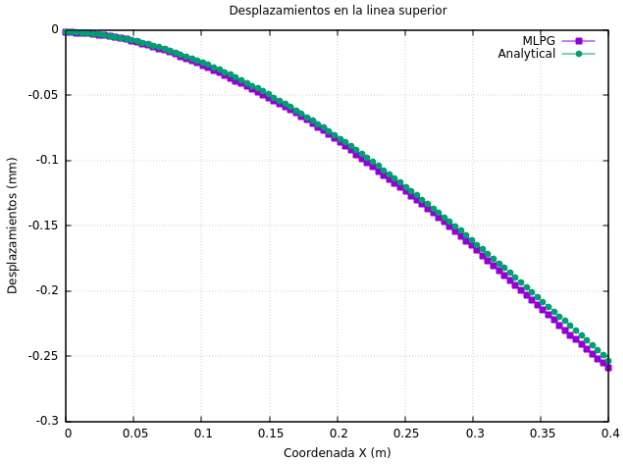

Figure 2: Displacement in x-axis along the blue line from the 1

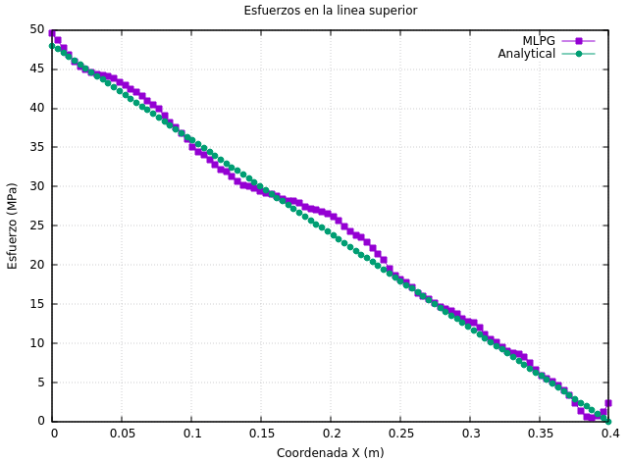

Figure 3: Normal stress in x-axis along the blue line from the 1

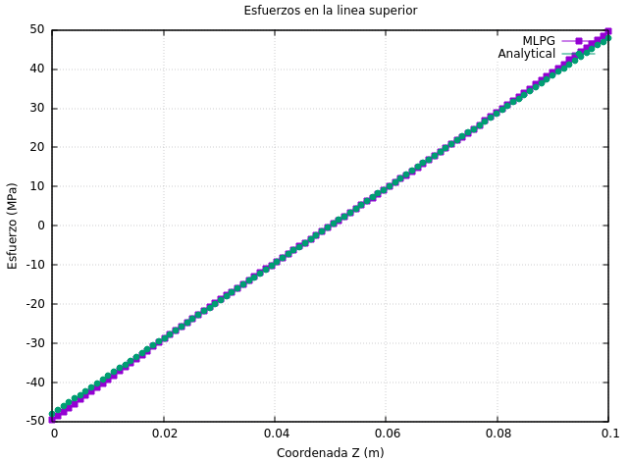

Figure 4: Normal stress in x-axis along the middle vertical line of the fixed extreme of the beam from 1

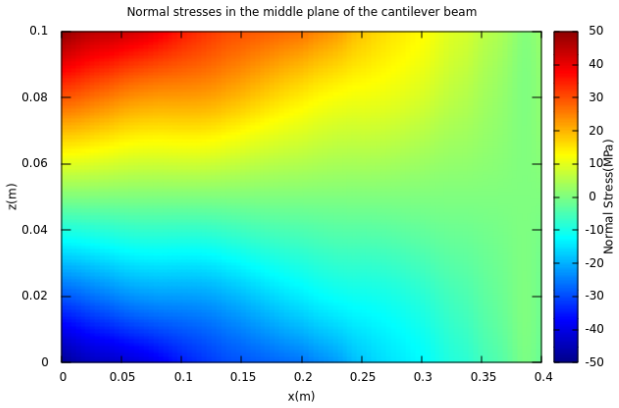

Figure 5: Normal stress in x-axis along the middle longitudinal section of the beam from 1

5.1.2 Cantilever beam with variable width

Many cases were considered, with T/H variable. Table 1 shows the displacement and energy norm relative errors obtained with the distribution of nodes used in the previous section. Good agreements were obtained for T/H relations above 0.005 (See Table 1 and Fig 6).

Table 1: Displacement and energy norm relative error for cantilever beam with variable width

T/H	r_u	r_e
1.0	0.0289	0.0679
0.5	0.0983	0.1077
0.2	0.0291	0.0566
0.1	0.00851	0.0416
0.05	0.0103	0.0383
0.02	0.0365	0.0386
0.01	0.0864	0.1788
0.005	0.1158	0.0603
0.002	0.2395	0.2596
0.001	0.5223	0.5599

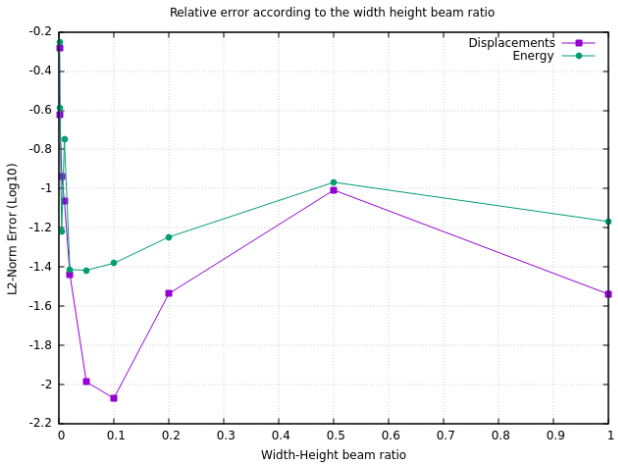

Figure 6: Relative error for cantilever beam with variable width

Finer nodal configurations (nodal spacing h less than 0.01) could not be tested due the computational limitations of the computer used in the calculations (Inspiron 3442 with a i5-4210U CPU of 1.7 GHz, 4 RAM GB), however there is the hypothesis that using cubic MLS functions can increase the convergence rate, yet the monomial basis vector has 20 elements, making the MLS calculations more difficult and more sensible to the nodal configuration.
Extremely low values of the T/H ratio suddenly increase the displacement and energy errors because of the MLS approximation. The A matrix calculated in equation (3) becomes ill-conditioned and doesn't have full rank (the rows involved with the y coordinate approach to zero or their values are so similar that those rows may look linearly dependent). The inversion of an ill-conditioned matrix may affect the stability and the approximation of the MLS basis functions. As their derivatives are less stable than the main function, the ill-conditioning effect will propagate until the calculation of the local weak form integrals of equation (9).

6 Conclusions

The Meshless Local Petrov-Galerkin Method applied to solid with shapes like-plate was presented. The weak local equations for three-dimensional elasticity and the Lagrange Multipliers method for boundary conditions enforcement were established. There is a good agreement between the analytical and numerical solutions of the three-dimensional elasticity for a cantilever beam with squared cross area. Therefore, when the width of the cantilever beam is decreasing, the relative errors of the numerical test are small, however tiny values of width make the MLS approximation unsuitable and strange results are obtained.

7 Acknowledgement

The main author thanks to Professor Arrieta and Professor Useche for their assessment in the elaboration of the paper and the required calculations.

References

[1] Li Q., Shen S., Han Z. D., Atluri S. N. Application of Meshless Local Petrov-Galerkin (MLPG) to problems with singularities, and material discontinuities, in 3-D elasticity. *C. - Comput. Model. Eng. Sci.*. **4**(5): 571585, 2003.

[2] Han Z. D., Atluri S. N. Meshless local Petrov-Galerkin (MLPG) approaches for solving 3D problems in elasto-statics. *C. - Comput. Model. Eng. Sci.* **6**(2): 169-188, 2003.

[3] Atluri S. N., Kim H-G, Cho J. Ya A critical assessment of the truly meshless local Petrov-Galerkin (MLPG), and local boundary integral equation (LBIE) methods. *Computational mechanics.* **24**(5): 348–372, 1999.

[4] Sladek J., Sladek V., Solek P. Elastic analysis in 3D anisotropic functionally graded solids by the MLPG *C. - Comput. Model. Eng. Sci.*. **43**(3): 223-251, 2009.

[5] Lai B., Bathe K. J. The method of finite spheres in three-dimensional linear static analysis *Computers and Structures.* **219**(19): 161–173, 2016.

[6] Rezaei Mojdehi A., Darvizeh A., Basti A., Rajabi H. Three dimensional static and dynamic analysis of thick functionally graded plates by the Meshless Local Petrov-Galerkin (MLPG) method. *Eng. Anal. Bound. Elem.* **35**(11): 1168-1180, 2011.

[7] Mojdehi A. R., Darvizeh A., Basti A. Application of meshless local petrov-galerkin (MLPG) method to three dimensional elasto-plastic problems based on deformation theory of plasticity *C. - Comput. Model. Eng. Sci.* **77**(1): 1-31, 2011.

[8] Rezaei Mojdehi A.,Darvizeh A., Basti A. Nonlinear dynamic analysis of three-dimensional elasto-plastic solids by the meshless local Petrov-Galerkin (MLPG) method *Comput. Mater. Contin.* **29**(1): 15-39, 2012.

[9] Chen J. P., Tang W. Y., Xu M. P. A numerical method of the ship structures analysis based on Meshless Local Petrov-Galerkin method. *Int. J. Steel Struct.* **15**(4): 777-783, 2015.

[10] Nguyen V. P., Rabczuk T., Bordas S., Duflot M. Meshless methods: A review and computer implementation aspects. *Mathematics and Computers in Simulation* **79**(3): 763-813, 2008.

VIGILADA MINEDUCACIÓN